Removal of Arsenic and Metals from Mine-impacted Groundwater Using Organic Carbon and Zero-valent Iron in Passive Remediation Systems

by

Joanne U. Angai

A thesis

presented to the University of Waterloo

in fulfilment of the

thesis requirement for the degree of

Master of Science

in

Earth Sciences

Waterloo, Ontario, Canada, 2020

Author’s Declaration

I hereby declare that I am the sole author of this thesis. This is a true copy of the thesis including any required final revisions, as accepted by my examiners.

I understand that my thesis may be made electronically available to the public.

Abstract

Arsenic (As) is a wide-spread contaminant, often encountered in drainage associated with Au mining. The oxidation state controls the mobility and toxicity of As in water. Passive remediation is a potential management approach for removing As and other contaminants from mine waters. Permeable reactive barriers (PRBs) are a passive management technology that utilizes reactive material to target the contaminant of interest through chemical interactions, including precipitation, reduction, and adsorption. The Long Lake field site is an abandoned Au mine located near Sudbury, ON, characterized by acidic conditions and high concentrations of As, Fe, SO_4^{2-}, and metals in the tailings porewater. This project aims to evaluate the potential for passive remediation to remove As and other contaminants from mine drainage at the Long Lake field site.

A series of laboratory column experiments were conducted to determine the potential of a reactive mixture, containing organic carbon substrates (OC), granular zero-valent iron (ZVI), limestone, and silica sand, to remove As and increase the pH of the water. Groundwater was collected directly from the Long Lake site and used as the influent solution for the column experiments. Results indicated an increase in pH and removal of As within the first 3 cm of reactive material. Removal of As in the three treatment columns represented 99.9% of the total As in the water. A decrease in Eh, the production of H_2S, a decline in SO_4^{2-} concentrations, an enrichment in $\delta^{34}S$, and the presence of microbial communities, indicated the presence of bacterially-mediated SO_4^{2-} reduction. The percentage of total reads that were sulfate-reducing bacteria (SRB) ranged from 2.4 – 10.0%. Sulfate reduction rates ranged from 0.18 to 0.20 mg L^{-1} d^{-1} g^{-1} dry wt. % OC for the three treatment columns. Synchrotron-radiation bulk S X-ray absorption near-edge structure (XANES) indicated that accumulation of reduced S phases including pyrite and elemental S occurred in the solid material during the experiments. Geochemical modelling results further indicate that precipitation of sulfides including mackinawite, greigite, pyrite, sphalerite, and chalcopyrite, was favoured. Removal of metals, including Cu, Ni, and Zn, is attributed to the precipitation of low-solubility metal sulfides following SO_4^{2-} reduction. Synchrotron As μXANES indicated that As was present in secondary precipitates in both the reduced phase, as realgar, orpiment, and arsenopyrite, and in the oxidized phase, as As(V) sorbed onto ferrihydrite. The addition of OC contributed to the development of sulfate-reducing conditions and resulted in bacterially-mediated SO_4^{2-} reduction. The presence of ZVI led to the formation of ferrous iron and ZVI corrosion products, providing additional surface sites for As adsorption.

Two separate field-reaction cell (30 cm inner diameter by 99 cm length) trials, were conducted at the Long Lake mine site, one in the summer (mean air temperature of 19 °C) and one in the autumn (mean air temperature of -1 °C), to evaluate the effect of temperature on As removal. A reactive mixture

containing ZVI, OC, limestone, and pea gravel (at similar proportions to the column experiments) was utilized. The results from the summer field cell were similar to those observed in the laboratory column experiments. A decrease in As, metals, SO_4^{2-}, and acidity, were observed within the first 9 cm of reactive media. Reactions contributing to metal and As removal include precipitation of low-solubility metal sulfides and adsorption on ZVI corrosion products. The results from the autumn field cell indicated that the development of bacterially-mediated SO_4^{2-} reduction was limited, with lower percentages of SRB observed in the autumn cell compared to the summer cell and laboratory column experiments. Removal of As, metals, and an increase in pH was observed in the autumn cell, however, aqueous chemistry results did not show a decline in SO_4^{2-} concentrations or an enrichment in $\delta^{34}S$. Optical microscopy indicated the presence of pyrite and pyrrhotite in the autumn cell material, but abundance was lower in the autumn cell than in the other two experiments. The results from bulk S XANES indicated the accumulation of sulfides in the solid material was also limited. The difference in results between the summer cell and autumn cell may be attributed to colder outside temperatures during the field trial or the shorter duration of the experiment.

The results from all three experiments indicate that the addition of OC to the reactive mixture was important for the development of sulfate-reducing conditions and the growth and activity of SRB. The addition of ZVI further enhanced the removal of As, metals, and Fe from the water through the formation of corrosion products and metal sulfide precipitation. Removal of As and metals and an increase in pH was observed in all three experiments despite varying flow rates and fluctuating temperatures. These results indicate that a mixture of OC and ZVI will likely be effective at removing As and metals from mine drainage waters under a range of flow rates and temperature conditions.

Acknowledgements

I would like to thank both of my supervisors, Dr. Carol Ptacek and Dr. David Blowes, for your support, guidance, patience, and belief in me over the past three years. I am incredibly grateful for the opportunity to work under the both of you. Thank you for providing me with countless opportunities and for sharing your knowledge with me. I would also like to extend thanks to my committee members, Dr. Laura Hug and Dr. Walter Illman, for your interest and support in my research project.

A huge thank you to all the members of the GGR group for creating an open, safe, and supportive work environment. I would like to thank Jeff Bain, for your unparalleled help in the field and laboratory and for spending countless hours going over the smallest of details with me. Steve Holland, thank you for your endless support throughout my entire degree and for your continued belief in my ability to succeed. I would like to thank Krista Elena, for your answers and input to my many questions, Laura Groza, for fixing every laboratory problem I encountered, Sara Fellin, for keeping me sane in EIT 1008 when I was ready to give up, Joy Hu, for your analytical support and shared love of plants, and Eva Pakostova, for your constant reminder of my strength and capability. Thank you to all the graduate, PDFs, and co-op students who helped me out in the field and laboratory.

A huge shoutout to all the friends I made over these past few years. This includes Gabi Blanton, David Hilger, David Geuder, Peter Van Eck, Adrienne Schmall, Emily Saurette, and Mason McAlary. Brent Verbuyst, thanks for being my first friend in Waterloo and for answering every single question I could possibly have. Your friendship and endless support have kept me going throughout my degree. And to all my friends back home, who called and comforted me despite the distance, I appreciate and love you.

Finally, I would like to thank my incredible family for supporting and encouraging me throughout this entire endeavor. Darrell and Ely, thank you for driving to pick me up whenever I was discouraged and for never doubting me. Frankie and SueAnn, thanks for the food, adventures, and much-needed clarity through all the hard times. Finally, thanks to my parents, for your endless love, faith, and support in me and everything that I do. I would not have made it without all of you.

Table of Contents

Author's Declaration ii
Abstract iii
Acknowledgements v
List of Figures ix
List of Tables xvii
List of Abbreviations xviii
Chapter 1: *Introduction* 1
1.1 Arsenic in Groundwater 1
1.2 Site Background 2
1.3 Permeable Reactive Barriers 2
1.4 Research Objectives 3
1.5 Experimental Approach 3
1.6 Thesis Organization 4
Chapter 2: *Removal of Arsenic and Metals from Groundwater Impacted by Mine Waste Using Zero-valent Iron and Organic Carbon: Laboratory Column Experiments* 6
2.1 Introduction 8
2.2 Methodology 10
2.2.1 Column Design and Experimental Setup 10
2.2.2 Sample Collection 11
2.2.3 Analytical Methods 12
2.3 Results 16
2.3.1 Water Chemistry 16
2.3.2 Microbiology 20
2.3.3 Mineralogy 21
2.4 Discussion 23
2.4.1 Water Chemistry 23
2.4.2 Dissolved Arsenic and Metal Removal 26
2.4.3 Carbon and Nutrient Release 31
2.4.4 Sulfate Reaction Rates 32
2.5 Conclusions 33
Chapter 3: *Removal of Arsenic and Metals from Groundwater Impacted by Mine Waste Using Zero-valent Iron and Organic Carbon: Field-reaction Cell* 54
Executive Summary 55

3.1 Introduction 55
3.2 Methodology 58
3.2.1 Reaction Cell Design 58
3.2.2 Reaction Cell Set-Up 58
3.2.3 Sample Collection 59
3.2.4 Analytical Methods 61
3.3 Results 64
3.3.1 Water Chemistry 64
3.3.2 Microbiology 66
3.3.3 Mineralogy 66
3.4 Discussion 67
3.4.1 Water Chemistry 67
3.4.2 Dissolved Arsenic and Metal Removal 69
3.4.3 Carbon and Nutrient Release 73
3.4.4 Sulfate Reaction Rates 74
3.5 Conclusions 75
Chapter 4: *Dissolved Arsenic Treatment using Permeable Reactive Materials: Evaluation of Temperature Dependence* 88
4.1 Introduction 89
4.2 Methodology 92
4.2.1 Reaction Cell Setup 92
4.2.2 Sample Collection 93
4.2.3 Analytical Techniques 94
4.3 Results 96
4.3.1 Temperature 96
4.3.2 Water Chemistry 96
4.3.3 Solid Phase Characterization 97
4.4 Discussion 98
4.4.1 Cold Temperature Reaction Cell 98
4.4.2 Comparison to Laboratory Columns and Warm Temperature Reaction Cell 101
4.5 Conclusions 107
Chapter 5: *Conclusions and Recommendations* 124
References 128
Appendix A: *Additional Data Presented in Chapter 2* 137
Appendix B: *Additional Data Presented for Chapter 3* 152

Appendix C: *Additional Data Presented for Chapter 4* 159

List of Figures

Figure 1.1 Map of Long Lake and surrounding area (left). The red star is the location of the sand-covered Long Lake Tailings Impoundment (TA-01, TA-02, and TA-03) to the south of Long Lake (right; modified after Verbuyst, 2020). 5

Figure 2.1 Map of Long Lake with respect to Sudbury, ON. The red star to the south of the southwest end of Long Lake is the location of the Long Lake Au Mine Tailings Impoundment (modified after Verbuyst, 2020). 35

Figure 2.2 Map of the southwest end of Long Lake and tailings impoundment to the south. TA-01, TA-02, and TA-03 are the three sand-covered tailings areas (modified after Verbuyst, 2020)..... 36

Figure 2.3 Schematic diagram of the experimental setup and column design. 37

Figure 2.4 pH, Eh, and alkalinity versus PVs in the influent and effluent of the four columns. The OC:ZVI ratio in column T0 is 0:0, T1 is 40:10, T2 is 30:20, and T3 is 20:30. 38

Figure 2.5 pH, Eh, and alkalinity in aqueous samples collected along the length of columns T0, T1, T2, and T3 at two different time points. Each column of graphs represents a different experimental column. Distance 0 cm represents the influent concentration and 30 cm represents the effluent concentration. The OC:ZVI ratio of column T0 is 0:0, T1 is 40:10, T2 is 30:20, and T3 is 20:30. 39

Figure 2.6 Concentrations of As, Fe, and SO_4^{2-} versus PVs in the influent and effluent of the four columns. Input of As was discontinuous throughout the experiment, with concentrations varying between four main stages (left). A spike of As and Fe was added at the third grey dashed line (35 PVs) following the end of stage III. The OC:ZVI ratio of column T0 is 0:0, T1 is 40:10, T2 is 30:20, and T3 is 20:30. 40

Figure 2.7 Concentrations of As, Fe, and SO_4^{2-} in aqueous samples collected along the length of columns T0, T1, T2, and T3 at two different time points. Each column of graphs represents a different experimental column. Distance 0 cm represents the influent concentration and 30 cm represents the effluent concentration. The OC:ZVI ratio of column T0 is 0:0, T1 is 40:10, T2 is 30:20, and T3 is 20:30. 41

Figure 2.8 Concentrations of metals (Al, Cd, Co, Cu, Ni, and Zn) versus PVs in the influent and effluent of the four columns. The OC:ZVI ratio of column T0 is 0:0, T1 is 40:10, T2 is 30:20, and T3 is 20:30. 42

Figure 2.9 Top row: Concentrations of S^{2-} compared to $\delta^{34}S\text{-}SO_4$ values in aqueous samples collected along the length of columns T0, T1, T2, and T3. Bottom row: Concentrations of dissolved inorganic carbon (DIC) are compared to $\delta^{13}C$-DIC along the column length. Data are from the second vertical profile collected. The OC:ZVI ratio of column T0 is 0:0, T1 is 40:10, T2 is 30:20, and T3 is 20:30. 43

Figure 2.10 Concentrations of dissolved organic carbon (DOC) versus PVs (left) compared to the changes in DOC values in aqueous samples collected along the length of columns T0, T1, T2, and T3 (right). The OC:ZVI ratio of column T0 is 0:0, T1 is 40:10, T2 is 30:20, and T3 is 20:30. 44

Figure 2.11 MPN enumeration results for solid-phase samples collected along the length of columns T0, T1, T2, and T3. The enumeration of both sulfate-reducing bacteria (SRB) and neutrophilic heterotrophs (nH) is shown. 45

Figure 2.12 Relative abundance of known SRB identified through 16S rRNA amplicon sequencing in the solid material collected along the length of columns T0, T1, T2, and T3. The five most abundant genera are plotted, and the remaining SRB grouped separately. The total number of reads of SRB obtained during sequencing (top bar) and the percentage of total reads including the distinction between major SRB genera (bottom bar) are shown. 46

Figure 2.13 Reflected light microscopy image of the replacement of OC by a secondary precipitate (A). The presence of S (B) and Fe (C) in the precipitate (right) is shown through SEM imaging. ... 47

Figure 2.14 Bulk S XANES spectra of solid samples collected from laboratory columns T1, T2, and T3. Spectra of unreacted, untreated ZVI and other standards are also shown. The spectral peak locations for pyrite (a), elemental S (b), tetramethylene sulfoxide (c), and gypsum (d) are shown with dashed lines. 48

Figure 2.15 Results from optical microscopy (A), Fe µXRF imaging (B), S µXRF imaging (C), and S µXANES spectra (right) of a secondary precipitate replacing cellular organic matter. Spectra from two separate scan locations (spots 1 and 4) are plotted with standards used for LCF. The

spectral peak locations of pyrite (a), elemental S (b), Na-thiosulfate (c), K-tetrathionate (d), and gypsum (e) are shown with dashed lines. 49

Figure 2.16 Results from optical microscopy (A), Fe µXRF imaging (B), As µXRF imaging (C), and As µXANES spectra (right) of a secondary precipitate that formed between grains of silica sand (column T2). The spectrum collected from spot 1 is plotted with the standards used for LCF. The spectral peak locations of realgar (a), orpiment (b), and As(V) sorbed onto ferrihydrite (c) are shown with dashed lines. 50

Figure 2.17 Left: Results from optical microscopy (A), Fe µXRF imaging (B), and close ups of As µXRF imaging (C) and Fe µXRF imaging (D) of a location noted in (B). Right: As µXANES spectra of a secondary precipitate that formed along the edge of a silica sand grain (column T3). The spectrum collected for spot 1 is plotted with the standards used for LCF. The spectral peak locations of arsenopyrite (a), realgar (b), and As(V) sorbed onto ferrihydrite (c) are shown with dashed lines. 51

Figure 2.18 Regression fits of SO_4^{2-} removal as a function of residence time in the three treatment columns. 52

Figure 3.1 Map of the approximate location where the reaction cell was installed. 77

Figure 3.2 Schematic of the reaction cell installation and design. 78

Figure 3.3 pH, Eh, alkalinity, and EC for aqueous samples collected along the reaction cell length. Distance 0 cm represents influent concentrations and 100 cm represents effluent concentrations. 79

Figure 3.4 As and Fe concentrations in aqueous samples collected along the reaction cell length. Distance 0 cm represents influent concentrations and 100 cm represents effluent concentrations. 80

Figure 3.5 Metal (Al, Cu, Ni, and Zn) concentrations in aqueous samples collected along the reaction cell length. Distance 0 cm represents influent concentrations and 100 cm represents effluent concentrations. 81

Figure 3.6 SO_4, S^{2-}, DOC, and DIC concentrations and $\delta^{34}S$-SO_4 and $\delta^{13}C$-DIC values along the reaction-cell length. Distance 0 cm represents influent concentrations and 100 cm represents effluent concentrations. 82

Figure 3.7 MPN enumeration results for solid-phase samples collected at different locations along the length of the reaction cell. The enumeration of sulfate-reducing bacteria (SRB), iron-reducing microorganisms (IRM), and neutrophilic heterotrophs (nH) are shown. One IRM data point is plotted outside of the graph area because an accurate enumeration could not be determined for $>10^{10}$ g^{-1}. 83

Figure 3.8 Percent of known SRB identified at different intervals along the reaction-cell length through DNA extraction analysis. The four most abundant genera are plotted, and the remaining SRB grouped separately. The unreacted material is represented by NM. 84

Figure 3.9 Reflected light microscopy images of grains showing (A) framboidal pyrite precipitated between grains of pea gravel, (B) exsolution texture observed on a grain of pyrrhotite, (C) Fe-sulfide precipitate replacement of the OC structure, and (D) blade-like texture found along the rim of a ZVI grain. 85

Figure 3.10 Bulk S XANES spectra of solid samples collected from the reaction cell. The number (cm) represents the distance from the influent end of the cell. Spectra for unreacted, acid-washed ZVI, and other standards are also shown. The spectral peak locations for pyrrhotite (a), elemental S (b), tetramethylene sulfoxide (c), and gypsum (d) are shown with dashed lines. 86

Figure 3.11 Regression fits for SO_4 removal as a function of residence time for four different sampling days. 87

Figure 4.1 Changes in temperature during the autumn 2018 field trial (red) compared to the summer 2019 field trial (blue; Chapter 3). The average temperature for the laboratory column experiments was 22 ℃ (dashed line; Chapter 2). 109

Figure 4.2 Profiles of pH, Eh, and alkalinity for select dates from the autumn reaction cell (top), summer reaction cell (middle; Chapter 3), and laboratory columns prior to termination of the experiment (bottom; Chapter 2). Distance 0 cm represents influent concentrations and 100 cm or 30 cm represents effluent concentrations. 110

Figure 4.3 Profiles of aqueous As and Fe for select dates from the autumn reaction cell (top), summer reaction cell (middle; Chapter 3), and laboratory column columns prior to termination of the experiment (bottom; Chapter 2). Distance 0 cm represents influent concentrations and 100 cm or 30 cm represents effluent concentrations. 111

Figure 4.4 Profiles of aqueous Al, Cu, Ni, and Zn for select dates from the autumn reaction cell (top), summer reaction cell (middle; Chapter 3), and laboratory column columns prior to termination of the experiment (bottom; Chapter 2). Distance 0 cm represents influent concentrations and 100 cm or 30 cm represents effluent concentrations. 112

Figure 4.5 Profiles of aqueous of SO_4, $\delta^{34}S$-SO_4, and S^{2-} for select dates from the autumn reaction cell (top), summer reaction cell (middle; Chapter 3), and from laboratory column columns prior to termination of the experiment (bottom; Chapter 2). Distance 0 cm represents influent concentrations and 100 cm or 30 cm represents effluent concentrations. 113

Figure 4.6 Profiles of aqueous of DOC, DIC, and $\delta^{13}C$-DIC for select dates from the autumn reaction cell (top), summer reaction cell (middle; Chapter 3), and from laboratory columns prior to termination of the experiment (bottom; Chapter 2). Distance 0 cm represents influent concentrations and 100 cm or 30 cm represents effluent concentrations. 114

Figure 4.7 Profiles of aqueous of NH_3-N and PO_4-P for select dates from the autumn reaction cell (top), summer reaction cell (middle; Chapter 3), and laboratory column columns prior to termination of the experiment (bottom; Chapter 2). Distance 0 cm represents influent concentrations and 100 cm or 30 cm represents effluent concentrations. 115

Figure 4.8 Percent known SRB identified through DNA extraction analysis in the autumn cell (top left), summer cell (right; Chapter 3) and laboratory column T3 with the closest ZVI:OC ratio (bottom left; Chapter 2) at different distances along the cell/column length. The most abundant genera are plotted and the remaining SRB are grouped separately. 116

Figure 4.9 Reflected light microscopy images of grains showing (A) Fe-sulfide precipitate replacement of OC structure and (B) corrosion rims on a ZVI grain. 117

Figure 4.10 Bulk S XANES spectra of solid samples collected from the reaction cell. The number (cm) represents the distance from the influent end of the cell. Unreacted, acid-washed ZVI and other standards are also shown. The spectral peak locations for pyrrhotite/FeS (a), pyrite (b), sphalerite (c), tetramethylene sulfoxide (d), and gypsum (e) are shown with dashed lines. 118

Figure 4.11 Bulk S XANES spectra of solid samples collected from the autumn reaction cell (W), summer reaction cell (S; Chapter 3), and laboratory column experiments (T; Chapter 2). The number (cm) represents the distance from the influent end of the cell. Unreacted untreated ZVI and acid-washed ZVI are also plotted. Dashed lines represent peak locations for pyrrhotite/FeS (a), pyrite (b), tetramethylene sulfoxide (c), and gypsum (d)..... 119

Figure 4.12 Comparison of the wt. % S in the solid material and aqueous SO_4 concentrations for the autumn reaction cell (RC1, top right), summer reaction cell (RC2, bottom right; Chapter 3), and laboratory column experiments (T1, T2, T3, left; Chapter 2), collected along the cell/column length. Distance 0 cm represents influent concentrations and 100 cm or 30 cm represents effluent concentrations. 120

Figure A.1 Concentrations of Al, Co, and Ni in aqueous samples collected along the length of columns T0, T1, T2, and T3 at two different time points. Each column of graphs represents a different experimental column. Distance 0 cm represents the influent concentration and 30 cm represents the effluent concentration. The OC:ZVI ratio of column T0 is 0:0, T1 is 40:10, T2 is 30:20, and T3 is 20:30. 138

Figure A.2 Concentrations of Cu, Zn, and Cd in aqueous samples collected along the length of columns T0, T1, T2, and T3 at two different time points. Each column of graphs represents a different experimental column. Distance 0 cm represents the influent concentration and 30 cm represents the effluent concentration. The OC:ZVI ratio of column T0 is 0:0, T1 is 40:10, T2 is 30:20, and T3 is 20:30. 139

Figure A.3 Concentrations of S^{2-}, NH_3-N, and PO_4-P versus PVs in the influent and effluent of the four columns. The OC:ZVI ratio of column T0 is 0:0, T1 is 40:10, T2 is 30:20, and T3 is 20:30.. 140

Figure A.4 Concentrations of S^{2-}, NH_3-N, and PO_4-P in aqueous samples collected along the length of columns T0, T1, T2, and T3 at two different time points. Each column of graphs represents a different experimental column. Distance 0 cm represents the influent concentration and 30 cm represents the effluent concentration. The OC:ZVI ratio of column T0 is 0:0, T1 is 40:10, T2 is 30:20, and T3 is 20:30. 141

Figure A.5 Reflected light microscopy images of a unreacted ZVI grain. 142

Figure A.6 Reflected light microscopy image of the formation of a secondary precipitate around silica sand grains (A). SEM imaging of Fe- (B) and S- (C) rich precipitate (right). 143

Figure A.7 Comparison between the wt. % S in the solid column material and the aqueous SO_4^{2-} concentrations in the column porewater. 144

Figure A.8 Saturation indices calculated using PHREEQCI with the WATEQ4F database for potential reaction products. The colours represent the different columns; the white circle is the influent, the blue triangle is T0, the red square is T1, the orange diamond is T2, and the green triangle is T3. 145

Figure A.9 Saturation indices calculated using PHREEQCI with the WATEQ4F database for sulfide phases. The colours represent the different columns; the white circle is the influent, the blue triangle is T0, the red square is T1, the orange diamond is T2, and the green triangle is T3... 146

Figure A.10 Saturation indices profiles calculated using PHREEQCI with the WATEQ4F database for goethite, $Fe(OH)_3$, and magnetite. The colours represent the different columns; the white circle is the influent, the blue triangle is T0, the red square is T1, the orange square is T2, and the green triangle is T3. The darker shade of the same colour represents an earlier profile and lighter shades represent a later profile, collected towards the end of the experiment. Distance 0 cm represents the influent SI and 30 cm represents the effluent SI. 147

Figure A.11 Saturation indices calculated using PHREEQCI with the WATEQ4F database for $FeS_{(s)}$, greigite, and mackinawite. The colours represent the different columns; the white circle is the influent, the blue triangle is T0, the red square is T1, the orange square is T2, and the green triangle is T3. The darker shade of the same colour represents an earlier profile and lighter shades represent a later profile, collected towards the end of the experiment. Distance 0 cm represents the influent SI and 30 cm represents the effluent SI. 148

Figure B.1 Nutrient (NH_3-N and PO_4-P) concentrations in aqueous samples collected along the reaction cell length. Distance 0 cm represents influent concentrations and 100 cm represents effluent concentrations..... 153

Figure B.2 Wt. % S in the solid reaction cell material and aqueous SO_4^{2-} concentrations from Day 49 in the reaction cell pore water. 154

Figure B.3 Saturation indices calculated using PHREEQCI with the WATEQ4F database for potential reaction products. Distance 0 cm represents influent SI and 100 cm represents effluent SI.... 155

Figure B.4 Saturation indices calculated using PHREEQCI with the WATEQ4F database for sulfide phases. Distance 0 cm represents influent SI and 100 cm represents effluent SI. 156

Figure C.1 Saturation indices calculated using PHREEQCI with the WATEQ4F database for potential reaction products. The profile shown was collected on Day 9 of the autumn cell trial. Distance 0 cm represents influent SI and 100 cm represents effluent SI. 160

Figure C.2 Saturation indices calculated using PHREEQCI with the WATEQ4F database for sulfide phases. The profile shown was collected on day 9 of the autumn cell trial. Distance 0 cm represents influent SI and 100 cm represents effluent SI. 161

List of Tables

Table 2.1 Average composition (dry wt. %), flow rate, residence time, and total pore volumes passed through each column..... 53

Table 4.1 Comparison of average flow rate and residence time for the laboratory and field studies. 121

Table 4.2 Comparison of the mean chemical compositions of the influent solution[a]. 122

Table 4.3 Chemical characteristics of reacted and unreacted solid organic carbon substrates on a dry wt. % basis. 123

Table A.1 Characteristics of the reactive material. 149

Table A.2 Average chemical composition of influent solution (n = 23). 150

Table A.3 A list of genera detected in the laboratory column samples that are known to catalyze sulfate reduction. 151

Table B.1 Mean chemical composition of influent solution (n = 10). 157

Table B.2 A list of genera detected in the reaction cell samples that are known to catalyze sulfate reduction.. 158

Table C.1 A list of genera detected in the autumn reaction cell samples that are known to catalyze sulfate reduction.. 157

List of Abbreviations

ADF	acid detergent fiber
AMD	acid mine drainage
APS	Advanced Photon Source
CLS	Canadian Light Source
DIC	dissolved inorganic carbon
DOC	dissolved organic carbon
EC	electrical conductivity
IRM	iron-reducing microorganisms
LCF	linear combination fitting
MPN	most probable number
N/A	parameter not measured
NDF	neutral detergent fiber
nH	neutrophilic heterotrophs
NM	native material
NIST	National Institute of Standards and Technology
OC	organic carbon
PRB	permeable reactive barrier
PV	pore volume
PVC	polyvinyl chloride
SEM	scanning electron microscopy
SI	saturation index
SRB	sulfate-reducing bacteria
XANES	X-ray absorption near edge structure
XRF	X-ray fluorescence
ZVI	zero-valent iron

Chapter 1: *Introduction*

1.1 Arsenic in Groundwater

The presence of arsenic (As) in groundwater is of increasing global concern. Elevated concentrations of As can occur in groundwater from both geological and anthropogenic sources. Geogenic As contamination in groundwater, derived from As-rich aquifer deposits and affected by regional climate, is especially prevalent in areas such as Bangladesh, Cambodia, and Vietnam (Fendorf et al., 2010; Nordstrom, 2002; Smedley & Kinniburgh, 2002), and in As-rich volcanogenic terrains (Smedley & Kinniburgh, 2013). Anthropogenic contamination can result from a variety of sources, including mining (McCreadie et al., 2000; Nordstrom, 2002; Wang & Mulligan, 2006), pesticide manufacturing (Nordstrom, 2002; Smedley & Kinniburgh, 2013), and wood preservation (Smedley & Kinniburgh, 2002; Wang & Mulligan, 2006). Mine wastes, including waste rock and mill tailings, are rich in metal(loid)-sulfide minerals. Oxidation of these minerals can release these metal(loid)s, including As, to groundwater (Blowes et al., 2014). Currently, the United States Environmental Protection Agency (EPA) maximum contaminant limit (MCL), Canada's maximum acceptable concentration (MAC), and the World Health Organization's (WHO) provisional guideline value, for As in drinking water is 10 $\mu g\ L^{-1}$. In addition, the Canadian Council of Ministers of Environment's (CCME) water quality guideline in Canada for the protection of freshwater aquatic wildlife is 5.0 $\mu g\ L^{-1}$ and 12.5 $\mu g\ L^{-1}$ for marine aquatic life. Over recent years, an increased understanding of As and the toxic effects it has on humans has resulted in stricter policies related to elevated As in drinking water.

The oxidation state of As is important in controlling As mobility and toxicity. Arsenic occurs in oxidation states of -3, 0, +3, and +5, but in natural groundwater aqueous As is commonly found as inorganic arsenite (As(III)) or arsenate (As(V)) (Smedley & Kinniburgh, 2002). More rarely, As may occur as a constituent of over 200 minerals or their alteration products including arsenopyrite (FeAsS), orpiment (As_2S_3), and realgar (As_4S_4) (Smedley & Kinniburgh, 2013). Of notable importance is arsenian pyrite ($Fe(S,As)_2$), an important source of arsenic in ore bodies (Smedley & Kinniburgh, 2013). Under oxidizing conditions, As(V) is the dominant species, but under reducing conditions As(III) tends to dominate (Hashim et al., 2011; Lien & Wilkin, 2005). As(III) is also typically more mobile and toxic than As(V) (Smedley & Kinniburgh, 2013). The current approaches for remediation of As-contaminated groundwater include pump-and-treat,

adsorption (Hashim et al., 2011; Zhu et al., 2009), filtration (Leupin & Hug, 2005), and permeable reactive barriers (Blowes et al., 1998; Hashim et al., 2011). In the past, pump-and-treat technologies were commonly used, but due to the high cost and extent of disruption to the above-ground environment, new technologies have emerged. Of these technologies, permeable reactive barriers (PRBs) are becoming more commonly used and studied (Blowes et al., 1998; Gibert et al., 2010; Ludwig et al., 2009).

1.2 Site Background

The Long Lake Gold Mine near Sudbury, Ontario is an abandoned mine with elevated metal and metalloid concentrations in the tailings porewater. The Long Lake mine was the site of intermittent Au production from 1909-1939, during which, tailings containing on average 5 wt. % As, were deposited without containment. All the tailings produced from the milling process were deposited into three tailings areas (TA-01, TA-02, TA-03), located between the mine site and Luke Creek, a tributary to Long Lake (**Figure 1.1**), and subsequently capped with a layer of sand (CH2MHill, 2014). The surface water drainage flows north through Luke Creek to Long Lake (**Figure 1.1**). Fugitive tailings from TA-01 have migrated north, forming channel deposits in Luke Creek, and resulting in the development of a delta of tailings at the southwestern end of Long Lake (CH2MHill, 2014). Arsenic is the major contaminant at the Long Lake tailings impoundment, with dissolved As concentrations reaching up to 600 mg L^{-1} in the tailings pore water, together with elevated concentrations of dissolved SO_4^{2-}, Fe and Al (Verbuyst, 2020). Planned remediation activities focus on the three major sources of As at the Long Lake site; the three tailings impoundments, the fugitive tailings in Luke Creek, and the Long Lake Tailings Delta (MNDM, 2017). This research project aims to evaluate the potential for application of passive remediation approaches at the Long Lake site and to determine the viability of incorporating a PRB into the remediation plan.

1.3 Permeable Reactive Barriers

PRBs are one of the treatment approaches under consideration for remediation of As at the Long Lake site. PRBs are passive, *in situ* barriers placed within the subsurface directly in the path of contaminant transport. During interaction between the contaminant plume and the barrier, processes such as adsorption, precipitation, and reduction occur to effectively remove or stabilize the contaminant (Blowes et al., 2000; Obiri-Nyarko et al., 2014). The geochemical conditions at

the Long Lake site and removal of As in previous laboratory and field studies suggest that a PRB will be effective at decreasing As concentrations (Bain et al., 2002; Biterna et al., 2007, 2010; Blowes et al., 2000; Lien & Wilkin, 2005; Ludwig et al., 2009; Su & Puls, 2001). These previous batch and column studies show As was removed using zero-valent iron (ZVI) and mixtures of ZVI and organic carbon (OC); removal mechanisms may be attributed to adsorption onto secondary ZVI surfaces and precipitation reactions. The composition of the reactive material used in the barrier varies based on site-specific biogeochemical conditions and flow rates on the target contaminant (Blowes et al., 2000). In this study, laboratory and field experiments utilizing OC and ZVI were conducted to evaluate the potential effectiveness of PRBs for the removal of As at the Long Lake site.

1.4 Research Objectives

The overall goal of the thesis is to evaluate the effectiveness of OC and ZVI amendments for the removal of As under the acidic conditions that predominate at Long Lake and to determine the viability of passive treatment to be incorporated as a remediation option. Furthermore, the thesis aims to better understand the mechanisms through which As is removed from groundwater.

The specific research project objectives are to:

1. Determine the optimal mixture of reactive material (ZVI and OC substrates) for removal of As from groundwater.
2. Understand the geochemical reactions contributing to As removal from groundwater.
3. Analyze the effectiveness of the reactive mixtures under laboratory and field conditions and to establish the rates of SO_4^{2-} removal.
4. Assess the potential viability for passive remediation at the Long Lake site.

1.5 Experimental Approach

Initial selection of optimal reactive mixtures was determined based on a literature review (Blowes et al., 1998; Gibert et al., 2003; Lindsay et al., 2008; Ludwig et al., 2009; Waybrant et al., 1998). Mixtures involving organic carbon and ZVI have been utilized in past experiments. A series of four column experiments were conducted to evaluate the treatment of As at a flow rate approximately three times that of groundwater velocity at the mine site. Arsenic-contaminated groundwater was pumped through columns containing different ratios of OC, ZVI, limestone,

and silica sand. Arsenic concentrations were determined on effluent water and profile samples collected along the column length, and the mass of As removal was determined. Following the laboratory column experiments, two field-reaction cell trials were conducted at the Long Lake site. Arsenic-contaminated water was pumped from a piezometer downgradient from the largest tailings impoundment into the reaction cell to evaluate the effectiveness of the optimum reactive mixture, identified through laboratory experiments, under field conditions. Two field trials were separately conducted at different times of the year to investigate the effect of temperature on the performance of the treatment system. Evaluation of treatment efficiencies of these reactive mixtures was investigated using geochemical, microbiological, and solid phase analyses, along with geochemical modelling using PHREEQCI. Removal of As and other metal(loid)s was observed in all three reactive columns. Consistent results were observed in the field-reaction cell experiments, under both warm and cold temperature field conditions.

1.6 Thesis Organization

The thesis is composed of three separate research papers that address the research objectives. Chapter 2 describes a series of four anaerobic laboratory column experiments using differing combinations of OC and ZVI. The chapter describes the geochemistry of the column effluent water as well as solid-phase analyses and microbial characterization of the column material. Chapter 3 is a field evaluation of the reactive mixture for As removal directly at the Long Lake site. The chapter describes a scaled-up field-reaction cell experiment, conducted during the summer, focusing on the geochemical characteristics of the reaction cell and the mechanisms through which As was removed from groundwater. Chapter 4 describes a similar field-reaction cell trial that was conducted in the autumn and examines the effect of colder temperatures on As removal in the reactive material. Chapter 4 provides a comparison between the two field cell trials and the varying mechanisms through which As is removed from the groundwater. Chapter 5 provides a summary of the conclusions of the study and recommendations for future research.

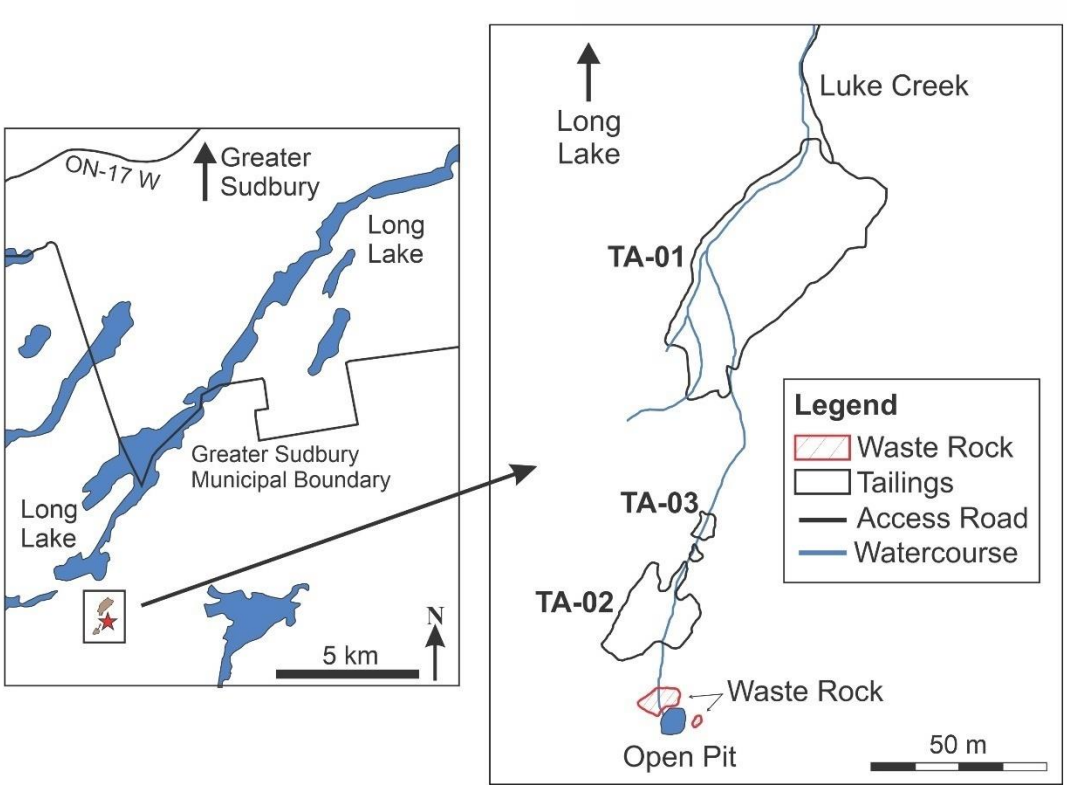

Figure 1.1 Map of Long Lake and surrounding area (left). The red star is the location of the sand-covered Long Lake Tailings Impoundment (TA-01, TA-02, and TA-03) to the south of Long Lake (right; modified after Verbuyst, 2020).

Chapter 2: *Removal of Arsenic and Metals from Groundwater Impacted by Mine Waste Using Zero-valent Iron and Organic Carbon: Laboratory Column Experiments*

Executive Summary

Acid mine drainage and the contaminants associated with mine-impacted water, including As and metals, are an ongoing environmental issue. Passive remediation technologies have the potential to remove As from mine waste effluents. A series of laboratory column experiments was conducted to evaluate the effectiveness of varying mixtures of organic carbon (OC), zero-valent iron (ZVI), and limestone for the treatment of As, metals, sulfate, and acidity in groundwater at an abandoned gold mine near Sudbury, ON. An increase in pH from 3.5 to circumneutral values was observed in all four columns throughout the experiment. The onset of bacterially-mediated SO_4^{2-} reduction was indicated by a decrease in Eh, a decline in aqueous SO_4^{2-} concentrations coupled with enrichment of $\delta^{34}S$ along the column length, the presence of sulfate-reducing bacteria (SRB), and the production of H_2S. *Desulfovibrio, Desulfobulbus*, *Desulfuromonas*, *Desulfomicrobium*, and *Desulfobacter* were the five most abundant SRB genera in the four columns. Sulfate reduction rates, calculated using linear regression on the decline of aqueous SO_4^{2-} concentrations along the column length, ranged from 0.18 to 0.20 mg L^{-1} d^{-1} g^{-1} dry OC. Removal of As was observed within the first 3 cm of reactive material in all three treatment columns to values below 10 µg L^{-1}, representing >99.9% removal. Removal of metals including Al, Cd, Co, Cu, Ni, and Zn was also observed in all four columns. Decreases in Fe were observed over time; however, concentrations remained high at the end of the experiment. Optical and scanning electron microscopic images indicated the presence of Fe sulfides, including pyrite and pyrrhotite, in the solid material from the column. Geochemical speciation modeling indicated the precipitation of secondary minerals such as amorphous FeS, mackinawite, and maghemite was favoured. Corrosion of ZVI grains and replacement of cellular organic matter with sulfides were also observed. Bulk S X-ray absorption near-edge structure spectroscopy (XANES) and S µX-ray fluorescence (µXRF) indicated the accumulation of reduced S phases (pyrite FeS, elemental S) on the coatings of ZVI grains during the experiment. Arsenic µXRF mapping and As-µXANES analyses indicated the presence of As in the secondary precipitates forming around grains of silica sand. The synchrotron results suggested the As was removed through precipitation of As-crystalline phases such as realgar, orpiment, and arsenopyrite or through adsorption as As(V) on ferrihydrite. Both reduced and oxidized phases were present in the secondary precipitates; however, the majority of As was present in the

reduced phase. The results from this study indicate the potential for a mixture of organic carbon and ZVI to remove As from acidic, mine-impacted water.

2.1 Introduction

One of the major sources of arsenic (As) in groundwater is mining. Gold (Au) mining in particular results in large amounts of As in wastes because As-bearing minerals are commonly present in Au-bearing ore bodies. During mining, rock is excavated to access the ore bodies, resulting in the production of large volumes of waste rock. Processing to concentrate valuable metals results in the production of fine-grained mill tailings that are typically deposited into impoundments. Arsenic occurs in waste rock and tailings in the form of gangue minerals and recalcitrant sulfide ore, including arsenopyrite (FeAsS), arsenian pyrite (As-rich FeS_2), and As-bearing Fe oxyhydroxides (Blowes et al., 2014). Unmanaged tailings deposits and waste-rock piles are of particular concern due to the potential for the oxidation of sulfide minerals (Blowes et al., 2014):

$$FeS_{2\,(s)} + \frac{7}{2}O_2 + H_2O \rightarrow 2SO_4^{2-} + Fe^{2+} + 2H^+ \quad [1]$$

and the oxidation of ferrous Fe:

$$Fe^{2+} + \frac{1}{4}O_2 + \frac{5}{2}H_2O \rightarrow Fe(OH)_{3(s)} + 2H^+ \quad [2]$$

H^+ is released in the above reactions, resulting in increased acidity. Sulfate (SO_4^{2-}) and metal(loid)s are also released into groundwater during oxidation processes (Blowes et al., 2014; Evangelou & Zhang, 1995). Tailings deposits can be of concern due to the potential to leach metals and metalloids into nearby water systems, resulting in contaminated acidic water that can persist for decades or centuries (Blowes & Jambor, 1990; Blowes et al., 2014; Moncur et al., 2005; Sprague et al., 2016). Migration of fugitive tailings downstream may result in the dispersion of metal(loid)-rich water and sediment into nearby environments, especially in cases where migration does not result in reduced toxicity (Sprague et al., 2016). Leaching of contaminated groundwater is especially prevalent at mine sites where the tailings are deposited without engineered containment. In carbonate-rich systems, low pH acidic drainage is often neutralized (Blowes et al., 2014). However, after the neutralization capacity is exceeded, the pH may decrease and the concentrations of other contaminants may again increase. Such acidic waters can pose a health risk to humans and organisms living nearby.

An established approach for the remediation of As-contaminated groundwater is permeable reactive barriers (PRBs). PRBs are passive, *in situ* barriers placed within the subsurface directly in the path of groundwater flow and contaminant transport (Blowes et al., 1998). The barrier is filled with material that reacts with the target contaminant. PRBs utilize processes such as adsorption, precipitation, and reduction to effectively remove and stabilize contaminants.

Zero-valent iron (ZVI) is often used in environmental remediation. Several laboratory studies have examined the processes by which ZVI removes As from water (Bain et al., 2002; Biterna et al., 2007, 2010; Lien & Wilkin, 2005; Su & Puls, 2001). Anaerobic corrosion of ZVI by water releases Fe(II) through (Gould, 1982):

$$2H_2O + Fe^0 \rightarrow Fe^{2+} + 2OH^- + H_2 \quad [3]$$

The release of Fe(II) allows for solid phases such as Fe (oxy)hydroxides and ferrous hydroxy carbonate to form (Jeen et al., 2007), which create highly reactive surface sites to which As can adsorb, and allows for retention of both As(III) and As(V) (Bang et al., 2005; Ludwig et al., 2009; Su & Puls, 2001). Furthermore, As can co-precipitate with green rust (Lien & Wilkin, 2005), which incorporates into the structure of pyrite during SO_4^{2-} reduction (Blowes et al., 2014) and, over time, may result in a more effective PRB (Su & Puls, 2001). Previous laboratory studies confirm the effectiveness of ZVI for removing As from water through co-precipitation and adsorption processes.

Organic carbon (OC) is another reactive material often utilized for environmental remediation. The addition of OC substrates promotes the growth and activity of sulfate-reducing bacteria (SRB) and results in bacterially-mediated SO_4^{2-} reduction (Benner et al., 1997):

$$SO_4^{2-} + 2CH_2O + 2H^+ \rightarrow H_2S + 2CO_2 + 2H_2O \quad [4]$$

The hydrogen sulfide produced reacts with soluble metals (Me) to form metal sulfide minerals (Ludwig et al., 2002):

$$H_2S + Me^{2+} \rightarrow MeS_{(s)} + 2H^+ \quad [5]$$

In addition to reaction [5], other elements such as As can react with H_2S to form sulfide minerals (Benner et al., 1997). If As-bearing sulfide metals are precipitated in an environment where O_2 is

limited, As is effectively immobilized provided the system remains anaerobic and oxidation reactions are limited. Such environments include fully saturated locations, such as tailings ponds. Past experiments have utilized OC in the form of compost, wood chips, and leaf compost (Benner et al., 1997; Lindsay et al., 2011b; Ludwig et al., 2009; Waybrant et al., 2002). Furthermore, varied mixtures of OC sources have been found to be more effective for contaminant removal as opposed to a single source (Waybrant et al., 1998, 2002).

Long Lake is an abandoned Au mine, near Sudbury, Ontario (**Figure 2.1**), with elevated metal(loid) concentrations in groundwater and tailings porewater. All of the tailings produced during the milling process were deposited into three tailings areas (**Figure 2.2**) and capped with a layer of sand (CH2MHill, 2014). The downstream migration of tailings has led to the formation of a tailings delta at the southwestern end of Long Lake. Arsenic is the primary contaminant of concern in the Long Lake tailings impoundment. Elevated concentrations of SO_4^{2-} as well as Fe, Al, and other metals are also observed.

Although several studies have explored the effectiveness of OC and ZVI for the removal of As from mine-impacted water, there is limited information on the potential for these materials to sustain low concentrations of As under low pH conditions (*e.g.*, pH < 4). The objective of this research is to further evaluate the effectiveness of OC and ZVI amendments for remediation under low pH conditions.

2.2 Methodology

2.2.1 Column Design and Experimental Setup

Four acrylic columns (30 cm long, 5 cm internal diameter) were used for the column experiments and named T0, T1, T2, and T3, respectively. Each was filled with various quantities of reactive material (**Table 2.1**), composed of silica sand (SS) (U.S. Silica Company), pulverized limestone (Beachville Quarries), granular ZVI (Connelly-GPM), and OC in the form of composted leaf mulch and wood chips (Waterloo Regional Landfill) obtained in the summer of 2018. The ZVI particles were predominantly in the 0.30 mm to 2.36 mm size range. The mixture of OC and ZVI was thoroughly mixed with silica sand, to increase permeability, and limestone, to neutralize the acidic pore water. The characteristics of the reactive material used for the mixtures are summarized in **Table A.1**. Approximately 2 g of organic-rich sediment collected from Laurel Creek, Waterloo was spread throughout each of the four columns during packing to

enhance the growth of bacterial populations in the reactive material. Each column was fit with an influent and effluent port, 13 water sampling ports spaced at 2-cm intervals along the length of one side of the column, and 8 larger solid sampling ports spaced at 3.25-cm intervals along the opposite side of the column. A 3-cm layer of nonreactive silica sand was placed at both the influent and effluent ends of the column to separate the reactive mixture from the end ports (**Figure 2.3**; Liu et al., 2014). The layers of silica sand were bounded by coarse- and fine-mesh NITEX™ screens. Prior to the start of groundwater pumping, the columns were flushed with CO_2 gas to displace the air within the columns.

A feed solution with 5% Na-lactate and 1000 mg L^{-1} SO_4^{2-} was then pumped through the columns to saturate the reactive material (Waybrant et al., 2002). Post-saturation, the influent and effluent ends of the columns were clamped before the columns were transferred into an anaerobic chamber and left for 12 d to allow the growth of bacterial populations. The columns were then subjected to continuous pumping of As-bearing groundwater collected from the Long Lake site. Water was pumped from the bottom upwards through the columns at an average rate of 3.24 mL h^{-1} using a multi-channel peristaltic pump (Ismatec and Rainin Dynamax) (Lindsay et al., 2011b). The influent water was collected monthly from the site to reduce any potential changes in the As(III):As(V) ratio during storage. Partway through the experiments, it became apparent that As was precipitating from the influent water before it was pumped through the columns. A spike of As(III) and $FeSO_4$ was used to increase the As and Fe concentrations going into the columns. The influent water was sampled every week to confirm the composition of the groundwater and ensure no major changes in geochemistry had occurred. The average chemical composition of the influent solution is shown in **Table A.2**. The column experiments were conducted for 30 (to 32) weeks. During this time, a number of pore volumes (PVs) passed through each column (60 PVs for T0, 35 PVs for T1, 52 PVs for T2, and 51 PVs for T3; **Table 2.1**). The influent PVs for all graphs correspond to the PVs from column T0.

2.2.2 Sample Collection

2.2.2.1 Effluent/Influent and Port Sampling

Water sampling took place directly in the glovebox. Collection of effluent and influent samples was conducted approximately once a week; secondary sampling was conducted four to five times over the course of the experiment. Effluent and influent sampling included the

collection of samples for pH, Eh, alkalinity, and determination of the concentrations of cations, anions, nutrients (NH_4-N and PO_4-P), and dissolved H_2S. Secondary sampling included the collection of water for the determination of dissolved organic carbon (DOC), dissolved inorganic carbon (DIC), carbon isotopes, and sulfur isotopes. To assess changes in geochemistry along the length of the columns, two profiles were collected over the course of the experiment. Profile samples were collected using a glass syringe starting at the effluent end of the column moving downwards, to prevent disturbance to flow. Water samples were collected from the effluent ports using 100-mL amber glass bottles that were connected using 0.32-cm outer diameter Teflon tubing and 0.32-cm outer diameter Pharmed® BPT tubing to 1-L polyethylene bottles. All samples were collected using syringes and passed through a 0.45-µm filter (Acrodisc®) into polyethylene and amber bottles. Samples were preserved with 67-70% OmniTrace® HNO_3 for analysis of cations and trace elements and with 95-98% A.C.S. Reagent H_2SO_4 for DOC and nutrient analyses, to a pH < 2. Samples for anions, DIC, $\delta^{13}C$, and $\delta^{34}S$ were not acidified. Samples for analysis of DIC were frozen prior to analysis. All other samples were refrigerated.

2.2.2.2 Solid-phase Sampling

Prior to removing solid material from the columns, the pumps were turned off and both ends of the column were clamped to prevent water from entering or leaving. Each column was placed horizontally with the solid sampling ports facing upward (**Figure 2.3)**. Ports were opened one at a time and material (12-15 g) removed using a sterilized metal scoopula, then placed in centrifuge tubes. The void formed due to the removal of reactive material from the column was refilled with silica sand. At the end of the experiments, the columns were sectioned every 3 to 5 cm and material samples placed in 20-mL glass vials. The glass bottles were sealed with vinyl tape and stored in the freezer until sample analysis.

2.2.3 Analytical Methods

2.2.3.1 Aqueous Analysis

The pH (Orion 3 Star meter connected to an Orion 815600 Ross Combination pH Probe) and Eh (Orion 3 Star meter connected to an Orion 9678B NWD Sure-Flow Combination redox electrode) were measured immediately after collection on unfiltered samples. The pH electrode was calibrated daily using pH 4, 7, and 10 buffers (traceable to NIST). The Eh electrode was checked for response against Zobell's and Light's solutions prior to sampling. Alkalinity (Hach

digital titrator and bromocresol green-methyl red indicators; Method 10244 from the HACH Hydraulic Fracturing Water Analysis Handbook, Edition 8) was measured immediately on filtered samples.

Samples from the water sampling ports, as well as influent- and effluent-water samples, were analyzed at the University of Waterloo, Groundwater Geochemistry and Remediation Laboratory, to determine concentrations of dissolved cations (inductively-coupled plasma mass spectrometry, Thermo Fisher Xseries II; inductively-coupled plasma optical emissions spectroscopy, Thermo Fisher iCAP 6000), dissolved anions (ion chromatography, Dionex IC-CO_3), and DIC and DOC (total organic carbon method, Aurora 1030 TOC Analyzer). Using a spectrophotometer (HACH DR 2800), concentrations of dissolved aqueous sulfide (S^{2-}) were measured using the methylene blue spectrophotometric method (Method 8131, DR 2800 Manual), NH_3-N using the salicylate method (Method 10031/10032, DR 2800 Manual), and PO_4-P using the ascorbic acid method (Method 8048, DR 2800 Manual).

2.2.3.2 Environmental Isotopes

Samples for determination of $\delta^{13}C$ were collected in 40-mL amber glass bottles and kept in the freezer prior to analysis by the Environmental Isotope Laboratory at the University of Waterloo. Samples for $\delta^{34}S$ were collected in polyethylene bottles and kept in the fridge until analysis prior to submission to the Isotope Science Laboratory at the University of Calgary where $BaSO_4$ was precipitated out of the sample before being analyzed for $\delta^{34}S$.

2.2.3.3 Carbon-Sulfur Analyzer

Samples for C/S measurements were anaerobically freeze-dried prior to analysis using an ELTRA CS 2000 Carbon Sulfur Determinator. After freeze-drying, the samples were transferred into an anaerobic chamber. A magnet was used to separate ZVI and dust from the OC. Due to the large variability in the reactive material (limestone, wood chips, leaf compost, etc.) and the inability to separate all components, measured C was determined to not provide an accurate representation of the C content. Therefore, only the S wt. % was used.

2.2.3.4 Microbiological Analyses

Microbiological analyses using the most probable number (MPN) technique were conducted on solid samples to enumerate SRB and neutrophilic heterotrophs (nH). Each cultivation was conducted in triplicate. For SRB, solid samples (1 g) were added to 20-mL serum

bottles that contained 9 mL of a modified Postgate C medium (Postgate, 1984), which was at a pH of 7.5 and contained 2.92 g L^{-1} Na-lactate (60%), 1.28 g L^{-1} Na acetate, and a resazurin supplement to indicate anaerobic conditions (Benner et al., 1999; Lindsay et al., 2008; Paulson et al., 2018). Following the MPN technique, the serum bottles were serially diluted (Gould et al., 2003). After being inoculated, the bottles were incubated in an anaerobic chamber for 5 weeks, after which inspection of the serum bottles commenced. The presence of a black precipitate indicated biogenic H_2S production via SO_4^{2-} reduction. Populations of SRB were counted following the MPN technique (Cochran, 1950). For nH, each sample was serially diluted and plated onto R2A agar (Sigma Aldrich, USA). The plates were incubated aerobically at room temperature (~23 °C) without agitation. After 7 d, the samples were counted. Duplicates were determined by two successive dilutions that showed colony growth.

2.2.3.5 DNA Extractions

DNA was extracted in duplicate using DNeasy PowerSoil Kits (Qiagen Inc., Germany) on samples stored in the freezer (−20 °C). After extraction, samples were stored at −20 °C before submission. Illumina MiSeq sequencing (Metagenom Bio Inc., Toronto, Canada), with the modified universal primers 515F/806R (Walters et al., 2015), was used to amplify the V4 region of 16S rRNA genes. Sequencing data was processed by Eva Pakostova (Pakostova et al., 2020), following DNA extraction, using the Mothur program v.1.39.5 (Schloss et al., 2009) and Mothur MiSeq Standard Operating Procedure (Kozich et al., 2013). Duplicate samples were merged and chimeric sequences discarded based on predictions by vsearch using the Silva database for 16S rRNA gene sequences (release 132 for Mothur, downloaded 18/03/2019) as a reference. Clustering of operational taxonomic units (OTUs) was conducted at a 97% similarity level using a *de novo* OTU picking process. Taxonomic annotation of individual OTUs was determined using the Mothur-formatted version of the Silva reference database (details above). Several taxa (unknown, mitochondria, and eukaryotes) were not considered for further data analyses, as advised in the Mothur MiSeq SOP. To control variation resulting from an unequal number of sequences across samples, subsampling was performed for each sample after OTU generation at a rarefaction level based on the sample with the fewest number of sequences (12,900 reads). Relative abundances of sulfate-reducing bacteria (SRB) were obtained by screening the taxonomy file for prokaryotic genera (or in a few instances higher taxa when identification to the genus level was not possible) containing at least one species with the investigated metabolic trait.

Table A.3 shows a list of SRB detected in the samples, as well as their mean % of total reads (in the whole data set, not individual samples).

2.2.3.6 Light Microscopy and SEM

Subsamples of the solids collected from the columns were sent to Spectrum Petrographics (Vancouver, Washington) for thin section preparation. Samples were anaerobically freeze-dried prior to submission and stored in an anaerobic chamber to prevent exposure to atmospheric O_2. Double-sided, polished, thin sections were prepared by mounting samples with Krazy Glue® onto a Suprasil 2A quartz plate. These slides were suitable for synchrotron-based µX-ray fluorescence (µXRF) and µX-ray diffraction (µXRD) analyses.

Thin sections were examined under both reflected and transmitted light using a Nikon Eclipse LV100N POL polarized light microscope to identify OC and ZVI grains. Grains of interest were marked on the slide and analyzed to determine the percentage of elements in the grain using scanning electron microscopy (SEM) and electron dispersion X-ray analysis (EDX) (Hitachi TM3000 Tabletop SEM coupled with a Bruker QUANTAX 70 EDS).

2.2.3.7 Synchrotron Analyses

Thin sections were analyzed using synchrotron µXRF mapping of As on beamline 20-ID at the Advanced Photon Source (APS) in Lemont, Illinois. Locations of interest on the grain were further analyzed for As µX-ray absorption near edge structure (µXANES). Synchrotron µXRF mapping of S was conducted on one thin section using beamline SXRMB at the Canadian Light Source (CLS) in Saskatoon, Saskatchewan. Points of interest on the grain were analyzed with S µXANES.

Samples of ZVI prepared for bulk S XANES analyses at the CLS were collected from the column under anaerobic conditions and then frozen in liquid N_2. The frozen samples were crushed under anaerobic conditions using a mortar and pestle, to remove grain coatings, sieved, and stored in 2-mL vials which were kept in an anaerobic chamber before transport to the CLS.

Processing of µXANES, XANES, and µXRF data was carried out using the program ATHENA (Ravel & Newville, 2005). Two to four scans were merged in µ(E) to reduce noise and create data that were easier to fit and interpret. In cases where beam damage was apparent, only the first scan was used. The merged scans were energy shifted with respect to the reference

standard gypsum, that was collected during the same beamline time. Linear combination fitting (LCF) of (μ)XANES provides a quantitative assessment of the species and, in some cases, can predict the phases present in the solid material to ±5-10 % (Foster & Kim, 2014).

2.2.3.8 Data Interpretation

Removal of As from all four columns was calculated from the cumulative mass in the column influent minus the cumulative mass in the column effluent. Mass removal was based on weekly gravimetric determinations of water volume combined with analytical determinations of As concentrations. Sulfate removal rates were calculated for each of the treatment columns (T1, T2, and T3). The best-fit SO_4^{2-} reduction equation was based on observed SO_4^{2-} removal for each column (SigmaPlot, SPSS Inc.). The rates were further normalized to per weight (g) of dry OC (Lindsay et al., 2008; Waybrant et al., 1998). Data from the column experiments were input into the geochemical modelling software PHREEQCI using the WATEQ4F (Ball & Nordstrom, 1991) database to determine the saturation indices.

2.3 Results

2.3.1 Water Chemistry

2.3.1.1 Geochemical Conditions

The geochemical conditions in treatment columns T1, T2, and T3 exhibited similar characteristics in terms of effluent pH, Eh, and alkalinity (**Figure 2.4**). The influent water pH remained at a mean value of 3.5 throughout the experiment; mean effluent pH values were 7.3, 7.6, and 7.9 for T1, T2, and T3, respectively. Column T0 (0 wt. % ZVI) exhibited similar pH values, with a mean effluent of 7.2. A sharp initial increase in pH within the first 3 cm was observed in all four columns (**Figure 2.5)**. The mean influent Eh value was 406 mV, and column effluents had a mean Eh of 32, 5, −5, and −27 mV for T0 to T3, respectively. A sharp initial decrease in Eh was observed in all four columns within the first 3 cm of reactive material but subsequent Eh values remained near 0 mV (**Figure 2.5**). The mean influent alkalinity was close to 0 mg L^{-1} as $CaCO_3$ and the four column effluents had mean values of 616, 1010, 764, and 730 mg L^{-1} as $CaCO_3$ (T0 to T3; **Figure 2.4**). Effluent alkalinity was initially high in the first 5 PVs of flow, then tapered off to lower, more constant, values after approximately 6 PVs. A substantial increase in alkalinity along the length of the column occurred early in the experiment (**Figure 2.5**). Near the end of the experiment, the magnitude of alkalinity increase was lower.

The mean alkalinity in all four columns, not including the initial increase, was close to 100 mg L^{-1} as $CaCO_3$.

2.3.1.2 As

The concentrations of As in the influent water were as high as 10 mg L^{-1} (**Figure 2.6**). Variations in influent As concentration occurred over the course of the experiment, likely due to O_2 exposure. The influent As concentration declined sharply at 21 PVs and remained low until 35 PVs, at which time As and Fe were added to the influent water. From 8 to 21 PVs, the As concentration varied between 2000 and 5500 µg L^{-1} **(Figure 2.6)**. After 21 PVs, the concentration declined to between 20 and 270 µg L^{-1}. The influent solution was spiked to 6800-9600 µg L^{-1} As from 35 PVs until the conclusion of the experiment.

Mean As concentrations in the column effluents were 3.6, 3.9, 2.7, and 2.2 µg L^{-1} for columns T0 to T3, respectively. The first column profile was collected following the initial flush of groundwater through the reactive columns. During this time, As concentrations going into the columns were low (57.5 µg L^{-1}). Despite low concentrations, all four columns showed a decrease in As concentrations upon reaching the first sampling port (**Figure 2.7)**. Arsenic concentrations dropped below 10 µg L^{-1} in T1, T2, and T3 but not T0. The second column profile was collected near the end of the experiments after 47, 27, 40, and 38 PVs for T0 to T3, respectively. The mean As concentration in the column influent was 8.9 mg L^{-1}. Pronounced removal of As was observed within the first 3 cm of T1, T2, and T3, whereas As concentrations remained elevated throughout the column length in T0 **(Figure 2.7**).

2.3.1.3 Fe

The influent Fe concentration ranged from 11 to 58 mg L^{-1}, with a mean of 13.6 mg L^{-1} prior to the $FeSO_4$ spike, and a mean of 52.3 mg L^{-1} following the addition of $FeSO_4$ (**Figure 2.6**). Starting at 35 PVs, dissolved Fe(II), as $FeSO_4$, was added to the influent, increasing concentrations to between 45-60 mg L^{-1}. The mean concentrations of Fe in the column effluents of T0, T1, T2, and T3 were 26.1, 50.0, 26.2, and 16.8 mg L^{-1}, respectively (**Figure 2.6)**. Column profile chemistry samples were collected two times during the experiment (**Figure 2.7**). The early profile showed an increase in Fe concentrations along the length of all columns. A larger change in concentration between the profile influent and effluent was observed in columns T0 and T1 (25 to 200 mg L^{-1}), whereas the change was less pronounced in columns T2 and T3 (25 to

100 mg L^{-1}). The second profile, collected at a later PV, showed the opposite trend. Iron concentrations decreased along the column length in all four columns, with T3 and T2 exhibiting the largest decrease in Fe concentrations along the column length, followed by T1 and then T0 (**Figure 2.7**).

2.3.1.4 Metals

The mean influent concentrations of dissolved metals varied (6.8 mg L^{-1} Al, 0.25 mg L^{-1} Co, 0.23 mg L^{-1} Ni, 0.14 mg L^{-1} Cu, 0.27 mg L^{-1} Zn, and 0.31 µg L^{-1} Cd; **Figure 2.8**). The effluent metal concentrations were less than 5 µg L^{-1}, except for Al which was < 25 µg L^{-1} for all columns. A sharp decrease in Al, Cu, and Co within the first 3 cm of reactive material was observed in columns T1, T2, and T3, followed by constant values for the remainder of the column length (**Figures A.1, A.2**). Profiles of Ni, Cd, and Zn concentrations show a sharp initial decrease, followed by variable concentrations along the length of columns T1, T2, and T3. Similarly, a sharp initial decrease was observed in column T0 for Al and Cu after which concentrations remained constant for the remainder of the column. For Zn and Cd in column T0, a similar trend to Al and Cu was observed at 47 PVs but, at 2 PVs, the concentrations were variable throughout the column length, with concentrations decreasing at the effluent end. Concentrations for Co and Ni progressively decreased along the length of column T0 (**Figure A.1**).

2.3.1.5 Sulfur Geochemistry

The mean influent SO_4^{2-} concentration was 214 mg L^{-1}. The mean column effluent SO_4^{2-} concentrations were 236, 26.2, 42.2, and 49.7 mg L^{-1} for T0 to T3, respectively (**Figure 2.6**). Port measurements for columns T1, T2, and T3 showed similar rates of SO_4^{2-} removal for both profile sampling episodes (**Figure 2.7**). The first profile sampling episode showed a sharp initial decrease in SO_4^{2-}, prior to reaching the first sampling port, with no further decline over the remainder of the column length. The decrease in SO_4^{2-} concentrations was more gradual during the second profile episode, measured toward the end of the experiment. The opposite trend was observed at 2 PVs for T0, with SO_4^{2-} concentrations increasing substantially along the column length. At 47 PVs, SO_4^{2-} concentrations decreased minimally, remaining relatively constant along the column length.

Dissolved aqueous S^{2-} in the influent water was relatively low, with a mean concentration of 5.8 µg L^{-1} (**Figure A.3**). The mean column effluent S^{2-} concentrations were 1.4 mg L^{-1} for T0 and 28.0, 31.6, and 39.3 µg L^{-1} for T1 to T3, respectively. Column T0 had high initial S^{2-} concentrations in the effluent, with values up to 24 mg L^{-1} at 4.5 PVs (**Figure A.3**). The maximum S^{2-} concentrations in the treatment columns were lower than observed in T0. The initial increase in S^{2-} concentrations was the largest in column T3 (maximum 183 µg L^{-1}), followed by T2 (91 µg L^{-1}) and T1 (58 µg L^{-1}). The column profiles for T1, T2, and T3 showed varied concentrations of S^{2-} along the column in the first collected profile but an increase in S^{2-} along the length of the column in the second profile (**Figure 2.9)**. The S^{2-} concentrations in both profiles collected for T0 showed very low concentrations of S^{2-} along the column length, which contrasts with the high concentrations observed in the T0 effluent.

The sulfur isotope ratio of the influent was 6.5 ‰. Sulfur isotope ratios measured along the column length showed a progressive enrichment of $\delta^{34}S\text{-}SO_4$, with maximum values of 28.7, 16.0, and 24.7 ‰ in T1 to T3, respectively (**Figure 2.9**). The extent of enrichment may not be properly displayed for column T2 because one less measurement was made due to sample limitations. Column T0 demonstrated an initial decrease in $\delta^{34}S\text{-}SO_4$ ratio to 3.0 ‰, followed by relatively constant values for the remainder of the column length.

2.3.1.6 Carbon

High DOC concentrations of up to 6000 mg L^{-1} as C were observed in all four column effluents during the first 5 PVs, after which concentrations decreased to between 0 and 30 mg L^{-1} (**Figure 2.10)**. The highest concentrations of DOC were observed for columns T0 and T1 (6028 and 5764 mg L^{-1}, respectively), followed by T2 and T3 (3330 and 4121 mg L^{-1}, respectively). Profiles collected for all four columns showed an increase in DOC along the column length, followed by a slight decrease in the effluent (**Figure 2.10**). A gradual increase in DIC values was observed in all four columns, with the highest value observed in the effluent of T1 (31 mg L^{-1} as C), followed by T2 (25 mg L^{-1} as C) and T3 (14 mg L^{-1} as C) (**Figure 2.9**). A slight increase in DIC occurred near the influent end of T0, followed by values of 3-5 mg L^{-1} as C over the remainder of the column length.

The mean $\delta^{13}C$-DIC values for the unreacted column materials were 2.4 ‰ for limestone, −27.1 ‰ for leaf compost, and −24.6 ‰ for wood chips. The $\delta^{13}C$-DIC trend displays a negative,

depleted δ^{13}C-DIC value of −23.6 ‰ in the influent water (**Figure 2.9**). Sharp increases in δ^{13}C-DIC to −8.8 ‰ (T1), −7.6 ‰ (T2), and −2.3 ‰ (T3) were observed within the first 3 cm of reactive material; following this initial increase, gradual decreases in δ^{13}C-DIC values were observed along the length of each column. A sharp increase from −23.6 to 0 ‰ δ^{13}C-DIC was observed in column T0, after which values remained relatively constant over the remaining length of the column.

2.3.1.7 Nutrients

The mean influent NH_3-N concentration was 0.85 mg L^{-1} with a maximum of 1.56 mg L^{-1} as NH_3-N (**Figure A.3)**. In the first 6-7 PVs, the NH_3-N effluent concentrations were up to 6.7, 6.2, and 8.3 mg L^{-1} as NH_3-N in T1 to T3, respectively. However, after the initial increase, concentrations remained relatively constant at values below 1 mg L^{-1}. The PO_4-P concentrations in the influent ranged from 0.31 to 1.56 mg L^{-1}, with a mean of 0.18 mg L^{-1} (**Figure A.3)**. The column effluent PO_4-P concentrations reached maximum values during the first 13-15 PVs followed by decreases to near 1 mg L^{-1} as PO_4-P. The highest PO_4-P values observed in T1, T2, and T3 were 3.6, 4.6, and 2.5 mg L^{-1} as PO_4-P, respectively. Effluent values of NH_3-N and PO_4-P observed for column T0 were similar to the influent. No obvious trends in NH_3-N values were observed along the column length for T0, T2, and T3, but column T1 demonstrated a decrease in NH_3-N concentrations at around 10 cm, followed by relatively constant concentrations for the remainder of the column (**Figure A.4**). Phosphate profile measurements for all four columns showed a general decrease in PO_4-P from the influent to the effluent (**Figure A.4**).

2.3.2 Microbiology

2.3.2.1 Most Probable Number (MPN)

Populations of SRB and nH were assessed through microbial enumeration of the solid material collected from four locations on each column (**Figure 2.11**). SRB populations remained relatively constant between 10^2 and 10^3 bacteria g^{-1} in columns T1, T2, and T3, while no culturable SRB were detected in column T0. Enumerations of nH bacterial populations for columns T1, T2, and T3 were 10^6-10^7 bacteria g^{-1} and near 10^4 bacteria g^{-1} for column T0. No obvious trends in nH populations were observed along the column length for T1, T2, and T3. Column T0 demonstrated a progressive increase in nH populations from the influent to the effluent end (**Figure 2.11**).

2.3.2.2 DNA Analysis

16S rRNA gene amplicon sequencing of the solid material indicated the presence of SRB in all four columns. Of the SRB identified, the five most abundant genera were *Desulfovibrio*, *Desulfobulbus*, *Desulfomicrobium*, *Desulfuromonas*, and *Desulfobacter* (**Figure 2.12)**. The relative abundance of SRB along the column lengths varied between 3.0 and 10.0% (T0), 2.4 and 4.1% (T1), 3.3 and 6.7% (T2), and 4.7 and 6.8% of total reads (T3) (**Figure 2.12**). In all three treatment columns, the highest total number of reads of SRB was observed closest to the influent end. The most abundant genus in T0 was *Desulfobulbus*, whereas *Desulfovibrio* was the most abundant genus in T1, T2, and T3. The highest relative abundance of SRB was observed in column T0; however, this column had a lower number of SRB compared to the other columns (**Figure 2.12**).

2.3.3 Mineralogy

2.3.3.1 Reflected and Transmitted Light Microscopy and SEM

Reflected and transmitted light microscopy was used to identify minerals in the starting materials and in samples collected from the columns at the end of the experiments. Unreacted grains of ZVI were analyzed to observe the structure and properties of the grains prior to the experiments (**Figure A.5**). This examination was used to distinguish whether reaction rims around the ZVI were due to chemical reactions in the column or if they were present prior to the experiments. Grains of interest were further examined with SEM to determine the dominant elements present in the grain.

The dominant sulfide mineral present in the reactive mixtures at the end of the experiment was pyrite, which occurred as framboids, both as clusters and as individual, isolated framboids. No single crystals or cubes of pyrite were observed. Small amounts of chalcopyrite ($CuFeS_2$) and pyrrhotite ($Fe_{(1-x)}S$) were also observed. Iron sulfide precipitates were observed between grains of silica sand and as rims around the ZVI grains (**Figure A.6**). The OC varied from anisotropic to isotropic. Internal cell structure was observed, with occasional infilling by Fe sulfide (**Figure 2.13**). Secondary Fe sulfides were white-grey in colour under reflected light and isotropic under transmitted light. The occurrence of both Fe and S in the secondary precipitates was confirmed by SEM-EDX.

Iron (oxy)hydroxides, both as separate grains and as corrosion products on ZVI, were observed. These corrosion products often replaced substantial sections of the ZVI grain and varied in texture.

2.3.3.2 Solid Sulfur

The average wt. % S content measured in the solid material from the treatment columns was compared to the aqueous SO_4^{2-} concentrations (**Figure A.7**). The S content of unreacted material was 0.12 wt. % for leaf mulch, 0.04 wt. % for wood chips, and 0.15 wt. % for untreated ZVI. The S content near the influent was 1.1, 1.1, and 0.76 wt. % in T1 to T3, respectively. The greatest mass of S was observed at the influent ends of the columns. A progressive decrease in solid-phase S content was observed toward the effluent end in all three columns. The decrease in S content was consistent with the observed decrease in dissolved SO_4^{2-} concentrations along the column length. The abundance of S present in the solid material was greatest in column T1, followed by T2 then T3.

2.3.3.3 Synchrotron-based Bulk S (μ)XANES and S μXRF Mapping

Synchrotron radiation-based bulk S XANES for the unreacted ZVI (**Figure 2.14)** indicates the presence of S in two predominant oxidation states: sulfate (2482 eV) and an intermediate, oxidized S species (2476 eV), similar to tetramethylene sulfoxide (C_4H_8OS; Wang et al., 2019). Spectral data indicate S occurs in three oxidation states (a/b, c, d; **Figure 2.14)** within the solid material from the treatment columns. The adsorption edge of the group designated "a/b" ranges from 2470 to 2472 eV, which is in the range of FeS, elemental S (S_8^0), and/or pyrrhotite (Fleet, 2005). Because the E0 of this group can vary 2 eV between sample spectra, it is not possible to distinguish which reduced S phase is present. The spectral peak indicating a second oxidation state, "c", occurs at 2476 eV and is in the range of the E0 of an organic, intermediate, oxidized S species. The highest energy edge, "d" occurs at 2482 eV, which is an oxidized sulfate species, likely gypsum ($CaSO_4 \cdot 2H_2O$), based on the E0 of the adsorption edge (Fleet, 2005).

Sulfur μXRF mapping targeted a grain where a secondary precipitate replaces the cellular organic material, as observed by optical microscopy and SEM (**Figure 2.15**). The results of sulfur μXRF analysis indicate S occurs primarily around the rim of the grain and only in localized hotspots in the center of the grain; in contrast, μXRF indicates Fe is dispersed

throughout the grain. Minimal variation is observed in the S μXANES spectra measured at five locations within the grain showing two major oxidation states (a/b, e; **Figure 2.15).** The majority of S is present as a reduced phase with an E0 of 2471 to 2472 eV, corresponding to pyrite and elemental S. The second peak located at 2482 eV corresponds to gypsum. A third, lesser component corresponds to intermediate oxidation states (*e.g.*, Na-thiosulfate or K-tetrathionate).

2.3.3.4 Synchrotron-based As μXRF Mapping and As μXANES

The μXRF mapping of secondary precipitates indicates the presence of As in grains containing both Fe and S (**Figures 2.16, 2.17**). Arsenic occurs both on the edges of grains and at localized spots rather than uniformly throughout the entire grain. Arsenic μXANES was collected at a location of relatively high concentration, identified through μXRF mapping. Two major oxidation states of As are observed as represented by peaks at 11867 to 11878 eV (−1/+3) and 11874 to 11875 eV (+5). Reduced and oxidized species are present in the solid material at each spot measured, but the majority of As is present in the reduced state. The predominant As species observed in the Fe-S secondary precipitates are consistent with arsenopyrite (FeAsS, −1), orpiment (As_2S_3, +3), realgar (AsS, +3), and As(V) sorbed onto ferrihydrite, or possibly as kankite ($FeAsO_4 \cdot 3.5H_2O$; Walker et al., 2005). The presence of kankite could not be confirmed because of low counts in the spectral data.

2.4 Discussion

2.4.1 Water Chemistry

The mean influent pH was 3.5 and the mean influent alkalinity was close to 0 mg L^{-1} as $CaCO_3$. The sharp increase in pH at the base of the columns corresponded to an increase in alkalinity within the first 3 cm of reactive material. The pH of the column effluents remained consistently circumneutral throughout the experiments. The alkalinity of the column effluents was initially high for the first 5-6 PVs, after which a substantial decrease followed by constant values on the order of 100 mg L^{-1} were observed in all four columns. The high initial pH and alkalinity of the column effluents may be attributed to the dissolution of limestone that was added to the reactive mixture and contributes to the neutralization of acidity through the production of HCO_3^-:

$$CaCO_3 + H^+ \leftrightarrow Ca^{2+} + HCO_3^- \quad [6]$$

Under anaerobic conditions, the oxidation of OC coupled with SO_4^{2-} reduction is catalyzed by SRB, which also contributes to alkalinity (Waybrant et al., 1998):

$$SO_4^{2-} + 2CH_2O \leftrightarrow H_2S + 2HCO_3^- \quad [7]$$

where CH_2O represents a simple organic compound. The highest effluent alkalinity was observed in the column with the greatest proportion of OC (T1). Finally, the anaerobic corrosion of ZVI likely resulted in further neutralization of the pH through the reduction of water and the formation of OH^- (reaction [3]; Blowes et al., 2000; Manning et al., 2002).

An increase in the mean pH in T1, T2, and T3 to 7.3, 7.6, and 7.9, respectively, was consistent with the increase in weight percentage of ZVI in the mixture. All three reactions ([6] to [8]) likely contributed to the sharp initial increase in pH and alkalinity and the stable pH values observed throughout the experiments. The addition of Na-lactate, used to stimulate conditions favourable for the growth and activity of SRB, also may have affected the pH and alkalinity at the onset of the experiments.

Decreases in Eh values were observed in all four columns, indicating the development of reducing conditions. The presence of OC and ZVI in the reactive mixture likely contributed to a further decrease of Eh values in T1, T2, and T3.

Decreases in Eh, the generation of alkalinity and H_2S, and a decrease in SO_4^{2-} concentrations along the column length of T1, T2, and T3 indicated the development of conditions favourable for SO_4^{2-} reduction at the onset of the experiments. Following the first 5 PVs, the concentrations of H_2S and alkalinity declined (**Figures 2.4, A.3)**. The high initial concentrations may be attributed to flushing of the Na-lactate solution present in the columns prior to the introduction of groundwater and to the addition of organic-rich creek sediment.

The MPN results suggest the inclusion of OC into the reactive mixture was important for the growth of SRB and microbial activity. Although similar relative abundances of SRB were determined by 16S rRNA sequencing, no culturable SRB were detected in T0. The greatest culturable counts of SRB were observed at the influent ends of columns T1, T2, and T3, suggesting greater SRB activity at these locations. No significantly greater ($P > 0.05$) relative abundance of SRB was detected in T1, despite the greatest mass of OC among the three

treatment columns. It is possible that bacterial abundance does not increase beyond a threshold mass of OC substrate (the lowest percentage of OC in all three columns was 20 wt. %).

Desulfovibrio was the most abundant SRB genus in columns T1, T2, and T3, whereas *Desulfobulbus* was the most abundant in T0, possibly reflecting differences in overall community structure due to the composition of the column material. *Desulfovibrio* and *Desulfobulbus* members have similar characteristics, including respiratory or fermentative metabolisms, incomplete oxidation of organic compounds, and the ability to use SO_4^{2-} as a terminal electron acceptor to be reduced to H_2S (Kuever et al., 2005). However, organisms within the *Desulfovibrio* genera have been shown to produce more sulfide per unit cell mass utilizing H_2, compared to lactate, as an electron donor (Steger et al., 2002). The oxidation of ZVI results in the formation of H_2 (reaction [8]) providing a source of H_2 for SRB metabolism. *Desulfovibrio* were more abundant in the treatment columns containing ZVI. Furthermore, *Desulfobulbus* is among the first sulfate-reducing groups to colonize biofilms and, in doing so, could create conditions suitable for other SRB (Achá et al., 2005; Okabe et al., 1999). Therefore, biofilms may have formed on the sand and limestone in T0 in the presence of Na-lactate and organic-rich creek sediment, allowing *Desulfobulbus* to dominate among SRB despite the absence of solid OC added to this column.

Other abundant genera, present in all columns, included *Desulfomicrobium*, *Desulfuromonas*, and *Desulfobacter*. Conditions within the columns fall in the ideal range of pH (6.5-7.5) and temperature (25-35 °C) for the five most abundant SRB genera identified in the column study (Rikihisa et al., 2015). *Desulfovibrio* and *Desulfomicrobium* are both considered important groups contributing to SO_4^{2-} reduction and As removal in remediation systems (Altun et al., 2014; Omoregie et al., 2013). In addition, some members of *Desulfovibrio* and *Desulfomicrobium* are able to reduce both arsenate and SO_4^{2-}; a strain of *Desulfomicrobium* may use arsenate as a terminal electron acceptor in the absence of SO_4^{2-}, without affecting SO_4^{2-} reduction (Macy et al., 2000). Some type species of *Desulfuromonas* and *Desulfovibrio* also contain a multiheme c-type cytochrome that may function as an Fe(III) reductase, promoting Fe(III) reduction (Macy et al., 2000).

Sulfate concentrations declined in all four columns with an observed order of removal of T1>T2=T3>>T0. The decline in SO_4^{2-} concentrations corresponded to the release of H_2S. The

greatest decrease in SO_4^{2-} and increase in H_2S concentrations was observed in column T1, followed by T2 and T3. No change in SO_4^{2-} concentrations or H_2S was observed in column T0. Lower H_2S values observed toward the middle and end of the experiment were likely due to the precipitation of Fe(II) and other metal sulfides, limiting the aqueous H_2S concentrations.

Bacteria preferentially utilize ^{32}S in metabolic function relative to the heavier ^{34}S, resulting in enrichment of ^{34}S in the residual SO_4^{2-} (Lindsay et al., 2011a; Nakai & Jensen, 1964; Waybrant et al., 2002). The enrichment in $\delta^{34}S\text{-}SO_4$ observed in the effluent versus the influent of columns T1, T2, and T3 (**Figure 2.9**), coupled with the decrease in SO_4^{2-} concentrations, is consistent with the occurrence of bacterially-mediated SO_4^{2-} reduction. The greatest enrichment of $\delta^{34}S\text{-}SO_4$ (up to 30 ‰) was observed for column T1, which contained the lowest abundance of ZVI. A $\delta^{34}S\text{-}SO_4$ enrichment factor (ε) of −28.9 was calculated for column T1 based on the $\delta^{34}S\text{-}SO_4$ profile collected at 27 PVs (Clark et al., 2008; Guo & Blowes, 2009). This enrichment factor is within the range of −20.8 to −46.1 observed in previous experiments utilizing OC to promote SO_4^{2-} reduction (Guo & Blowes, 2009; Lindsay et al., 2009; Waybrant et al., 2002).

Increased alkalinity and H_2S concentrations and decreased Eh were observed in column T0; however, no enrichment of $\delta^{34}S\text{-}SO_4$ or decrease in SO_4^{2-} concentrations were observed. These differences indicate lower rates of bacterially-mediated SO_4^{2-} reduction in column T0 compared to the other columns. At the end of the experiments, effluent concentrations of SO_4^{2-} in all four columns remained above 40 mg L^{-1}, suggesting SO_4^{2-} reduction was not limited by the availability of SO_4^{2-} during the experiment. If the experiments had continued for longer, the OC source may have become depleted, resulting in an OC-limited system (Waybrant et al., 1998).

2.4.2 Dissolved Arsenic and Metal Removal

2.4.2.1 Iron

Iron concentrations remained above the secondary maximum contaminant level of 0.3 mg L^{-1} (EPA), and were up to 50 mg L^{-1} in the column effluents. The increase in Fe along the column length at the onset of the experiments may have been due to the development of reducing conditions that resulted in reductive dissolution of Fe (oxy)hydroxide corrosion products on ZVI and Fe mobilization. The largest increase in Fe concentration was observed in T1, the column with the highest percentage of OC. The final measured effluent Fe concentration was as low as 2 mg L^{-1}; this suggests that, with time, Fe concentrations may have decreased further.

Iron-reducing microorganisms (IRM) likely contributed to the higher concentrations of Fe in the effluent. Oxidation of OC can occur by pairing with Fe(III) oxyhydroxides as a terminal electron acceptor (Brock et al., 2006; Lovley & Phillips, 1988):

$$CH_2O + 4FeOOH + 8H^+ \rightarrow 4Fe^{2+} + CO_2 + 7H_2O \quad [8]$$

Iron(II) can be mobilized through bacterially-mediated reduction of Fe (oxy)hydroxides, which may have resulted in the initial increase in Fe concentrations along the column profiles. Characterization of the microbial community following the termination of the experiment indicated total reads of IRM were low (< 0.1 % of the total microbial reads). However, some SRB genera are capable of directly utilizing Fe(III) as a terminal electron acceptor. The formation of H_2S and subsequent precipitation of Fe sulfides likely resulted in the retention of Fe(II). SEM and optical microscopy confirmed the presence of pyrite, including framboidal pyrite, pyrrhotite, and chalcopyrite. Geochemical modeling indicates the precipitation of other Fe sulfides such as mackinawite ($(Fe,Ni)_{1+x}S$) and amorphous FeS is favoured (**Figures A.8, A.9**). Geochemical modeling also indicates the potential precipitation of secondary minerals previously observed in reactive barrier studies, including magnetite (Fe_3O_4), maghemite (Fe_2O_3), sphalerite ((Zn, Fe)S), greigite (Fe_3S_4), and amorphous FeS (Gu et al., 1999; Jambor et al., 2005; Lindsay et al., 2008; Rao et al., 2009; **Figures A.10, A.11**).

The formation of pyrite typically proceeds with the formation of disordered mackinawite first (Wolthers et al., 2003), followed by cubic or amorphous FeS, then tetragonal FeS or mackinawite, greigite, and finally marcasite (FeS_2) or pyrite (Jambor et al., 2005). This pathway indicates the importance of mackinawite for the removal of Fe and other metals from the water, and several studies have noted mackinawite is one of the most abundant Fe sulfides present in the reacted material (Gu et al., 1999; Lindsay et al., 2008). The presence of mackinawite and pyrite, based on the results of geochemical modelling and optical microscopy, indicate Fe was likely removed through the above pathway. Other secondary products such as magnetite and maghemite likely contributed to Fe removal (Gu et al., 1999; Jambor et al., 2005).

Corrosion of ZVI grains, or replacement by secondary precipitates, was observed on grain boundaries and in the form of alteration rims, or on the darkened sections of the grains. Jambor et al. (2005) observed the replacement of ZVI by Fe (oxy)hydroxides as rims and veins around the grain or on the exterior of the grain at sites containing graphite. The Fe

(oxy)hydroxides observed in these column experiments are similar in appearance to those observed by Jambor et al. (2005).

Synchrotron-radiation bulk S XANES analysis indicates the accumulation of sulfides on the coatings of the ZVI grain. A comparison between the spectra for the untreated ZVI and the reacted column material shows similar spectral features (c, d) that correspond to tetramethylene sulfoxide (2476 eV) and gypsum (2482 eV) adsorption edges (**Figure 2.14**). However, "a/b" is absent in the untreated ZVI compared to the column material. This change indicates that, during the experiment, a reduced S phase (pyrite, pyrrhotite, elemental S) accumulated as a coating on the ZVI grains (**Figure 2.14**). The accumulation of sulfides, including pyrite and pyrrhotite, is consistent with the aqueous, microbiological, and solid phase results that indicate the formation of sulfides through bacterially-mediated SO_4^{2-} reduction. In anoxic environments, the presence of Fe(III) may result in the chemical oxidation of sulfide to S^0 (Lovley & Phillips, 1994; Thamdrup et al., 1993). This process may explain the presence of elemental S in the reactive material. In addition, the S μXRF and S μXANES indicate the majority of S present in the secondary precipitates is in reduced phases (pyrite or elemental S). Additional SO_4^{2-} probably accumulated in the column material derived from SO_4^{2-} in the influent water.

The majority of the organic carbon appeared to be unreacted; however, the cellular structure of several particles was replaced by Fe sulfides. SEM analyses indicate the precipitate replacing OC is composed of Fe and S (**Figure 2.13**). The μXRF and S μXANES results indicate the majority of S present in the secondary precipitate is in the reduced phase, as pyrite or elemental S (**Figure 2.15**). Replacement of cellular organic matter by sulfides was observed in a similar study, with the sulfide consisting mainly of pyrite and appearing opaque in transmitted light and white under reflected light (Jambor et al., 2005). The formation of secondary carbon is also a common characteristic in sulfate-reducing PRB systems (Jambor et al., 2005).

2.4.2.2 Arsenic

Influent As concentrations fluctuated during the experiment, which can be divided into four main stages (**Figure 2.6**). In stage I, As concentrations are low (24 μg L^{-1}), probably due to O_2 influx into the bottles during storage. Improved collection methods maintained higher As concentrations in the influent in stage II (4 mg L^{-1} for approximately 10 PVs). In stage III, As concentrations decrease (103 μg L^{-1}). Finally, in stage IV, dissolved As and Fe added to the

influent solution results in increased concentrations (7.9 mg L^{-1} As, 52.3 mg L^{-1} Fe) for the remainder of the experiment.

The effluent As concentrations in column T0 ranged from 0.3 to 8.3 mg L^{-1}, with a mean of 3.6 mg L^{-1}. Column T0 removed a cumulative mass of 17.8 mg of As, which represents 22.6% removal of the total influent As. In all three treatment columns, effluent As concentrations remained below the EPA maximum contaminant limit of 10 µg L^{-1} over the duration of the experiment. Removal occurred within the first 3 cm of reactive material in T1, T2, and T3, with the cumulative masses of As removed (79.6, 93.4, and 86.8 mg for T1, T2, and T3, respectively), which represents >99.9% removal of the total influent As.

The reducing conditions that developed within the columns likely contributed to As removal and immobilization due to two reactions. First, the formation of H_2S through bacterially-mediated SO_4^{2-} reduction may have resulted in the precipitation of As-bearing secondary sulfide minerals (reactions [4] and [5]; Blowes et al., 2000; Jambor et al., 2005). High concentrations of H_2S at the onset of the experiment, followed by lower concentrations, reflect removal through metal sulfide precipitation. Synchrotron results also indicate the presence of As in secondary precipitates containing Fe and S. Second, the ZVI in the mixture and the formation of Fe (oxy)hydroxides and secondary sulfide precipitates (reaction [3]) likely created surfaces suitable for As adsorption. Synchrotron results indicate the presence of sorbed arsenate onto ferrihydrite on secondary precipitates. Retention of As may be due to mechanisms such as incorporation into the tetrahedral Fe-S layers of mackinawite or adsorption onto Fe oxyhydroxides (Bowell, 1994; Mullet et al., 2002). Water samples from profile measurements were undersaturated with respect to crystalline As-bearing phases including realgar and orpiment. However, As concentrations in the treatment column profiles declined sharply upstream from to the first sampling port; for example, in the second profile (27 PVs) for column T1 the As concentration declined from 8.9 mg L^{-1} to < 5 µg L^{-1} upstream from port 1, suggesting any removal of As by sulfide precipitation occurred upstream from the first sampling port. Iron corrosion products including maghemite, magnetite, hematite (Fe_2O_3), and goethite (FeO(OH)) may have affected the ZVI and As interaction and also contributed to the rapid removal of As (Rao et al., 2009; Su & Puls, 2001). Arsenic may have been removed through co-precipitation

with Fe sulfides or incorporation by inner-sphere adsorption onto the surface of goethite and other FeOOH polymorphs (Ludwig et al., 2009; Stichbury, 2000).

Synchrotron-radiation based µXRF and µXANES results indicate the presence of As in the secondary precipitates, which contain Fe and S and surround grains of silica sand (**Figures 2.16, 2.17**). The µXANES spectral features associated with As(V) are most similar to arsenate sorbed to ferrihydrite. Reduced As phases, including realgar, orpiment, and arsenopyrite, were also observed. Kankite may also occur within the secondary product replacing cellular organic material. These observations indicate As is likely incorporated into the structure of secondary precipitates through sorption or co-precipitation. A combination of µXANES/µXRF results indicate the formation of As-sulfide minerals occurs, despite geochemical modelling results indicating undersaturation with respect to realgar and orpiment. As noted above, the majority of these minerals likely formed upstream from the first sampling port. Both reduced and oxidized forms of As are present in the secondary precipitates; however, the majority of As is in the reduced form (−1, +3). Reduced As is anticipated to be present due to the reducing conditions that were sustained within the column. In addition, the reducing and anoxic conditions maintained throughout the experiment suggest the As immobilized in the sulfide form should be geochemically stable.

2.4.2.3 Metals

A sharp decrease in metal concentrations was observed between the influent and effluent (Al, Cd, Co, Cu, Ni, Zn; **Figure 2.8**). The increase in pH and the precipitation of secondary Al (oxy)hydroxides, including gibbsite (γ -$Al(OH)_3$) and boehmite (γ-AlO(OH)), likely contributed to the removal of Al (**Figure A.8**). The presence of higher concentrations of H_2S early in the experiment further suggests the decline in metal concentrations is due to the precipitation of low-solubility metal sulfides (reactions [4] and [5]). In the presence of dissolved Fe(II) and H_2S, disordered mackinawite is predicted to be the first phase to precipitate (Wolthers et al., 2003). Geochemical modeling indicates the water is saturated with respect to sulfide minerals such as sphalerite, chalcopyrite, covellite (CuS), and chalcocite (Cu_2S; **Figure A.9**); this suggests the formation of these sulfide minerals, or less crystalline precursors, likely contributed to the removal of Cu and Zn. Retention of metals may be due to incorporation into the tetrahedral Fe-S layers of mackinawite (Mullet et al., 2002). In addition, adsorption onto organic matter and other

(co)precipitated phases such as Fe and Al (oxy)hydroxides may also contribute to retention of metals (Gibert et al., 2005). The removal and retention of metals including Cu, Zn, and Ni are likely due to the formation of low-solubility metal sulfides and adsorption onto Fe sulfides and Fe (oxy)hydroxides.

2.4.3 Carbon and Nutrient Release

The initial release of NH_3-N and PO_4-P in T1, T2, and T3 could be due to the breakdown of organic matter containing N and P (Paulson et al., 2018; Waybrant et al., 2002). Decomposition of organic material likely promoted the growth of heterotrophic SRB that utilize SO_4^{2-} as an electron acceptor (Herbert Jr et al., 2000). Although column T1 contained the highest OC content, the concentrations of PO_4-P and NH_3-N were similar to columns T2 and T3; PO_4-P and NH_3-N were lower in column T0 (**Figure A.3**). Despite high effluent concentrations of NH_3-N and PO_4-P early in the experiments, an overall decrease in concentrations occurred over time. PO_4-P and NH_3-N concentrations persisted in the porewater in later stages of the experiment (**Figure A.3)**.

High DOC concentrations observed at the onset of the experiment are attributed to the initial flush of groundwater through the OC present in the reactive material (Lindsay et al., 2011a). The highest concentration of DOC released in the initial surge corresponded to T1, the column with the highest percentage of OC. The highest concentrations of Fe were also observed in column T1 during the initial surge. Organic carbon may be utilized as an electron donor for Fe reduction (reactions [4] and [5]), suggesting the high initial DOC concentrations may have contributed to an increase in Fe concentrations. Following the initial surge in DOC and Fe, concentrations progressively decreased.

The initial increase in DOC concentrations could be due to two reasons. First, Na-lactate solution and residual carbon, added as creek sediment, was likely broken down and released during the first few PVs. Second, the initial surge could be attributed to the rapid depletion of labile organic carbon from the initial labile OC present in the reactive mixture. Following depletion of this initial labile OC, *in situ* OC degradation may have become the main source of OC available for bacterially-mediated SO_4^{2-} reduction (Lindsay, 2009). Increases in DIC concentrations were also observed in all four columns. The largest increase in DIC was observed in column T1, corresponding to the highest percentage of OC in the reactive mixture. DIC

concentrations may increase due to mineralization of organic matter coupled with bacterially-mediated SO_4^{2-} reduction (Asmussen & Strauch, 1998).

An enrichment in δ^{13}C-DIC at the first sampling port was followed by a gradual decrease in δ^{13}C-DIC along the length of columns T1, T2, and T3 (**Figure 2.9**). In column T0, following the initial enrichment the δ^{13}C-DIC values remained relatively constant at near 0 ‰ for the remainder of the column length. The observed trend in column T0 reflects the influence of limestone from the reactive material. The slight increase in alkalinity within the first 3 cm of reactive material corresponds to a sharp increase in δ^{13}C-DIC values. Column T3, with the lowest percentage of OC in the reactive mixture, showed the sharpest increase in δ^{13}C-DIC, followed by T2 and then T1. Despite the increase in δ^{13}C-DIC ratios, values remained relatively depleted, especially in columns T1 (−14.8 ‰) and T2 (−15.1 ‰). The enrichment of δ^{34}S-SO_4 combined with the depletion of δ^{13}C-DIC is indicative of SO_4^{2-} reduction coupled with oxidation of organic carbon. A slight decrease in δ^{13}C-DIC was observed along the column length. The lower ratios observed in T1 may be attributed to a contribution from labile OC (leaf mulch and wood chips).

2.4.4 Sulfate Reaction Rates

The removal rates of SO_4^{2-} in the treatment columns were calculated based on the second profiles collected from columns T1, T2, and T3 at 27, 40, and 38 PVs, respectively (**Figure 2.18**). Sulfate removal rates within all three columns are consistent with a zero-order rate equation, $C = -k_o t$, where C is the SO_4^{2-} concentration (mg L^{-1}), t is the residence time (d), and k_0 is the zero-order rate constant for SO_4^{2-} removal (mg L^{-1} d^{-1}). The three treatment columns had similar SO_4^{2-} removal rates, with $R_{S,1} = -33.10$ mg L^{-1} d^{-1} for T1, $R_{S,2} = -33.13$ mg L^{-1} d^{-1} for T2, and $R_{S,3} = -30.39$ mg L^{-1} d^{-1} for T3. The negative rate constants indicate SO_4^{2-} was removed. The zero-order rate expression provides a reasonable description for the rate of SO_4^{2-} reduction ($R^2 > 0.93$). The weight percentage of dry OC varied in each of the three treatment columns from 20 to 40 wt. %. The normalized SO_4^{2-} removal rates were −0.18 (T1), −0.18 (T2), and −0.20 mg L^{-1} d^{-1} g^{-1} of dry OC (T3).

The zero-order equation for reaction rates has been used in similar studies (Benner et al., 2002). Reported rates vary from −0.14 to −4.23 mg L^{-1} d^{-1} g^{-1} of dry OC (Waybrant et al., 2002) to −1.24 to −1.40 µg L^{-1} d^{-1} g^{-1} of dry OC (Lindsay et al., 2008) in studies utilizing similar

material. The bulk SO_4^{2-} removal rate for a field barrier system (Benner et al., 2002), was between 40 and 58 mmol L^{-1} a^{-1} (10.5-15.3 mg L^{-1} d^{-1}), which is of similar magnitude to the rates observed in our study. Sulfate reduction rates were very similar to a laboratory system containing only OC (Waybrant et al., 2002). The removal rate observed in our system was approximately two orders of magnitude higher than a study containing both OC and ZVI and that determined SO_4^{2-} removal rates using a mass-based approach rather than an aqueous concentration-based method (Lindsay et al., 2008). Variances in the reactive material used may also have affected SO_4^{2-} reduction rates. Mixtures varied from those containing only organic carbon (Benner et al., 2002; Waybrant et al., 2002) to those that included ZVI (Lindsay et al., 2008).

Of the three treatment columns, T3, containing the lowest wt. % of OC, had a slightly higher SO_4^{2-} removal rate. In a similar experiment, a higher removal rate was observed in a mixture containing 50 vs. 40 dry wt. % OC in a microcosm study (Lindsay et al., 2008). Even though the addition of OC has been shown to enhance SO_4^{2-} reduction rates, a substantial enhancement in reaction rates may not occur above a certain dry wt. % of OC (Lindsay et al., 2008). Based on the similar rates calculated for all three of our treatment columns, the SO_4^{2-} reaction rate may not be further enhanced at OC contents above 20 wt. % (the lowest percentage of OC considered). However, the abundance of OC may affect the longevity of the reactive mixture (Lindsay et al., 2008).

2.5 Conclusions

Removal of As, metals, and SO_4^{2-} was observed in all treatment columns. The pH of the groundwater increased from pH < 4 to circumneutral values before the first sampling port, and a pH > 7 was maintained throughout the experiment. The onset of reducing conditions and bacterially-mediated SO_4^{2-} reduction resulted in decreases in SO_4^{2-} concentrations, H_2S production, enrichment of $\delta^{34}S\text{-}SO_4$, and the presence of SRB populations in all treatment columns. Column T0, containing minimal amounts of OC, removed metals from the groundwater, but did not contain sufficient OC to sustain sulfate-reducing conditions and result in As removal. A higher relative abundance of SRB was observed at the influent vs. effluent end of the treatment columns. Above 20 wt. % OC, no additional increase in SRB abundance or activity was observed. Sulfate removal rates ranged from 0.18 to 0.20 mg L^{-1} d^{-1} g^{-1} dry OC for the three treatment columns. Removal rates were within one order of magnitude of previous

laboratory column experiments utilizing similar reactive material. Varying the wt. % of ZVI and OC resulted in modest changes to SO_4^{2-} removal rates.

Results from synchrotron radiation bulk S XANES indicate the accumulation of reduced S phases, including pyrite and FeS, on ZVI grain coatings. Removal of Fe and other metals is attributed to bacterially-mediated SO_4^{2-} reduction and the subsequent precipitation of low solubility metal sulfides including pyrite, sphalerite, chalcopyrite, or less-crystalline precursors. Removal of Fe may also be due to the replacement of cellular organic material by an Fe-sulfide precipitate. A decrease in effluent Fe concentrations was observed over time, but concentrations remained above 2 mg L^{-1} throughout the experiment.

The removal of As is attributed to adsorption onto Fe (oxy)hydroxides and precipitation of As-bearing secondary sulfide minerals. Arsenic is present as both oxidized and reduced species in the form of secondary precipitates and adsorbed products. Arsenite is immobilized as As-crystalline phases including realgar and orpiment, and arsenate is removed through adsorption onto ferrihydrite. The reducing and anoxic conditions of the column material indicate that immobilized As should be geochemically stable.

This study demonstrates the potential for the reactive material, which contains a mixture of OC, ZVI, and limestone, to remove metal(loids) from acidic groundwater. No significant difference among the three treatment columns was observed, suggesting a cost-effective composition of reactive material may utilize minimal ZVI (20 wt. %). Further evaluation of the reactive material is needed to determine the long-term capabilities of the mixture. In addition, evaluation of the material under field conditions would increase our understanding of the influence of changing temperatures on the reactivity of the column material.

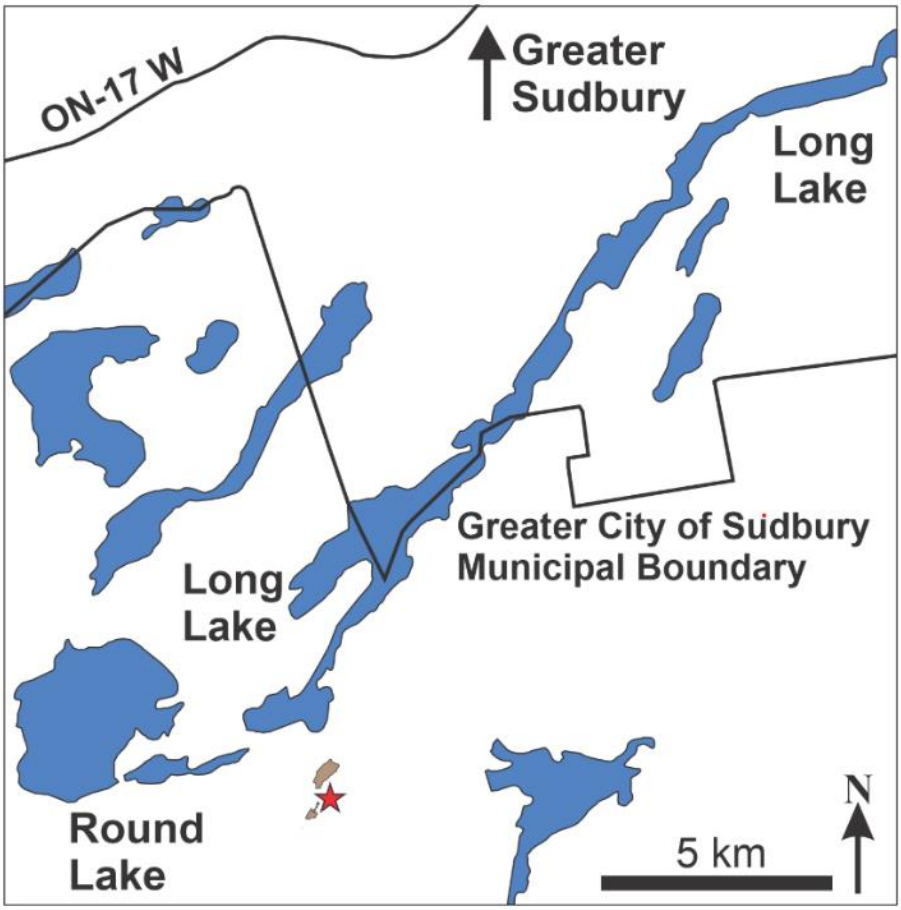

Figure 2.1 Map of Long Lake with respect to Sudbury, ON. The red star to the south of the southwest end of Long Lake is the location of the Long Lake Au Mine Tailings Impoundment (modified after Verbuyst, 2020).

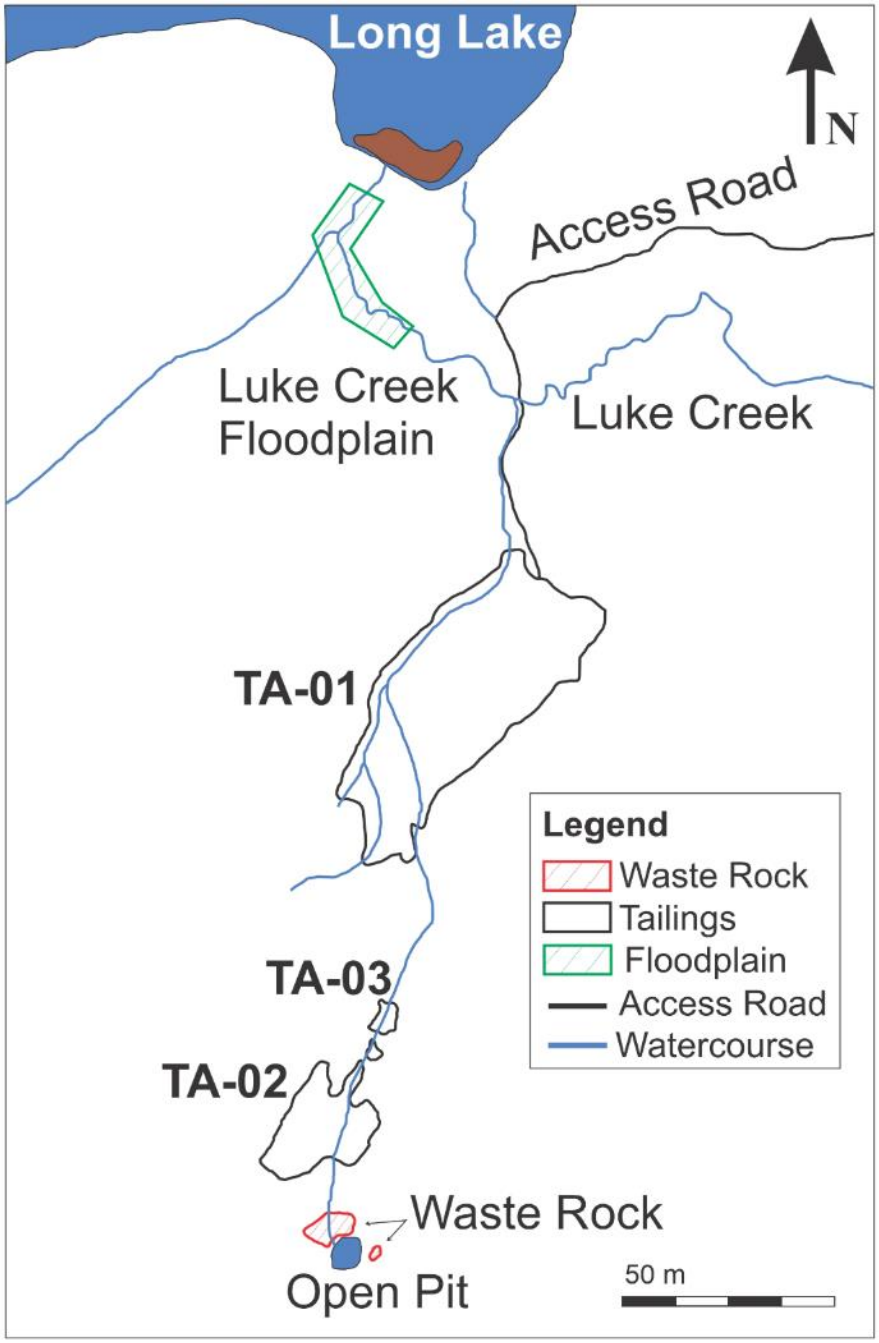

Figure 2.2 Map of the southwest end of Long Lake and tailings impoundment to the south. TA-01, TA-02, and TA-03 are the three sand-covered tailings areas (modified after Verbuyst, 2020).

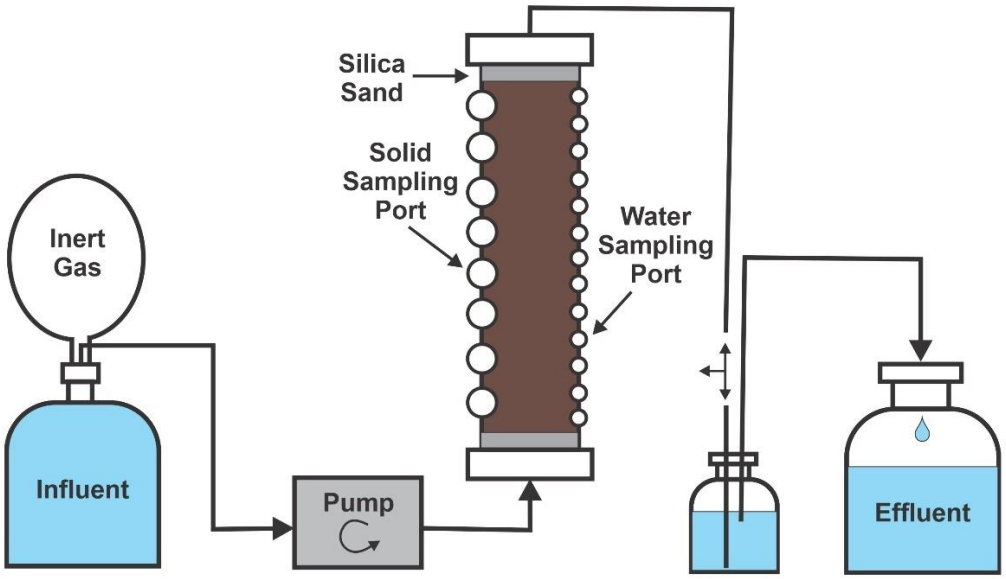

Figure 2.3 Schematic diagram of the experimental setup and column design.

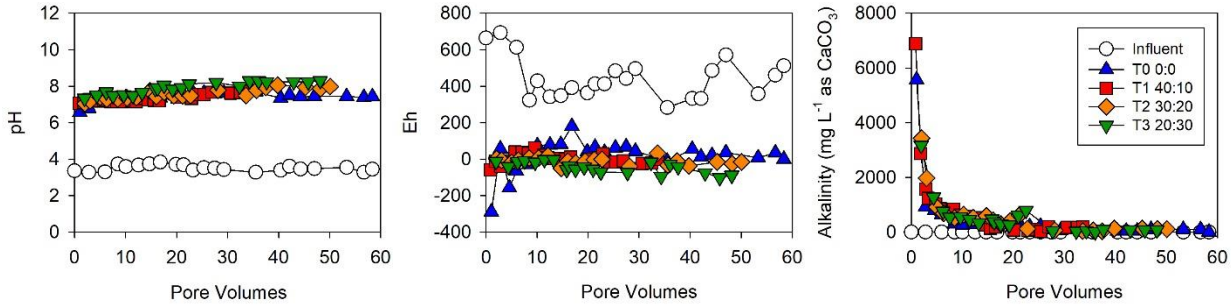

Figure 2.4 pH, Eh, and alkalinity versus PVs in the influent and effluent of the four columns. The OC:ZVI ratio in column T0 is 0:0, T1 is 40:10, T2 is 30:20, and T3 is 20:30.

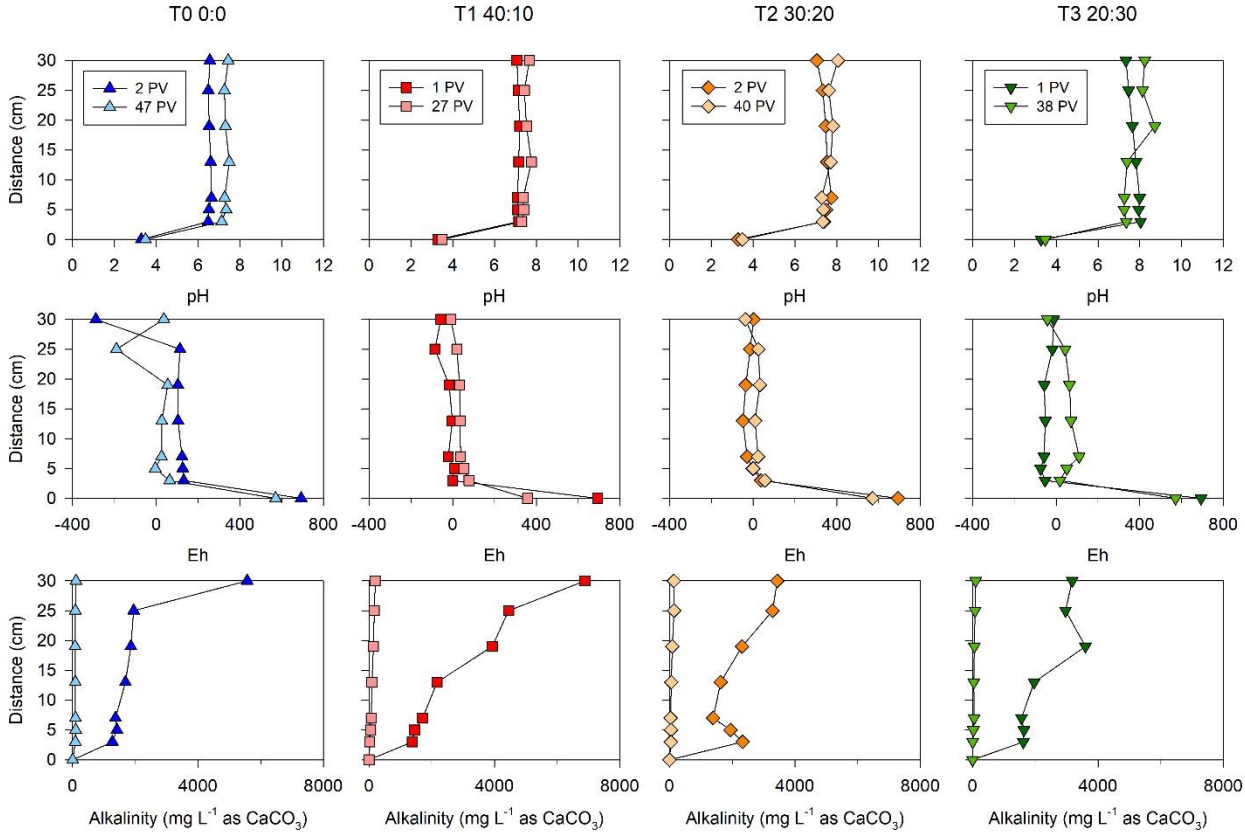

Figure 2.5 pH, Eh, and alkalinity in aqueous samples collected along the length of columns T0, T1, T2, and T3 at two different time points. Each column of graphs represents a different experimental column. Distance 0 cm represents the influent concentration and 30 cm represents the effluent concentration. The OC:ZVI ratio of column T0 is 0:0, T1 is 40:10, T2 is 30:20, and T3 is 20:30.

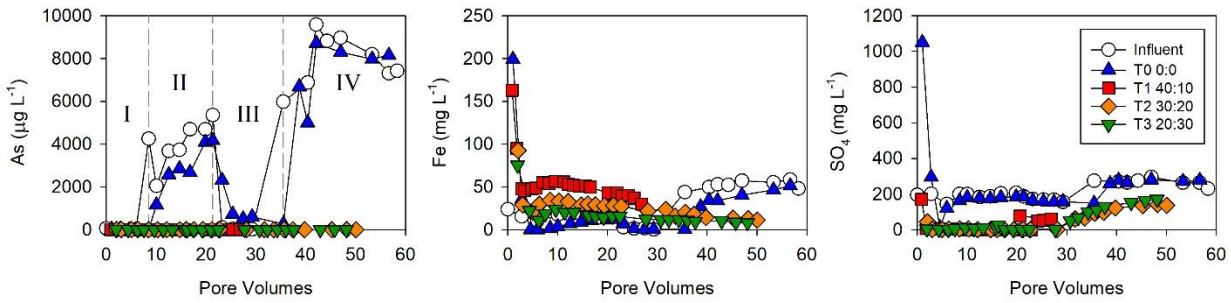

Figure 2.6 Concentrations of As, Fe, and SO_4^{2-} versus PVs in the influent and effluent of the four columns. Input of As was discontinuous throughout the experiment, with concentrations varying between four main stages (left). A spike of As and Fe was added at the third grey dashed line (35 PVs) following the end of stage III. The OC:ZVI ratio of column T0 is 0:0, T1 is 40:10, T2 is 30:20, and T3 is 20:30.

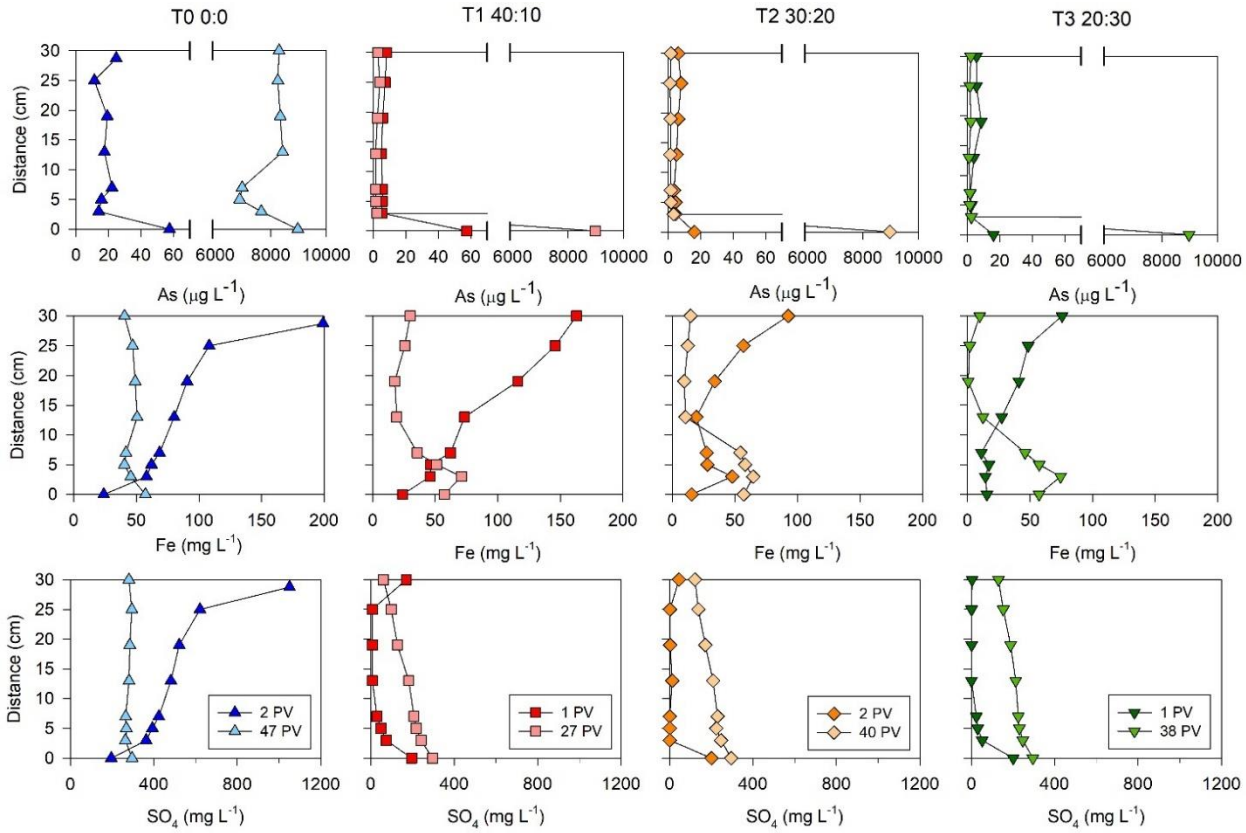

Figure 2.7 Concentrations of As, Fe, and SO_4^{2-} in aqueous samples collected along the length of columns T0, T1, T2, and T3 at two different time points. Each column of graphs represents a different experimental column. Distance 0 cm represents the influent concentration and 30 cm represents the effluent concentration. The OC:ZVI ratio of column T0 is 0:0, T1 is 40:10, T2 is 30:20, and T3 is 20:30.

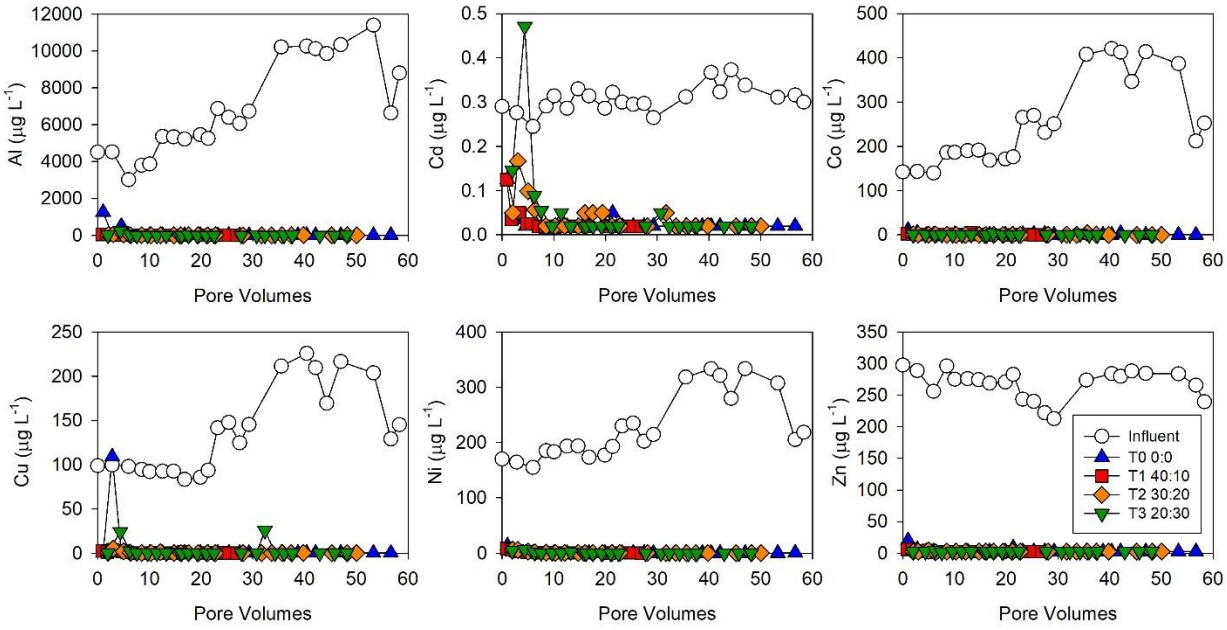

Figure 2.8 Concentrations of metals (Al, Cd, Co, Cu, Ni, and Zn) versus PVs in the influent and effluent of the four columns. The OC:ZVI ratio of column T0 is 0:0, T1 is 40:10, T2 is 30:20, and T3 is 20:30.

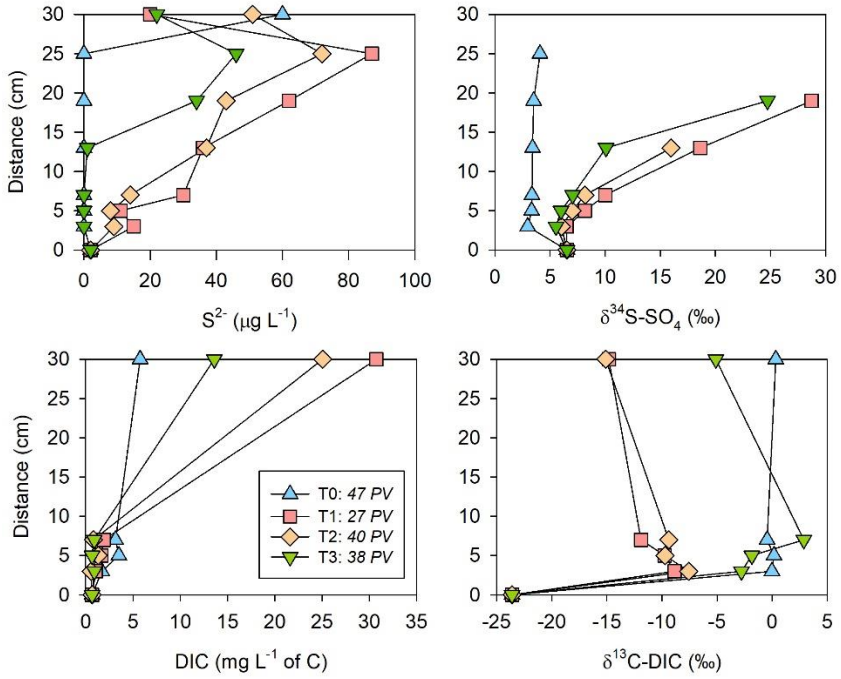

Figure 2.9 Top row: Concentrations of S^{2-} compared to $\delta^{34}S$-SO_4 values in aqueous samples collected along the length of columns T0, T1, T2, and T3. Bottom row: Concentrations of dissolved inorganic carbon (DIC) are compared to $\delta^{13}C$-DIC along the column length. Data are from the second vertical profile collected. The OC:ZVI ratio of column T0 is 0:0, T1 is 40:10, T2 is 30:20, and T3 is 20:30.

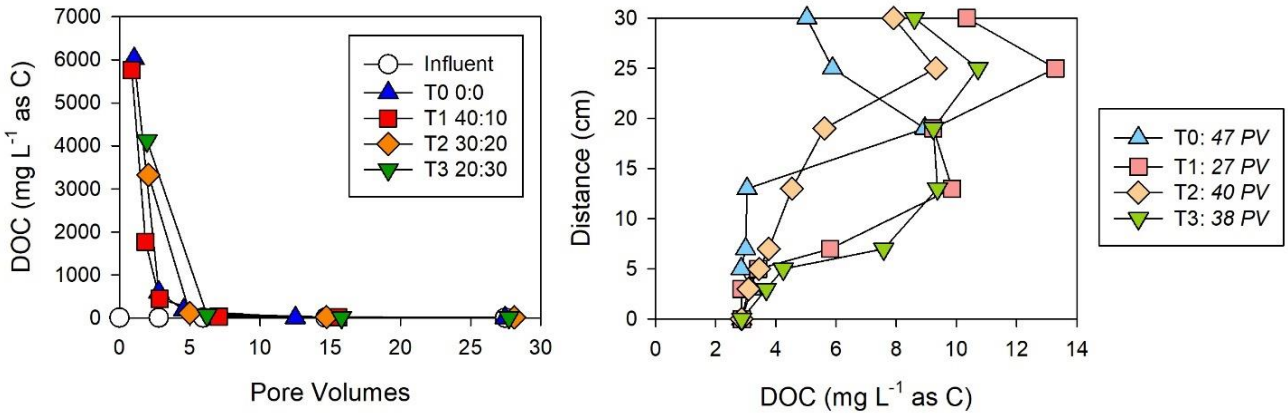

Figure 2.10 Concentrations of dissolved organic carbon (DOC) versus PVs (left) compared to the changes in DOC values in aqueous samples collected along the length of columns T0, T1, T2, and T3 (right). The OC:ZVI ratio of column T0 is 0:0, T1 is 40:10, T2 is 30:20, and T3 is 20:30.

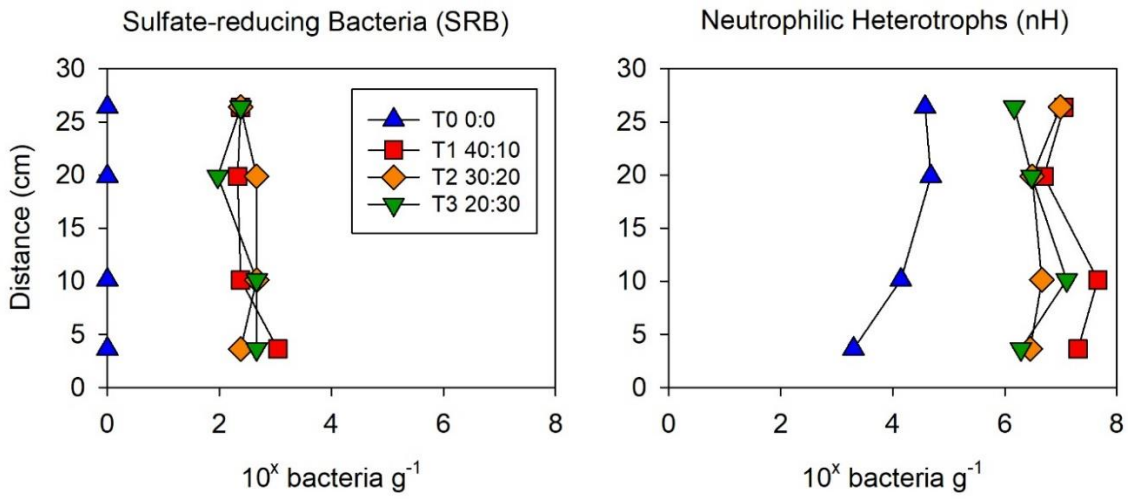

Figure 2.11 MPN enumeration results for solid-phase samples collected along the length of columns T0, T1, T2, and T3. The enumeration of both sulfate-reducing bacteria (SRB) and neutrophilic heterotrophs (nH) is shown.

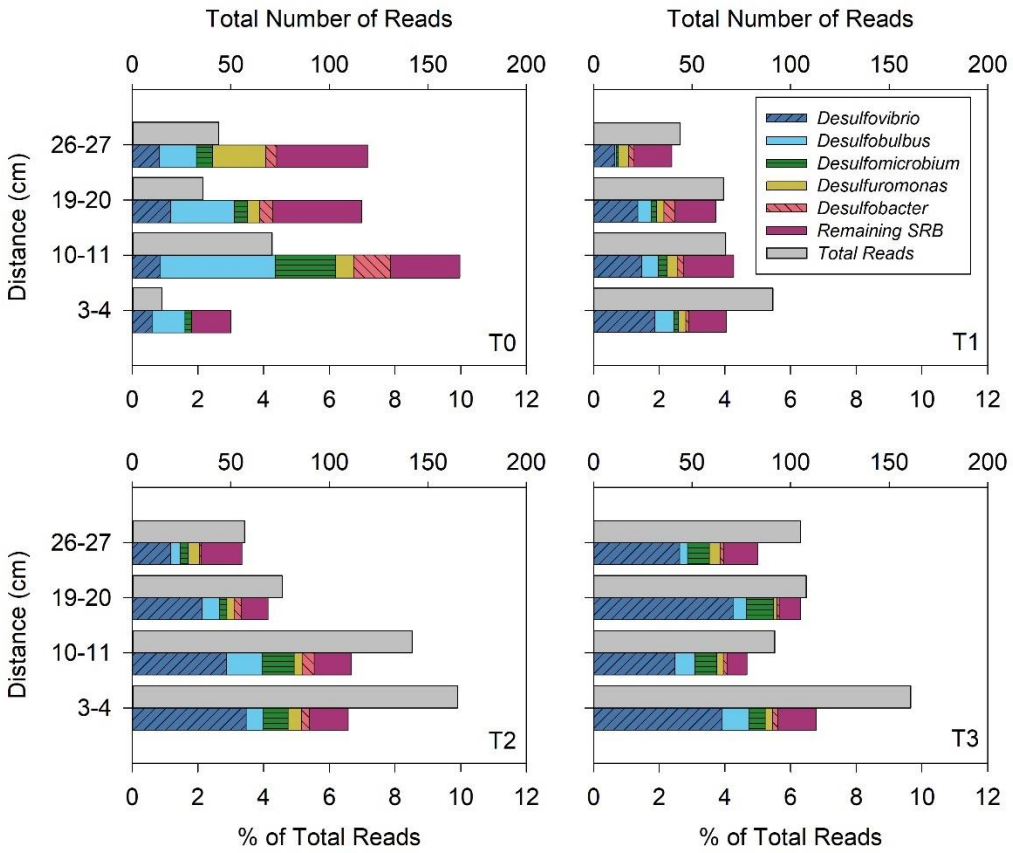

Figure 2.12 Relative abundance of known SRB identified through 16S rRNA amplicon sequencing in the solid material collected along the length of columns T0, T1, T2, and T3. The five most abundant genera are plotted, and the remaining SRB grouped separately. The total number of reads of SRB obtained during sequencing (top bar) and the percentage of total reads including the distinction between major SRB genera (bottom bar) are shown.

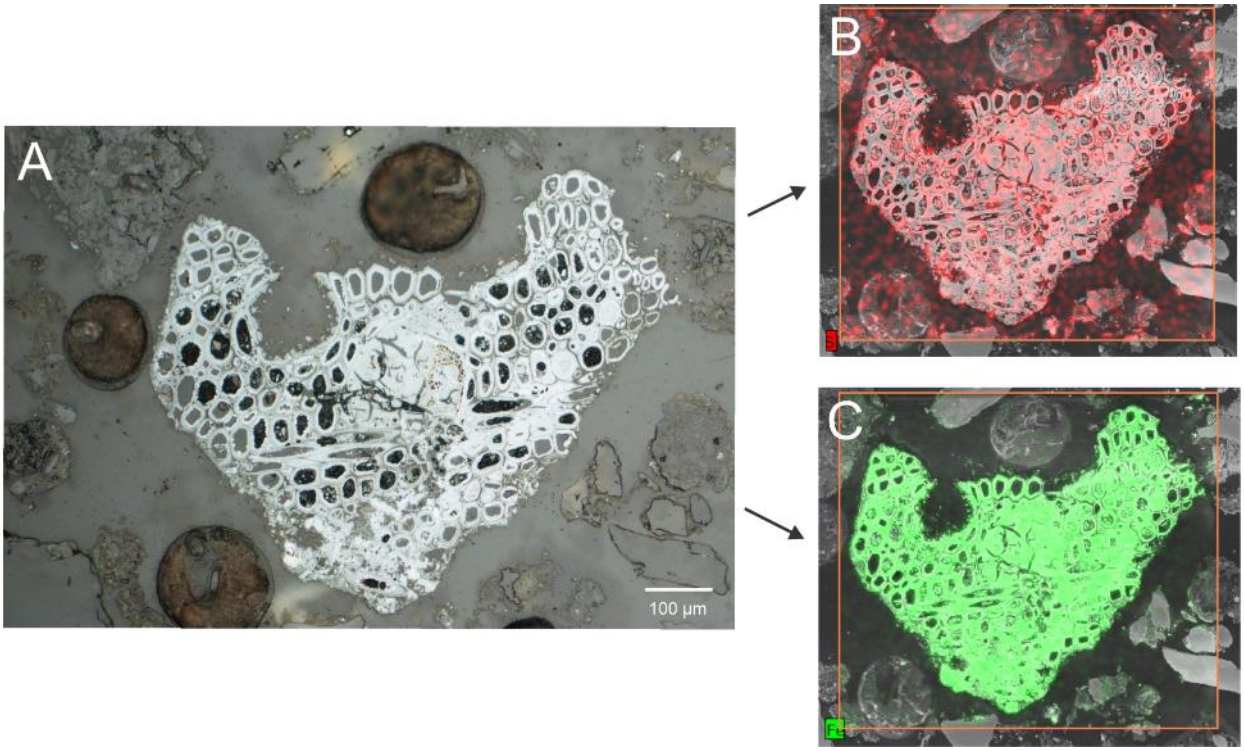

Figure 2.13 Reflected light microscopy image of the replacement of OC by a secondary precipitate (A). The presence of S (B) and Fe (C) in the precipitate (right) is shown through SEM imaging.

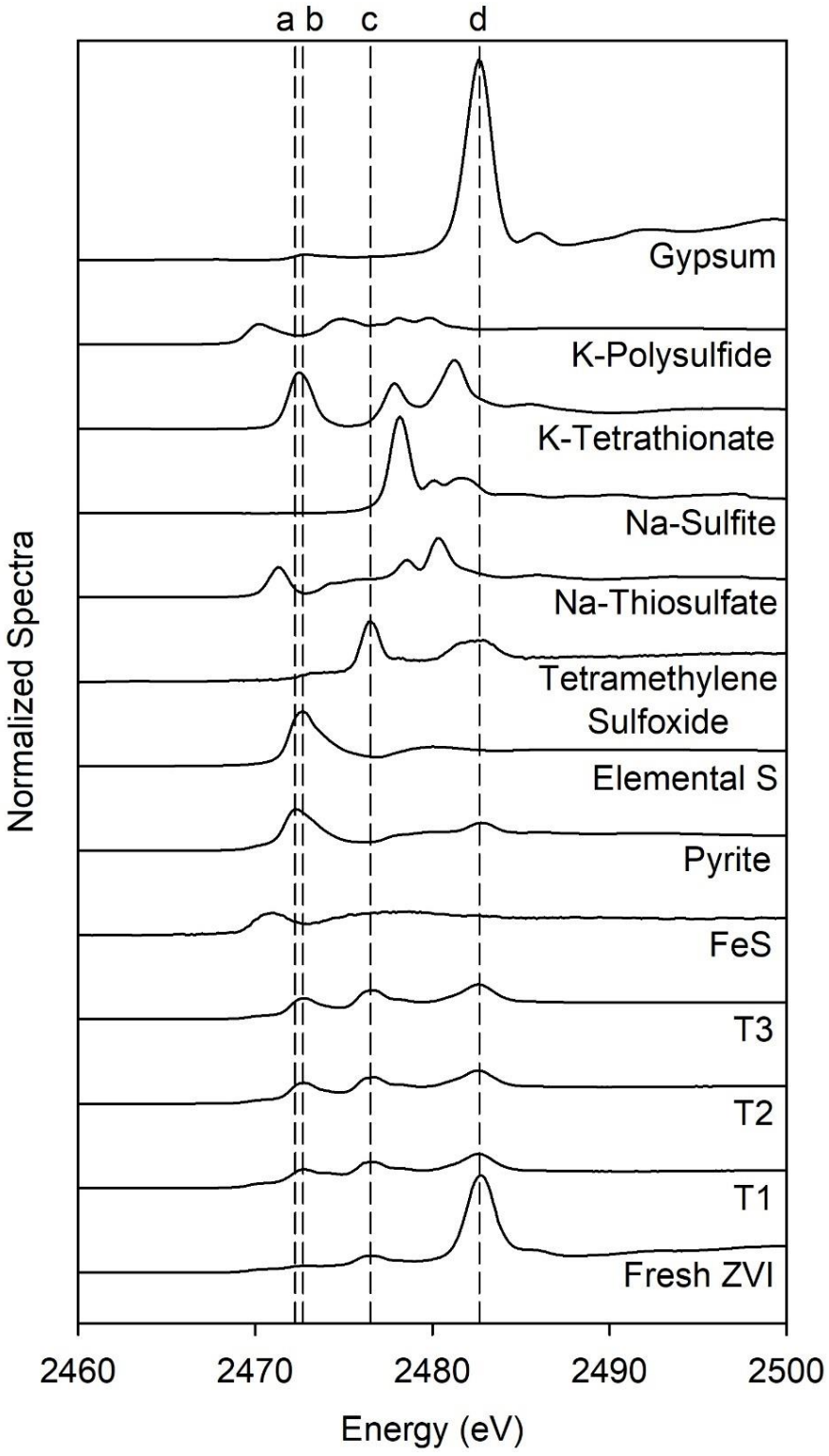

Figure 2.14 Bulk S XANES spectra of solid samples collected from laboratory columns T1, T2, and T3. Spectra of unreacted, untreated ZVI and other standards are also shown. The spectral peak locations for pyrite (a), elemental S (b), tetramethylene sulfoxide (c), and gypsum (d) are shown with dashed lines.

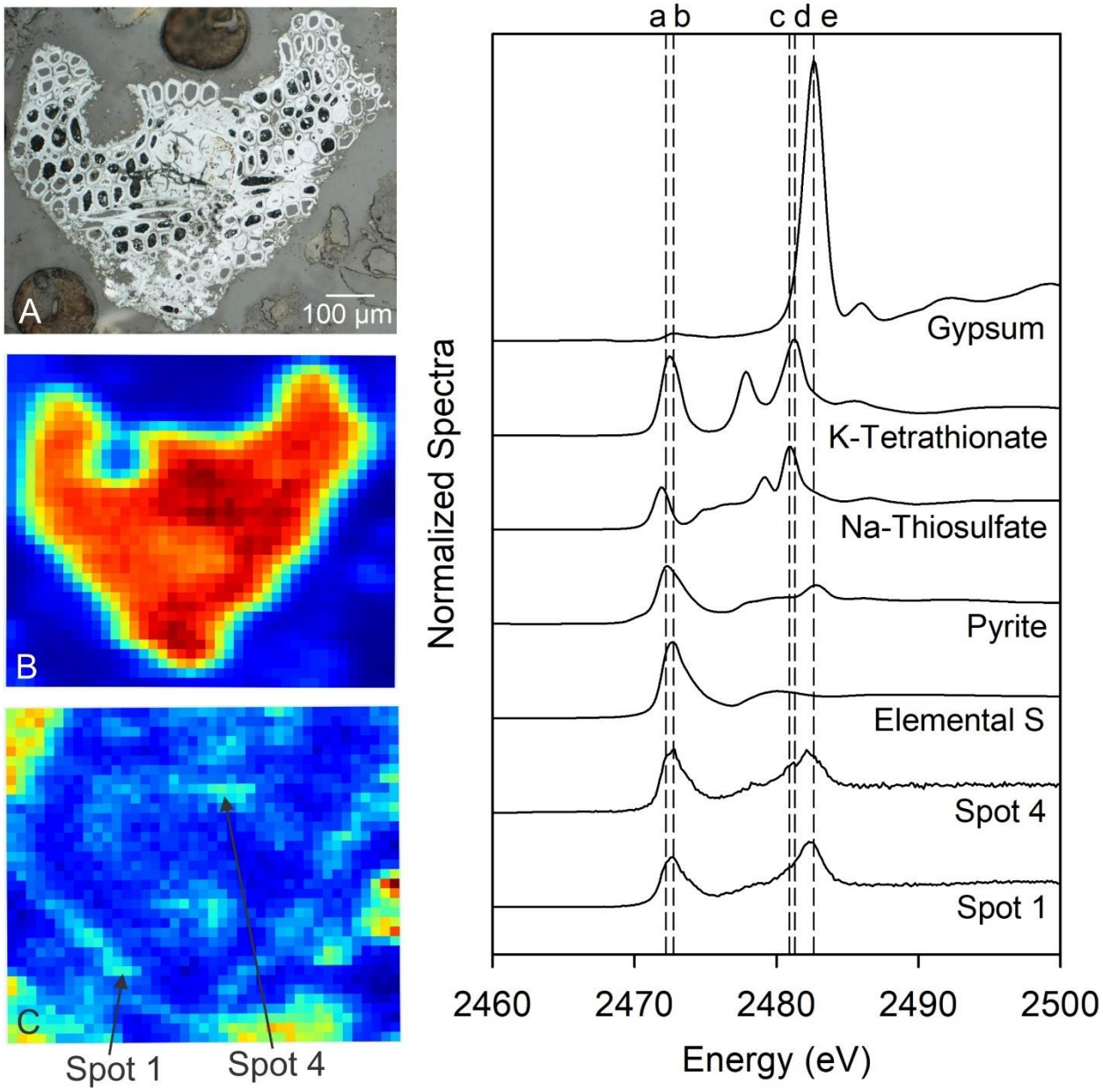

Figure 2.15 Results from optical microscopy (A), Fe µXRF imaging (B), S µXRF imaging (C), and S µXANES spectra (right) of a secondary precipitate replacing OC substrate. Spectra from two separate scan locations (spots 1 and 4) are plotted with standards used for LCF. The spectral peak locations of pyrite (a), elemental S (b), Na-thiosulfate (c), K-tetrathionate (d), and gypsum (e) are shown with dashed lines.

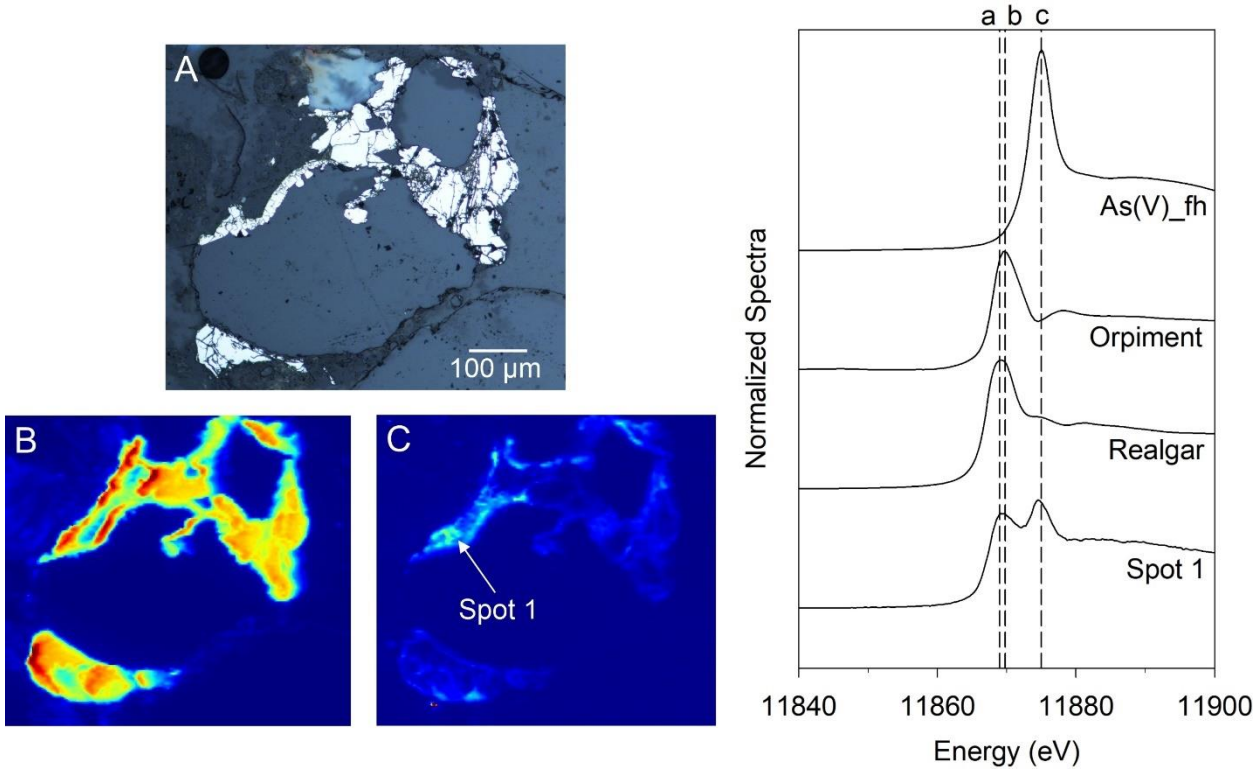

Figure 2.16 Results from optical microscopy (A), Fe µXRF imaging (B), As µXRF imaging (C), and As µXANES spectra (right) of a secondary precipitate that formed between grains of silica sand (column T2). The spectrum collected from spot 1 is plotted with the standards used for LCF. The spectral peak locations of realgar (a), orpiment (b), and As(V) sorbed onto ferrihydrite (c) are shown with dashed lines.

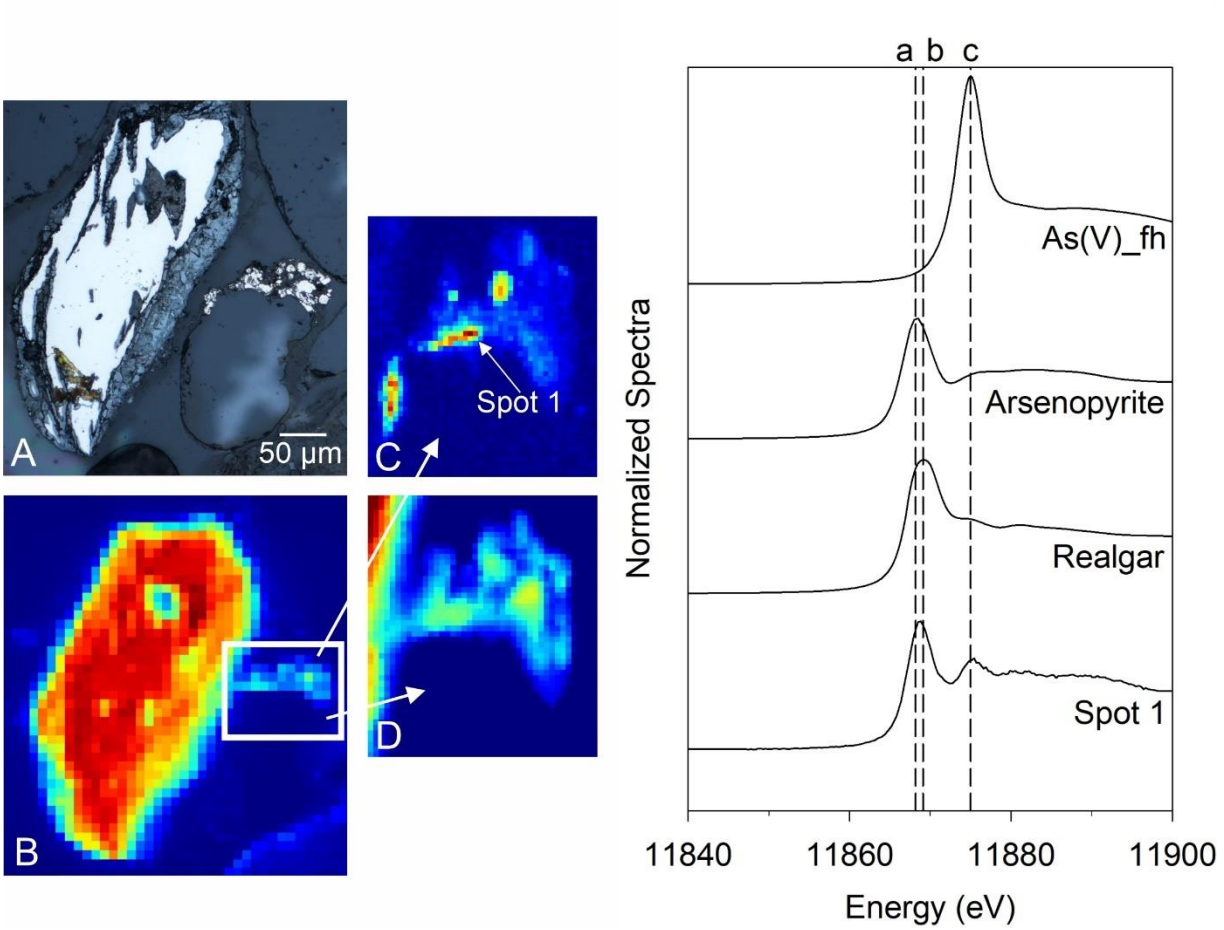

Figure 2.17 Left: Results from optical microscopy (A), Fe µXRF imaging (B), and close ups of As µXRF imaging (C) and Fe µXRF imaging (D) of a location noted in (B). Right: As µXANES spectra of a secondary precipitate that formed along the edge of a silica sand grain (column T3). The spectrum collected for spot 1 is plotted with the standards used for LCF. The spectral peak locations of arsenopyrite (a), realgar (b), and As(V) sorbed onto ferrihydrite (c) are shown with dashed lines.

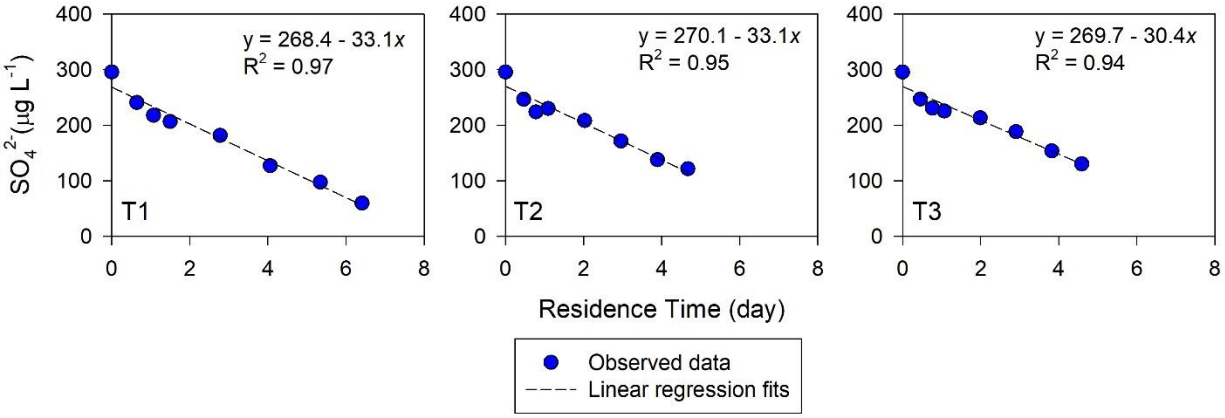

Figure 2.18 Regression fits of SO_4^{2-} removal as a function of residence time in the three treatment columns.

Table 2.1 Average composition (dry wt. %), flow rate, residence time, porosity, and total pore volumes passed through each column.

Column Name	Organic Carbon (wt. %)	Zerovalent Iron (wt. %)	Silica Sand (wt. %)	Limestone (wt. %)	Avg Flow Rate (mL h^{-1})	Residence Time (d)	Total PV	Porosity
T0 0:0	0	0	90	10	3.0	3.69	59.9	0.37
T1 40:10	40	10	45	5	3.1	6.41	34.5	0.64
T2 30:20	30	20	45	5	3.4	4.67	52.3	0.47
T3 20:30	20	30	45	5	3.4	4.59	50.9	0.45

Chapter 3: *Removal of Arsenic and Metals from Groundwater Impacted by Mine Waste Using Zero-valent Iron and Organic Carbon: Field-reaction Cell*

Executive Summary

Arsenic (As) is a widespread contaminant throughout the world and is frequently associated with gold mining. Passive remediation technologies have the potential to remove As from contaminated groundwater and mine waste effluents. This study evaluated the effectiveness of a reactive mixture containing zero-valent iron, organic carbon, and limestone to remove As and metals from acidic groundwater. Specifically, a field-reaction cell, 30 cm in diameter and 99 cm in length, was installed to treat groundwater impacted by the mill tailings impoundment at the Long Lake mine, Sudbury, ON. The experiment builds on a laboratory column study using groundwater from the same site. Results from the field cell indicate it successfully increased groundwater alkalinity and pH to circumneutral values. Conditions favourable for bacterially-mediated SO_4^{2-} reduction were indicated by a decrease in Eh, a decrease in SO_4^{2-} concentrations coupled with an enrichment of $\delta^{34}S$, and the presence of microbial communities of sulfate-reducing bacteria, iron-reducing bacteria, and neutrophilic heterotrophs. The most abundant SRB genera were *Desulfomicrobium*, *Desulfosporosinus*, *Desulfitibacter*, and the order *Desulfovibrionales.* A mean SO_4^{2-} removal rate of 6.3 µg L^{-1} d^{-1} g^{-1} of dry organic carbon was calculated based on the decline in SO_4^{2-} concentrations measured along the length of the cell. Removal of As and metals (Al, Cu, Ni, Zn) was observed within the first 9 cm of reactive material. Iron concentrations remained relatively constant between the influent and effluent ends of the reaction cell. Optical microscopy indicated the presence of Fe (oxy)hydroxides and Fe sulfides including pyrite and pyrrhotite, as well as other metal sulfides such as chalcopyrite, in the solid material from the cell. The removal of metals is attributed to the precipitation of low-solubility metal sulfides due to bacterially-mediated SO_4^{2-} reduction; geochemical modelling confirmed the precipitation of metal sulfides was favoured. Synchrotron-radiation based bulk S X-ray absorption near-edge structure spectroscopy (XANES) analyses indicated the majority of S was present in the reduced form as sulfides and elemental S. Removal of As is attributed to sorption onto Fe (oxy)hydroxides and ZVI corrosion products and co-precipitation with metal sulfides. The results from this study confirm the potential of the reactive mixture to remove As and metals from acidic water under conditions typical of mine sites.

3.1 Introduction

Acid mine drainage (AMD) is an ongoing environmental issue worldwide. Drainage released from mine waste deposits can have a large impact on the quality of nearby water bodies,

with effects that can persist for decades to centuries (Blowes & Jambor, 1990; Moncur et al., 2005). Acid mine drainage is associated with sulfide-bearing waste rock and tailings produced through mining of sulfidic ore bodies. The oxidation of sulfide minerals (Blowes et al., 2014):

$$FeS_{2\,(s)} + \frac{7}{2}O_2 + H_2O \rightarrow 2SO_4^{2-} + Fe^{2+} + 2H^+ \quad [1]$$

and the subsequent oxidation of Fe(II):

$$Fe^{2+} + \frac{1}{4}O_2 + \frac{5}{2}H_2O \rightarrow Fe(OH)_{3(s)} + 2H^+ \quad [2]$$

results in increased acidity through the release of H^+. In the oxidation process, metal(loids) such as arsenic (As) are released and result in contaminated, acidic water (Blowes et al., 2014). Further acidification may also accelerate the rate of sulfide mineral oxidation and increase the solubility of metals. Neutralization of the acidic water may occur through a series of mineral dissolution reactions, including the dissolution of carbonate minerals such as dolomite and calcite (Jurjovec et al., 2002). However, the depletion of carbonate minerals through neutralization processes results in an increased persistence of AMD. Therefore, proper management of water quality is critical for mining practices.

Permeable reactive barriers (PRBs) comprising reactive material placed in the subsurface perpendicular to contaminant flow can be utilized to manage tailings pore water and drainage waters at mine sites (Blowes et al., 1998; Powell et al., 1998). Chemical interactions including precipitation, reduction, and adsorption then remove contaminants from the groundwater. Barrier thickness and groundwater flow rate affect the ability of the barrier to remove contaminants and sustain low concentrations for an extended period of time (Powell et al., 1998).

Zero-valent iron (ZVI), organic carbon (OC), and mixtures thereof have been utilized as reactive materials in experiments focused on removing As and metals from groundwater (Bain et al., 2002; Guo & Blowes, 2009; Lindsay et al., 2008; Ludwig et al., 2009; Waybrant et al., 2002). The oxidation of ZVI (Gould, 1982):

$$2H_2O + Fe^0 \rightarrow Fe^{2+} + 2OH^- + H_2 \quad [3]$$

produces surface corrosion products, such as Fe (oxy)hydroxide and green rust, that may create highly reactive surfaces and result in the retention of As from the water (Ludwig et al., 2009).

The addition of OC substrates promotes the growth and activity of sulfate-reducing bacteria (SRB) and often leads to bacterially-mediated SO_4^{2-} reduction (Benner et al., 1997):

$$SO_4^{2-} + 2CH_2O + 2H^+ \rightarrow H_2S + 2CO_2 + 2H_2O \quad [4]$$

The production of H_2S results in the formation of low-solubility sulfide precipitates:

$$H_2S + Me^{2+} \rightarrow MeS_{(s)} + 2H^+ \quad [5]$$

and the subsequent removal of metals and metalloids (Me^{2+}) from the water (Benner et al., 1997; Ludwig et al., 2002). Varied mixtures of organic material are more effective than single sources (Waybrant et al., 1998). Arsenic may co-precipitate with a metal sulfide or be incorporated into the structure of a mineral such as pyrite (FeS_2) (Blowes et al., 2014). Provided the metal sulfide remains in an anoxic environment, As is generally considered stable.

Zero-valent iron, OC, and mixtures of these materials have been utilized in reactive mixtures in the field, emplaced as either a trench or wall of reactive material (Bain et al., 2009; Benner et al., 1997; Ludwig et al., 2002; Wilkin et al., 2009). Removal of metals and SO_4^{2-} was reported by monitoring the barrier over a period of months to years. Processes contributing to metal and SO_4^{2-} removal include adsorption, precipitation, and bacterially-mediated SO_4^{2-} reduction. Furthermore, the increase in alkalinity may result in the conversion of the system from acid-producing to acid-consuming (Benner et al., 1997). Passive treatment technologies are an effective method of remediation that requires minimal attention following initial installation, and previous experiments indicate the barrier material can sustain low contaminant concentrations for >15 years (Benner et al., 1997).

The Long Lake Gold (Au) Mine, an abandoned site located near Sudbury, Ontario, is characterized by acidic conditions and high concentrations of As and metals in the tailings pore water. The mine operated intermittently from 1908 to 1939. Tailings from the milling process were deposited into low-lying areas (CH2MHill, 2014). In the 1970s, a layer of sand was added to the three tailings areas: TA-01, TA-02, and TA-03 (**Figure 3.1**). Prior to being capped with sand, migration of the tailings downstream through Luke Creek occurred, resulting in the formation of a tailings delta in the southwestern end of Long Lake (CH2MHill, 2014; MNDM, 2017). High concentrations of As, up to 600 mg L^{-1} (Verbuyst, 2020), have been observed in the tailings pore water. The extent of contamination and the remaining sources of As that continue to

contribute contaminants to the groundwater necessitate a long-term remediation plan. Furthermore, the remoteness of the abandoned site makes passive remediation a desirable option.

A field reaction cell was installed at the Long Lake site to evaluate the effectiveness of ZVI and OC for the removal of As and metals from the groundwater. Previous laboratory column experiments (Chapter 2) indicate the potential for the reactive material to remove As and metals from the Long Lake groundwater. Results from small-scale test cells can indicate the transferability of a remediation technology to a full-scale field setting (Benner et al., 1997). The effect of field conditions on As removal, including changing temperatures and geochemistry, was also evaluated. Results from this study will increase our understanding of the viability of passive treatment to sustain low concentrations of As in acidic groundwater from the Long Lake site.

3.2 Methodology

3.2.1 Reaction Cell Design

The reaction cell was constructed using PVC pipe (schedule 30; 99 cm long, 30 cm inner diameter). A PVC Van Stone flange was cemented onto either side of the PVC pipe, enabling a PVC blind flange to be bolted onto either end of the pipe. Each end plate included four 2.54-cm ball valves connected to bulkhead fittings covered with layers of fine and coarse NITEX™ mesh screen. The cell included eight aqueous sampling ports, each consisting of a 27.9-cm long, schedule 40, 1.27-cm PVC pipe. Holes were drilled along the side of each pipe, the pipe covered with a layer of fine NITEX™ mesh, and an end cap cemented on one end, creating a piezometer that was installed into the reaction cell. The sampling piezometers were connected to a 1.27-cm ball valve using a 1.27-cm PVC nipple inserted to a bulkhead fitting on the side of the reaction cell. The water sampling ports were spaced every 7 cm, starting 26 cm from the influent end piece. Water samples were collected using syringes attached to 0.64-cm nylon barbs, connected to the ball valves with reducer bushings. Seven solid-sampling ports were installed by drilling and threading 2.54-cm holes into the PVC pipe into the side of the reaction cell, enabling a 2.54-cm, schedule 30, PVC plug to be inserted.

3.2.2 Reaction Cell Set-Up

The reaction cell was filled with reactive material containing 40 vol.% OC (wood chips and leaf compost), 10 vol.% ZVI, 45 vol.% pea gravel, and 5 vol.% limestone. The reactive mixture is similar in composition to the reactive mixture of column T3, from a laboratory column

experiment conducted with groundwater from the same site (Chapter 2, Table 2.1). Approximately 50 g of organic-rich creek sediment collected from Laurel Creek (Waterloo, ON) was spread throughout the reactive material during packing. A 17-cm layer of pea gravel was added to the influent end and a 15-cm layer added to the effluent end to prevent disturbance of the reactive material during flow. The first sampling port corresponds to a distance of 9 cm into the reactive material, or 26 cm from the influent end. All reactive material added was weighed, and an empty weight of the cell was also obtained.

The cell was placed adjacent to Luke Creek, north of the TA-01 tailings impoundment (**Figure 3.1**). The cell was situated at a 45° angle to the creek level, with the influent end closest to the ground (**Figure 3.2**). A piezometer installed in Luke Creek was used to provide influent groundwater for the experiment. The reaction cell was first flushed with CO_2 for 1 h to displace any air bubbles. A solution containing 1000 mg L^{-1} SO_4 and 3 wt.% Na-lactate was then pumped through the cell, and after saturation all valves were closed and the cell left for 20 d before beginning groundwater flow. A full profile of samples was collected from the cell prior to introducing groundwater flow. During the first flush of groundwater, the effluent end was sampled and two full profiles of the cell were obtained over a 7-h period. A chloride tracer test was initiated the following day, with tracer solution (0.04 mol L^{-1} NaCl; EC: 5.57 mS cm^{-1}) pumped into the cell at 50 mL min^{-1} for 4 min. Two full profiles of the cell were collected during the tracer test and the effluent port was sampled at 15- to 30-min intervals. The first flush of saline tracer was used to determine the pore volume of the reaction cell using the computer software package STANDMOD (Simunek et al., 1999) with the CXTFIT model (Toride et al., 1995). The average flow rate of groundwater flow into the cell during the experiment was 960 mL h^{-1}, with a residence time of 1.14 d. The temperature at the field site during the experiment ranged from 11 to 30 °C, with a mean of 19 °C.

3.2.3 Sample Collection

3.2.3.1 Water Sampling

Water samples were collected from the reaction cell at least once a week during the 53-d trial. A syringe was connected directly to the barb on each water sampling port and 10 mL of standing water were expelled from the port. To prevent disturbance in water chemistry during water sampling, samples (60 mL) were collected starting with the effluent port, then

progressively moving through five intermediate ports and ending at the influent port. The total amount of water removed from the cell was recorded. The flow rate of the water into the cell was measured four times during the experiment by determining the mass of water flowing out of the cell over a specific length of time; the mean flow rate was 16 mL min^{-1}. A Solinst Levellogger™ was attached to the outside of the reaction cell to record the temperature twice per hour.

Water samples were collected for analysis of pH, Eh, alkalinity, electrical conductivity (EC), cations, anions, nutrients (NH_3-N and PO_4-P), and dissolved H_2S. Additional secondary samples were collected three times over the entire field trial for analysis of dissolved organic carbon (DOC), dissolved inorganic carbon (DIC), C isotopes, and S isotopes. All samples were collected using syringes and were passed through 0.45-µm filters (Acrodisc®) into polyethylene or amber glass bottles. When necessary, a 1.0-µm prefilter (Acrodisc®) was used. Direct measurements of pH, Eh, and EC (on unfiltered samples) and alkalinity, dissolved H_2S, and nutrients (on filtered samples) were conducted in the field. The remaining samples were preserved at pH < 2 with 67-70% OmniTrace® HNO_3 for analysis of cations and trace elements and with 95-98% A.C.S. Reagent H_2SO_4 for DOC analysis. Samples for anions, DIC, $\delta^{13}C$, and $\delta^{34}S$ were not acidified. Samples were kept under ice and transported directly to the University of Waterloo on the same day. All samples were refrigerated except samples for DIC and $\delta^{13}C$ analyses, which were placed in the freezer.

3.2.3.2 Solid-phase Sampling

At the termination of the experiment, excess water was drained from the column and solid samples collected in the field. Solid-sampling ports were opened one at a time and samples collected by inserting an aluminum tube (2.54 cm diameter × 40 cm) into the cell and slowly extracting the sample. Sample tubes were capped with low-density polyethylene end caps and sealed. After samples were collected from all seven solid-phase sampling ports, the cell was opened and sampled into nine sections. At each section, three centrifuge tubes were embedded into the reactive material, across the axis of the cell, and immediately extracted and capped. Four samples were collected within the first 6 cm of reactive material (every 1.5 cm), after which samples were collected every 10 cm for a total of nine samples. All solid samples were kept under ice during transport to the University of Waterloo, where they were placed in the freezer or refrigerator for microbiology analyses.

3.2.4 Analytical Methods

3.2.4.1 Aqueous Analyses

pH, Eh, and alkalinity analyses were conducted in the field using an Orion meter and combination pH probe (pH), an Orion meter and combination redox electrode (Eh), and a Hach digital titrator with bromocresol green-methyl red indicators (alkalinity). Electrical conductivity measurements were conducted using an Oakton® Instruments EcoTestr (Conductivity and TDS pocket meter). Measurements of dissolved H_2S (methylene blue; method 8131 from DR 2800 Manual), NH_3-N (salicylate; method 10031/10032 from the DR 2800 Manual), and PO_4-P (ascorbic acid; Method 8048 from DR 2800 Manual), were measured in the field using a Hach DR/2400 Portable Spectrophotometer. Remaining samples were transported to the University of Waterloo and analyzed at the Groundwater Geochemistry and Remediation Laboratory, to determine concentrations for dissolved cations (inductively-coupled plasma mass spectrometry, Thermo Fisher Xseries II; inductively-coupled plasma optical emission spectroscopy, Thermo Fisher iCAP 6000), dissolved anions (ion chromatography, Dionex IC-CO_3), and carbon (total organic carbon method, Aurora 1030 TOC Analyzer).

3.2.4.2 Microbiology – Most Probable Number (MPN)

The most probable number (MPN) technique was used on solid subsamples to enumerate sulfate-reducing bacteria (SRB), iron-reducing microorganisms (IRM), and neutrophilic heterotrophs (nH). Cultivations were performed in triplicate and populations were counted following the MPN technique (Cochran, 1950). To enumerate SRB, 1 g of sample was added to a 20-mL serum bottle containing 9 mL of modified Postgate C medium (Postgate, 1984). The ratio of the dissolved reagents in g/L was as follows: 0.5 KH_2PO_4, 1.0 NH_4Cl, 4.5 Na_2SO_4, 0.04 $CaCl_2 \cdot 2H_2O$, 0.06 $MgSO_4 \cdot 7H_2O$, 0.004 $FeSO_4 \cdot 7H_2O$, 2.92 60 % Na-lactate, 1.28 Na-acetate, 1.0 yeast extract, and 0.3 Na-citrate dihydrate (Benner et al., 1999). A solution of 1 M NaOH was used to adjust the pH to 7.5. Following the MPN technique, the serum bottles were serially diluted and then incubated in an anaerobic chamber for 5 weeks. Biogenic H_2S production by SO_4^{2-} reduction was determined based on the presence of a black precipitate (Gould et al., 2003; Paulson et al., 2018).

Enumeration of IRM was conducted following similar methods. The cultivations were performed in triplicate by adding 1 g of solid sample to a 20-mL serum bottle containing 9 mL of

growth medium prepared by dissolving the reagents at the following ratio (in g/L) in deionized water: 2.5 $NaHCO_3$, 1.5 NH_4Cl, 0.7 $NaH_2PO_4 \cdot 2H_2O$, 0.1 $CaCl_2 \cdot 2H_2O$, 0.1 KCl, 0.005 $MnCl_2 \cdot 4H_2O$, 0.01 $NaMoO_4 \cdot 2H_2O$, 1.84 Fe(III) EDTA, and 1.5 peptone (Gould et al., 2003; Lindsay et al., 2011a). The medium was buffered to a final pH of 7.0 using 1M NaOH. The serum bottles were serially diluted and then incubated in an anaerobic chamber for 5 weeks. Iron reduction was determined by adding a ferrozine reagent (Stookey, 1970) to the serum bottle, with the development of a purple colour indicating the presence of Fe(II).

To enumerate nH, samples were serially diluted, plated onto R2A agar (Sigma Aldrich, USA), then aerobically incubated at room temperature (23 °C) without agitation. Samples were counted after 7 d and duplicates determined by two successive dilutions showing colony growth.

3.2.4.3 Microbiology - DNA Analysis

DNA was extracted using DNeasy PowerSoil Kits (Qiagen Inc., Germany) in duplicate on frozen samples (-20 °C). Extracted samples were stored at -20 °C before submission. The V4 region of the 16S rRNA genes were amplified using Illumina MiSeq sequencing (Metagenom Bio Inc., Toronto, Canada) with modified university primers 515F/806R (Walters et al., 2015). Following DNA extraction, sequencing data was processed by Eva Pakostova (Pakostova et al., 2020), using the Mothur program v.1.39.5 (Schloss et al., 2009) and Mothur MiSeq Standard Operating Procedure (Kozich et al., 2013). Duplicate samples were merged. Based on predictions by vsearch using the Silva database for 16S rRNA gene sequences (release 132 for Mothur, downloaded 18/03/2019) as a reference, chimeric sequences were discarded. A *de novo* operational taxonomic unit (OTU) picking process was used to cluster OTUs at a 97% similarity level. A Mothur-formatted version of the Silva reference database (details above) was used to determine taxonomic annotation of individual OTUs. Based on the Mothur MiSeq SOP, some taxa were not considered for further data analyses (unknown, mitochondria, eukaryotes). The unequal number of sequences across samples resulted in variation. To control this variation, subsampling was conducted for each sample after OTU generation at a rarefaction level based on the sample with the fewest number of reads (25,500 reads). Relative abundances of SRB were determined based on screening of the taxonomy file for prokaryotic genera (or higher taxa when identification to the genus level was not possible) containing a minimum of one species with the

investigated metabolic trait. The list of SRB detected in the samples and the mean % of total reads (in the whole data set, not individual samples) is shown in **Table B.2**.

3.2.4.4 Optical Microscopy

Portions of the solid samples collected from the reaction cell were used for thin section preparation (Spectrum Petrographics, Vancouver, WA, USA). Grains were examined under reflected and transmitted light microscopy using a Nikon Eclipse LV100N POL polarized light microscope.

3.2.4.5 Synchrotron Bulk S XANES

Synchrotron bulk S X-ray absorption near edge structure (XANES) analyses were conducted on solid materials from the reaction cell. Samples of ZVI grain coatings for synchrotron analyses on beamline SXRMB at the Canadian Light Source (CLS), Saskatoon, Saskatchewan, were prepared by cooling the grains with liquid nitrogen, grinding the sample in an anaerobic chamber, and sieving out the grain coatings. All samples were maintained under anaerobic conditions prior to analysis at the CLS. XANES data were processed using ATHENA (Ravel & Newville, 2005). The scans were shifted with respect to the reference standard E0 of gypsum, which was collected during the same beamtime. Linear combination fitting of the XANES results was used to predict the solid phases present in the solid material.

3.2.4.6 Carbon-Sulfur Analysis

Samples were anaerobically freeze-dried and the ZVI magnetically separated from the OC prior to determination of S concentrations (ELTRA CS 2000). Because of the heterogeneity of carbon sources in the reactive material and the difficulty associated with separating each component, the C concentrations measured are not reported.

3.2.4.7 Data Interpretation

Sulfate removal rates were calculated using four of the aqueous SO_4^{2-} profiles measured over the course of the experiment. A best-fit linear reduction equation was calculated based on the profile measurements (SigmaPlot, SPSS Inc.). The rates were normalized based on the mass of dry OC in the reaction cell (Lindsay et al., 2008; Waybrant et al., 2002). Saturation indices of minerals were determined using the geochemical modelling software PHREEQCI, with the WATEQ4F database (Ball & Nordstrom, 1991).

3.3 Results

3.3.1 Water Chemistry

3.3.1.1 Geochemical Conditions

The mean pH for the influent water was 3.5, and a sharp initial increase to pH 6.8 was observed between the influent port and the first water sampling port at 26 cm (**Figure 3.3**). The pH values remained relatively constant over the remainder of the reaction cell, with a mean effluent pH of 7.5. The mean influent Eh was 500 mV and the mean effluent Eh was 136 mV (**Figure 3.3**). A sharp initial decrease was observed in the first 26 cm, with values then remaining relatively consistent for the remainder of the cell length. The mean influent alkalinity was close to 0 mg L^{-1} and the mean effluent alkalinity was 256 mg L^{-1} as $CaCO_3$ (**Figure 3.3**). A sharp initial increase in alkalinity was observed, followed by a steady increase along the length of the cell. The mean influent and effluent EC values were 0.38 and 0.58 mS cm^{-1}, respectively (**Figure 3.3**). A steady increase in EC was observed along the reaction cell length.

3.3.1.2 Arsenic, Fe, and Other Metals

Arsenic concentrations in the influent water varied during the experiment with a maximum of 3.2 mg L^{-1} and a mean of 1.1 mg L^{-1} (**Figure 3.4**). The mean effluent concentration of As was 5.4 µg L^{-1}, with only one recorded As concentration above 10 µg L^{-1}. A sharp initial decrease in As concentration was observed within the first 26 cm, after which concentrations remained low for the remainder of the cell length.

The mean concentration of Fe was 17.7 mg L^{-1} in the influent water and 6.8 mg L^{-1} in the effluent water (**Figure 3.4**). An initial increase in Fe concentrations was observed within the first 40 cm of the reaction cell followed by a steady decrease for the remainder of the cell length.

The concentrations of other dissolved metals in the influent water varied (**Figure 3.5**). The mean influent concentrations of Al, Cu, Ni, and Zn were 3.4 mg L^{-1}, 74 µg L^{-1}, 0.13 mg L^{-1}, and 0.26 mg L^{-1}, respectively. The mean effluent metal concentrations were < 10 µg L^{-1} for all metals except Al, for which the mean was < 72 µg L^{-1}. A sharp initial decrease in concentration was observed for all four metals within the first 26 cm, followed by relatively low concentrations for the remainder of the cell length. One exception was Cu, where an increase between the last intermediate port and the effluent port was observed (up to 40 µg L^{-1}) on Day 5 and Day 8, after which concentrations remained below 13 µg L^{-1} in the effluent.

3.3.1.3 Sulfur Geochemistry

The mean influent SO_4^{2-} concentration was 137 mg L^{-1} and the mean effluent concentration was 57.6 mg L^{-1}, with SO_4^{2-} concentrations increasing slightly from Day 5 to Day 53 (**Figure 3.6**). A progressive decrease in SO_4^{2-} concentrations was observed between the influent and effluent ends of the cell. The mean influent H_2S concentration was 1 µg L^{-1} and the mean effluent H_2S concentration was 60 µg L^{-1} (**Figure 3.6**). Effluent H_2S concentrations were highest at the beginning of the experiment but decreased over time. Dissolved H_2S concentrations remained relatively constant along the cell length. The mean $\delta^{34}S\text{-}SO_4$ of the influent water was 8.2 ‰ (**Figure 3.6**). A progressive enrichment of $\delta^{34}S\text{-}SO_4$ was observed along the cell length, with a maximum value of 14.6 ‰. Similar trends were observed in the $\delta^{34}S\text{-}SO_4$ profiles from Day 26 and Day 53.

3.3.1.4 Carbon

The mean influent DOC concentration was 5 mg L^{-1} as C. In all three profiles, an increase from the influent to effluent end was observed (**Figure 3.6**). On Day 8, the effluent DOC concentration peaked at 590 mg L^{-1}, but only minimal increases, to 26 mg L^{-1} (Day 26) and 13 mg L^{-1} (Day 53), were observed in the remaining two profiles. An increase in DIC values was observed along the cell length from a mean influent concentration of 2.5 mg L^{-1} as C. The maximum effluent DIC concentration was observed on Day 8 (47 mg L^{-1}), followed by Day 26 (31 mg L^{-1}) and Day 53 (20 mg L^{-1}). The mean $\delta^{13}C$-DIC values for unreacted materials were 2.4 ‰ for limestone, −24.6 ‰ for wood chips, and −27.1 ‰ for leaf compost. A negative $\delta^{13}C$-DIC was observed for the influent water (−21.6 ‰) followed by an increase to -12.8‰ before the first sampling port, and relatively constant values for the remainder of the cell length.

3.3.1.5 Nutrients

The mean influent NH_3-N concentration was 0.61 mg L^{-1}, with a maximum of 0.93 mg L^{-1} (**Figure B.1**). The mean reaction cell effluent concentration was 2.3 mg L^{-1}. Except for Day 19, when NH_3-N concentrations increased substantially toward the effluent end (13 mg L^{-1}), minimal increases were noted along the reaction cell length. The mean influent concentration of PO_4-P was 0.28 mg L^{-1} and the mean effluent concentration was 0.39 mg L^{-1} (**Figure B.1**). Slight increases in PO_4-P concentrations were observed from the influent to effluent end of the cell. During the first five sampling trips, an initial decrease in the first 26 cm was followed by an

increase in concentrations; for the remaining five sampling trips, concentrations remained relatively stable along the reaction cell length.

3.3.2 Microbiology

3.3.2.1 Most Probable Number (MPN)

SRB populations remained relatively constant along the length of the reaction cell, with a mean of 300 bacteria g^{-1}; populations of IRM were much larger, varying along the cell length from 10^6 to $>10^{10}$ bacteria g^{-1} (**Figure 3.7)**. No trend in IRM populations was observed along the length of the cell. Enumeration of nH ranged from 10^6 to 10^8 bacteria g^{-1} along the cell length, with a gradual increase in population observed from the influent to the effluent end (**Figure 3.7**).

3.3.2.2 DNA Extractions

The percentage of SRB reads in the initial reaction cell material was 0.33% of total reads. The results from 16S rRNA amplicon sequencing indicated the presence of SRB throughout the length of the reaction cell. Of the SRB observed, the three most abundant genera were *Desulfitibacter*, *Desulfomicrobium*, and *Desulfosporosinus*, and the most abundant order was *Desulfovibrionales* (**Figure 3.8**). A slight decline in the total percentage of reads was observed from the influent to the effluent end. The percentage of SO_4^{2-} reducers along the cell length ranged from 1.8 to 2.5% of total reads (**Figure 3.8**). Along the cell length, a decrease in the total percentage was observed for *Desulfovibrionales* and an increase in percentage was observed for *Desulfomicrobium*.

3.3.3 Mineralogy

3.3.3.1 Reflected and Transmitted Light Microscopy and SEM

Iron sulfides, including pyrrhotite ($Fe_{(1-x)}S$) and pyrite, were observed using reflected and transmitted light microscopy (**Figure 3.9**). Pyrite was present as framboids, both isolated and clustered (**Figure 3.9A**), and as secondary precipitates between grains of pea gravel and ZVI. An exsolution texture was sometimes observed on individual, isolated, pyrrhotite grains (**Figure 3.9B**). Organic carbon varied from isotropic to anisotropic under transmitted light. Typically, the internal structure of the OC remained intact with occasional infilling by a secondary sulfide precipitate (**Figure 3.9C**). This secondary sulfide was yellow-white in colour under reflected light and isotropic under transmitted light. Different shades of grey and white corrosion products were observed in rough, uneven rims around the ZVI grains. In some cases, a white, blade-like

texture was observed around the ZVI grains (**Figure 3.9D**). Fe (oxy)hydroxides were common corrosion products, replacing sections of the ZVI grains.

3.3.3.2 Solid Sulfur

The average wt. % S was greatest near the influent end (0.43 wt. %) and decreased toward the effluent end (0.28 wt. %; **Figure B.2**). The observed trend in wt. % S was consistent with the trend observed for aqueous SO_4^{2-} along the reaction cell length on Day 49.

3.3.3.3 Synchrotron Bulk S XANES Analysis

S was present in two predominant oxidation states in the unreacted, acid-washed ZVI. The first oxidation state at 2476 eV corresponds to an intermediate, oxidized, S species, similar to tetramethylene sulfoxide (C_4H_8OS; Wang et al., 2019). The second dominant state at 2482 eV corresponds to gypsum ($CaSO_4 \cdot 2H_2O$). The spectral results for samples collected from the reaction cell at the conclusion of the experiment indicate S occurs in three oxidation states (a/b, c, d; **Figure 3.10**). The absorption edge of group "a/b" ranges from 2470 to 2472 eV; a 2-eV variation in the position of the spectral edge of this group limits the specification of the reduced S phase present in the material. Minerals within this energy range, which are likely to contribute to this peak, include pyrrhotite, chalcopyrite ($CuFeS_2$), and elemental S (S_8^0). The group designated "c" corresponds to the second spectral peak at 2476 eV and may represent organic S species, tetramethylene sulfoxide, or a sulfoxide-like phase (Wang et al., 2019), which was also detected in the initial ZVI material. The highest energy edge observed at 2482 eV is likely gypsum based on the E0 of the absorption edge (Fleet, 2005). A shift from a peak feature at 2470.5 eV in the influent spectra to a pre-edge feature at 2470 to 2471 eV was observed along the cell length.

3.4 Discussion

3.4.1 Water Chemistry

The observed increase in pH and alkalinity of the groundwater upon interaction with the cell material is likely due to the dissolution of limestone, the oxidation of ZVI, and the oxidation of OC (Chapter 2; Benner et al., 2002; Lindsay et al., 2008; Waybrant et al., 1998). The mean influent water pH was 3.5 and the alkalinity was near 0 mg L^{-1} as $CaCO_3$. The initial increase to pH 6.8 and alkalinity to 130 mg L^{-1} occurred between the base of the reaction cell and the first sampling port at 26 cm from the influent end, or 9 cm into the reactive material, indicating rapid

neutralization (**Figure 3.3**), after which the pH and alkalinity remained constant. The presence of limestone in the reactive material likely contributed to the increase in pH and alkalinity values due to the production of HCO_3^- and the subsequent neutralization of acidity:

$$CaCO_3 + H^+ \leftrightarrow Ca^{2+} + HCO_3^- \quad [6]$$

The corrosion of ZVI may have resulted in a further increase in pH through the formation of OH^- (reaction [3]; Blowes et al., 2000; Manning et al., 2002). Finally, the oxidation of OC coupled with the reduction of SO_4^{2-} may contribute to a further increase in alkalinity (Waybrant et al., 1998):

$$SO_4^{2-} + 2CH_2O \leftrightarrow H_2S + 2HCO_3^- \quad [7]$$

These three reactions likely contributed to the initial increase in pH and alkalinity and the stable values that were maintained for the remainder of the experiment. The addition of Na-lactate used to initially saturate the cell may also have affected the pH and alkalinity of the water at the onset of the experiment. The development of reducing conditions, indicated by a decrease in Eh within the first 9 cm of reactive material (**Figure 3.3**), may have been due to the addition of OC and ZVI to the reactive material. The Eh remained < 300 mV for the remainder of the cell length. Similar reactions were observed in the laboratory column experiments (Chapter 2).

The development of conditions favourable for SO_4^{2-} reduction was indicated by a decrease in Eh, the generation of alkalinity and H_2S, a decrease in SO_4^{2-} concentrations, and an enrichment in $\delta^{34}S$ along the length of the reaction cell (**Figure 3.6**). The presence of SRB, IRM, and nH (**Figure 3.7**) further indicated bacterially-mediated SO_4^{2-} reduction occurred in the reaction cell. A low percentage of SRB reads was observed in the non-reacted material (**Figure 3.8**), indicating SO_4^{2-}-reducing conditions developed in the reaction cell. The overall decrease in aqueous H_2S concentrations as the experiment progressed was likely due to the precipitation of Fe(II) and other metal sulfides.

The most abundant genus in the solid material was *Desulfomicrobium*, followed by *Desulfovibrionales* (order), *Desulfitibacter*, and *Desulfosporosinus* (**Figure 3.8**). The order *Desulfovibrionales* includes the family *Desulfovibrionaceae* and the genus *Desulfovibrio*. The genera *Desulfovibrio* and *Desulfomicrobium* have been identified as important groups contributing to SO_4^{2-} reduction and removal of metals (Altun et al., 2014; Omoregie et al., 2013)

and were also identified as two of the major genera observed in the column study from Chapter 2. Members of the *Desulfomicrobium* and *Desulfovibrio* genera are able to reduce arsenate and SO_4^{2-}; while some described members of *Desulfomicrobium* can also use arsenate as a terminal electron acceptor in the absence of SO_4^{2-} (Macy et al., 2000). Members of the genus *Desulfosporosinus* are typically anaerobic bacteria that can grow autotrophically with H_2, which is the product of the reduction of H_2O by ZVI (reaction [4]). Similar to *Desulfomicrobium*, some *Desulfosporosinus* members may utilize both SO_4^{2-} and arsenate as terminal electron acceptors (Dworkin et al., 2006). Some *Desulfosporosinus* organisms may also thrive in low-pH environments, including type species that have been observed in AMD-impacted sediments (Senko et al., 2009). The presence of ZVI provided an additional source for SRB metabolism and may have enabled the growth of H_2-utilizers such as *Desulfosporosinus* and *Desulfovibrio*.

During bacterially-mediated SO_4^{2-} reduction, bacteria preferentially utilize ^{32}S in metabolic function as opposed to ^{34}S, resulting in an enrichment of ^{34}S in the residual, aqueous SO_4^{2-} (Lindsay et al., 2011a; Nakai & Jensen, 1964; Waybrant et al., 2002). The enrichment of $\delta^{34}S\text{-}SO_4$, coupled with the decrease in aqueous SO_4^{2-} concentrations along the length of the reaction cell, indicates bacterially-mediated SO_4^{2-} reduction. An enrichment factor (ε) of −23.2 ‰ was calculated based on the profile for $\delta^{34}S\text{-}SO_4$ collected on sampling Day 53 (Clark & Johnson, 2008). This enrichment factor is similar to the ε calculated in Chapter 2 (−28.9 ‰) and is within the range of ε values (−20.8 to −42.1 ‰) observed in similar studies (Guo & Blowes, 2009; Lindsay et al., 2009; Waybrant et al., 2002). The shift in $\delta^{34}S\text{-}SO_4$ may reflect the extent of SO_4^{2-} reduction, but the ε value may not be representative of all reactive materials (Guo & Blowes, 2009). At the end of the field trial, the aqueous concentrations of SO_4^{2-} remained above 40 mg L^{-1}, suggesting SO_4^{2-} was not limited during the experiment.

3.4.2 Dissolved Arsenic and Metal Removal

3.4.2.1 Iron

The large population of IRM (10^6-10^{10} bacteria g^{-1}) in the reaction cell solid material probably contributed to the increase in Fe from a mean influent concentration of 17.7 mg L^{-1} to maximum concentrations of up to 40 mg L^{-1} within the reaction cell, prior to declining to a mean effluent concentration of 6.8 mg L^{-1} (**Figures 3.4, 3.7**). Utilization of Fe(III) (oxy)hydroxides as a terminal electron acceptor can mobilize Fe(II) (Brock et al., 2006; Lovley & Phillips, 1988):

$$CH_2O + 4FeOOH + 8H^+ \rightarrow 4Fe^{2+} + CO_2 + 7H_2O \quad [8]$$

Greater numbers of IRM were present near the influent end of the reaction cell, which may correspond to the initial increase in Fe concentrations. However, the formation of H_2S and precipitation of Fe sulfides probably contributed to the retention of Fe(II), resulting in lower concentrations of Fe in the cell effluent over time (**Figure 3.4**). Iron concentrations in the effluent were not as high as those observed in the laboratory column experiments (Chapter 2). This difference may be due to the ZVI used as the initial reactive material; partly-oxidized ZVI was used for the laboratory columns, whereas the ZVI used in the reaction cell was acid-washed to remove Fe(III) (oxy)hydroxide coatings prior to the experiment.

Solid-phase analyses indicated the presence of both pyrite and pyrrhotite in the solid material. Geochemical modelling suggested the precipitation of additional sulfide phases, including greigite (Fe_3S_4), amorphous FeS, marcasite (FeS_2), and mackinawite ($(Fe, Ni)_{1+x}S$), was favoured (**Figures B.3, B.4**). The formation of Fe sulfides likely occurred concurrent with bacterially-mediated SO_4^{2-} reduction. Geochemical modelling also indicated the likely precipitation of siderite ($FeCO_3$) and ZVI corrosion products, including maghemite (Fe_2O_3), goethite (FeO(OH)), hematite (Fe_2O_3), and ferrihydrite (**Figure B.3**), which also may have contributed to the retention of Fe. Similar phases including magnetite (Fe_3O_4), greigite, and amorphous FeS have been observed as secondary precipitates in other studies (Gu et al., 1999; Jambor et al., 2005; Lindsay et al., 2008).

Reactive transport modelling of a column experiment utilizing organic carbon for treatment of Fe indicated both siderite and mackinawite are important sinks for Fe (Amos et al., 2004). However, the precipitation of mackinawite is preferred because it has a lower solubility and is more stable than siderite, which may dissolve again under changing pH or Fe(II) concentrations and limit the precipitation of mackinawite (Amos et al., 2004). The presence of pyrite observed under optical microscopy indicates mackinawite may be the major sink for Fe retention. The formation of pyrite often follows a specific pathway, beginning with the formation of disordered mackinawite, followed by cubic or amorphous FeS, tetragonal FeS or mackinawite, greigite, and finally marcasite or pyrite (Wolthers et al., 2003). The presence of pyrite indicates the likely removal of Fe by this pathway. Therefore, the removal of Fe is likely attributed to

mackinawite or other Fe sulfide precipitates; the immobilized Fe should be stable despite possible changes to geochemical conditions.

Optical microscopy also indicated the corrosion of ZVI grains and the replacement of ZVI by secondary precipitates. Alteration of the ZVI was observed around the edges of the grain. The ZVI grains were similar in appearance to those described in the laboratory column experiments, and most of the organic carbon appeared unreacted (Chapter 2). However, in some grains a secondary Fe-rich precipitate replaced the cellular organic material (**Figure 3.9C**) and may have created an additional sink for Fe (Chapter 2). Previous S µXRF and µXANES analyses indicate the presence of elemental S and pyrite in the secondary replacement product (Chapter 2; Jambor et al., 2005). The presence of reduced phases corresponds to the reducing conditions that developed within the cell, and the formation of pyrite further suggests the formation of metal sulfides contributed to the removal of Fe from the water.

Synchrotron-radiation bulk S XANES analyses indicated the presence of pyrrhotite, elemental S, chalcopyrite, K-tetrathionate, tetramethylene sulfoxide, and gypsum, in the reaction cell material. A comparison of spectra of the reacted material and the unreacted, acid-washed ZVI indicated two similar spectral features (c, d; **Figure 3.10**), which correspond to tetramethylene sulfoxide (c; 2476 eV) and gypsum (d; 2482 eV) and were similar to those observed in the spectra from untreated ZVI in Chapter 2. However, the spectral feature at "a/b" was absent in the unreacted ZVI spectra (**Figure 3.10**), which indicates a reduced S phase (pyrrhotite, elemental S, chalcopyrite) accumulated as coatings on the grains of ZVI during the experiment (Chapter 2). This accumulation is consistent with the results from microbiological, geochemical, and mineralogical analyses that indicated the formation of sulfides during bacterially-mediated SO_4^{2-} reduction (Chapter 2). As previously observed, the sulfides formed, including pyrrhotite and chalcopyrite, represent important sinks for Fe removal (Chapter 2).

3.4.2.2 Arsenic

Arsenic removal and immobilization, from a mean influent concentration of 1.1 mg L^{-1} (max: 3.2 mg L^{-1}) to a mean effluent concentration of 5.4 µg L^{-1}, are attributed to reducing conditions that developed within the reaction cell (**Figure 3.4**). The formation of H_2S, through bacterially-mediated SO_4^{2-} reduction, likely contributed to the precipitation of As, as an As-sulfide phase. This removal mechanism is indicated by the high initial concentrations of H_2S

followed by a decrease over time, consistent with sulfide-mineral precipitation. These results are consistent with those from Chapter 2. As-μXANES of laboratory column reaction products indicated the presence of As in secondary precipitates containing Fe and S as well as the presence of arsenate sorbed to ferrihydrite (Chapter 2). In the reaction cell experiment, the formation of Fe (oxy)hydroxides and metal sulfides likely contributed to As removal. Corrosion products, such as hematite, goethite, and maghemite, can result in the rapid removal of As through adsorption (Rao et al., 2009; Su & Puls, 2001). Adsorbed As may diffuse into the interior sites on Fe-oxide minerals or form bidentate surface complexes on the oxide surface, both of which may result in decreased leaching potential and stable As retention (Su & Puls, 2001). The transformation of poorly crystalline Fe (oxy)hydroxides into more crystalline phases may also enhance As stability (Pedersen et al., 2006). Similarly, co-precipitation with Fe-sulfides and inner-sphere adsorption onto goethite and FeOOH-polymorph surfaces can contribute to As immobilization (Ludwig et al., 2009; Stichbury, 2000).

Geochemical modelling results indicated the precipitation of As-crystalline phases, including realgar and orpiment, was not favoured (**Figure B.4**). However, the precipitation of Fe sulfide phases was favoured, and secondary Fe sulfides were identified in the reactive material at the conclusion of the experiment. Arsenic possibly co-precipitated with Fe-sulfide minerals, as observed in laboratory column experiments that also indicated the presence of realgar and orpiment as phases in the secondary precipitates (Chapter 2). In the field cell, the majority of As was removed within the first 9 cm of reactive material, suggesting any As-crystalline phases were likely to have precipitated prior to the first sampling port. Therefore, the geochemical modelling results reflect conditions that prevailed after the majority of As had precipitated or adsorbed prior to the first port (Chapter 2).

3.4.2.3 Metals

A decrease in metal concentrations (Al, Cu, Ni, Zn) was observed between the influent and effluent ends of the reaction cell (**Figure 3.5**). A sharp initial decrease was observed within the first 9 cm of reactive material, after which concentrations remained relatively constant at 72, 5.9, 3.3, and 8.1 μg L^{-1} for Al, Cu, Ni, and Zn, respectively. The decline in Al concentrations is probably due to the increase in pH and precipitation of secondary Al (oxy)hydroxides. Geochemical modelling results indicated supersaturation with respect to gibbsite (γ -$Al(OH)_3$)

and boehmite (γ-AlO(OH)) (**Figure B.3**). The decline in Cu, Ni, and Zn concentrations and the formation of H_2S suggests the removal of these metals was due to the precipitation of low-solubility metal sulfides (reaction [5]). The geochemical modelling indicated precipitation of metal sulfides, including sphalerite ((Zn, Fe)S), chalcopyrite, chalcocite (Cu_2S), and covellite (CuS), was favoured (**Figure B.4**). In addition, the results from bulk S XANES analyses indicated the presence of chalcopyrite in the solid material. Precipitation of these minerals, or less crystalline precursors, likely contributed to the removal of metals such as Cu and Zn. (Co)precipitation or retention of the metals into tetrahedral Fe-S layers of mackinawite also may have occurred (Mullet et al., 2002). Additional processes, including adsorption onto Fe sulfides, Fe (oxy)hydroxides, or organic matter, may have contributed to a decline in metal concentrations (Gibert et al., 2005).

3.4.3 Carbon and Nutrient Release

Aqueous concentrations of PO_4-P initially increased along the reaction cell length but, as the experiment progressed, concentrations remained relatively constant. A slight increase from the influent to effluent end was observed for NH_3-N concentrations. Throughout the experiment, effluent concentrations of both PO_4-P and NH_3-N gradually decreased (**Figure B.1**). The breakdown of organic matter containing N and P resulted in the increase in NH_3-N and PO_4-P concentrations along the cell length (Paulson et al., 2018; Waybrant et al., 2002). The growth of heterotrophic sulfate-reducing bacteria, and other heterotrophs, likely contributed to the breakdown in organic material (Herbert Jr et al., 2000).

High concentrations of DOC were observed early in the experiment (**Figure 3.6**). The high values may be attributed to the decomposition of the most reactive organic carbon in the cell (e.g., Na-lactate solution and organic-rich creek sediment). Following the rapid decomposition of labile organic carbon, DOC concentrations declined to a level sustained by the slower degradation of more complex OC, which probably contributed the majority of OC available for SO_4^{2-} reduction (Chapter 2; Benner et al., 2002; Lindsay et al., 2008; Waybrant et al., 2002).

Increases in DIC were observed along the cell length (**Figure 3.6**). The observed increase may be attributed to the production of alkalinity during bacterially-mediated SO_4^{2-} reduction and other bacterially-mediated processes coupled with organic matter mineralization (Asmussen &

Strauch, 1998). An initial increase in δ^{13}C-DIC, from −21.6 to −12.8 ‰, was observed in the first 26 cm of the cell, followed by relatively stable values for the remainder of the cell length. This initial enrichment may be due to the dissolution of limestone in the reactive material. Despite the initial enrichment, δ^{13}C-DIC values remained relatively depleted (−10 to −14 ‰), consistent with SO_4^{2-} reduction coupled with organic carbon oxidation. Furthermore, the labile OC in the reactive mixture may also have contributed to the depletion of δ^{13}C-DIC ratios (Londry & Des Marais, 2003).

3.4.4 Sulfate Reaction Rates

Removal rates for SO_4^{2-} in the reaction cell were calculated based on aqueous SO_4^{2-} profiles collected during the experiment (**Figure 3.11)**. A zero-order rate equation was used to calculate SO_4^{2-} removal rates, $C = k_o t$, where C is the SO_4^{2-} concentration (mg L^{-1}), k_0 is the zero-order rate constant (mg L^{-1} d^{-1}), and t is the residence time (d). Similar rates were observed over the course of the experiment. The SO_4^{2-} removal rates calculated for four profiles are as follows: $R_{S,1}$ = −58.2 mg L^{-1} d^{-1} for Day 8, $R_{S,2}$ = −79.2 mg L^{-1} d^{-1} for Day 15, $R_{S,3}$ = −76.7 mg L^{-1} d^{-1} for Day 49, and $R_{S,4}$ = −50.9 mg L^{-1} d^{-1} for Day 53. The mean SO_4^{2-} removal rate for these four sampling days is −66.3 mg L^{-1} d^{-1}. The negative sign indicates SO_4^{2-} was removed and a R^2 value > 0.90 for all four profiles indicates the zero-order equation is a good fit for the data. Removal rates normalized to the wt. % dry OC are −5.6 (Day 8), −7.6 (Day 15), −7.3 (Day 49), and −4.9 (Day 53) µg L^{-1} d^{-1} g^{-1} of dry OC. The mean normalized SO_4^{2-} removal rate is −6.3 µg L^{-1} d^{-1} g^{-1} of dry OC. Uncertainty in these reaction rates is attributed to limitations associated with determining the masses of the reaction cell and reactive material during packing as well as estimating the residence time.

The rates in this experiment are similar to those calculated in a batch experiment utilizing both OC and ZVI (−1.24 to −1.40 µg L^{-1} d^{-1} g^{-1} of dry OC; Lindsay et al., 2008). Removal rates from the previous laboratory column experiments range from −180 to −200 µg L^{-1} d^{-1} g^{-1} of dry OC (Chapter 2), and the range of SO_4^{2-} reduction rates from other laboratory experiments utilizing similar reactive material is −1.40 to −140 µg L^{-1} d^{-1} g^{-1} of dry OC (Guo & Blowes, 2009; Lindsay et al., 2008; Waybrant et al., 2002). The δ^{34}S-SO_4 enrichment factor (ε) was lower for the reaction cell experiments compared to the laboratory column experiments (Chapter 2), suggesting the extent of SO_4^{2-} reduction was greater in the laboratory columns. Removal rates

from a field barrier system containing only OC were initially 15.3 mg L^{-1} d^{-1}, but decreased to 10.5 mg L^{-1} d^{-1} over time (Benner et al., 2002); these rates are lower than those observed in this reaction cell experiment (50.9 to 79.2 mg L^{-1} d^{-1}). Overall, the range of SO_4^{2-} removal rates were more variable than observed in previous laboratory and field studies, but generally remain within the same range of previously reported values (Benner et al., 2002; Lindsay et al., 2008; Waybrant et al., 2002).

The difference in SO_4^{2-} removal rates may be attributed to five main causes. First, the temperature in the reaction cell was lower than for the laboratory column experiments, and rates of SO_4^{2-} reduction decline with decreasing temperatures (Benner et al., 2002). Second, the field cell contained ZVI whereas some of the other experiments did not include ZVI in the reactive mixture. Third, the reaction cell trial was not operated for as long as the column experiments, limiting the period for bacterial growth and activity. Compared to a field barrier system (Benner et al., 2002), the reaction cell was conducted for several months as opposed to several years, limiting comparisons at early times. Fourth, the groundwater velocity and resulting residence time varied substantially between a field barrier system (Benner et al., 2002) and the field reaction cell; groundwater velocity was 16 m a^{-1} for a with a residence time of 90 d (Benner et al., 2002), and average flow rate into the reaction cell was 960 mL h^{-1} or 7140 m a^{-1} with a residence time of 1.14 d. Fifth, errors may have occurred when calculating the pore volume and residence time of the reaction cell. Despite the lower rates observed in the reaction cell, the geochemical results indicate extensive removal of metals and As from the groundwater as also observed in the laboratory column experiments (Chapter 2).

3.5 Conclusions

A mixture of OC, ZVI, and limestone has the potential to remove As and metals from acidic groundwater (pH <4) and maintain circumneutral conditions under rapid groundwater flow conditions. The increase in pH and alkalinity is attributed to the dissolution of limestone, oxidation of ZVI, and oxidation of OC in the reactive mixture.

A rapid onset of reducing conditions was observed in the field reaction cell following the initiation of groundwater flow. The onset of bacterially-mediated SO_4^{2-} reduction resulted in the precipitation of low-solubility sulfides that contributed to the removal of As and metals. Solid bulk S XANES results indicated low-solubility metal sulfides accumulated on ZVI grain coatings

during the experiment. Metal sulfides including pyrite, chalcopyrite, sphalerite, amorphous FeS, and mackinawite, likely contributed to metal removal. The addition of ZVI to the reactive mixture also contributed to the removal of As through the formation of corrosion products and Fe (oxy)hydroxides that created surfaces for As adsorption.

Sulfate removal rates ranged from 50.9 to 79.2 mg L^{-1} d^{-1} and were greater than, but within an order of magnitude of, those resulting from a field barrier system that utilized only OC in the reactive mixture (Benner et al., 2002). Compared to previous laboratory experiments utilizing both OC and ZVI (Chapter 2), the removal rate of SO_4^{2-} from the field reaction cell was two orders of magnitude lower. The difference is attributed to varying daily temperatures, the length of the experiments, varying flow rate and groundwater velocity through the barrier, cell, or column, and corresponding differences in residence times.

Removal of As and metals was observed within the first 9 cm of reactive material, indicating rapid removal and the high treatment capacity of the mixture; at least 59 cm of reactive material remained available for treatment in the reaction cell at the termination of the experiment. Overall, the results suggest the long-term potential of the reactive material, but additional testing is needed to estimate the long-term capacity and the impact of varying temperatures on removal of As and dissolved metals from groundwater.

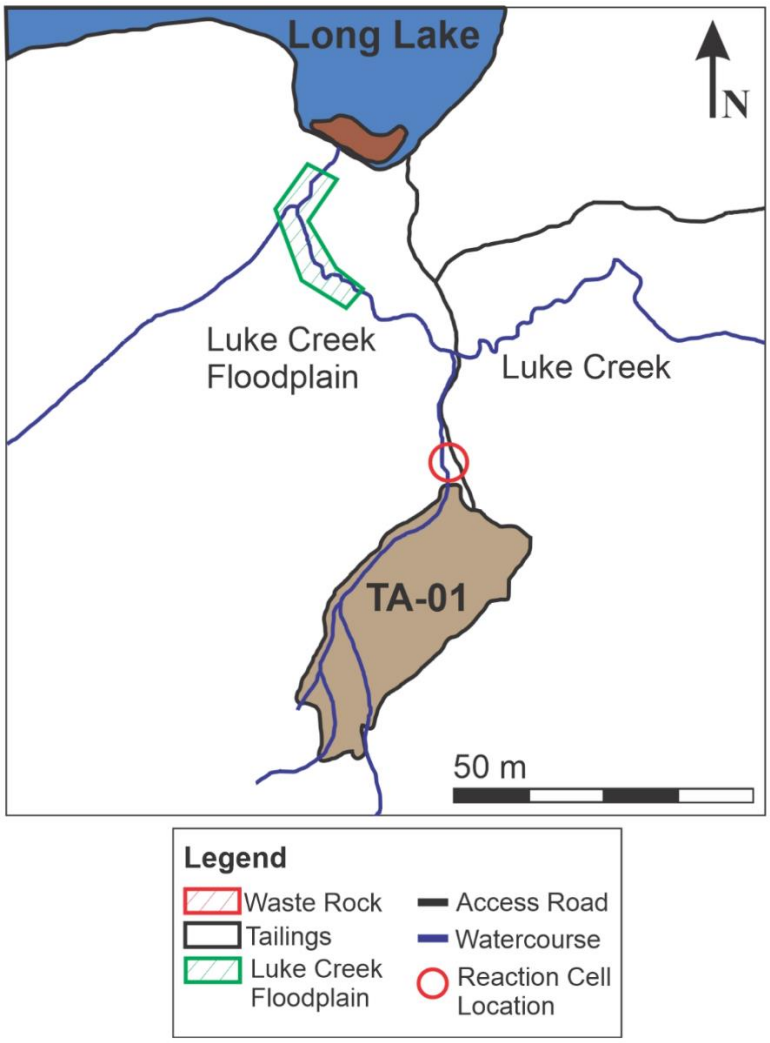

Figure 3.1 Map of the approximate location where the reaction cell was installed.

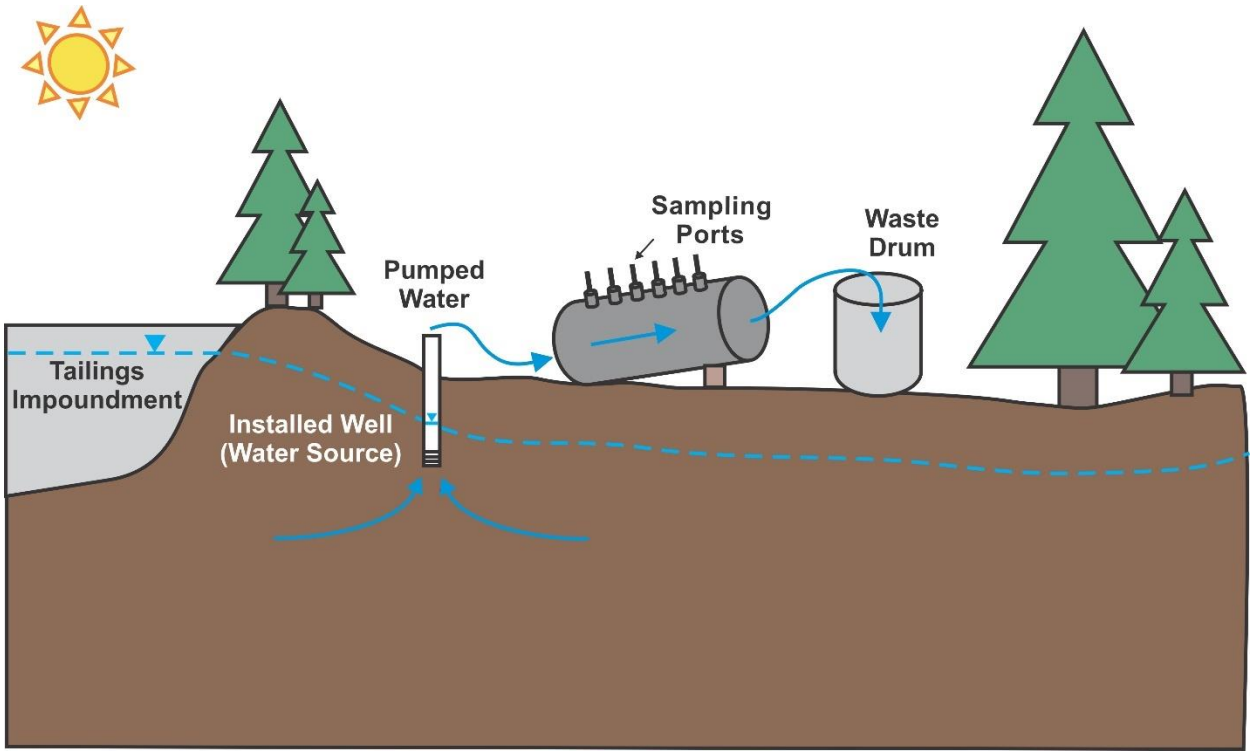

Figure 3.2 Schematic of the reaction cell installation and design.

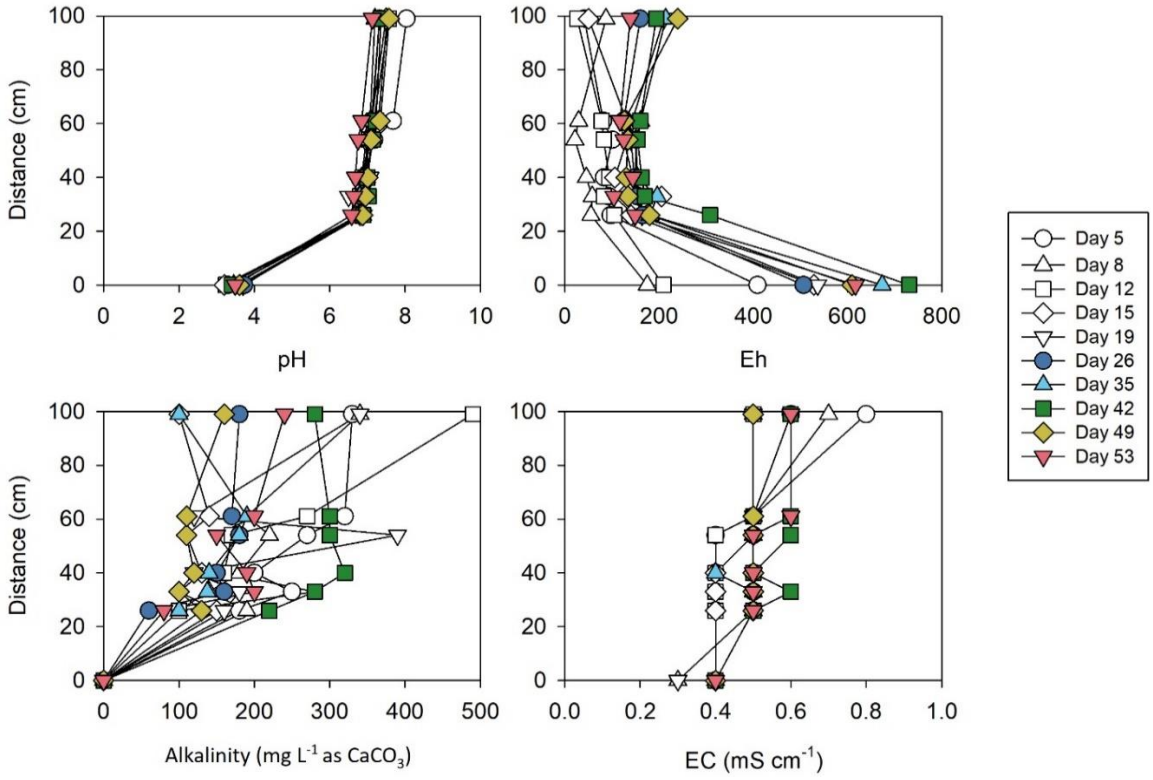

Figure 3.3 pH, Eh, alkalinity, and EC for aqueous samples collected along the reaction cell length. Distance 0 cm represents influent concentrations and 100 cm represents effluent concentrations.

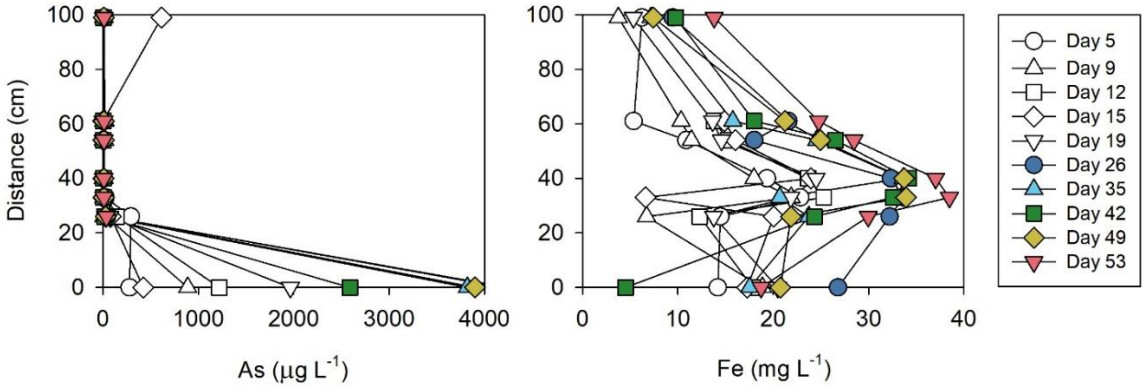

Figure 3.4 As and Fe concentrations in aqueous samples collected along the reaction cell length. Distance 0 cm represents influent concentrations and 100 cm represents effluent concentrations.

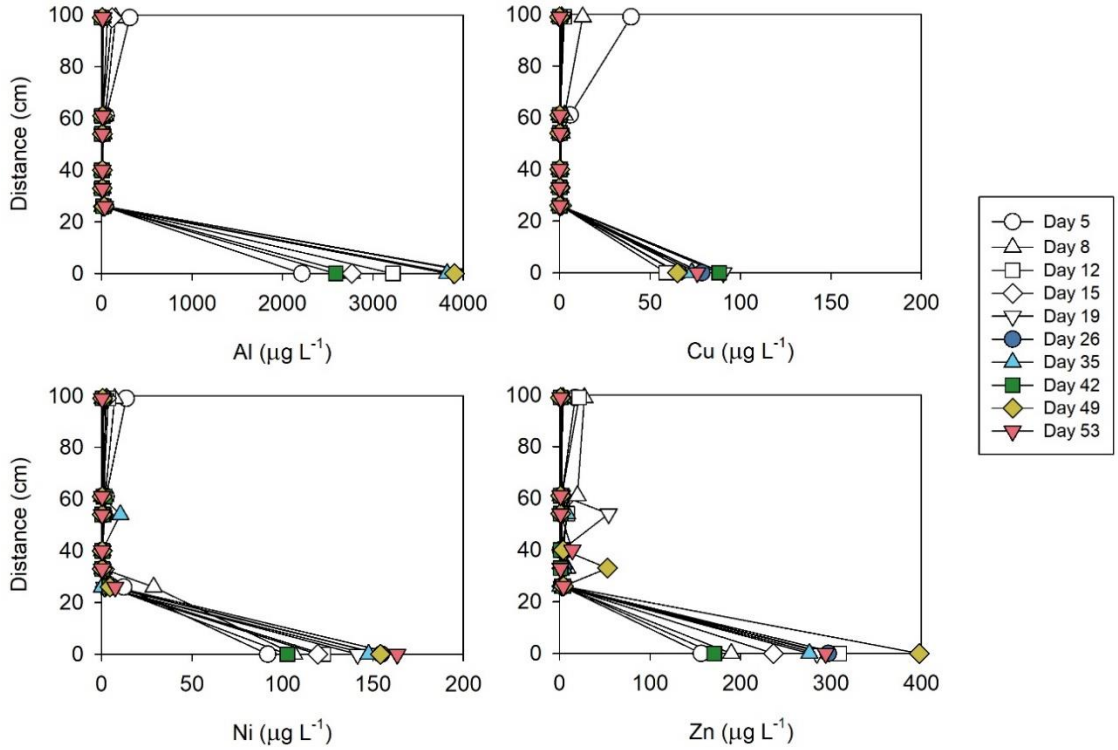

Figure 3.5 Metal (Al, Cu, Ni, and Zn) concentrations in aqueous samples collected along the reaction cell length. Distance 0 cm represents influent concentrations and 100 cm represents effluent concentrations.

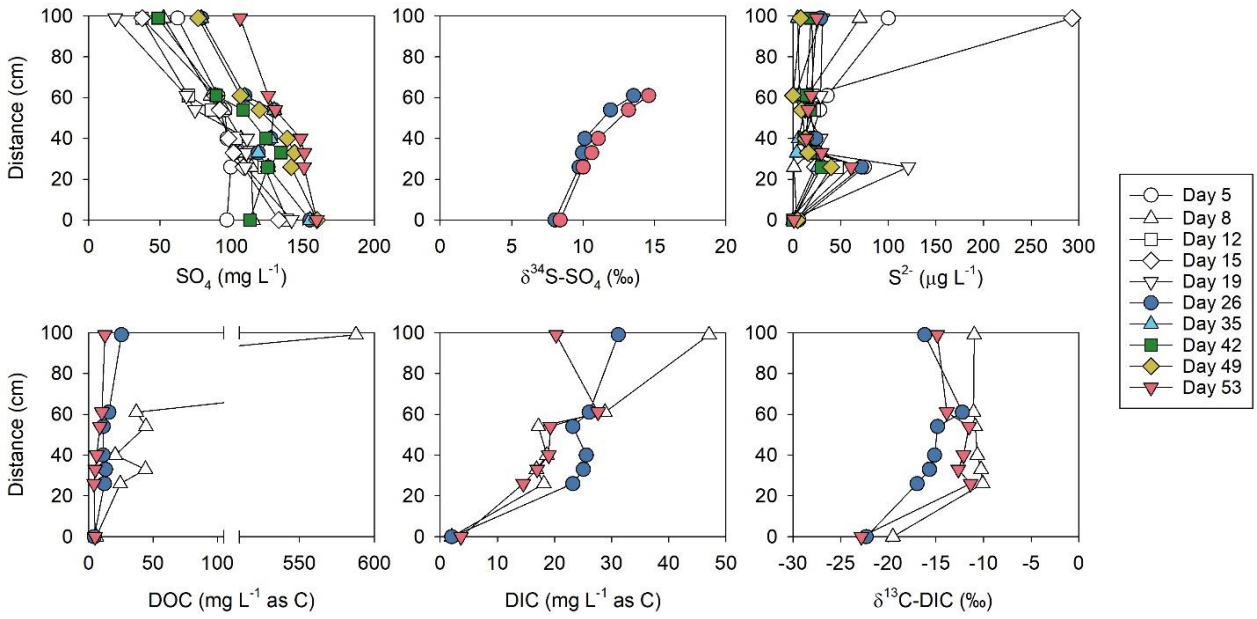

Figure 3.6 SO_4, S^{2-}, DOC, and DIC concentrations and $\delta^{34}S\text{-}SO_4$ and $\delta^{13}C$-DIC values along the reaction-cell length. Distance 0 cm represents influent concentrations and 100 cm represents effluent concentrations.

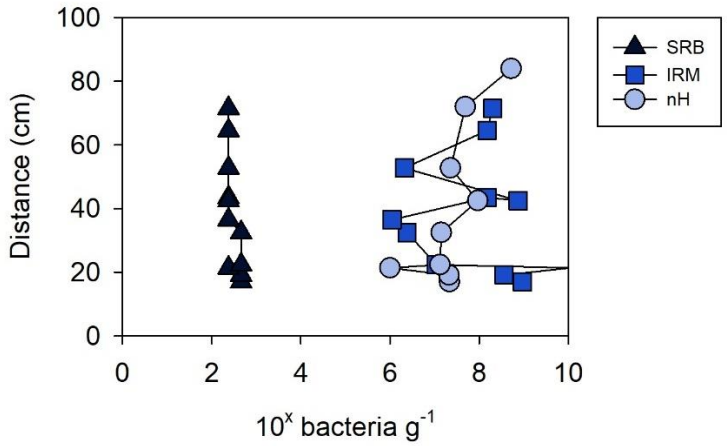

Figure 3.7 MPN enumeration results for solid-phase samples collected at different locations along the length of the reaction cell. The enumeration of sulfate-reducing bacteria (SRB), iron-reducing microorganisms (IRM), and neutrophilic heterotrophs (nH) are shown. One IRM data point is plotted outside of the graph area because an accurate enumeration could not be determined for $>10^{10}$ g^{-1}.

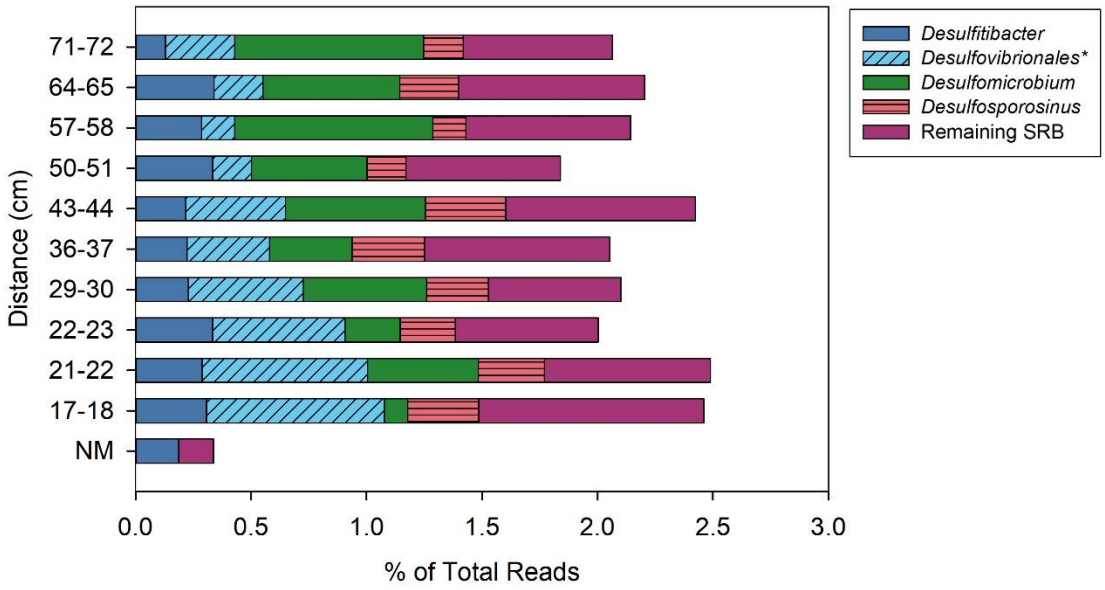

Figure 3.8 Percent of known SRB identified at different intervals along the reaction-cell length through DNA extraction analysis. The four most abundant genera (or higher taxa, marked with an asterisk) are plotted, and the remaining SRB grouped separately. The unreacted material is represented by NM.

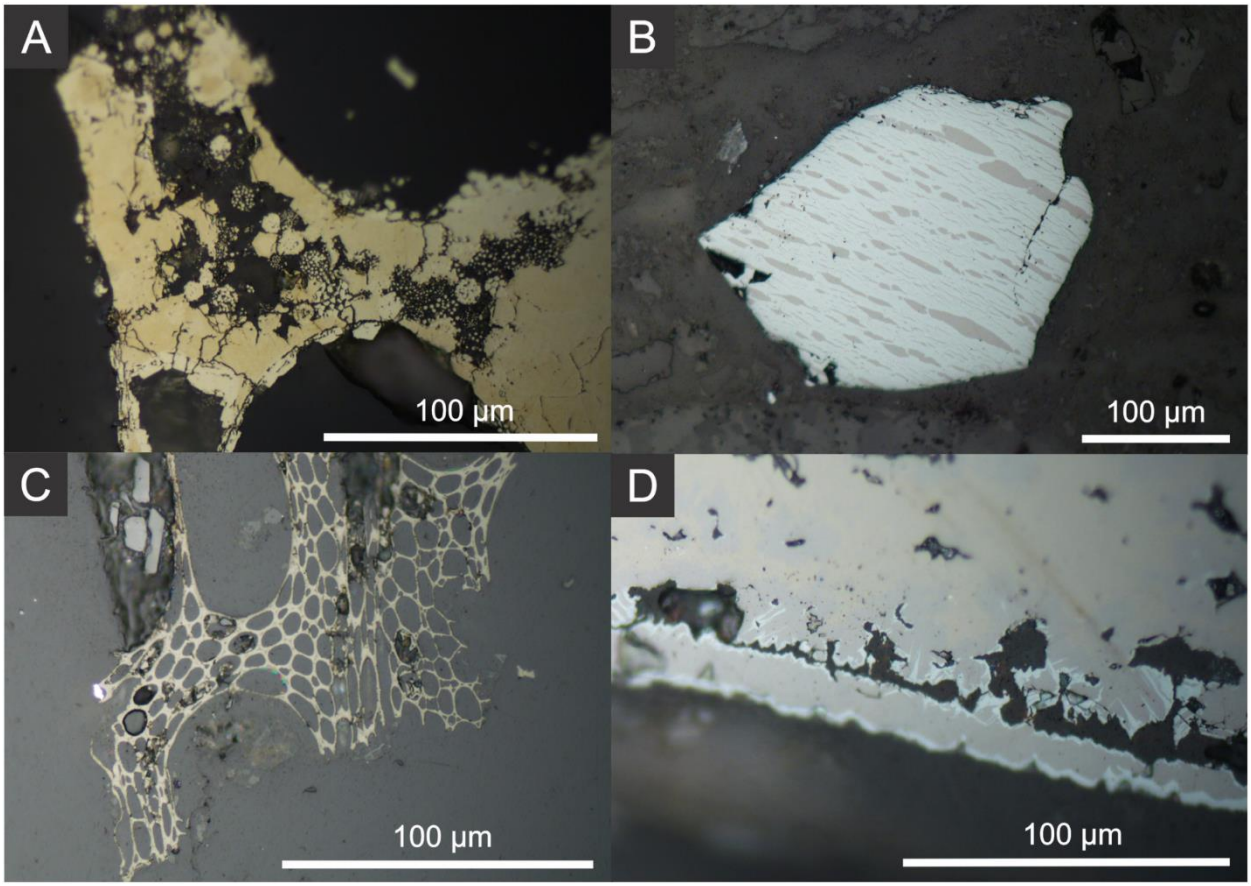

Figure 3.9 Reflected light microscopy images of grains showing (A) framboidal pyrite precipitated between grains of pea gravel, (B) exsolution texture observed on a grain of pyrrhotite, (C) Fe-sulfide precipitate replacement of the OC structure, and (D) blade-like texture found along the rim of a ZVI grain.

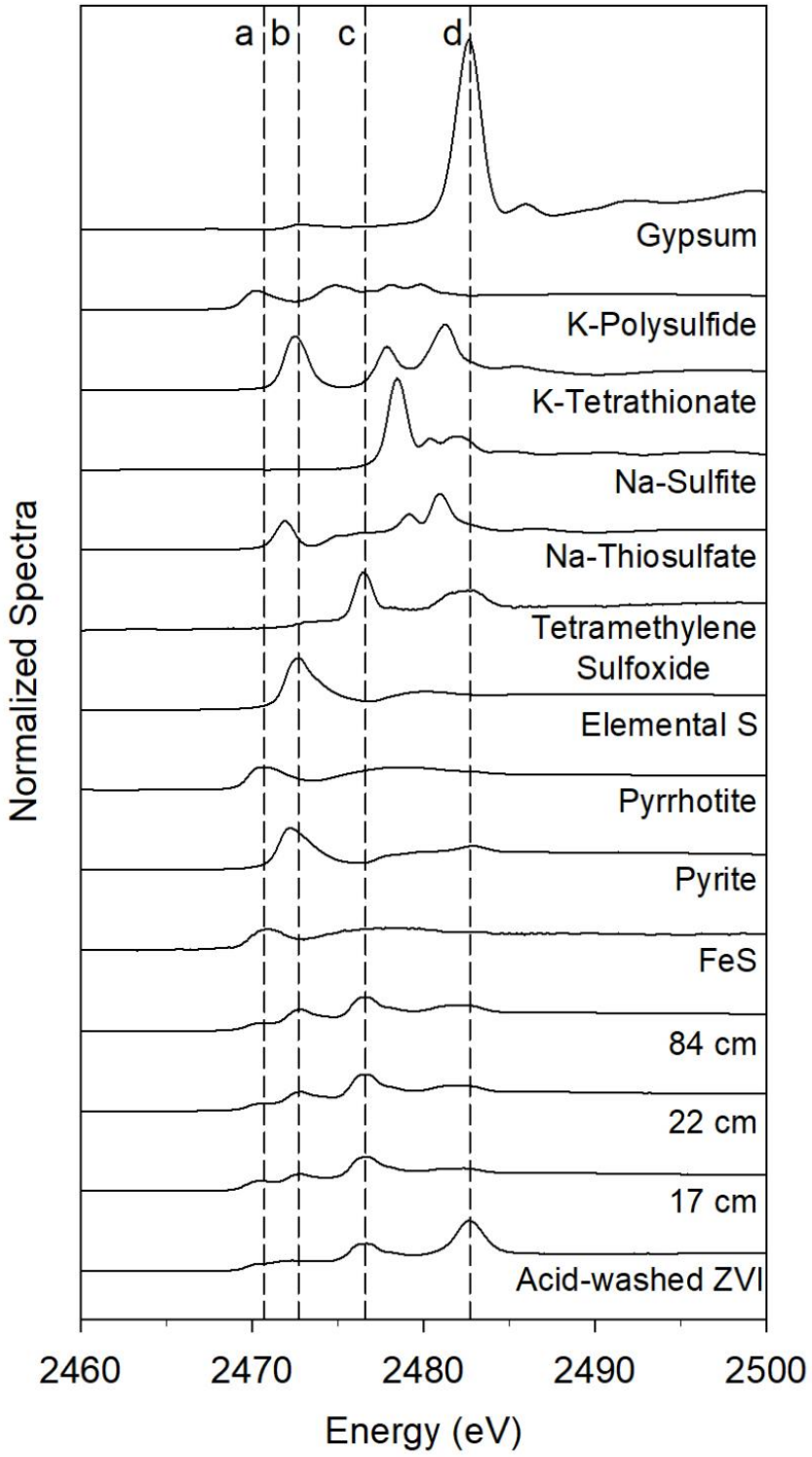

Figure 3.10 Bulk S XANES spectra of solid samples collected from the reaction cell. The number (cm) represents the distance from the influent end of the cell. Spectra for unreacted, acid-washed ZVI, and other standards are also shown. The spectral peak locations for pyrrhotite (a), elemental S (b), tetramethylene sulfoxide (c), and gypsum (d) are shown with dashed lines.

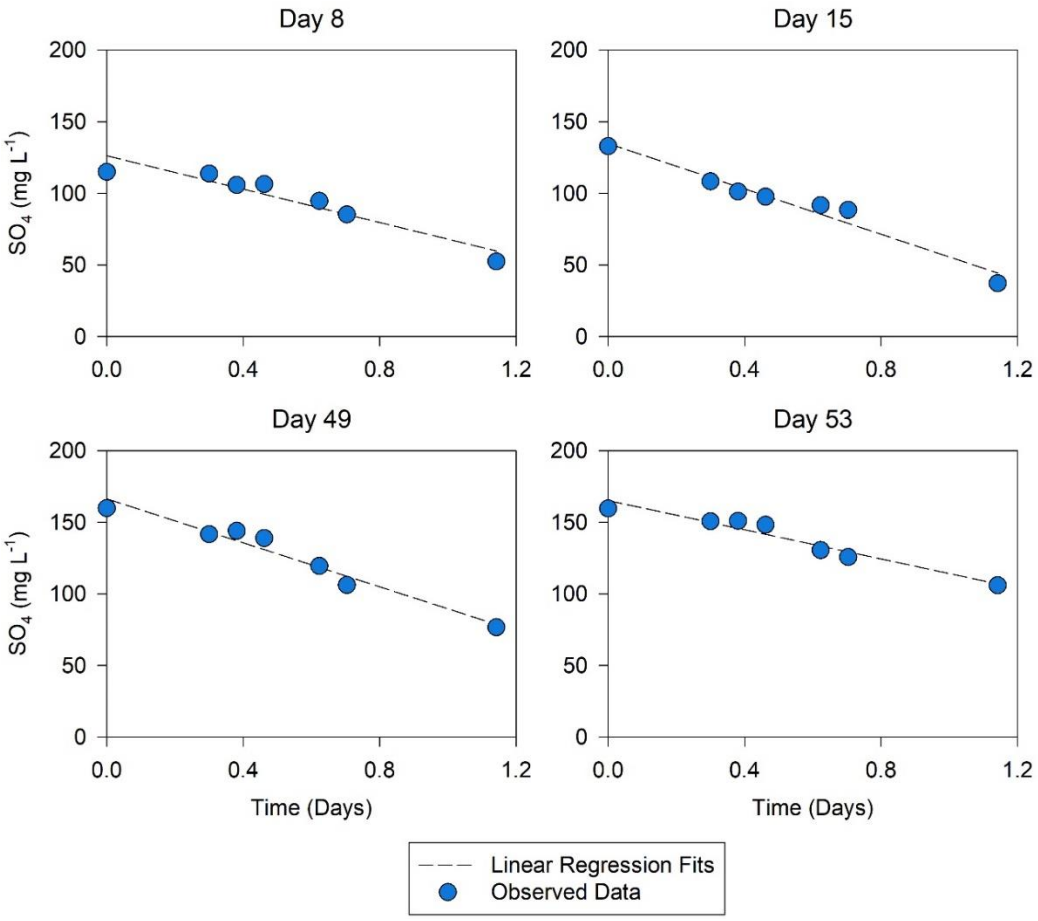

Figure 3.11 Regression fits for SO_4 removal as a function of residence time for four different sampling days.

Chapter 4: *Dissolved Arsenic Treatment using Permeable Reactive Materials: Evaluation of Temperature Dependence*

Executive Summary

The occurrence of As in groundwater is often associated with mine-impacted water. Passive remediation in the form of permeable reactive barriers or reaction cells provides an approach for removal of dissolved As and other contaminants. Reactive material placed within the ground or treatment cells promotes interactions between the groundwater and reactive material that result in contaminant removal. A field reaction cell, 99 cm long × 30 cm diameter, was installed at the Long Lake mine site in the late autumn to determine the effect of colder temperatures (mean daily temperature -1 °C) on contaminant removal using a reactive mixture containing zero-valent iron, organic carbon, limestone, and pea gravel. The results from the cold temperature field cell were compared to previous results from a warm temperature field cell (mean daily temperature 19 °C) and laboratory column experiments (mean daily temperature 22 °C) containing the same reactive material. Water chemistry results were similar in all three experiments. Removal of As, SO_4^{2-}, and metals and an increase in pH to circumneutral values were observed, except in the autumn cell in which SO_4^{2-} concentrations remained constant. Populations of sulfate-reducing bacteria (SRB) were observed in all experiments, with the lowest abundance in the autumn cell. Similarly, optical microscopy results indicated the presence of pyrite, pyrrhotite, amorphous FeS, and Fe (oxy)hydroxides in the solid material of all three experiments, but sulfide phases were less abundant in the autumn cell. Bulk S X-ray absorption near-edge structure (XANES) spectroscopy also indicated the accumulation of sulfide phases in all three experiments, with limited accumulation in the autumn cell. The results indicate similar chemical reactions occurred in all three experiments; however, the extent of bacterially-mediated SO_4^{2-} reduction and subsequent precipitation of low-solubility metal sulfides was limited in the autumn cell. This difference may be due to temperature limitations or to the shorter trial length. Despite these limitations, the overall goal to remove As and increase groundwater pH from acidic to circumneutral values was achieved.

4.1 Introduction

The generation of acidic conditions and release of metal(loids) into groundwater are major issues facing the international mining industry. Large volumes of waste rock and fine-grained tailings are produced through the excavation of ore bodies and milling processes. Waste rock and tailings are often sulfide-rich, and exposure of these materials to water and O_2 leads to the oxidation of sulfide minerals, accompanied by the oxidation of Fe(II), an increase in acidity,

and the release of metal(loids) (Blowes et al., 2014). These processes persist for decades to centuries and the resulting acid mine drainage (AMD) can be detrimental to nearby water bodies and ecosystems if left unremediated (Blowes & Jambor, 1990; Moncur et al., 2005).

Arsenic (As) is a contaminant common to gold (Au) mine sites due to the mineralogy of the host rocks and gangue minerals associated with Au formation. The mobility and stability of As are dependent on the oxidation state and pH. Arsenic can occur in oxidation states of −3, −1, 0, +3, and +5; common forms of inorganic aqueous As include arsenite (As(III)) and arsenate (As(V)) (Nordstrom & Campbell, 2002; Smedley & Kinniburgh, 2002). As(III) tends to dominate under anaerobic conditions, and As(V) tends to be present in aerobic waters (Nordstrom, 2002). Treatment systems for As often manipulate the geochemical conditions of the water to promote As sequestration and immobilization (Powell et al., 1998).

Passive treatment systems, composed of zones of reactive material, are increasingly being utilized to treat contaminated groundwater and surface water. These passive treatment systems may consist of permeable reactive barriers (PRBs) that intercept groundwater, or containerized systems that capture surface water, to remove the contaminant of interest (Blowes et al., 1998). Chemical reactions include reduction, oxidation, adsorption, and (co)precipitation.

Arsenic attenuation is controlled by a series of geochemical reactions. A thorough understanding of the site and geochemical conditions that persist are required to determine the viability and effectiveness of a potential barrier. Additional factors including barrier thickness and groundwater flow rate are also important for determining the potential for the barrier to remove As and other contaminants to sustain decreased concentrations for extended periods of time (Powell et al., 1998).

Treatment systems and experiments have utilized mixtures of organic carbon (OC) and zero-valent iron (ZVI) as reactive materials for the removal of As and metal(loids) from groundwater (Beaulieu & Ramirez, 2013; Guo & Blowes, 2009; Lindsay et al., 2008; Ludwig et al., 2009). The addition of ZVI results in the formation of Fe(II) and Fe corrosion products, both of which create surfaces for As adsorption. The OC in the reactive mixture promotes the growth of sulfate-reducing bacteria (SRB) and the development of sulfate-reducing conditions (Benner et al., 1997). H_2S is formed during microbial SO_4^{2-} reduction, which promotes the formation of low-solubility metal sulfides and results in the immobilization of metal(loids) (Benner et al.,

1997; Ludwig et al., 2002). Removal of As may occur through co-precipitation with metal sulfides, incorporation into the mineral structure, or adsorption onto metal sulfide surfaces (Blowes et al., 2014). Removal of As with mixtures utilizing both OC and ZVI has been observed (Chapter 2; Chapter 3). The addition of limestone to the reactive mixture increases the pH of the water. The addition of pea gravel to the reactive material can provide a significant increase in hydraulic conductivity; a 5% difference in the pea gravel fraction may result in an order of magnitude change in conductivity (Benner et al., 2002).

Passive systems remain in place and are expected to perform for many years following initial installation. Variable temperatures affect the growth and activity of SRB and result in changes to rates of SO_4^{2-} reduction and subsequent metal(loid) removal (Benner et al., 2002). Warmer summer temperatures are accompanied by higher rates of SO_4^{2-} reduction; the opposite effect is observed in the winter (Benner et al., 2002). The effect of varying temperature is important to consider, along with site geochemistry, prior to barrier installation.

The abandoned Long Lake Au mine is located near Sudbury, Ontario. High concentrations of As and metal(loids) are observed in the tailings porewater (CH2MHill, 2014; MNDM, 2017; Verbuyst, 2020). Tailings produced during the milling process were discharged into low-lying topographic depressions. In the 1980s, three of the tailings impoundments were capped with a layer of sand to prevent wind-blown transport of fugitive dust. Water-borne transport of tailings through Luke Creek resulted in the formation of a tailings delta in the southwestern end of Long Lake (CH2MHill, 2014; MNDM, 2017). The extent of contamination necessitates a remediation strategy to prevent migration of contaminated groundwater from the tailings impoundment toward Long Lake and control As release from tailings in Luke Creek and the greater Long Lake watershed.

Laboratory experiments (Chapter 2) and a field-reaction cell installation (Chapter 3) indicate the potential for the mixture of ZVI and OC to remove As at flow rates greater than those typically observed in aquifers. This study expands on these previous laboratory column experiments (Chapter 2) and a summer reaction cell trial (Chapter 3). A separate field-reaction cell experiment utilizing a mixture of ZVI and OC was implemented at the Long Lake site in late autumn 2018. Temperatures were several degrees colder than those prevalent during the summer field trial. This paper examines the effects of different temperatures on microbial activity and the

potential freezing of the cell and reactive material during the experiment. The results from all three experiments are also compared to assess the ability of the reactive material to remove As and other contaminants present at the site over a range of temperatures and groundwater velocities and contribute to our understanding of factors influencing SRB activity and metal removal.

4.2 Methodology

4.2.1 Reaction Cell Setup

The reaction cell was constructed using a PVC pipe (schedule 30; 99 cm long, 30 cm inner diameter) sealed with PVC Van Stone flange end plates. Each end plate included four sampling ports that were covered with a layer of fine and coarse Nitex™ mesh. Eight aqueous sampling ports were installed at 7-cm intervals along the length of the reaction cell, starting 26 cm from the influent end. Each aqueous sampling port included a piezometer, which extended 28 cm into the reactive material and was composed of 1.27-cm PVC pipe (schedule 40) with holes drilled along the side and covered with a layer of fine NITEX™ mesh. The aqueous sampling ports were sealed in place using bulkhead fittings. A ball valve connected to a 0.64-cm nylon barb, to enable water sample collection using a syringe, was installed at each sampling port.

The reactive mixture was composed of 40 vol. % OC (wood chips and leaf compost), 10 vol. % ZVI (acid-washed), 45 vol. % pea gravel, and 5 vol. % limestone. Approximately 50 g of organic-rich creek material collected from Laurel Creek (Waterloo, ON) was dispersed throughout the reaction cell during packing and a 15-cm layer of pea gravel was added to the influent and effluent ends of the cell.

The cell was installed north of the TA-01 tailings impoundment (Chapter 3). Water was pumped into the cell from a piezometer installed in Luke Creek (Chapter 3). Following packing of the reactive material, the cell was flushed with CO_2 for 2 h. A solution of 1000 mg L^{-1} SO_4^{2-} and 2.5 % Na-lactate was pumped through the cell until fully saturated, after which the cell was closed and left for 2 d before the start of groundwater flow. A Cl^- tracer test was conducted to determine the pore volume and residence time. The computer program STANMOD (Simunek et al., 1999) with the CXTFIT model (Toride et al., 1995) was used to assist in the interpretation of tracer test data.

To minimize freezing, pipe heating cables were wrapped around the cell and a light bulb used to produce heat near the influent tubing. A timer was connected to the water pump, heating wires, and light bulb to optimize battery usage. The pump operated at 1 min on/3 min off intervals, with the pump speed adjusted accordingly. However, the reaction cell froze as temperatures fell below −10 °C at times during the experiment. A propane tank heater was used to thaw the reaction cell to restart water flow and allow sample collection. The average pumping rate during the experiment was 8.2 mL min^{-1}, but freezing of the cell may have affected the flow (**Table 4.1)**.

4.2.2 Sample Collection

4.2.2.1 Aqueous Sampling

Water samples (60 mL) were collected from the reaction cell using syringes. To minimize disturbance to the flow rate, sample collection began at the effluent port and proceeded downward (ports 7, 5, 3, 2, 1) to the influent port (Chapter 3). Four full profiles were collected over the experimental period. A Solinst Levellogger™ was attached to the outside of the reaction cell to record temperatures bi-hourly during the experiment.

Water samples were collected to measure electrical conductivity (EC), pH, and Eh (unfiltered); anions, alkalinity, dissolved inorganic carbon (DIC), δ^{13}C-DIC isotopes, δ^{34}S-SO_4 isotopes, and dissolved H_2S (filtered, unacidified); cations and trace elements (filtered, acidified; pH < 2 with 67-70% OmniTrace® HNO_3); and nutrients and dissolved organic carbon (DOC) (filtered, acidified; pH < 2 with 95-98% A.C.S. Reagent H_2SO_4). Samples were passed through a 0.45-µm Acrodisc® filter and into polyethylene or amber glass bottles. Determinations of pH, Eh, alkalinity, EC, and dissolved H_2S were conducted in the field. Samples for all other parameters were refrigerated or frozen until analysis at the University of Waterloo.

4.2.2.2 Solid sampling

Following the experiment, a 2.54-cm Al core tube (40 cm long) was inserted into each solid-sampling port to extract solid-phase samples. Each end was capped and samples were stored frozen prior to microbiological and solid-phase analyses. A second core tube was inserted into the cell to collect any remaining material.

4.2.3 Analytical Techniques

4.2.3.1 Aqueous Analysis

Field measurements focused on pH (Orion 3 Star meter connected to an Orion 815600 Ross Combination pH Probe), Eh (Orion 3 Star meter connected to an Orion 9678B NWD Sure-Flow Combination redox electrode), alkalinity (Hach digital titrator and bromocresol green-methyl red indicators; Method 10244 from the HACH Hydraulic Fracturing Water Analysis Handbook, Edition 8), EC (Conductivity and TDS pocket meter), and H_2S (Hach DR/2400 Portable Spectrophotometer using methylene blue spectrophotometric method; Method 8131 from the DR 2800 Manual). Laboratory analyses were conducted at the University of Waterloo, Groundwater Geochemistry and Remediation Laboratory, to determine the concentrations of dissolved cations and trace elements (inductively-coupled plasma mass spectrometry, Thermo Fisher Xseries II; inductively-coupled plasma optical emission spectroscopy, Thermo Fisher iCAP 6000), dissolved anions (ion chromatography, Dionex IC-CO_3), and inorganic and organic carbon (total organic carbon method, Aurora 1030 TOC Analyzer). Samples were analyzed for NH_3-N using the salicylate method (Method 10031/10032 from the DR 2800 Manual), and for PO_4-P using the ascorbic acid method (Method 8048 from DR 2800 Manual) on a spectrophotometer (HACH DR 2800).

4.2.3.2 Light Microscopy and Synchrotron Analysis

A section of the solid column material was freeze-dried and sent to Spectrum Petrographics in Vancouver, WA for thin section preparation. A Nikon Eclipse LV100N POL polarized light microscope was used to examine the thin sections under reflected and transmitted light. Some grains of interest were further analyzed to determine elemental percentage using scanning electron microscopy (SEM; Hitachi TM3000 Tabletop SEM) with electron dispersion X-ray analysis (EDX; Bruker QUANTAX 70 EDS). Samples were analyzed using synchrotron radiation bulk S X-ray absorption near-edge structure spectroscopy (XANES) at the Canadian Light Source (CLS) in Saskatoon, Saskatchewan. ZVI grain coatings were prepared by cooling the sample in liquid N_2, transferring the sample to an anaerobic chamber, grinding the grains with a mortar and pestle, and sieving the ground material. Prepared samples were stored in an anaerobic chamber prior to transport to the CLS. Processing of the bulk S XANES data was conducted using the computer program ATHENA (Ravel & Newville, 2005). Two to three scans were merged in μ(E) to reduce the noise in the spectra. Spectra were collected for gypsum

($CaSO_4 \cdot 2H_2O$) during the same beamtime; spectra were shifted to the standard reference E0 of gypsum (Fleet, 2005). Merged scans were shifted accordingly (+0.82 eV).

4.2.3.3 Solid Organic Carbon Analysis

Portions of the unreacted organic carbon substrates used for the experiment (wood chips and leaf compost) were chemically characterized to determine the abundance of protein, lignin, acid detergent fiber (ADF), and neutral detergent fiber (NDF). Calculations were conducted to determine the cellulose content, hemi-cellulose content, C:N ratio, and degree of biodegradability of the material (Richards et al., 2005).

4.2.3.4 DNA Extractions

DNA was extracted in duplicate on solid samples stored in the freezer (-20 °C) following the kit instructions from DNeasy PowerSoil Kits (Qiagen Inc., Germany). Extracted samples were stored in the freezer at −20 °C prior to submission. Amplicon sequencing (Illumina MiSeq) of the data was conducted using modified universal primers 515F/806R (Walters et al., 2015) to amplify the V4 region of 16S rRNA genes. Processing of the sequencing data was conducted by Eva Pakostova (Pakostova et al., 2020), using the Mothur program v.1.39.5 (Schloss et al., 2009) and Mothur MiSeq Standard Operating Procedure (Kozich et al., 2013). Duplicate samples were merged and based on reference predictions by vsearch, using the Silva database for 16S rRNA gene sequences, chimeric sequences were discarded. Clustering of operational taxonomic units (OTUs) at a 97% similarity level were conducted using a *de novo* picking process. Taxonomic annotation of individual OTUs was determined with the Silva Reference database (Mothur-formatted version, details above). Several taxa, including mitochondria, eukaryotes and unknown, were not used for further data analysis based on the Mothur MiSeq SOP. To control variation due to the unequal number of sequences across samples, subsampling on each sample after OTU generation at a rarefaction level based on the sample with the fewest number of sequences (28,600 reads) was conducted. SRB relative abundances were determined by screening the taxonomy file for prokaryotic genera (or higher taxa when identification to the genus level was not possible) containing at least one species with the investigated metabolic trait. A list of SRB detected in the samples and the mean % of total reads from the whole data set, not individual samples, was determined (**Table C.1**).

4.2.3.5 Geochemical Modelling

Saturation indices were calculated using the geochemical software PHREEQCI with the WATEQ4F (Ball & Nordstrom, 1991) database.

4.3 Results

4.3.1 Temperature

The temperature varied from −19 to 9 ℃ with a mean value of −1 ℃ (**Figure 4.1**).

4.3.2 Water Chemistry

The mean influent pH was 3.78 and the mean effluent pH was 7.79 (**Table 4.2; Figure 4.2**). An increase from acidic to circumneutral values was observed at the first sampling port, 26 cm from the influent end or 11 cm into the reactive material. Following the initial increase, pH remained relatively constant for the remainder of the cell length. A decrease in Eh was observed within the first sampling port from a mean influent value of 480 mV to a mean effluent value of 120 mV, after which values remained relatively constant for the remainder of the cell length (**Figure 4.2)**. An increase in alkalinity was observed, from a mean influent value of near 0 mg L^{-1} as $CaCO_3$ to a mean effluent value of 150 mg L^{-1}.

The mean influent As concentration was 2.5 mg L^{-1} (**Figure 4.3**). Arsenic concentrations decreased within the first 11 cm of reactive material and remained low for the remainder of the cell length; the mean effluent As concentration was 2.7 µg L^{-1}. Iron concentrations varied along the length of the reaction cell (**Figure 4.3**). An increase from a mean influent value of 9.3 mg L^{-1} was observed until 40 cm along the cell length, after which concentrations began to decrease. Effluent Fe concentrations (mean 5.5 mg L^{-1}) were lower than influent concentrations. A decrease in the concentration of metals was observed by the first sampling port (**Figure 4.4**). Concentrations of metals, including Al, Co, Cu, Ni, and Zn, decreased, respectively, from mean influent values of 8.3 mg L^{-1}, 270 µg L^{-1}, 110 µg L^{-1}, 220 µg L^{-1}, and 270 µg L^{-1} to mean effluent values of 26 µg L^{-1}, 1.27 µg L^{-1}, 2.5 µg L^{-1}, 5.9 µg L^{-1}, and 2.5 µg L^{-1}. Following the initial decrease, concentrations of all metals remained relatively constant for the remainder of the cell length.

The mean influent H_2S concentration was < 5 µg L^{-1} (detection limit). Increased concentrations of H_2S were observed along the cell length, with a mean effluent value of 8 mg L^{-1} (**Figure 4.5**). No consistent change in the concentration of SO_4^{2-} was observed along the length

of the reaction cell. Mean influent and effluent concentrations were similar (166 vs. 170 mg L^{-1}, respectively). The mean $\delta^{34}S\text{-}SO_4$ value was 6.4 ‰ and no trend in $\delta^{34}S\text{-}SO_4$ was observed along the length of the reaction cell (**Figure 4.5**).

On the first two sampling days, DOC concentrations rose to a maximum of 110 mg L^{-1} as C, but on the last two sampling days decreased along the cell length (**Figure 4.6**). An increase in DIC from an influent concentration of 2.5 mg L^{-1} as C to an effluent concentration of 19 mg L^{-1} as C was observed on Day 9. The carbon isotope profile collected for Day 9 increased initially from an influent value of −23 ‰ and remained relatively constant for the remainder of the cell length at an effluent value of −10 ‰ (**Figure 4.6**).

An increase in NH_3-N was observed along the reaction cell length, from a mean influent concentration of 0.73 mg L^{-1} to a mean effluent concentration of 1.3 mg L^{-1} (**Figure 4.7**). Concentrations of PO_4-P decreased slightly along the length of the cell from a mean of 0.18 mg L^{-1} in the influent to 0.10 mg L^{-1} in the effluent.

4.3.3 Solid Phase Characterization

16S rRNA amplicon sequencing of the solid cell material indicated the presence of SRB communities throughout the reaction cell. The two most abundant genera of SRB were *Desulfitibacter* and *Desulfuromonas*. The relative abundance of SRB along the length of the cell ranged from 1.0 to 1.5 %, with no observed trend between the influent and effluent ends (**Figure 4.8**).

Pyrrhotite ($Fe_{(1-x)}S$), pyrite (FeS_2), and Fe (oxy)hydroxides were observed under optical microscopy. Corrosion products and white-grey rims were observed on grains of ZVI (**Figure 4.9**). Replacement of organic cellular material by a secondary precipitate was also observed.

Synchrotron radiation-based bulk S XANES analyses indicate the presence of two dominant peaks in the unreacted ZVI spectra, corresponding to an organic S species (2476 eV) and an oxidized sulfate species (2482 eV). Three spectral features (a/b, c, d) are observed in the spectra from the reaction cell samples (**Figure 4.10**). The first feature (a/b), appearing as a raised plateau as opposed to a peak, is observed within the range from 2471 and 2473 eV. Because of the low intensity, this feature, which may be attributed to pyrite or sphalerite ((Zn, Fe)S), could not be resolved. The second (c) and third (d) features are attributed to be an organic S species

(tetramethylene sulfoxide; C_4H_8OS) and oxidized sulfate species (gypsum; 2482 eV), respectively, based on the E0 of the absorption edge (Fleet, 2005; Wang et al., 2019). Both the second (c) and third (d) spectral features correspond to the two dominant peaks in the unreacted ZVI spectra (**Figure 4.10, 4.11**).

On a dry wt. % basis, leaf compost made up 5 wt.% and wood chips made up 14 wt.% of the total reactive mixture. Analysis of the unreacted organic material indicated a higher protein and lignin content in the leaf compost (P: 8.7 %, L: 18.6 %) compared to the wood chips (P: 4.7 %, L: 16.9 %). However, higher NDF and ADF values were observed in the wood chips (N: 52.7 %, A: 70.2 %) compared to the leaf compost (N: 61.2 %, A: 44.9 %). The C:N ratio of the leaf compost and wood chips was 28.8 and 53.8, respectively.

4.4 Discussion

4.4.1 Cold Temperature Reaction Cell

4.4.1.1 Water Chemistry

The increase in pH and alkalinity of the groundwater within the first 11 cm of reactive material (**Figure 4.2**) was likely due to the oxidation of ZVI, dissolution of limestone, and oxidation of OC (Chapter 2; Chapter 3; Benner et al., 2002; Lindsay et al., 2011):

$$2H_2O + Fe^0 \rightarrow Fe^{2+} + 2OH^- + H_2 \quad [1]$$

$$CaCO_3 + H^+ \leftrightarrow Ca^{2+} + HCO_3^- \quad [2]$$

$$SO_4^{2-} + 2CH_2O \leftrightarrow H_2S + 2HCO_3^- \quad [3]$$

The generation of H_2S, decrease in Eh values, presence of SRB in the solid material, and presence of secondary sulfides (**Figures 4.2, 4.5, 4.8**) indicates sulfate-reducing conditions in the reaction cell. However, SO_4^{2-} concentrations and $\delta^{34}S$ remained relatively unchanged along the length of the reaction cell (**Figure 4.5**), indicating the extent of sulfate-reducing conditions was limited.

The occurrence of secondary Fe sulfides indicates the development of sulfate-reducing conditions contributed to the decline in dissolved Fe through these phases:

$$SO_4^{2-} + 2CH_2O + 2H^+ \rightarrow H_2S + 2CO_2 + 2H_2O. \quad [4]$$

$$H_2S + Me^{2+} \rightarrow MeS_{(s)} + 2H^+ \quad [5]$$

The results from geochemical modelling indicate the precipitation of Fe sulfides such as amorphous FeS, greigite (Fe_3S_4), and mackinawite ($(Fe, Ni)_{1+x}S$) was favoured, resulting in Fe immobilization (**Figures C1, C2**). The formation of ZVI corrosion products, including goethite (FeO(OH)), ferrihydrite ($5Fe_2O_3 \cdot 9H_2O$), and ferrous hydroxy carbonate ($Fe_2(OH)_2(CO_3)$), also likely contributed to a decline in Fe concentrations (Jeen et al., 2007):

$$Fe^{3+} + 2H_2O \rightarrow FeOOH_{(s)} + 3H^+ \quad [6]$$

$$2Fe^{2+} + 2H_2O + HCO_3^- \rightarrow Fe_2(OH)_2CO_{3(s)} + 3H^+ \quad [7]$$

The sharp decrease in As concentrations (**Figure 4.3**) is attributed to the incorporation of As in secondary sulfide phases or secondary Fe (oxy)hydroxides. Incorporation of As into Fe sulfides (amorphous FeS, greigite, mackinawite) or formation of a distinct As-sulfide phase (orpiment(As_2S_3) or realgar (AsS)) following SO_4^{2-} reduction contributed to As immobilization in laboratory column and field experiments (Chapter 2; Chapter 3; Blowes et al., 2000, 2014; Jambor et al., 2005). The decrease in As concentrations is also likely due to adsorption onto ZVI corrosion products (Chapter 2; Lien & Wilkin, 2005; Ludwig et al., 2009; Su & Puls, 2001). Possibly because of low abundances, attempts to isolate secondary As-bearing phases by optical microscopy and SEM were unsuccessful.

A decline in metal concentrations including Al, Cu, Ni, and Zn was observed within the first 11 cm of reactive material (**Figure 4.4**). The decrease in Al concentrations is attributed to the increase in pH and precipitation of Al (oxy)hydroxides (*e.g.*, gibbsite (γ -$Al(OH)_3$), boehmite (γ-AlO(OH))) (**Figure C1**). Geochemical modelling indicates supersaturation with respect to these phases. The declines in concentrations of Cu, Ni, and Zn are likely due to the development of sulfate-reducing conditions and subsequent precipitation of metal sulfides such as chalcopyrite ($CuFeS_2$), covellite (CuS), mackinawite, and sphalerite ((Zn, Fe)S), or less crystalline precursors. Geochemical modelling indicates the precipitation of these phases is favoured.

The slight increase in NH_3-N concentrations along the length of the column (**Figure 4.7**) may be attributed to the breakdown of organic material, whereas the slight decline in PO_4-P may be due to adsorption onto Fe (oxy)hydroxides or precipitation of vivianite ($Fe_3(PO_4)_2 \cdot 8H_2O$) (**Figure C.1**). The high DOC concentrations (> 100 mg L^{-1}) observed early in the experiment

may be due to the initial decomposition of Na-lactate and organic-rich creek sediment added to the reaction cell material. The decrease in DOC concentrations observed for Days 23 and 36 is likely due to the slow degradation of complex OC following the rapid breakdown of labile organic carbon (Benner et al., 2002). The increase in DIC observed along the cell length may be due to an increase in alkalinity during sulfate-reduction or organic matter mineralization (Asmussen & Strauch, 1998). Initial enrichment in δ^{13}C-DIC is likely due to the dissolution of limestone, and the sustained, negative, δ^{13}C-DIC values (−10 ‰) following initial enrichment are likely due to limited sulfate-reduction and OC oxidation (Londry & Des Marais, 2003).

4.4.1.2 Microbial Community

The low abundance of SRB suggests SO_4^{2-} reduction is likely limited (**Figure 4.8**). The two most abundant SRB genera were *Desulfuromonas* and *Desulfitibacter*, both of which contain members that can use S^0 as a terminal electron acceptor (Nielsen et al., 2006; Rikihisa et al., 2015). *Desulfitibacter* bacteria produce sulfide through the reduction of S^0 (Nielsen et al., 2006), and *Desulfuromonas* organisms can reduce S^0 to H_2S through dissimilatory S reduction (Rikihisa et al., 2015). Other less abundant SRB genera observed in the solid material include *Desulfomicrobium* and *Desulfobulbus*. Some *Desulfomicrobium* members can reduce both arsenate and SO_4^{2-}. The addition of ZVI to the reactive mixture promoted the formation of H_2 (reaction [1]) and may have enabled the growth of *Desulfobulbus* members capable of reducing SO_4^{2-} to H_2S and utilizing H_2 for growth. The optimal temperature for growth of these genera is 30 ℃, which is much higher than the colder temperatures of this reaction cell experiment.

4.4.1.3 Solid-phase Characterization

The presence of pyrrhotite, pyrite, and Fe (oxy)hydroxides observed in the solid material using optical microscopy indicates the precipitation of Fe sulfides and the formation of ZVI corrosion products occurred (**Figure 4.9**). The results from bulk S XANES indicate the accumulation of a reduced S species in the solid material and is consistent with the precipitation of Fe sulfides during bacterially-mediated SO_4^{2-} reduction (**Figure 4.10**). The presence of a raised plateau as opposed to a sharp peak in the bulk S XANES spectra suggests the accumulation of a reduced species in the solid material was limited.

4.4.1.4 Characterization of Organic Carbon

The long-term effectiveness of OC substrates in the reactive mixture, to support bacterially-mediated SO_4^{2-} reduction and removal of metals, can be variable. Factors such as the rate of degradation of the solid material by bacteria (*e.g.,* cellulose, proteins, lignins) and the type of nutrients available in the reactive material (carbohydrates, nitrogen) may affect the long-term rate of DOC release into the water. Quantifying the characteristics of an OC substrate may contribute to understanding the short- and long-term capability of the material.

In the fresh wood chips, the more degradable cellulose (36 %) and hemi-cellulose (18 %) made up about 54 % of the carbohydrates, and the less degradable lignins made up 17 % of the carbohydrates. About 42 % of the carbohydrates in the leaf compost were composed of cellulose (26 %) and hemi-cellulose (16 %), and 19 % of carbohydrates were in the form of lignins. The C:N ratio for the leaf compost (29) is lower than for the wood chips (54). The values for NDF and ADF are also lower in the leaf compost than in the wood chips. The (C+H)/L ratio, where C is the cellulose content, H is the hemi-cellulose content, and L is the lignin content, was calculated (**Table 4.3**). This ratio typically indicates the degree of biodegradation that has occurred in a certain material (Richards et al., 2005). Using this indicator, a lower degree of biodegradability was determined for the leaf compost (2.3) compared to the wood chips (3.2). These results suggest the leaf compost may be more bioavailable than the wood chips and therefore more suitable for initial SO_4^{2-} reduction. However, both materials are suitable for SO_4^{2-} reduction, and wood chips are likely important as a long-term source of OC due to the slower breakdown. Another study that evaluated the chemical characteristics of oak leaf and compost reports cellulose content ranging from 34 to 37 wt.% for both materials and lignin content of around 15 wt. % (Gibert et al., 2004). These numbers are comparable to the cellulose and lignin content of the leaf compost and wood chips in the reaction cell. Other factors such as residence time also contribute to the overall performance of the reactive mixture in a system (Gibert et al., 2004).

4.4.2 Comparison to Laboratory Columns and Warm Temperature Reaction Cell

A primary objective of the autumn field cell experiment was to compare results with laboratory experiments (Chapter 2) and a summer reaction cell trial (Chapter 3) packed with comparable reactive materials (ZVI and OC). Three laboratory column experiments were

conducted using varied OC:ZVI mixtures (wt. %) of 40:10 (T1), 30:20 (T2), 20:30 (T3). Determining the ability of the reactive material to remove As and other contaminants present at the site over a range of temperatures and groundwater velocities contributes to our understanding of factors influencing SRB activity and metal removal.

4.4.2.1 Water Chemistry and Microbiology

A decrease in SO_4^{2-} was observed along the summer cell and laboratory column lengths, but no change was observed in the aqueous SO_4^{2-} concentrations of the autumn cell (**Figure 4.5)**. Sulfate removal rates ranged from −180 to −200 µg L^{-1} d^{-1} g^{-1} of dry OC for the column experiments and from −4.9 to −7.6 µg L^{-1} d^{-1} g^{-1} of dry OC for the summer cell. Sulfate removal rates could not be calculated for the autumn cell due to the lack of SO_4^{2-} removal; however, a rate can be predicted by determining the temperature dependence of the reaction. The Arrhenius equation can be used to predict the effect of changing temperatures on the rate of SO_4^{2-} reduction (Benner et al., 2002):

$$log\frac{k_1}{k_2} = \frac{E_a}{2.303R}[\frac{1}{T_2} - \frac{1}{T_1}]$$

where k_1 is the rate coefficient at temperature T_1 (Kelvin), k_2 is the rate coefficient at temperature T_2, R is the universal gas constant (8.314×10^{-3} kJ mol^{-1} K^{-1}), and E_a (kJ mol^{-1}) is the activation energy of the reaction in reference to the temperature dependence of the overall SO_4^{2-} removal rate (Benner et al., 2002). Benner et al. (2002) calculated an E_a of 40 kJ mol^{-1} based on seasonal variations for an organic carbon barrier installed at a mine site and monitored for a period of several years. Using this E_a, for a mean outside temperature of −0.5 °C (autumn cell), the rate of SO_4^{2-} reduction ranges from 15.7 to 20.4 mg L^{-1} d^{-1}, corresponding to SO_4^{2-} removal between 37.9 and 49.2 mg L^{-1}. The SO_4^{2-} removal is within the range of influent SO_4^{2-} concentrations (146.3 to 186.6 mg L^{-1}), and would not be detectable in field observations.

The enrichment factor of $\delta^{34}S\text{-}SO_4$ was greater for the column experiments (ε: −28.9 ‰, columns; ε: −23.2 ‰, summer cell), which is consistent with the greater extent of SO_4^{2-} removal observed in the columns. No change in $\delta^{34}S\text{-}SO_4$ was observed in the autumn cell. This difference is consistent with limited SO_4^{2-} removal in the autumn reaction cell, indicating the colder temperatures limited bacterial growth and activity and affected the development of strong sulfate-reducing conditions. The difference in lactate incubation time between the three

experiments (autumn: 2 d; summer: 20 d; laboratory columns: 12 d), may also have contributed to the limited growth and activity of SRB in the autumn cell; the autumn cell was incubated for a shorter length of time compared to the other two experiments.

An increase in DOC was observed along the length of the cells and columns, but the initial increase in DOC concentrations was substantially greater in the laboratory column experiments (max: 6000 mg L^{-1}), compared to the summer reaction cell (max: 590 mg L^{-1}) and autumn reaction cell (max: 110 mg L^{-1}; **Figure 4.6**). The difference in nutrient and DOC trends may be attributed to the varying temperatures in the experiments. Temperatures in the laboratory were consistently at 22 °C during the experiment; however, temperatures in the field varied daily and were substantially colder during the autumn trial (mean air temperature −1 °C) than for the summer cell (19 °C) (**Figure 4.1**). Decomposition rates of organic material increase with increasing temperature (Kirschbaum, 1995). The lower DOC concentrations observed in the autumn cell, compared to the summer cell and laboratory experiments, are consistent with the slow rates of OC decomposition at low temperatures.

Nutrient concentrations varied between the reaction cell and laboratory column experiments (**Figure 4.7)**. Ammonia and PO_4-P concentrations were relatively similar between the influent and effluent ends of both reaction cell experiments; only a slight increase was observed toward the effluent end. In the laboratory column experiments, however, NH_3-N and PO_4-P were much greater in the column effluents compared to the influent, which indicates both NH_3-N and PO_4-P were probably released by more extensive oxidation of OC in the column experiments.

The total percentage of SRB reads was lower for the autumn reaction cell (1.0-1.5 %) and greater for the summer reaction cell (1.8-2.5 %) and laboratory column experiments (2.4-10.0 %) (**Figure 4.8**; results shown for laboratory column T3, with a ratio of ZVI:OC most similar to the reaction cell mixtures, after conversion from wt.% to vol.%). The major SRB genera observed in the laboratory column experiments were *Desulfovibrio, Desulfobulbus, Desulfomicrobium, Desulfuromonas,* and *Desulfobacter*, whereas the major genera observed in the summer cell were *Desulfomicrobium, Desulfitibacter, Desulfosporosinus,* and the order, *Desulfovibrionales* (which includes the genera *Desulfovibrio*). Similar major genera between the laboratory columns and the summer cell were *Desulfovibrio* and *Desulfomicrobium*. In the autumn cell, the most abundant

genera were *Desulfitibacter* and *Desulfuromonas*, which were also one of the most abundant in the summer cell (*Desulfitibacter*) and laboratory columns (*Desulfuromonas*). The lower abundance and activity of SRB in the autumn trial may be attributed to the lower temperatures. Different genera may have dominated in the autumn cell based on the ability to survive under more extreme conditions. The genus *Desulfuromonas*, observed in both the column experiments and autumn cell, contains a strain called *Desulfuromonas svalbardensis*, which has been observed to grow within a temperature range of −2 to 20 °C (Vandieken et al., 2006). The predominance of *Desulfuromonas* in the autumn cell is consistent with the ability of this strain to survive under colder temperatures. However, other strains of *Desulfuromonas*, such as *Desulfuromonas acetoxidans*, have a higher optimal temperature range, which may explain why the genus also dominated in the laboratory columns under warmer temperatures (Pfennig & Biebl, 1976).

Similar trends in aqueous geochemistry were observed between the laboratory column experiments and the two field reaction cell experiments. An increase in pH from acidic to circumneutral values and a decrease in Eh before the first sampling port was observed in all experiments (**Figure 4.2**). Sharp decreases in dissolved As concentrations to < 10 µg L^{-1} (**Figure 4.3**) and dissolved metal concentrations of Al, Cu, Ni, and Zn (**Figure 4.4**) were observed. In all cases, removal of As and metals was observed at the first sampling port, indicating only a small proportion of the reactive material was consumed, and that substantial reactive capacity remained at the end of the experiments.

An increase in DIC along the cell and column lengths, attributed to dissolution of $CaCO_3$ and oxidation of OC, was observed in all three experiments. Specifically, influent δ^{13}C-DIC values ranged from −20 to −25 ‰, with a sharp increase observed at the first sampling port near −10 ‰; δ^{13}C-DIC was then constant for the remainder of the cell or column length (**Figure 4.6**). This change in δ^{13}C-DIC suggests the dissolution of limestone was a predominant source of the additional δ^{13}C-DIC; however, oxidation of OC through SO_4^{2-} reduction may also have contributed to the increase in alkalinity.

The concentration of Fe in the laboratory column effluents was substantially greater than influent values, whereas a minimal difference was observed between influent and effluent concentrations in both reaction cell trials (**Figure 4.3)**. The initially high Fe concentrations in the

laboratory columns decreased over time and concentrations were substantially lower toward the end of the experiments. Acid-washed ZVI was used for the reaction cell experiments, but untreated ZVI was used for the column experiments. Untreated ZVI particles are coated with oxidation products, principally Fe(III) (oxy)hydroxides, which are susceptible to reductive dissolution under the conditions prevalent within the column experiments. The observed differences in Fe concentrations between the experiments may be attributed to the difference in ZVI utilized for the cells compared to the columns.

4.4.2.2 Solid-phase Characterization

The presence of white-grey, blade-like rims on ZVI grains, replacement of organic cellular material by a secondary precipitate, and the presence of sulfide and Fe (oxy)hydroxide minerals were observed in all three experiments; however, a few differences were also noted. Less corrosion was observed on the ZVI grains and a lower abundance of sulfide minerals, including pyrite and pyrrhotite, was evident in the autumn cell material compared to that from the laboratory columns and summer reaction cell. These results indicate similar mechanisms occurred in all three experiments, but the extent of these processes and the resulting accumulation of reaction products was limited in the autumn cell material.

Geochemical modelling for all of the experiments indicates conditions favourable for the precipitation of greigite (Fe_3S_4), mackinawite ($(Fe,Ni)_{1+x}S$), pyrite, sphalerite, chalcopyrite ($CuFeS_2$), covellite (CuS), and $ZnS_{(a)}$ (**Figures C.1, C.2)**. In addition, greater accumulations of solid phase S were observed near the influent end of the columns and cells, but the trend was not as pronounced in the autumn cell (**Figure 4.12**). Bulk S XANES spectra of the unreacted ZVI (both untreated and acid-washed), indicated the presence of two dominant oxidation states: SO_4^{2-}, represented by gypsum, and an organic S compound, included in the XANES analysis as tetramethylene sulfoxide (c, d; **Figure 4.11**). The spectra from the reacted column and cell material indicate three spectral features; the second and third peaks are similar to those observed in the unreacted ZVI spectra. The first peak, which is absent in the unreacted ZVI coatings, is characteristic of reduced S species and indicates reduced S phases accumulated on the ZVI grains during the experiments. This observation, which was consistent in all three experiments, indicates sulfides accumulated in the solid material due to microbially-mediated interactions between the groundwater and reactive mixture. In the autumn reaction cell spectra, however, the

first spectral feature appears as a raised plateau, which extends to the second spectral peak (tetramethylene sulfoxide), rather than the well-defined peak observed in spectra obtained for the laboratory columns and the summer reaction cell (**Figure 4.11**). The occurrence of this plateau suggests the accumulation of a reduced S species during the autumn cell trial was limited.

Solid-phase characterization of all three experiments indicated the As removal mechanisms in the reactive material were similar. The likely removal mechanism for As was adsorption onto ZVI corrosion products or precipitation as an As-sulfide phase. Bacterially-mediated SO_4^{2-} reduction and the subsequent precipitation of low-solubility metal sulfides likely contributed to the removal of Fe and metals (Cu, Ni, Zn) in all three experiments, however, this process was likely more limited in the autumn cell and additional reactions may have contributed to a further decrease in metal concentrations. The increase in pH and precipitation of Al (oxy)hydroxides likely resulted in the immobilization of Al. The results from geochemical modelling, optical microscopy, microbiology, and solid-phase characterization of all three experiments are consistent with these observations. However, the extent to which the processes occurred appears to have been limited in the autumn reaction cell.

4.4.2.3 Temperature Dependence

The outside temperature during the autumn cell trial ranged from −19 to 9 °C, and was approximately 15 to 20 °C colder than the average outside temperature during the summer trial (11 to 30 °C; **Figure 4.1**). These lower temperatures resulted in lower reaction rates during the autumn experiment. The decrease in Eh, presence of SRB microbial communities, generation of alkalinity, and production of low amounts of H_2S, suggest the development of sulfate-reducing conditions occurred in all of the experiments. However, changes between influent and effluent SO_4^{2-} concentrations observed in the autumn cell fall within the range of variability of the input concentrations; the absence of $\delta^{34}S$-SO_4 enrichment indicates that bacterially-mediated SO_4^{2-} reduction was modest and may have occurred at rates too low to be detected (Nakai & Jensen, 1964). The absence of SO_4^{2-} removal and the lack of $\delta^{34}S$ enrichment were also observed in column T0 during the laboratory study (**Figure 4.5**). Column T0 contained minimal amounts of OC and 0 wt. % ZVI. A decrease in metal concentrations was observed in both the autumn cell and column T0, however As was removed from the autumn cell but not from column T0. The removal of metals from column T0 was attributed to bacterially-mediated SO_4^{2-} reduction. The

removal of metals in the autumn cell is likely due to the limited presence of bacterially-mediated SO_4^{2-} reduction or adsorption or co-precipitation with alteration coatings on the ZVI. The results from column T0 indicate that removal of As from the autumn cell may be attributed to the presence of ZVI, which can create surfaces for As adsorption through the anaerobic corrosion of Fe^0 to Fe(II). Therefore, the addition of ZVI appears to be important for the removal of As, under conditions where bacterially-mediated SO_4^{2-} reduction is limited.

The limited development of bacterially-mediated SO_4^{2-} reduction may be due to the colder temperatures but also to the shorter duration of the autumn cell experiment. Sulfate-reducing bacteria are able to adapt to changing temperature conditions and may survive in a wide range of temperatures from below −5 °C up to +75 °C (Postgate, 1984; Waybrant et al., 1998). The colder temperatures in the autumn cell likely slowed the rate of bacterial activity and the reduction of aqueous SO_4^{2-} concentrations. The results suggest a future barrier system should be installed during the warmer months when sulfate-reducing conditions are able to fully develop.

4.5 Conclusions

Arsenic and dissolved metals were removed from acidic groundwater under cold temperature conditions with a reactive mixture of ZVI, OC, and limestone. The results from this study were compared to previous laboratory and field experiments utilizing similar reactive material and influent water to determine the effect of a lower temperature.

Daily temperatures were 10-15 °C colder in the autumn cell than in the summer reaction cell and laboratory column experiments, which resulted in the development of limited sulfate-reducing conditions in the autumn cell. The absence of aqueous SO_4^{2-} removal was consistent with the limited formation of reduced S species in the bulk S XANES spectra and with the lower abundance of pyrite and pyrrhotite grains observed under optical microscopy in the autumn reaction cell. A lower abundance of SRB populations was also observed in the solid autumn cell material compared to the other two experiments. Limited SO_4^{2-} reduction is attributed to the colder temperature conditions of the autumn cell experiment or the shorter trial length.

Despite decreased microbial activity in the autumn reaction cell, the water chemistry of all of the experiments was similar, including a decrease in dissolved As and metal concentrations, an increase in pH to circumneutral values, and similar trends in alkalinity, Eh, and carbon. Iron concentrations were relatively constant between the influent and effluent

concentrations of both reaction cell experiments but were greater in the laboratory column effluents. This difference may be attributed to the use of unreacted ZVI in the column experiments compared to acid-washed ZVI in the reaction cell experiments.

The autumn reaction cell results indicate a reactive mixture containing ZVI and OC may be influenced by temperature. The colder temperatures and shorter incubation period likely limited the initial development of sulfate-reducing conditions in the autumn cell; however, the addition of ZVI contributed to As and metal removal despite the limited microbial activity. Overall, aqueous chemistry results were similar across all three experiments, indicating the potential for the reactive material to remove contaminants under varying temperature and flow conditions.

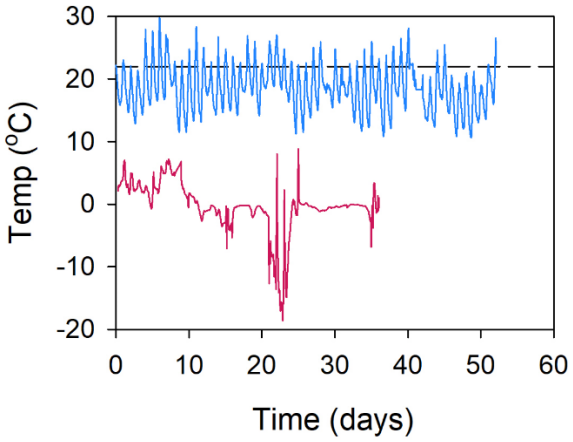

Figure 4.1 Changes in temperature during the autumn 2018 field trial (red) compared to the summer 2019 field trial (blue; Chapter 3). The average temperature for the laboratory column experiments was 22 °C (dashed line; Chapter 2).

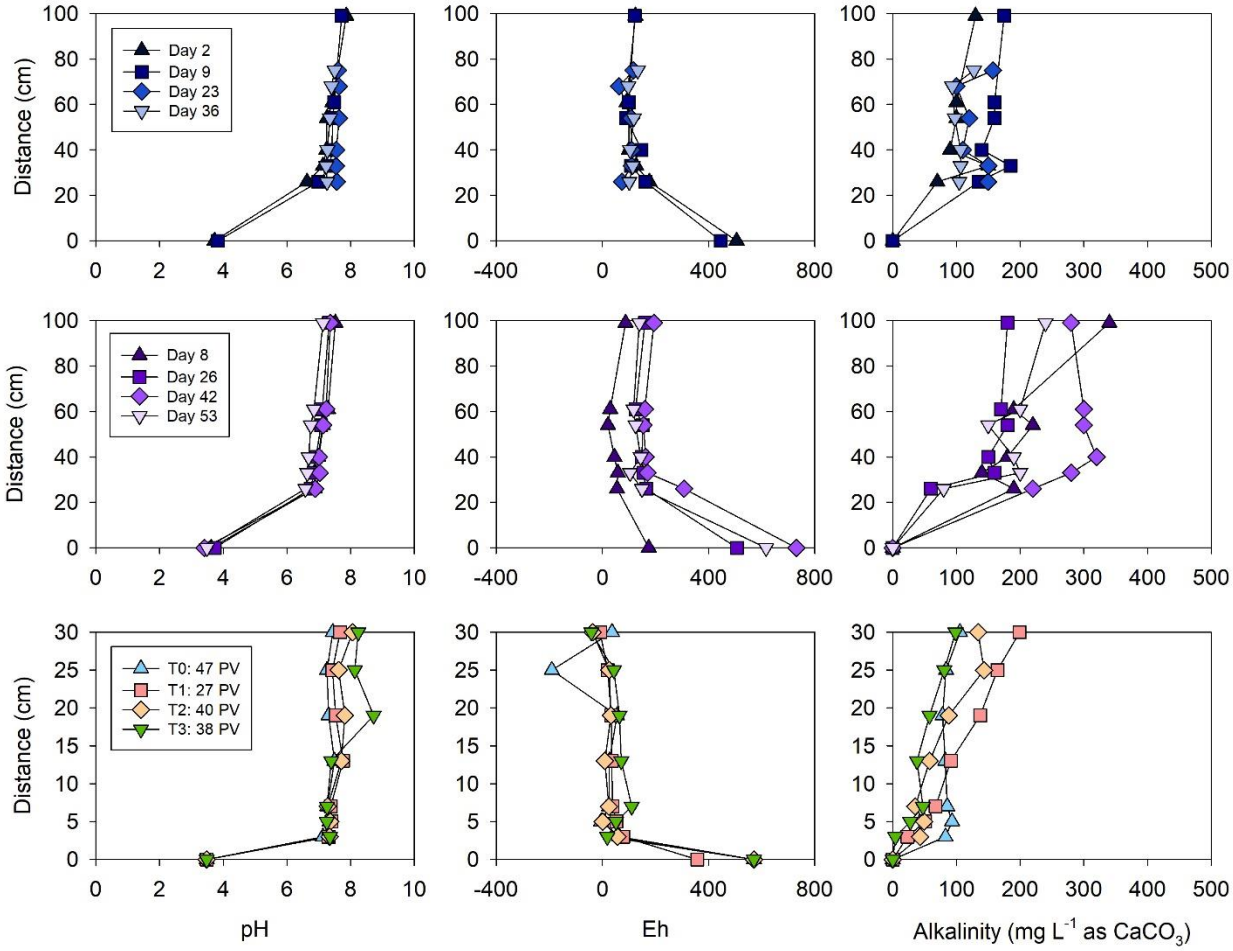

Figure 4.2 Profiles of pH, Eh, and alkalinity for select dates from the autumn reaction cell (top), summer reaction cell (middle; Chapter 3), and laboratory columns prior to termination of the experiment (bottom; Chapter 2). Distance 0 cm represents influent concentrations and 100 cm or 30 cm represents effluent concentrations.

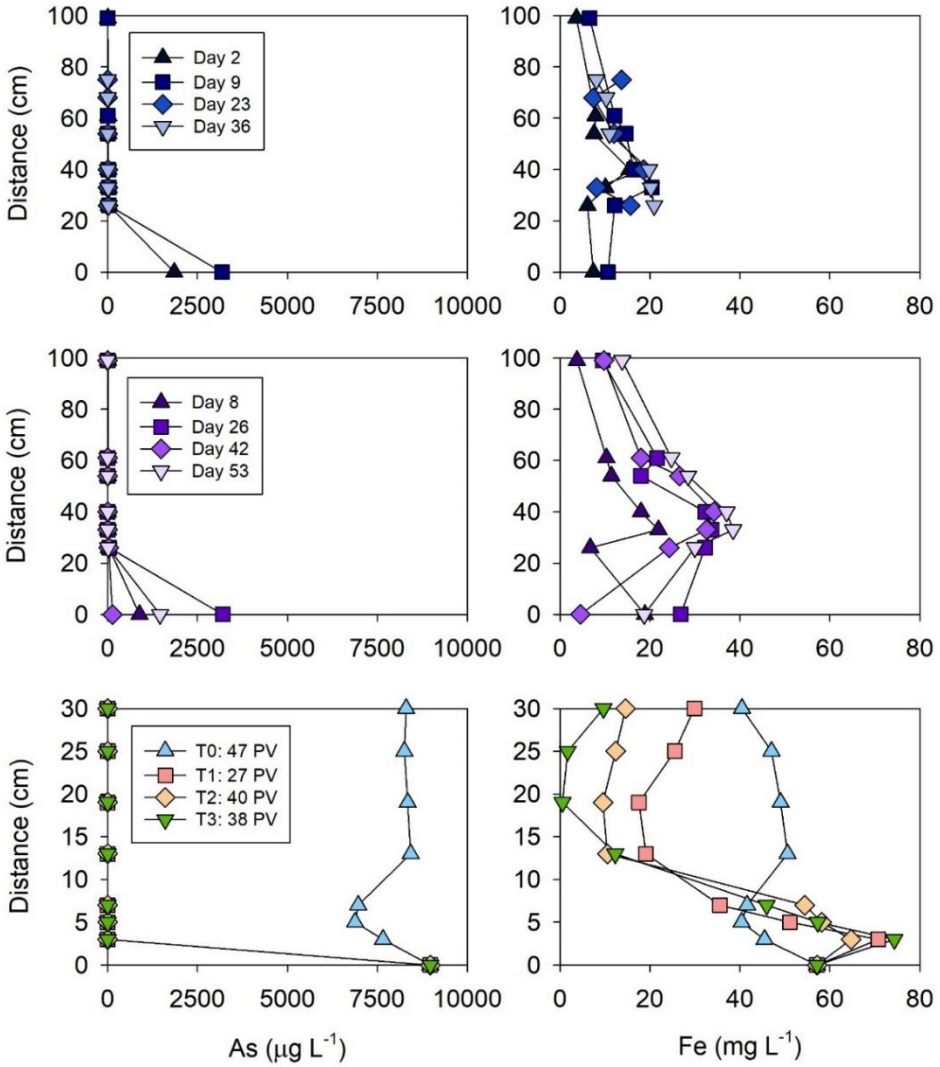

Figure 4.3 Profiles of aqueous As and Fe for select dates from the autumn reaction cell (top), summer reaction cell (middle; Chapter 3), and laboratory column columns prior to termination of the experiment (bottom; Chapter 2). Distance 0 cm represents influent concentrations and 100 cm or 30 cm represents effluent concentrations.

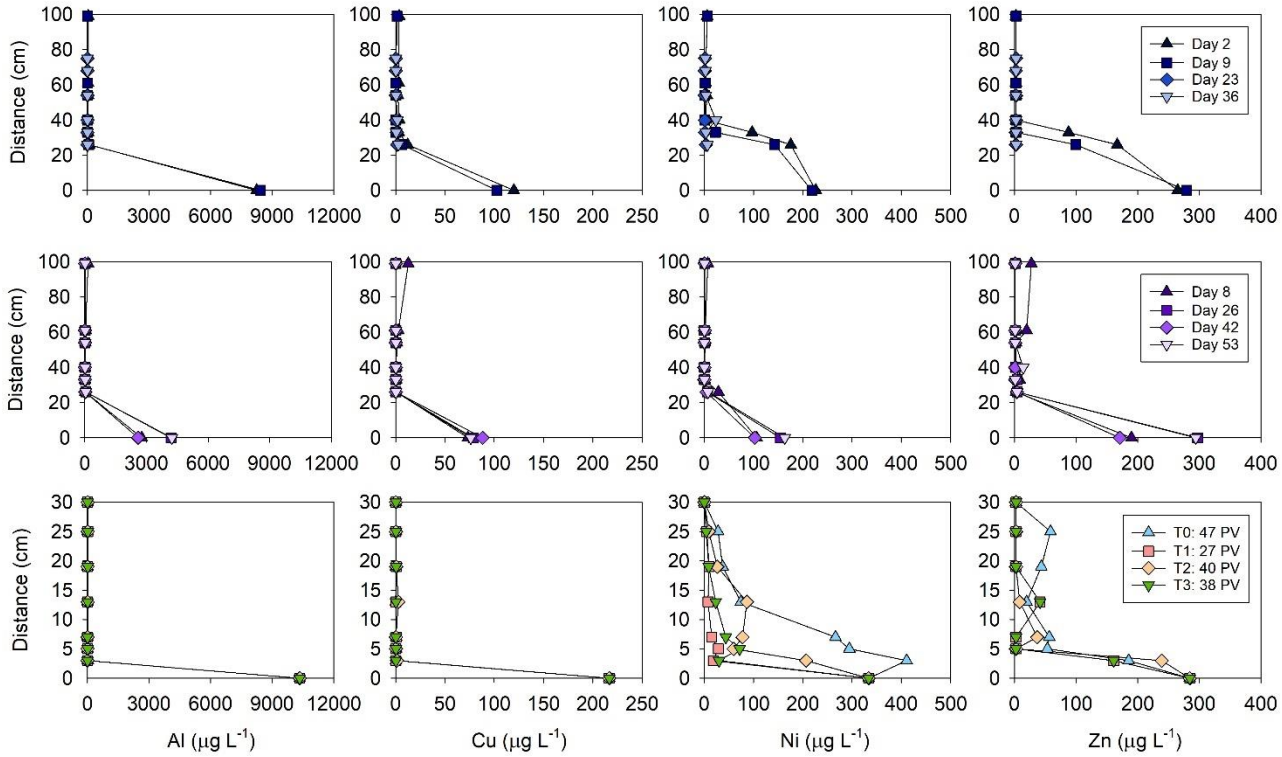

Figure 4.4 Profiles of aqueous Al, Cu, Ni, and Zn for select dates from the autumn reaction cell (top), summer reaction cell (middle; Chapter 3), and laboratory column columns prior to termination of the experiment (bottom; Chapter 2). Distance 0 cm represents influent concentrations and 100 cm or 30 cm represents effluent concentrations.

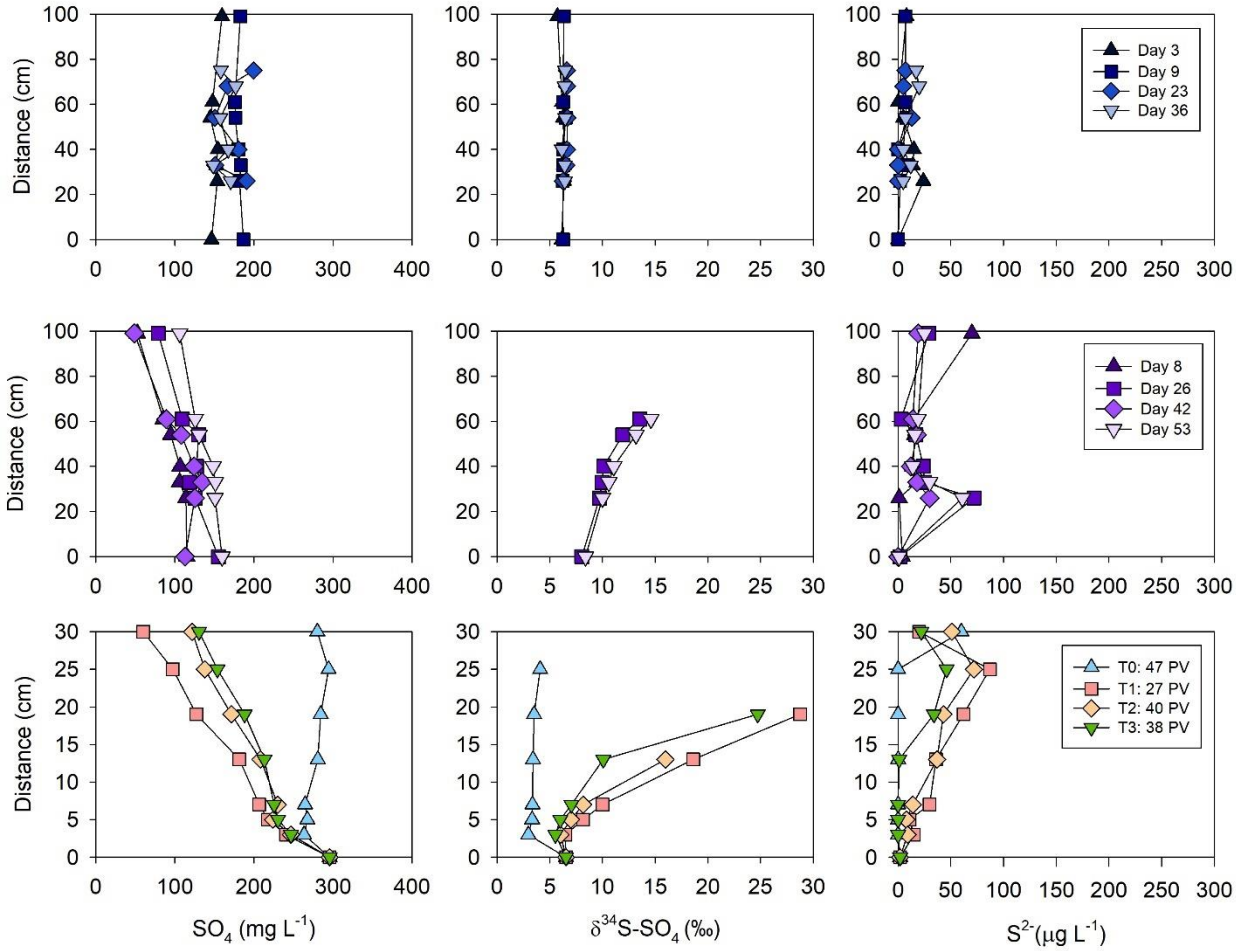

Figure 4.5 Profiles of aqueous of SO_4, $\delta^{34}S\text{-}SO_4$, and S^{2-} for select dates from the autumn reaction cell (top), summer reaction cell (middle; Chapter 3), and from laboratory column columns prior to termination of the experiment (bottom; Chapter 2). Distance 0 cm represents influent concentrations and 100 cm or 30 cm represents effluent concentrations.

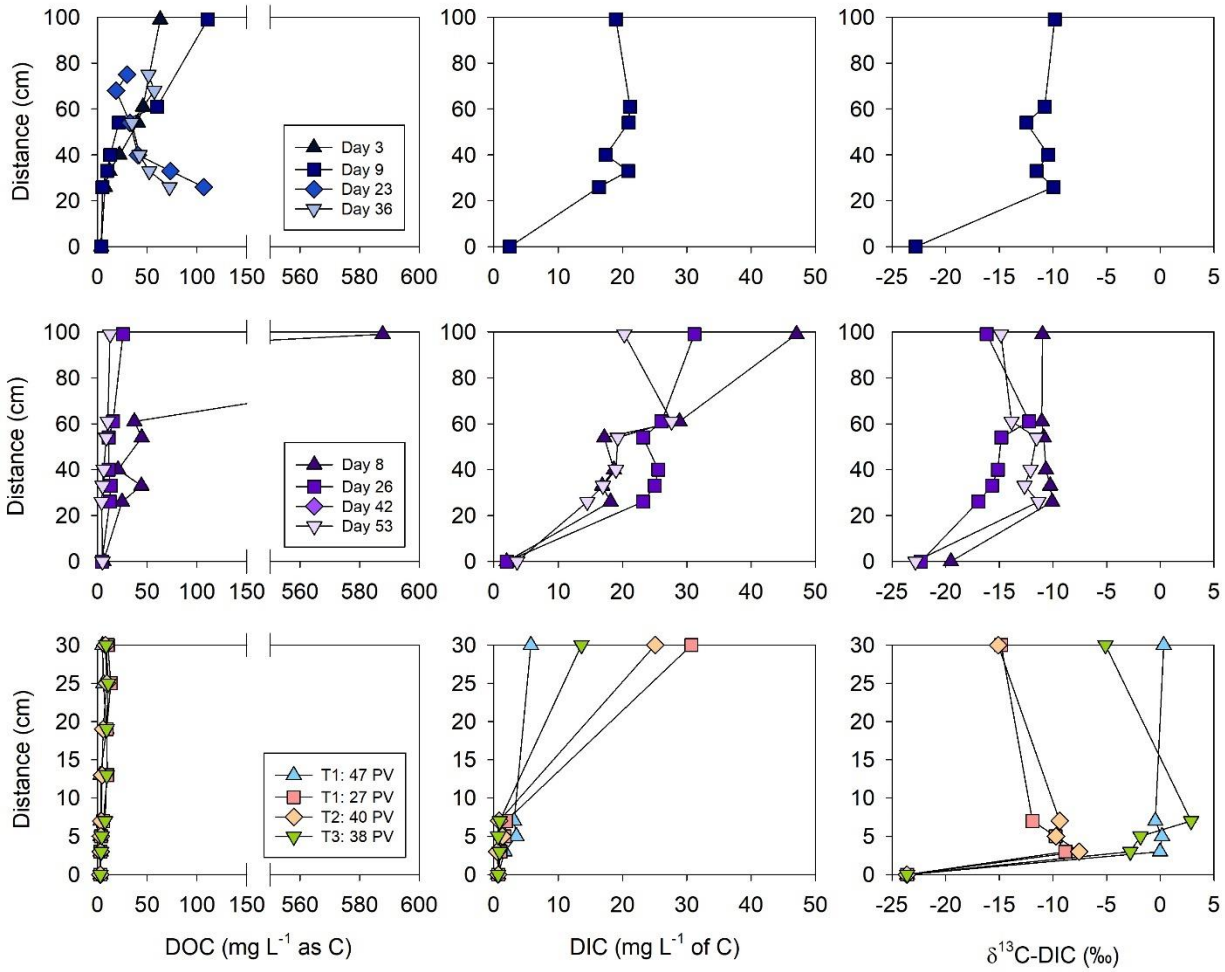

Figure 4.6 Profiles of aqueous of DOC, DIC, and δ^{13}C-DIC for select dates from the autumn reaction cell (top), summer reaction cell (middle; Chapter 3), and from laboratory columns prior to termination of the experiment (bottom; Chapter 2). Distance 0 cm represents influent concentrations and 100 cm or 30 cm represents effluent concentrations.

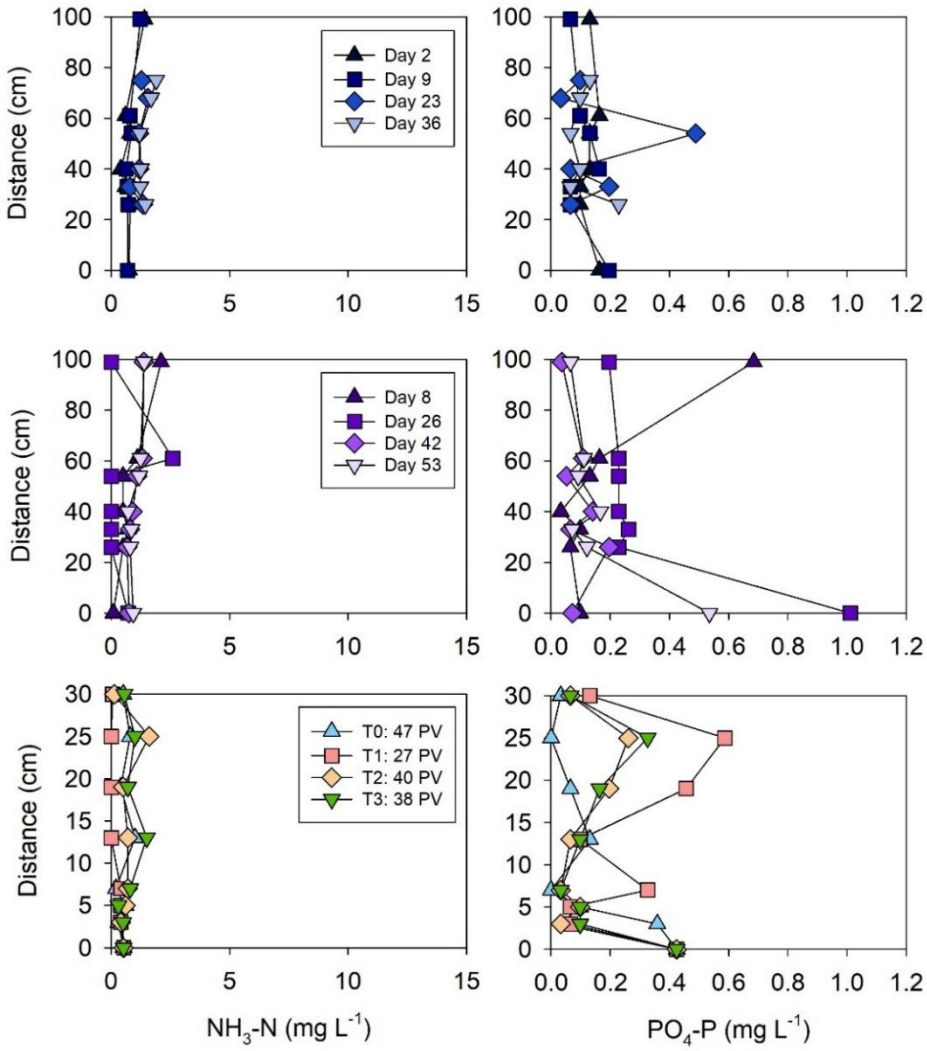

Figure 4.7 Profiles of aqueous of NH_3-N and PO_4-P for select dates from the autumn reaction cell (top), summer reaction cell (middle; Chapter 3), and laboratory column columns prior to termination of the experiment (bottom; Chapter 2). Distance 0 cm represents influent concentrations and 100 cm or 30 cm represents effluent concentrations.

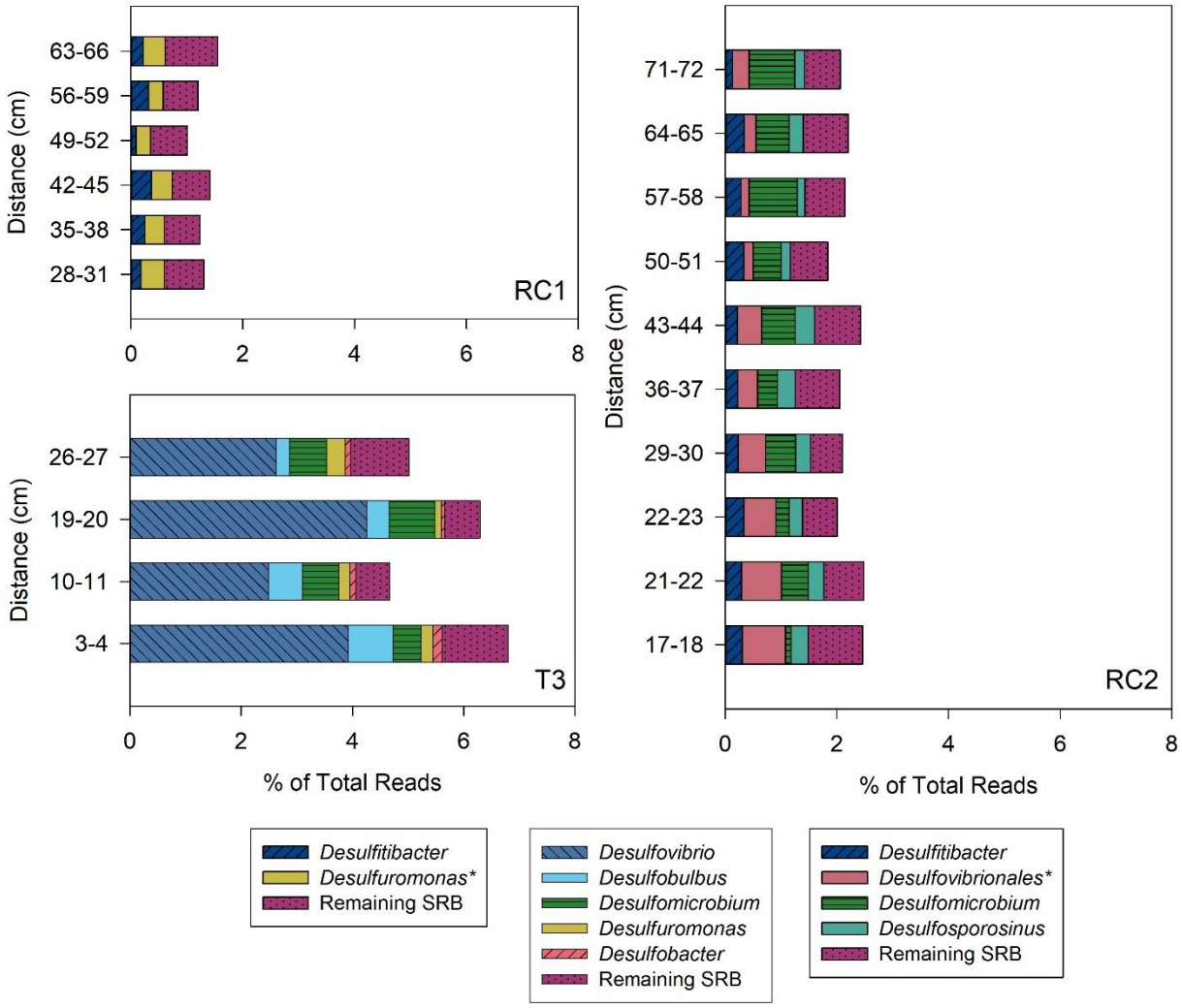

Figure 4.8 Percent known SRB identified through DNA extraction analysis in the autumn cell (top left), summer cell (right; Chapter 3) and laboratory column T3 with the closest ZVI:OC ratio (bottom left; Chapter 2) at different distances along the cell/column length. The most abundant genera (marked with asterisks when pooled together with higher taxa) are plotted and the remaining SRB are grouped separately.

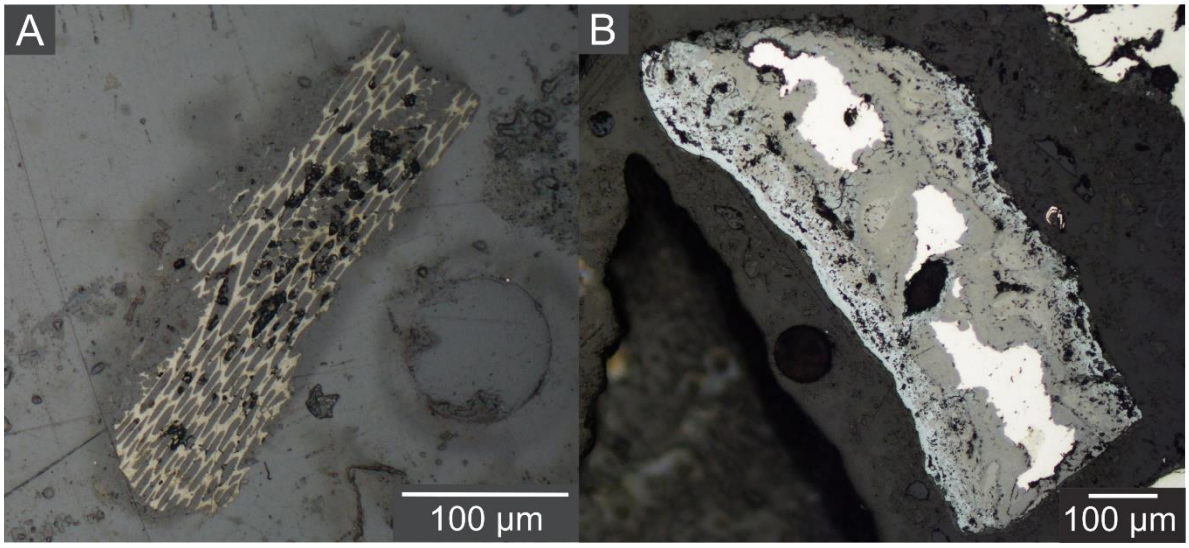

Figure 4.9 Reflected light microscopy images of grains showing (A) Fe-sulfide precipitate replacement of OC structure and (B) corrosion rims on a ZVI grain.

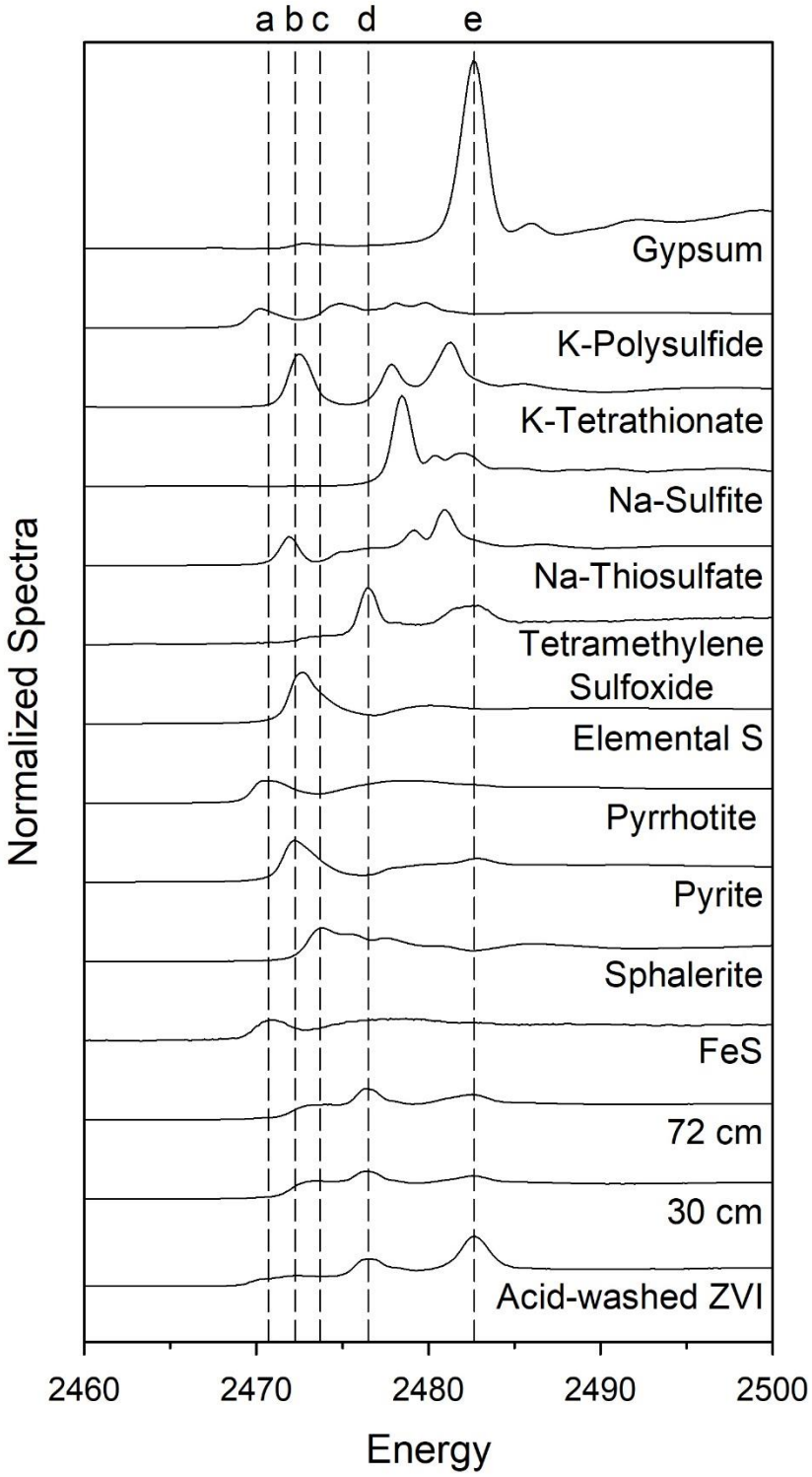

Figure 4.10 Bulk S XANES spectra of solid samples collected from the reaction cell. The number (cm) represents the distance from the influent end of the cell. Unreacted, acid-washed ZVI and other standards are also shown. The spectral peak locations for pyrrhotite/FeS (a), pyrite (b), sphalerite (c), tetramethylene sulfoxide (d), and gypsum (e) are shown with dashed lines.

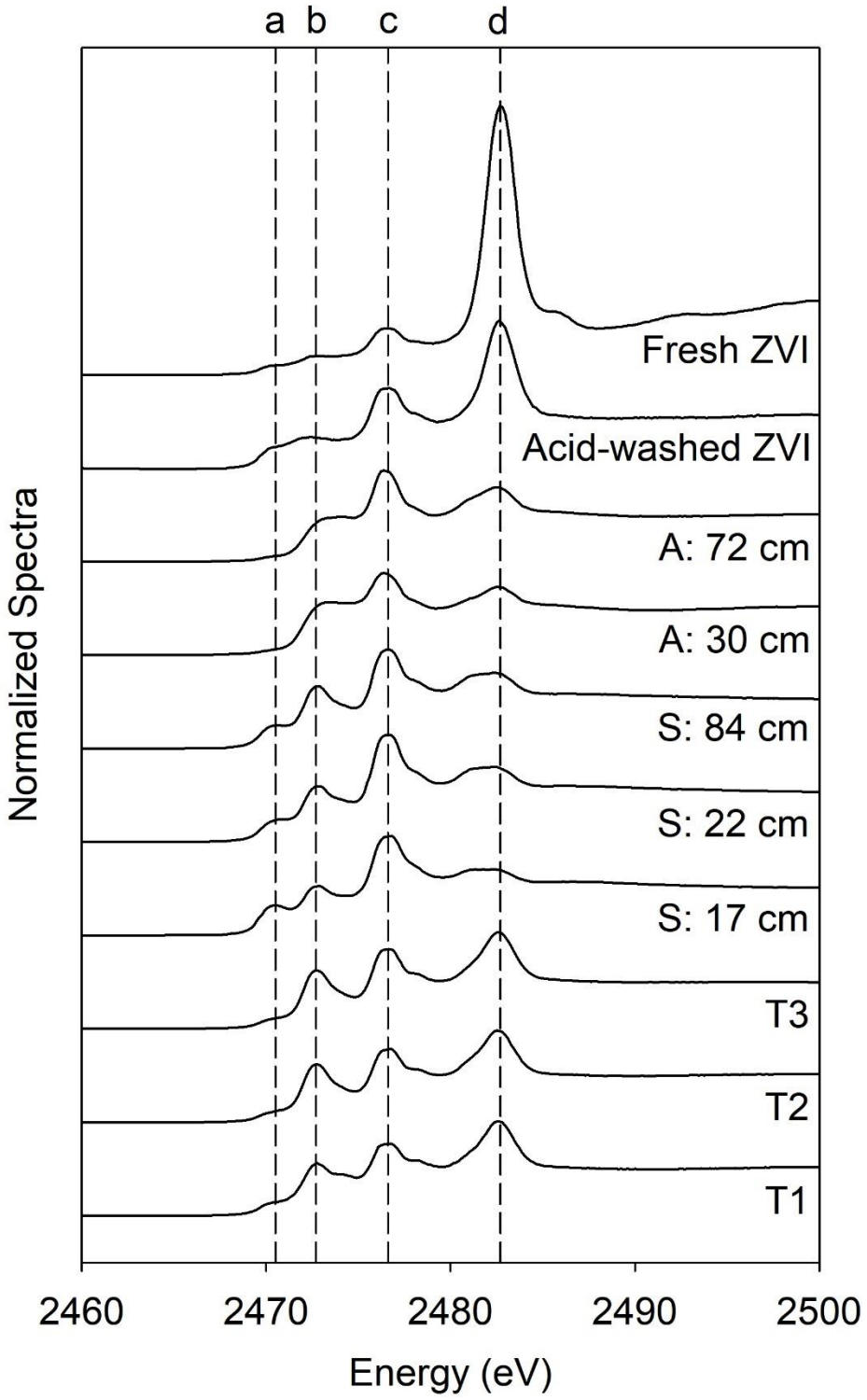

Figure 4.11 Bulk S XANES spectra of solid samples collected from the autumn reaction cell (W), summer reaction cell (S; Chapter 3), and laboratory column experiments (T; Chapter 2). The number (cm) represents the distance from the influent end of the cell. Unreacted untreated ZVI and acid-washed ZVI are also plotted. Dashed lines represent peak locations for pyrrhotite/FeS (a), pyrite (b), tetramethylene sulfoxide (c), and gypsum (d).

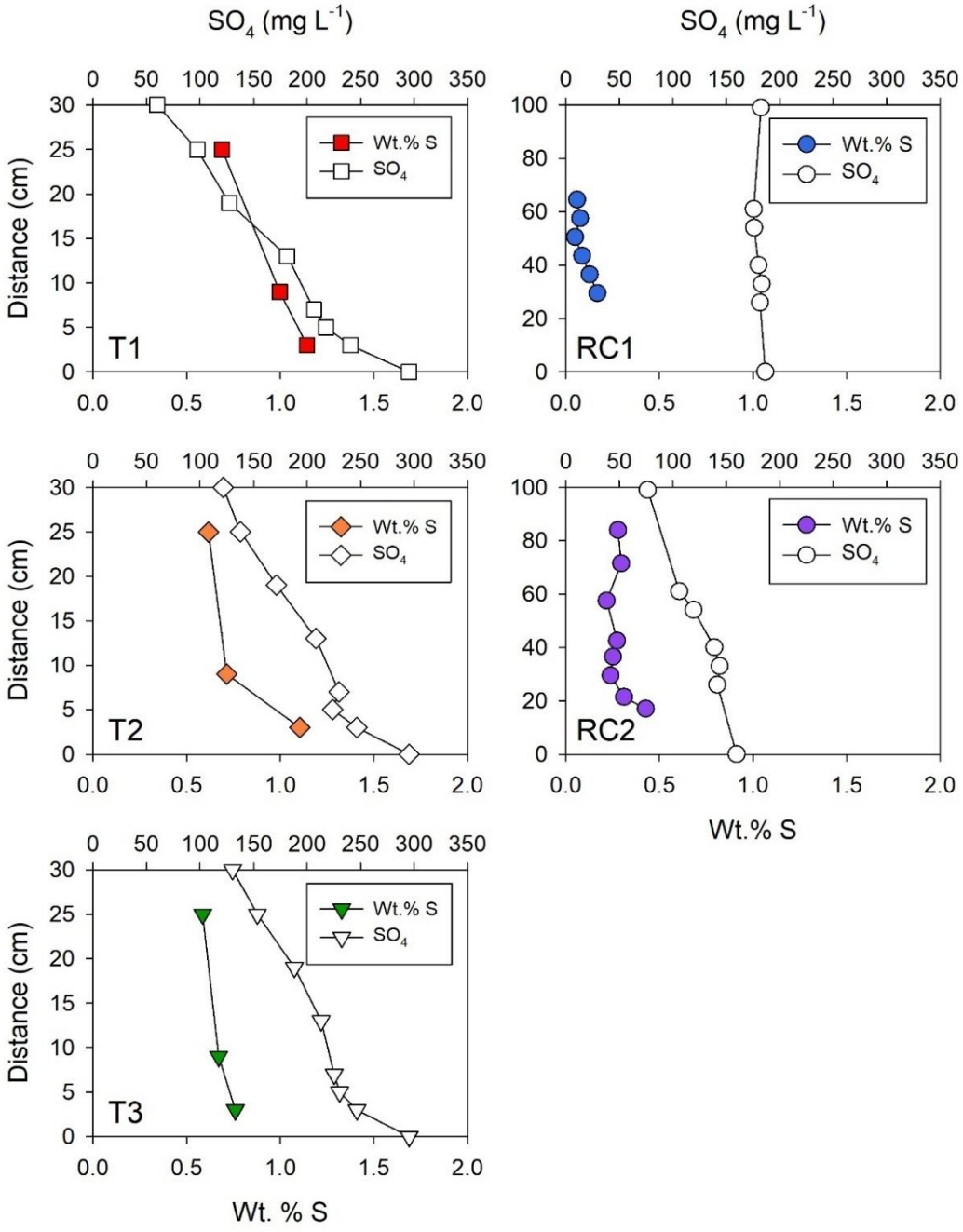

Figure 4.12 Comparison of the wt. % S in the solid material and aqueous SO_4 concentrations for the autumn reaction cell (RC1, top right), summer reaction cell (RC2, bottom right; Chapter 3), and laboratory column experiments (T1, T2, T3, left; Chapter 2), collected along the cell/column length. Distance 0 cm represents influent concentrations and 100 cm or 30 cm represents effluent concentrations.

Table 4.1 Comparison of average flow rate and residence time for the laboratory and field studies.

Name	Average Flow Rate (mL h^{-1})	Residence Time (d)
Autumn Cell	490[a]	2.42
Summer Cell[b]	960	1.14
Laboratory Column[c]	3.4	4.59

[a] *Freezing of the cell may have affected the flow rate and residence time.*
[b] *From Chapter 3*
[c] *From Chapter 2*

Table 4.2 Comparison of the mean chemical compositions of the influent solution[a].

Parameter	Autumn Cell	Summer Cell	Laboratory Columns
pH	3.78	3.48	3.50
Eh (mV)	480	500	420
Alk (mg L^{-1} as $CaCO_3$)	< 1	< 1	< 1
As (mg L^{-1})	2.5	1.1	6.2
Mn (mg L^{-1})	0.70	0.41	0.66
Cl (mg L^{-1})	24.4	0.20	0.40
NO_3-N (mg L^{-1})	0.03	0.02	0.05
SO_4^{2-} (mg L^{-1})	166	137	214
Ca (mg L^{-1})	24.6	15.0	25.4
K (mg L^{-1})	1.3	1.6	1.5
Mg (mg L^{-1})	12.1	7.3	12.0
Na (mg L^{-1})	6.9	6.7	10.2
Si (mg L^{-1})	20.8	22.8	22.8
Fe (mg L^{-1})	9.3	17.7	52.3
Al (mg L^{-1})	8.3	3.4	6.9
Cu (mg L^{-1})	0.11	0.07	0.14
Ni (mg L^{-1})	0.22	0.13	0.23
Zn (mg L^{-1})	0.27	0.26	0.27

[a] *Sample sizes: Autumn cell (n=2), Summer cell (n=10), Laboratory columns (n=23).*
[b] *From Chapter 3*
[c] *From Chapter 2*

Table 4.3 Chemical characteristics of reacted and unreacted solid organic carbon substrates on a dry wt. % basis.

Property	Unreacted Wood Chips	Unreacted Leaf Compost
Crude Protein (%)	4.7	8.7
Acid Detergent Fiber, ADF (%)	52.7	44.9
Neutral Detergent Fiber, NDF (%)	70.2	61.2
Lignin (%)	16.9	18.6
Cellulose (%)	35.8	26.2
Hemi-cellulose (%)	17.5	16.4
(C+H)/L Degree of Biodegradability	3.2	2.3
C:N Ratio	53.8	28.8

Chapter 5: *Conclusions and Recommendations*

The remediation of abandoned mine sites is challenging due to the long duration of release of acidic, metal-rich groundwater and the large-scale of mining wastes. At the Long Lake Au Mine, the limited implementation of mitigation techniques resulted in the migration of tailings into the adjacent Long Lake and the continued persistence of acidic conditions and high concentrations of arsenic (As), Fe, metals, and sulfate (SO_4^{2-}), in the tailings pore water and groundwater. The laboratory column experiments demonstrated the potential for a reactive mixture, containing zero-valent iron (ZVI), organic carbon (OC), limestone, and silica sand, to remove dissolved As and metals from the Long Lake groundwater. A summer reaction cell implemented at the Long Lake site indicated the ability of this material to treat contaminated water under field conditions, including daily temperature fluctuations and more rapid flow rates. An autumn reaction cell demonstrated the effect of colder temperatures encountered at the Long Lake site, including below-freezing conditions.

In the laboratory columns, the addition of OC to the reactive mixture enhanced the growth and activity of sulfate-reducing bacteria (SRB) and the development of sulfate-reducing conditions. Column T0, containing a minimal amount of OC, showed removal of metals including Al, Cu, Ni, and Zn, but only limited removal of As and SO_4^{2-} occurred. Extensive removal of dissolved As, metals, and SO_4^{2-} was observed in the other columns. Determination of SO_4^{2-} removal rates indicates that above 20 wt. % OC, there is no additional benefit to increasing the OC content. Decreases in concentrations of As, Fe, and other metals was accompanied by the accumulation of secondary sulfide phases. Arsenic was likely removed through precipitation as an As-sulfide phase such as realgar and orpiment, or adsorption as As(V) onto ferrihydrite.

The addition of ZVI resulted in the accumulation of Fe corrosion products, including ferrihydrite and goethite, in the column material. These reaction products provide additional surfaces for As adsorption and subsequent As immobilization. Greater proportions of ZVI in the reactive mixture increased pH values in the column effluents. Iron concentrations in the column effluents were high at the onset of the experiment, but decreased as the experiment progressed. Iron-reducing bacteria may have contributed to initial increases in Fe concentrations through the reductive dissolution of Fe (oxy)hydroxides. The varying percentages of ZVI (10 – 30 wt. %) did not affect SO_4^{2-} removal rates. Lower effluent concentrations of dissolved Fe were observed for

columns containing greater masses of ZVI. Similar declines in Al, As, Cu, Ni, and Zn concentrations were observed in all three treatment columns despite the varying percentages of OC and ZVI.

Despite differences in temperature and flow rate in the field reaction-cell experiments, the removal of As and metals, an increase in pH, a decrease in Eh, the generation of alkalinity, and the presence of SRB communities, were similar to the laboratory column experiments. The decrease in SO_4^{2-} concentrations was more clearly observed in the summer cell and column experiments than in the autumn cell. This difference is attributed the effect of low temperatures on the development of sulfate-reducing conditions. It is likely that SO_4^{2-} reduction occurred, but rates were too low to be determined. Lower Fe concentrations were observed in the reaction cell effluents compared to the column effluents; this difference may be attributed to the use of acid-washed ZVI as opposed to the untreated ZVI.

Differences in major SRB genera were observed in all three experiments and may be attributed to changing temperatures or the limited development of sulfate-reducing conditions in the autumn field trial. In addition, concentrations of nutrients (NH_3-N, PO_4-P) were lower in the reaction cell effluents than in the column effluents. This difference may be due to a decreased rate of OC decomposition at the lower and more variable field temperatures (Kirschbaum, 1995).

Solid-phase characterization of the reactive material indicated that similar removal processes occurred in all the experiments. Metal sulfide and Fe (oxy)hydroxide formation, replacement of cellular organic matter by a secondary Fe-sulfide precipitate, and development of alteration rims around ZVI grains, were observed in thin sections under optical microscopy. Geochemical modelling indicated conditions favourable for the formation of metal sulfides, including mackinawite ($(Fe,Ni)_{1+x}S$), pyrite (FeS_2), chalcopyrite ($CuFeS_2$), and sphalerite ((Zn, Fe)S); the removal of Fe, Cu, Ni, and Zn was attributed to the precipitation of these, and other, metal sulfides or less-crystalline precursors. The precipitation of As-sulfides was not favoured, however precipitation may have occurred prior to the first sampling port in all three experiments. Synchrotron-radiation As μXANES indicated that As was present in secondary precipitates in the reactive material. Both oxidized and reduced forms of As were observed; reduced As was present as As-sulfide minerals including realgar (AsS), orpiment (As_2S_3), and arsenopyrite (FeAsS), and oxidized As was present as arsenate sorbed onto ferrihydrite. Bulk S XANES

analyses indicated that reduced S phases (pyrite and elemental S) accumulated in the solid material during all the experiments, but was limited in the autumn reaction cell. The accumulation of sulfides is consistent with the results from geochemical modeling, microbiology, and aqueous chemistry.

The results from these three studies indicate some factors that may improve the effectiveness of a passive barrier installation at the Long Lake site. First, lower Fe concentrations in the effluent could be achieved by using acid-washed ZVI in the reactive mixture as opposed to untreated ZVI. The results from the autumn cell indicate the importance of ZVI for the removal of As and metals from the groundwater under limited sulfate-reducing conditions. The addition of ZVI may also assist in sustaining reactive material longevity after the OC in the reactive mixture becomes limited (Lindsay, 2009). Despite the varying percentages of ZVI used in the column experiments, no major difference was observed in the decrease of As, metals or SO_4^{2-} concentrations. Second, installation of the barrier should be conducted during the summer or spring when warmer temperatures may contribute to the rapid development of sulfate-reducing conditions and aid in the removal of aqueous SO_4^{2-}. In addition, SRB can adapt to new temperature conditions and may tolerate a wide range of temperatures (Postgate, 1984; Waybrant et al., 1998) suggesting that, given the initial development of sulfate-reducing conditions during the warmer season, these conditions are likely to continue throughout the colder months. Installation of the barrier below ground would also moderate temperatures. Overall, the initial goal, to decrease As concentrations and neutralize acidic conditions in the groundwater, was achieved in all the experiments.

The results from all three experiments demonstrate the potential for the reactive material to remove dissolved As and metals from groundwater at the Long Lake Au mine. Potential next steps include the installation of a pilot-scale PRB. A better understanding of the site is required prior to installation including: the groundwater flow system in the tailings and the underlying aquifer, the variability of mass loading of As and metals throughout the year, the stability of secondary precipitates accumulated in the reactive material, the possibility for remobilization of As and metals, and the longevity of the reactive material. However, results from these experiments indicate the potential for a passive barrier technology to remove As and metals at the Long Lake mine site. These results also suggest that a mixture containing ZVI and OC may

effectively remove As from water at other mine sites with similar aqueous chemistry and geochemical conditions.

References

Achá, D., Iñiguez, V., Roulet, M., Remy, J., Guimarães, D., Luna, R., Alanoca, L., & Sanchez, S. (2005). Sulfate-reducing bacteria in floating macrophyte rhizospheres from an amazonian floodplain lake in Bolivia and their association with Hg methylation. *Applied and Environmental Microbiology*, *71*(11), 7531–7535. https://doi.org/10.1128/AEM.71.11.7531-7535.2005

Altun, M., Sahinkaya, E., Durukan, I., Bektas, S., & Komnitsas, K. (2014). Arsenic removal in a sulfidogenic fixed-bed column bioreactor. *Journal of Hazardous Materials*, *269*, 31–37. https://doi.org/10.1016/j.jhazmat.2013.11.047

Amos, R. T., Mayer, K. U., Blowes, D. W., & Ptacek, C. J. (2004). Reactive transport modeling of column experiments for the remediation of acid mine drainage. *Environmental Science and Technology*, *38*(11), 3131–3138. https://doi.org/10.1021/es0349608

Asmussen, G., & Strauch, G. (1998). Sulfate reduction in a lake and the groundwater of a former lignite mining area studied by stable sulfur and carbon isotopes. *Water, Air, and Soil Pollution*, *108*(3–4), 271–284.

Bain, J., Blowes, D. W., & Wilkens, J. A. (2009). Evaluation of the treatment of groundwater arsenic at mining and industrial sites using ZVI and BOFS permeable reactive barriers. *Proceedings of Securing the Future and 8th ICARD*.

Bain, J., Spink, L., Blowes, D. W., & Smyth, D. (2002). The removal of arsenic from groundwater using permeable reactive materials. *9th International Conference on Tailings and Mine Waste*, 213–216.

Ball, J. W., & Nordstrom, D. K. (1991). User's manual for WATEQ4F, with revised thermodynamic data base and test cases for calulcating speciation of major, trace, and redox elements in natural waters. *U.S. Geological Survey*. https://doi.org/10.3133/ofr91183

Bang, S., Korfiatis, G. P., & Meng, X. (2005). Removal of arsenic from water by zero-valent iron. *Journal of Hazardous Materials*, *121*(1–3), 61–67. https://doi.org/10.1016/j.jhazmat.2005.01.030

Beaulieu, B., & Ramirez, R. E. (2013). Arsenic remediation field study using a sulfate reduction and zero-valent iron PRB. *Groundwater Monitoring and Remediation*, *33*(2), 85–94. https://doi.org/10.1111/gwmr.12007

Benner, S. G., Blowes, D. W., Gould, W. D., Herbert Jr., R. B., & Ptacek, C. J. (1999). Geochemistry of a permeable reactive barrier for metals and acid mine drainage. *Environmental Science and Technology*, *33*(16), 2793–2799. https://doi.org/10.1021/es981040u

Benner, S. G., Blowes, D. W., & Ptacek, C. J. (1997). A full-scale porous reactive wall for prevention of acid mine drainage. *Groundwater Monitoring and Remediation*, *17*(4), 99–107.

Benner, S. G., Blowes, D. W., Ptacek, C. J., & Mayer, K. U. (2002). Rates of sulfate reduction and metal sulfide precipitation in a permeable reactive barrier. *Applied Geochemistry*, *17*(3),

301–320. https://doi.org/10.1016/S0883-2927(01)00084-1

Biterna, M., Antonoglou, L., Lazou, E., & Voutsa, D. (2010). Arsenite removal from waters by zero valent iron: Batch and column tests. *Chemosphere*, *78*(1), 7–12. https://doi.org/10.1016/j.chemosphere.2009.10.007

Biterna, M., Arditsoglou, A., Tsikouras, E., & Voutsa, D. (2007). Arsenate removal by zero valent iron: Batch and column tests. *Journal of Hazardous Materials*, *149*(3), 548–552. https://doi.org/10.1016/j.jhazmat.2007.06.084

Blowes, D. W., & Jambor, J. L. (1990). The pore-water geochemistry and the mineralogy of the vadose zone. *Applied Geochemistry*, *5*, 327–346. https://doi.org/10.1016/0883-2927(90)90008-S

Blowes, D. W., Ptacek, C. J., Benner, S. G., McRae, C. W. T., Bennett, T. A., & Puls, R. W. (2000). Treatment of inorganic contaminants using permeable reactive barriers. *Journal of Contaminant Hydrology*, *45*(1–2), 123–137. https://doi.org/10.1016/S0169-7722(00)00122-4

Blowes, D. W., Ptacek, C. J., Benner, S. G., Waybrant, K. R., & Bain, J. G. (1998). Porous reactive walls for the prevention of acid mine drainage: a review. *Mineral Processing and Extractive Metallurgy Review*, *19*(1), 25–37. https://doi.org/10.1080/08827509608962426

Blowes, D. W., Ptacek, C. J., Jambor, J. L., Weisener, C. G., Paktunc, D., Gould, W. D., & Johnson, D. B. (2014). The geochemistry of acid mine drainage. In H. D. Holland & K. K. Turekian (Eds.), *Treatise on Geochemistry: Second Edition* (Vol. 11). Elsevier Science. https://doi.org/10.1016/B978-0-08-095975-7.00905-0

Bowell, R. J. (1994). Sorption of arsenic by iron oxides and oxyhydroxides in soils. *Applied Geochemistry*, *9*, 279–286. https://doi.org/10.1016/0883-2927(94)90038-8

Brock, F., Parkes, R. J., & Briggs, D. E. G. (2006). Experimental pyrite formation associated with decay of plant material. *Palaios*, *21*(5), 499–506. https://doi.org/10.2110/palo.2005.p05-077r

CH2MHill. (2014). *Site Characterization Report and Data Analysis – Long Lake Gold Mine Tailings Areas, Eden Township, Ontario*.

Clark, S. K., & Johnson, T. M. (2008). Effective isotopic fractionation factors for solute removal by reactive sediments: A laboratory microcosm and slurry study. *Environmental Science and Technology*, *42*(21), 7850–7855. https://doi.org/10.1021/es801814v

Cochran, W. G. (1950). Estimation of bacterial densities by means of the "most probable number." *Biometrics*, *6*(2), 105–116. https://www.jstor.org/stable/3001491

Dworkin, M., Falkow, S., Rosenberg, E., Schleifer, K., & Stackebrandt, E. (2006). *The prokaryotes third edition*. https://doi.org/10.1007/0-387-30744-3

Evangelou, V. P., & Zhang, Y. L. (1995). A review: Pyrite oxidation mechanisms and acid mine drainage prevention. *Critical Reviews in Environmental Science and Technology*, *25*(2), 141–199. https://doi.org/10.1080/10643389509388477

Fendorf, S., Michael, H. A., & Van Geen, A. (2010). Spatial and temporal variations of groundwater arsenic in south and southeast asia. *Science*, *328*(5982), 1123–1127. http://science.sciencemag.org/

Fleet, M. E. (2005). XANES spectroscopy of sulfur in earth materials. *The Canadian Mineralogist*, *43*(6), 1811–1838.

Foster, A. L., & Kim, C. S. (2014). Arsenic speciation in solids using X-ray absorption spectroscopy. *Reviews in Mineralogy & Geochemistry*, *79*, 257–369. https://doi.org/10.2138/rmg.2014.79.5

Gibert, O., De Pablo, J., Cortina, J. L., & Ayora, C. (2003). Evaluation of municipal compost/limestone/iron mixtures as filling material for permeable reactive barriers for in-situ acid mine drainage treatment. *Journal of Chemical Technology and Biotechnology*, *78*(5), 489–496. https://doi.org/10.1002/jctb.814

Gibert, O., De Pablo, J., Cortina, J. L., & Ayora, C. (2005). Municipal compost-based mixture for acid mine drainage bioremediation: Metal retention mechanisms. *Applied Geochemistry*, *20*(9), 1648–1657. https://doi.org/10.1016/j.apgeochem.2005.04.012

Gibert, O., De Pablo, J., Cortina, J. L., & Ayora, C. (2010). In situ removal of arsenic from groundwater by using permeable reactive barriers of organic matter/limestone/zero-valent iron mixtures. *Environmental Geochemistry and Health*, *32*(4), 373–378. https://doi.org/10.1007/s10653-010-9290-1

Gibert, Oriol, De Pablo, J., Luis Cortina, J., & Ayora, C. (2004). Chemical characterisation of natural organic substrates for biological mitigation of acid mine drainage. *Water Research*, *38*(19), 4186–4196. https://doi.org/10.1016/j.watres.2004.06.023

Gould, J. P. (1982). The kinetics of hexavalent chromium reduction by metallic iron. *Water Research*, *16*(6), 871–877. https://doi.org/10.1016/0043-1354(82)90016-1

Gould, W. D., Stichbury, M., Francis, M., Lortie, L., & Blowes, D. W. (2003). An MPN method for enumeration of iron-reducing bacteria. *Mining and the Environment Conference*.

Gu, B., Phelps, T. J., Liang, L., Dickey, M. J., Roh, Y., Kinsall, B. L., Palumbo, A. V., & Jacobs, G. K. (1999). Biogeochemical dynamics in zero-valent iron columns: Implications for permeable reactive barriers. *Environmental Science and Technology*, *33*(13), 2170–2177. https://doi.org/10.1021/es981077e

Guo, Q., & Blowes, D. W. (2009). Biogeochemistry of two types of permeable reactive barriers, organic carbon and iron-bearing organic carbon for mine drainage treatment: Column experiments. *Journal of Contaminant Hydrology*, *107*(3–4), 128–139. https://doi.org/10.1016/j.jconhyd.2009.04.008

Hashim, M. A., Mukhopadhyay, S., Sahu, J. N., & Sengupta, B. (2011). Remediation technologies for heavy metal contaminated groundwater. *Journal of Environmental Management*, *92*(10), 2355–2388. https://doi.org/10.1016/j.jenvman.2011.06.009

Herbert Jr, R. B., Benner, S. G., & Blowes, D. W. (2000). Solid phase iron-sulfur geochemistry of a reactive barrier for treatment of mine drainage. *Applied Geochemistry*, *15*(9), 1331–1343. https://doi.org/10.1016/S0883-2927(00)00005-6

Jambor, J. L., Raudsepp, M., & Mountjoy, K. (2005). Mineralogy of permeable reactive barriers for the attenuation of subsurface contaminants. *Canadian Mineralogist*, *43*(6), 2117–2140. https://doi.org/10.2113/gscanmin.43.6.2117

Jeen, S. W., Jambor, J. L., Blowes, D. W., & Gillham, R. W. (2007). Precipitates on granular iron in solutions containing calcium carbonate with trichloroethene and hexavalent chromium. *Environmental Science and Technology*, *41*(6), 1989–1994. https://doi.org/10.1021/es0618393

Jurjovec, J., Ptacek, C. J., & Blowes, D. W. (2002). Acid neutralization mechanisms and metal release in mine tailings: A laboratory column experiment. *Geochimica et Cosmochimica Acta*, *66*(9), 1511–1523. https://doi.org/10.1016/S0016-7037(01)00874-2

Kirschbaum, M. U. F. (1995). The temperature dependence of soil organic matter decomposition, and the effect of global warming on soil organic C storage. *Soil Biology and Biochemistry*, *27*(6), 753–760. https://doi.org/10.1016/0038-0717(94)00242-S

Kozich, J. J., Westcott, S. L., Baxter, N. T., Highlander, S. K., & Schloss, P. D. (2013). Development of a Dual-Index Sequencing Strategy and Curation Pipeline for Analyzing Amplicon Sequence Data on the MiSeq Illumina Sequencing Platform. *Applied and Environmental Microbiology*, *79*(17), 5112–5120. https://doi.org/10.1128/AEM.01043-13

Kuever, J., Rainey, F. A., & Widdel, F. (2005). Class IV. Deltaproteobacteriaclass nov. In D. J. Brenner, N. R. Krieg, & J. T. Staley (Eds.), *Bergey's Manual® of Systematic Bacteriology: Volume Two The Proteobacteria Part C The Alpha-, Beta-, Delta-, and Epsilonproteobacteria* (pp. 922–1144). Springer US. https://doi.org/10.1007/978-0-387-29298-4_3

Leupin, O. X., & Hug, S. J. (2005). Oxidation and removal of arsenic (III) from aerated groundwater by filtration through sand and zero-valent iron. *Water Research*, *39*(9), 1729–1740. https://doi.org/10.1016/j.watres.2005.02.012

Lien, H. L., & Wilkin, R. T. (2005). High-level arsenite removal from groundwater by zero-valent iron. *Chemosphere*, *59*(3), 377–386. https://doi.org/10.1016/j.chemosphere.2004.10.055

Lindsay, M. B. J. (2009). *Passive In Situ Treatment of Acidic and Neutral Mine Drainage: Field and Laboratory Investigations*. Ph.D Thesis, University of Waterloo, Waterloo, Ontario, Canada.

Lindsay, M. B. J., Blowes, D. W., Condon, P. D., & Ptacek, C. J. (2009). Managing pore-water quality in mine tailings by inducing microbial sulfate reduction. *Environmental Science and Technology*, *43*(18), 7086–7091. https://doi.org/10.1021/es901524z

Lindsay, M. B. J., Blowes, D. W., Condon, P. D., & Ptacek, C. J. (2011). Organic carbon amendments for passive in situ treatment of mine drainage: Field experiments. *Applied Geochemistry*, *26*(70), 1169–1183. https://doi.org/10.1016/j.apgeochem.2011.04.006

Lindsay, M. B. J., Blowes, D. W., Ptacek, C. J., & Condon, P. D. (2011). Transport and attenuation of metal(loid)s in mine tailings amended with organic carbon: Column experiments. *Journal of Contaminant Hydrology*, *125*(1–4), 26–38.

https://doi.org/10.1016/j.jconhyd.2011.04.004

Lindsay, M. B. J., Ptacek, C. J., Blowes, D. W., & Gould, W. D. (2008). Zero-valent iron and organic carbon mixtures for remediation of acid mine drainage: Batch experiments. *Applied Geochemistry*, *23*(8), 2214–2225. https://doi.org/10.1016/j.apgeochem.2008.03.005

Liu, Y. Y., Ptacek, C. J., & Blowes, D. W. (2014). Treatment of dissolved perchlorate, nitrate, and sulfate using zero-valent iron and organic carbon. *Journal of Environmental Quality*, *43*(3), 842–850. https://doi.org/10.2134/jeq2013.03.0077

Londry, K. L., & Des Marais, D. J. (2003). Stable carbon isotope fractionation by sulfate-reducing bacteria. *Applied and Environmental Microbiology*, *69*(5), 2942–2949. https://doi.org/10.1128/AEM.69.5.2942-2949.2003

Lovley, D. R., & Phillips, E. J. P. (1988). Novel mode of microbial energy metabolism: organic carbon oxidation coupled to dissimilatory reduction of iron or manganese. *Applied and Environmental Microbiology*, *54*(6), 1472–1480. http://aem.asm.org/

Lovley, D. R., & Phillips, E. J. P. (1994). Novel processes for anaerobic sulfate production from elemental sulfur by sulfate-reducing bacteria. *Applied and Environmental Microbiology*, *60*(7), 2394–2399. http://aem.asm.org/

Ludwig, R. D., McGregor, R. G., Blowes, D. W., Benner, S. G., & Mountjoy, K. (2002). A permeable reactive barrier for treatment of heavy metals. *Ground Water*, *40*(1), 59–66. https://doi.org/10.1111/j.1745-6584.2002.tb02491.x

Ludwig, R. D., Smyth, D. J. A., Blowes, D. W., Spink, L. E., Wilkin, R. T., Jewett, D. G., & Weisener, C. J. (2009). Treatment of arsenic, heavy metals, and acidity using a mixed ZVI-compost PRB. *Environmental Science and Technology*, *43*(6), 1970–1976. https://doi.org/10.1021/es802394p

Macy, J. M., Santini, J. M., Pauling, B. V., O'Neill, A. H., & Sly, L. I. (2000). Two new arsenate/sulfate-reducing bacteria: mechanisms of arsenate reduction. *Archives of Microbiology*, *173*(1), 49–57. https://doi.org/10.1007/s002030050007

Manning, B., Hunt, M., Amrhein, C., & Yarmoff, J. (2002). Arsenic(III) and arsenic(V) reactions with zerovalent iron corrosion products. *Environmental Science and Technology*, *36*(24), 5455–5461. https://doi.org/10.1021/es0206846

McCreadie, H., Blowes, D. W., Ptacek, C. J., & Jambor, J. L. (2000). Influence of reduction reactions and solid-phase composition on porewater concentrations of arsenic. *Environmental Science and Technology*, *34*(15), 3159–3166. https://doi.org/10.1021/es991194p

MNDM. (2017). *Category C Environmental Assessment - Long Lake Gold Mine Rehabilitation Project Geographic Township of Eden, Ontario*.

Moncur, M. C., Ptacek, C. J., Blowes, D. W., & Jambor, J. L. (2005). Release, transport and attenuation of metals from an old tailings impoundment. *Applied Geochemistry*, *20*(3), 639–659. https://doi.org/10.1016/j.apgeochem.2004.09.019

Mullet, M., Boursiquot, S., Abdelmoula, M., Génin, J. M., & Ehrhardt, J. J. (2002). Surface

chemistry and structural properties of mackinawite prepared by reaction of sulfide ions with metallic iron. *Geochimica et Cosmochimica Acta*, *66*(5), 829–836. https://doi.org/10.1016/S0016-7037(01)00805-5

Nakai, N., & Jensen, M. L. (1964). The kinetic isotope effect in the bacterial reduction and oxidation of sulfur. *Geochimica et Cosmochimica Acta*, *28*(12), 1893–1912. https://doi.org/10.1016/0016-7037(64)90136-X

Nielsen, M. B., Kjeldsen, K. U., & Ingvorsen, K. (2006). Desulfitibacter alkalitolerans gen. nov., sp. nov., an anaerobic, alkalitolerant, sulfite-reducing bacterium isolated from a district heating plant. *International Journal of Systematic and Evolutionary Microbiology*, *56*(12), 2831–2836. https://doi.org/10.1099/ijs.0.64356-0

Nordstrom, D. K. (2002). Worldwide cccurrences of arsenic in ground water. *Science*, *296*(5576), 2143–2145. https://doi.org/10.1126/science.1072375

Nordstrom, D. K., & Campbell, K. M. (2002). Arsenic speciation and sorption in natural environments. *Reviews in Mineralogy and Geochemistry*, *79*(3), 185–216. https://doi.org/10.1177/109625060200500303

Obiri-Nyarko, F., Grajales-Mesa, S. J., & Malina, G. (2014). An overview of permeable reactive barriers for in situ sustainable groundwater remediation. *Chemosphere*, *111*, 243–259. https://doi.org/10.1016/j.chemosphere.2014.03.112

Okabe, S., Itoh, T., Satoh, H., & Watanabe, Y. (1999). Analyses of spatial distributions of sulfate-reducing bacteria and their activity in aerobic wastewater biofilms. *Applied and Environmental Microbiology*, *65*(11), 5107–5116. https://doi.org/10.1128/AEM.65.11.5107-5116.1999

Omoregie, E. O., Couture, R.-M., Cappellen, P. Van, Corkhill, C. L., Charnock, J. M., Polya, D. A., Vaughan, D., Vanbroekhoven, K., & Lloyd, J. R. (2013). Arsenic bioremediation by biogenic iron oxides and sulfides. *Applied and Environmental Microbiology*, *79*(14), 4325–4335. https://doi.org/10.1128/AEM.00683-13

Paulson, K. M. A., Ptacek, C. J., Blowes, D. W., Gould, W. D., Ma, J., Landis, R. C., & Dyer, J. A. (2018). Role of organic carbon sources and sulfate in controlling net methylmercury production in riverbank sediments of the South River, VA (USA). *Geomicrobiology Journal*, *35*(1), 1–14. https://doi.org/10.1080/01490451.2016.1247483

Pedersen, H. D., Postma, D., & Jakobsen, R. (2006). Release of arsenic associated with the reduction and transformation of iron oxides. *Geochimica et Cosmochimica Acta*, *70*(16), 4116–4129. https://doi.org/10.1016/j.gca.2006.06.1370

Pfennig, N., & Biebl, H. (1976). Desulfuromonas acetoxidans gen. nov. and sp. nov., a new anaerobic, sulfur-reducing, acetate-oxidizing bacterium. *Archives of Microbiology*, *110*(1), 3–12. https://doi.org/10.1007/BF00416962

Postgate, J. R. (1984). *The Sulphate-Reducing Bacteria, 2nd Ed.* Cambridge University Press, Cambridge.

Powell, R. M., Puls, R. W., Blowes, D. W., Vogan, J. L., Gillham, R. W., Powell, P. D., Schultz, D., Landis, R., & Sivavec, T. (1998). *Permeable reactive barrier technologies for*

contaminant remediation: Vol. US EPA, 60. https://doi.org/10.1007/s002280050316

Rao, P., Mak, M. S. H., Liu, T., Lai, K. C. K., & Lo, I. M. C. (2009). Effects of humic acid on arsenic(V) removal by zero-valent iron from groundwater with special references to corrosion products analyses. *Chemosphere*, *75*(2), 156–162. https://doi.org/10.1016/j.chemosphere.2008.12.019

Ravel, B., & Newville, M. (2005). Synchrotron radiation ATHENA, ARTEMIS, HEPHAESTUS: data analysis for X-ray absorption spectroscopy using IFEFFIT. *Journal of Synchrotron Radiation*, *12*, 537–541. https://doi.org/10.1107/S0909049505012719

Richards, D. J., Ivanova, L. K., Smallman, D. J., & Zheng, B. (2005). Assessment of waste degradation using acid digestible fibre analysis. *International Workshop Hydro-Physico-Mechanics of Landfills. LIRIGM, Grenoble*, *1*, 1–5. https://www.researchgate.net/publication/267304077

Rikihisa, Y., Stephen Dumler, J., & Dasch, G. A. (2015). *Bergey's Manual of Systematics Bacteriology*. https://doi.org/10.1002/9781118960608.gbm00905

Schloss, P. D., Westcott, S. L., Ryabin, T., Hall, J. R., Hartmann, M., Hollister, E. B., Lesniewski, R. A., Oakley, B. B., Parks, D. H., Robinson, C. J., Sahl, J. W., Stres, B., Thallinger, G. G., Van Horn, D. J., & Weber, C. F. (2009). Introducing mothur: Open-Source, Platform-Independent, Community-Supported Software for Describing and Comparing Microbial Communities. *Applied and Environmental Microbiology*, *75*(23), 7537–7541. https://doi.org/10.1128/AEM.01541-09

Senko, J. M., Zhang, G., Mcdonough, J. T., Bruns, M. A., & Burgos, W. D. (2009). Metal reduction at low pH by a Desulfosporosinus species: implications for the biological treatment of acidic mine drainage. *Geomicrobiology Journal*, *26*(2), 71–82. https://doi.org/10.1080/01490450802660193

Simunek, J., Van Genuchten, M. T., Sejna, M., Toride, N., & Leij, F. J. (1999). *The STANMOD computer software for evaluating solute transport in porous media using analytical solutions of convection-dispersion equation versions 1.0 and 2.0*.

Smedley, P. L., & Kinniburgh, D. G. (2002). A review of the source, behaviour and distribution of arsenic in natural waters. *Applied Geochemistry*, *17*(5), 517–568. https://doi.org/10.1016/S0883-2927(02)00018-5

Smedley, P. L., & Kinniburgh, D. G. (2013). Arsenic in groundwater and the environment. In *Essentials of medical geology* (pp. 279–310). Springer, Dordecht. https://doi.org/10.1007/978-94-007-4375-5_12

Sprague, D. D., Michel, F. A., & Vermaire, J. C. (2016). The effects of migration on ca. 100-year-old arsenic-rich mine tailings in Cobalt, Ontario, Canada. *Environmental Earth Sciences*, *75*(5), 1–12. https://doi.org/10.1007/s12665-015-4898-1

Steger, J. L., Vincent, C., Ballard, J. D., & Krumholz, L. R. (2002). Desulfovibrio sp. Genes Involved in the Respiration of Sulfate during Metabolism of Hydrogen and Lactate Downloaded from. *Applied and Environmental Microbiology*, *68*(4), 1932–1937. https://doi.org/10.1128/AEM.68.4.1932-1937.2002

Stichbury, M. K. (2000). *Mechanisms of Release and Attenuation of Arsenic in Gold Mine Tailings, Campbell Mine, Balmertown, Ontario*. M.Sc. Thesis, University of Waterloo, Waterloo, Ontario, Canada.

Stookey, L. L. (1970). Ferrozine - a new spectrophotometric reagent for iron. *Analytical Chemistry*, *42*(7), 779–781. https://doi.org/10.1021/ac60289a016

Su, C., & Puls, R. W. (2001). Arsenate and arsenite removal by zerovalent iron: Kinetics, redox transformation, and implications for in situ groundwater remediation. *Environmental Science and Technology*, *35*(7), 1487–1492. https://doi.org/10.1021/es001607i

Thamdrup, B., Finster, K., Hansen, J. W., & Bak, F. (1993). Bacterial disproportionation of elemental sulfur coupled to chemical reduction of iron or manganese. *Applied and Environmental Microbiology*, *59*(1), 101–108. http://aem.asm.org/

Toride, N., Leij, F. J., & Van Genuchten, M. T. (1995). *The CXTFIT code for estimating transport parameters from laboratory or field tracer experiments version 2.0*.

Vandieken, V., Mußmann, M., Niemann, H., & Jørgensen, B. B. (2006). Desulfuromonas svalbardensis sp. nov. and Desulfuromusa ferrireducens sp. nov., psychrophilic, Fe(III)-reducing bacteria isolated from Arctic sediments, Svalbard. *International Journal of Systematic and Evolutionary Microbiology*, *56*(5), 1133–1139. https://doi.org/10.1099/ijs.0.63639-0

Verbuyst, B. R. (2020). *Evaluating Controls on Arsenic Geochemistry at the Long Lake Gold Mine in Sudbury, ON*. M.Sc. Thesis, University of Waterloo, Waterloo, ON, Canada.

Walker, S. R., Jamieson, H. E., Lanzirotti, A., & Andrade, C. F. (2005). The speciation of arsenic in iron oxides in mine wastes from the giant gold mine, N.W.T.: Application of synchrotron micro-XRD and micro-XANES at the grain scale. In *The Canadian Mineralogist* (Vol. 43).

Walters, W., Hyde, E. R., Berg-Lyons, D., Ackermann, G., Humphrey, G., Parada, A., Gilbert, J. A., Jansson, J. K., Gregory Caporaso, J., Fuhrman, J. A., Apprill, A., Knight, R., & Walters, C. W. (2015). Improved bacterial 16S rRNA gene (V4 and V4-5) and fungal internal transcribed spacer marker gene primers for microbial community surveys. *MSystems*, *1*(1). https://doi.org/10.1128/mSystems.00009-15

Wang, A. O., Ptacek, C. J., Blowes, D. W., Gibson, B. D., Landis, R. C., Dyer, J. A., & Ma, J. (2019). Application of hardwood biochar as a reactive capping mat to stabilize mercury derived from contaminated floodplain soil and riverbank sediments. *Science of the Total Environment*, *653*, 549–561. https://doi.org/10.1016/j.scitotenv.2018.10.213

Wang, S., & Mulligan, C. (2006). Occurrence of arsenic contamination in Canada: Sources, behavior and distribution. *Science of the Total Environment*, *366*(2–3), 701–721. https://doi.org/10.1016/j.scitotenv.2005.09.005

Waybrant, K. R., Blowes, D. W., & Ptacek, C. J. (1998). Selection of reactive mixtures for use in permeable reactive walls for treatment of mine drainage. *Environmental Science and Technology*, *32*(13), 1972–1979. https://doi.org/10.1021/es9703335

Waybrant, K. R., Ptacek, C. J., & Blowes, D. W. (2002). Treatment of mine drainage using

permeable reactive barriers: Column experiments. *Environmental Science and Technology*, *36*(6), 1349–1356. https://doi.org/10.1021/es010751g

Wilkin, R. T., Acree, S. D., Ross, R. R., Beak, D. G., & Lee, T. R. (2009). Performance of a zerovalent iron reactive barrier for the treatment of arsenic in groundwater: Part 1. Hydrogeochemical studies. *Journal of Contaminant Hydrology*, *106*(1–2), 1–14. https://doi.org/10.1016/j.jconhyd.2008.12.002

Wolthers, M., Van Der Gaast, S. J., & Rickard, D. (2003). The structure of disordered mackinawite. *American Mineralogist*, *88*(11–12), 2007–2015. https://doi.org/10.2138/am-2003-11-1245

Zhu, H., Jia, Y., Wu, X., & Wang, H. (2009). Removal of arsenic from water by supported nano zero-valent iron on activated carbon. *Journal of Hazardous Materials*, *172*(2–3), 1591–1596. https://doi.org/10.1016/j.jhazmat.2009.08.031

Appendix A: *Additional Data Presented in Chapter 2*

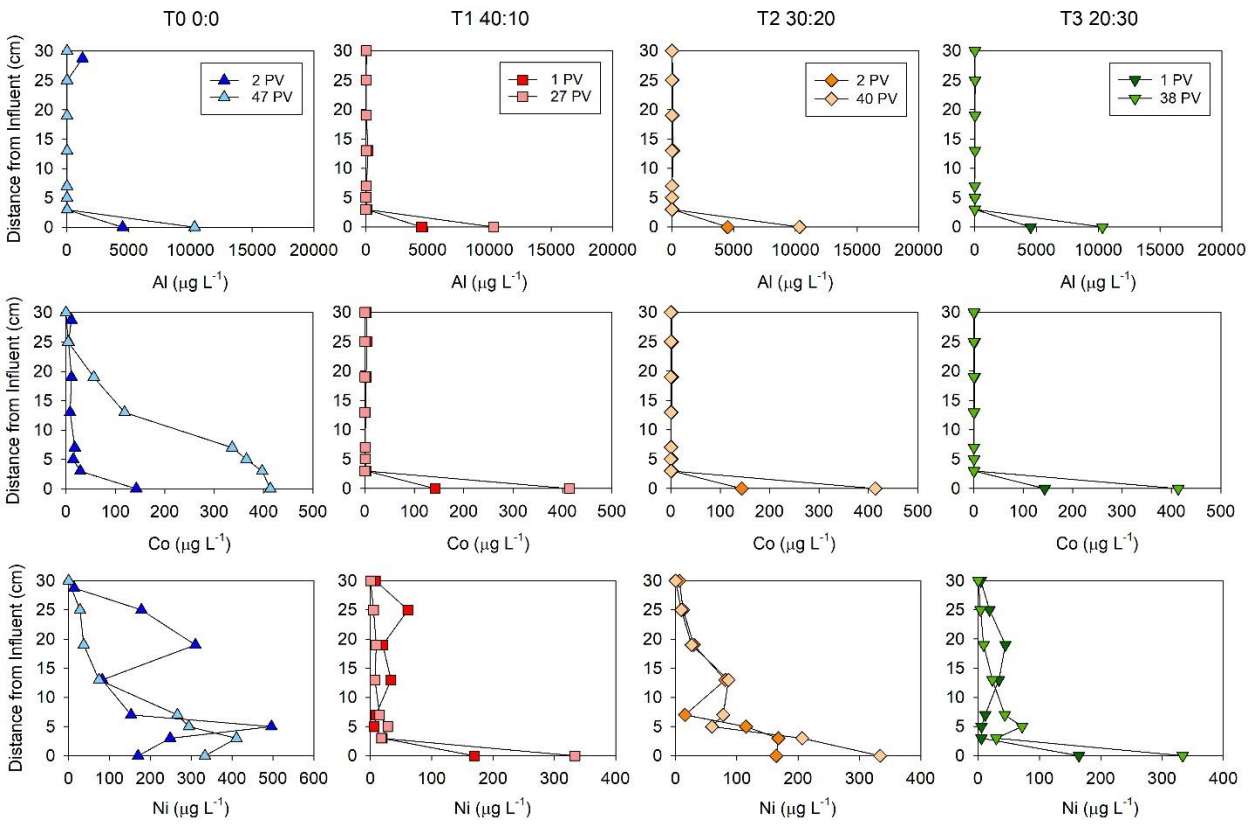

Figure A.1 Concentrations of Al, Co, and Ni in aqueous samples collected along the length of columns T0, T1, T2, and T3 at two different time points. Each column of graphs represents a different experimental column. Distance 0 cm represents the influent concentration and 30 cm represents the effluent concentration. The OC:ZVI ratio of column T0 is 0:0, T1 is 40:10, T2 is 30:20, and T3 is 20:30.

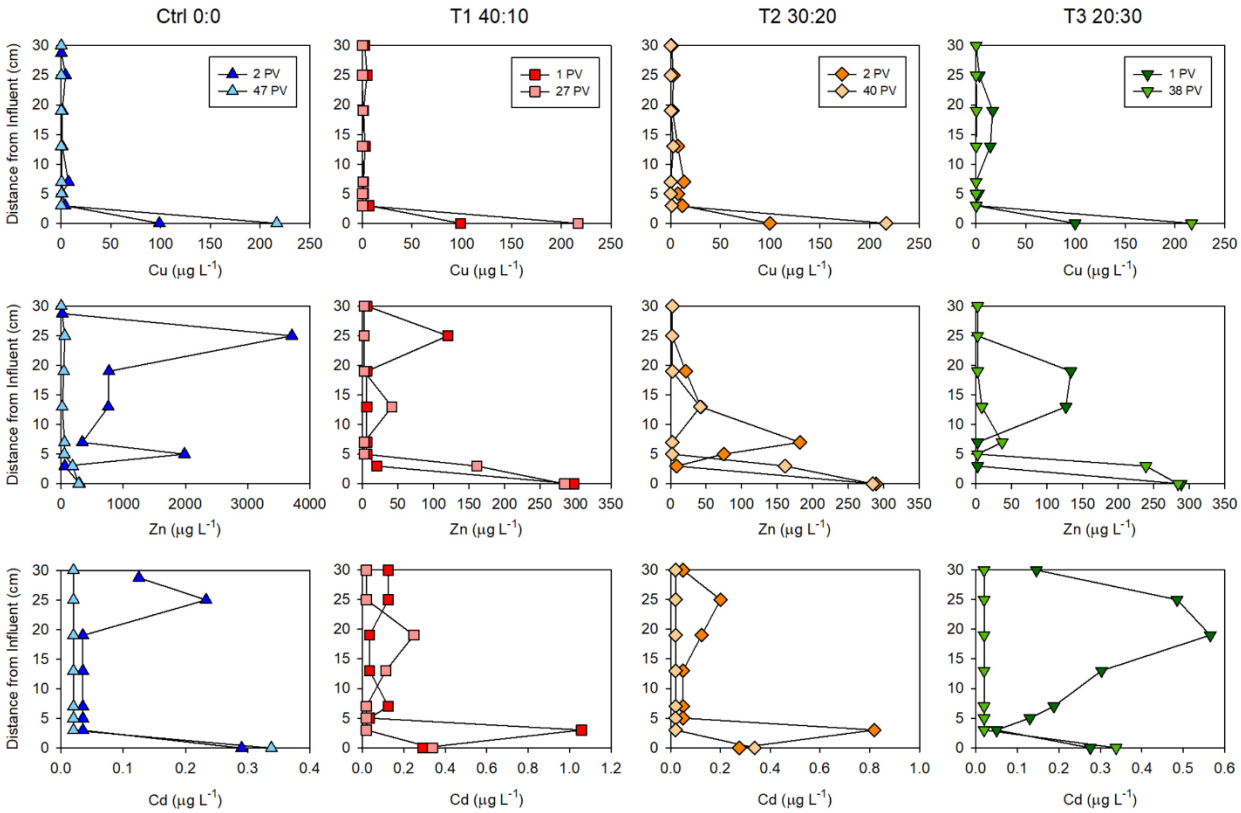

Figure A.2 Concentrations of Cu, Zn, and Cd in aqueous samples collected along the length of columns T0, T1, T2, and T3 at two different time points. Each column of graphs represents a different experimental column. Distance 0 cm represents the influent concentration and 30 cm represents the effluent concentration. The OC:ZVI ratio of column T0 is 0:0, T1 is 40:10, T2 is 30:20, and T3 is 20:30.

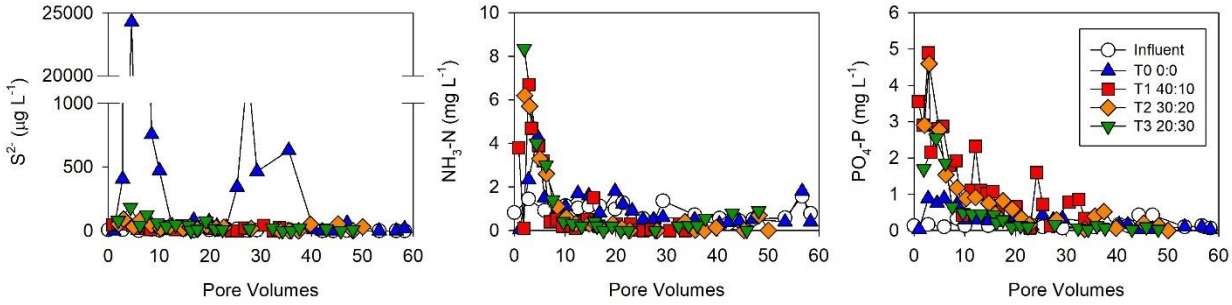

Figure A.3 Concentrations of S^{2-}, NH_3-N, and PO_4-P versus PVs in the influent and effluent of the four columns. The OC:ZVI ratio of column T0 is 0:0, T1 is 40:10, T2 is 30:20, and T3 is 20:30.

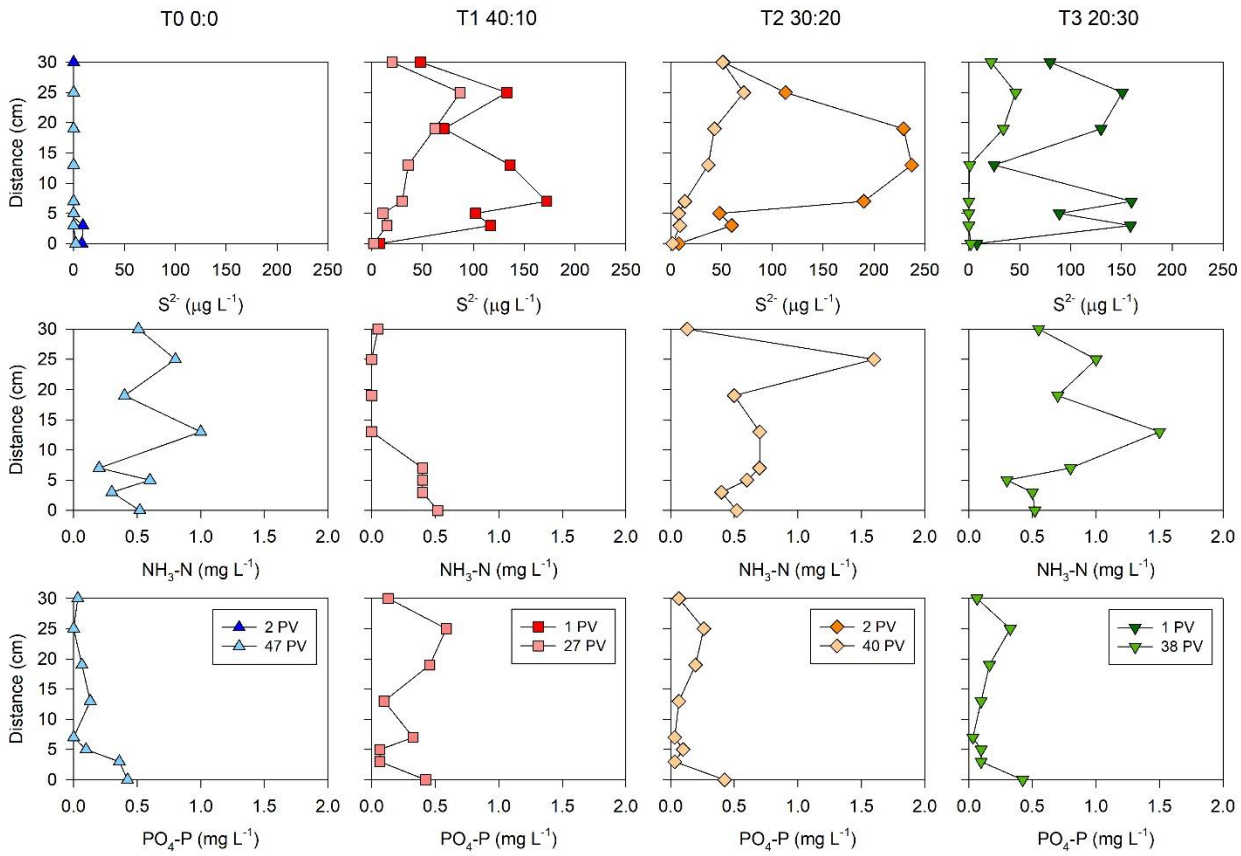

Figure A.4 Concentrations of S^{2-}, NH_3-N, and PO_4-P in aqueous samples collected along the length of columns T0, T1, T2, and T3 at two different time points. Each column of graphs represents a different experimental column. Distance 0 cm represents the influent concentration and 30 cm represents the effluent concentration. The OC:ZVI ratio of column T0 is 0:0, T1 is 40:10, T2 is 30:20, and T3 is 20:30.

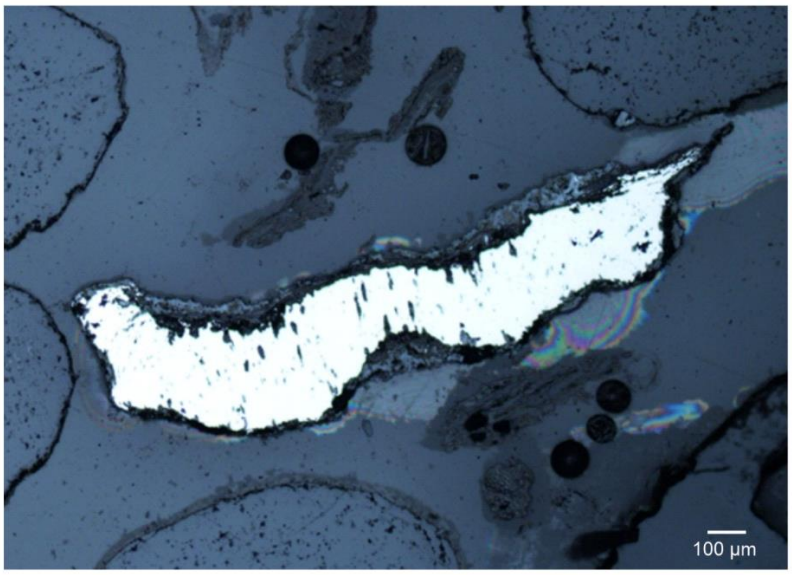

Figure A.5 Reflected light microscopy images of a unreacted ZVI grain.

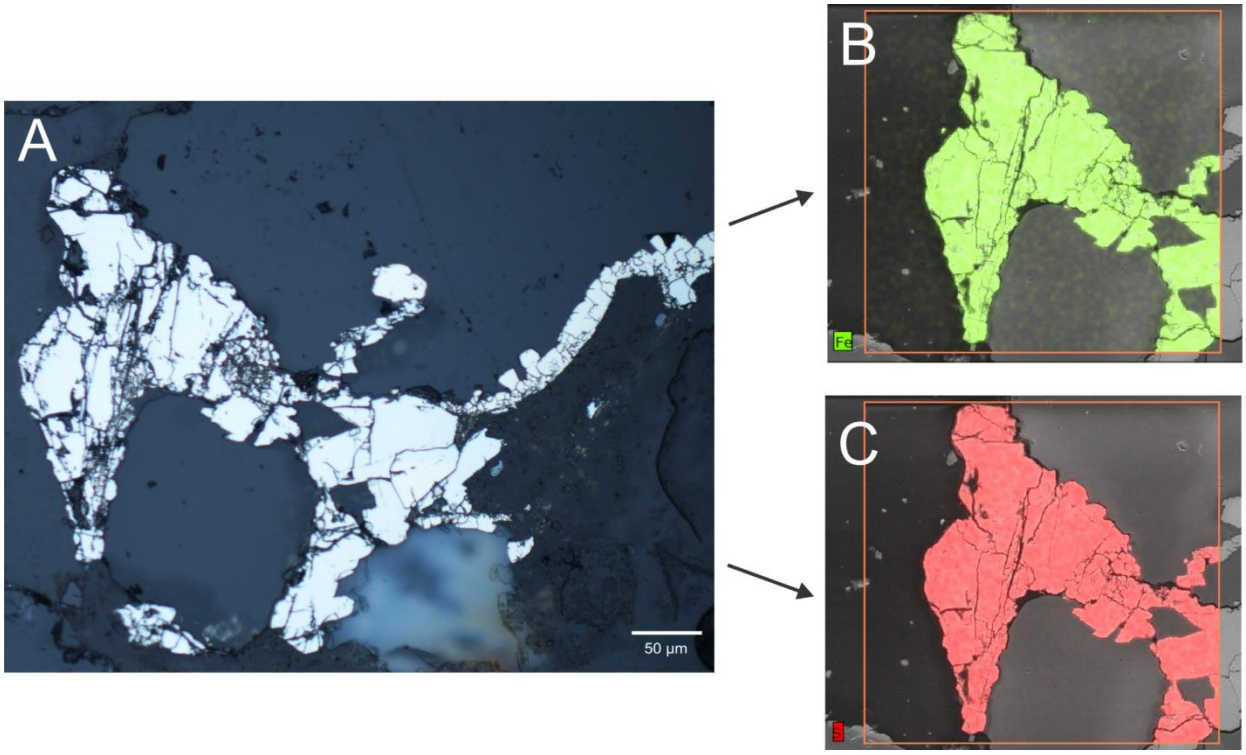

Figure A.6 Reflected light microscopy image of the formation of a secondary precipitate around silica sand grains (A). SEM imaging of Fe- (B) and S- (C) rich precipitate (right).

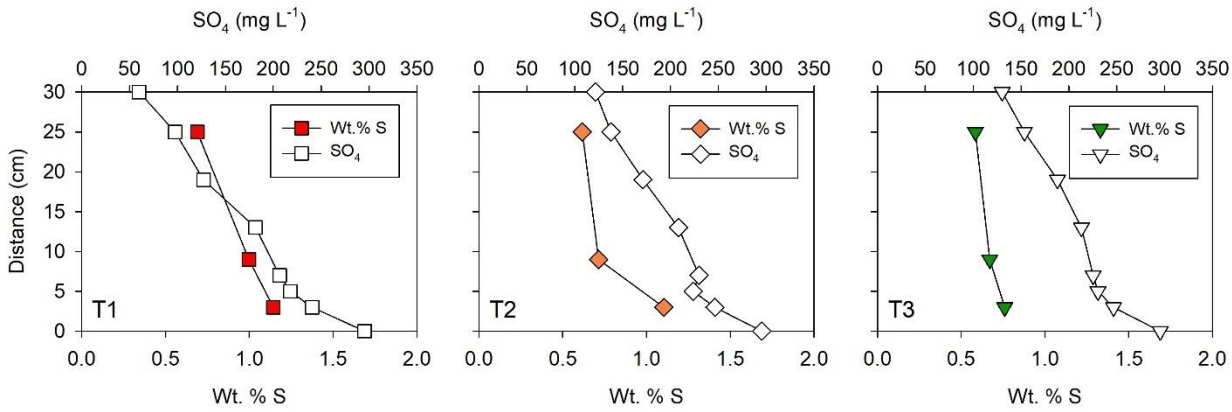

Figure A.7 Comparison between the wt. % S in the solid column material and the aqueous SO_4^{2-} concentrations in the column porewater.

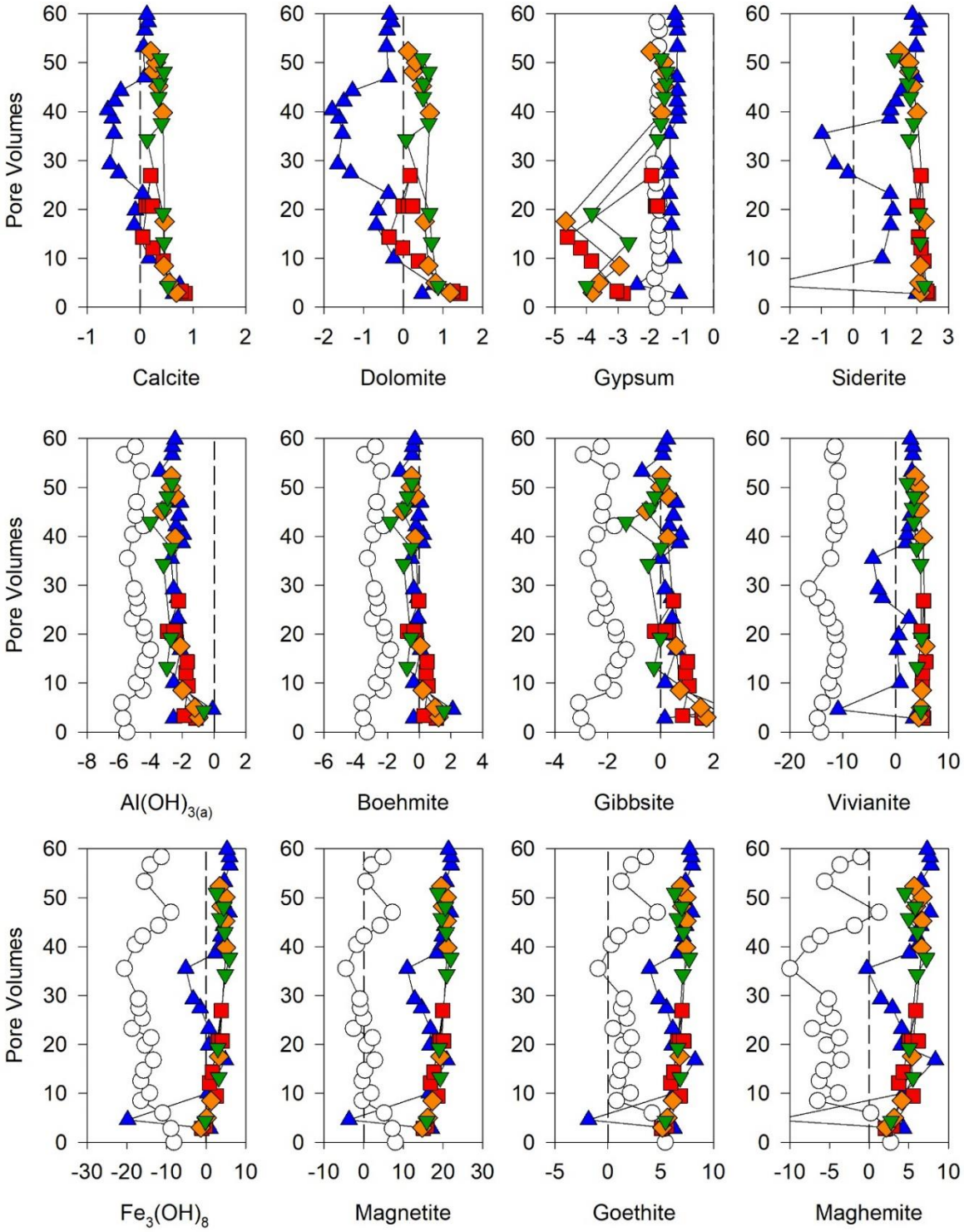

Figure A.8 Saturation indices calculated using PHREEQCI with the WATEQ4F database for potential reaction products. The colours represent the different columns; the white circle is the influent, the blue triangle is T0, the red square is T1, the orange diamond is T2, and the green triangle is T3.

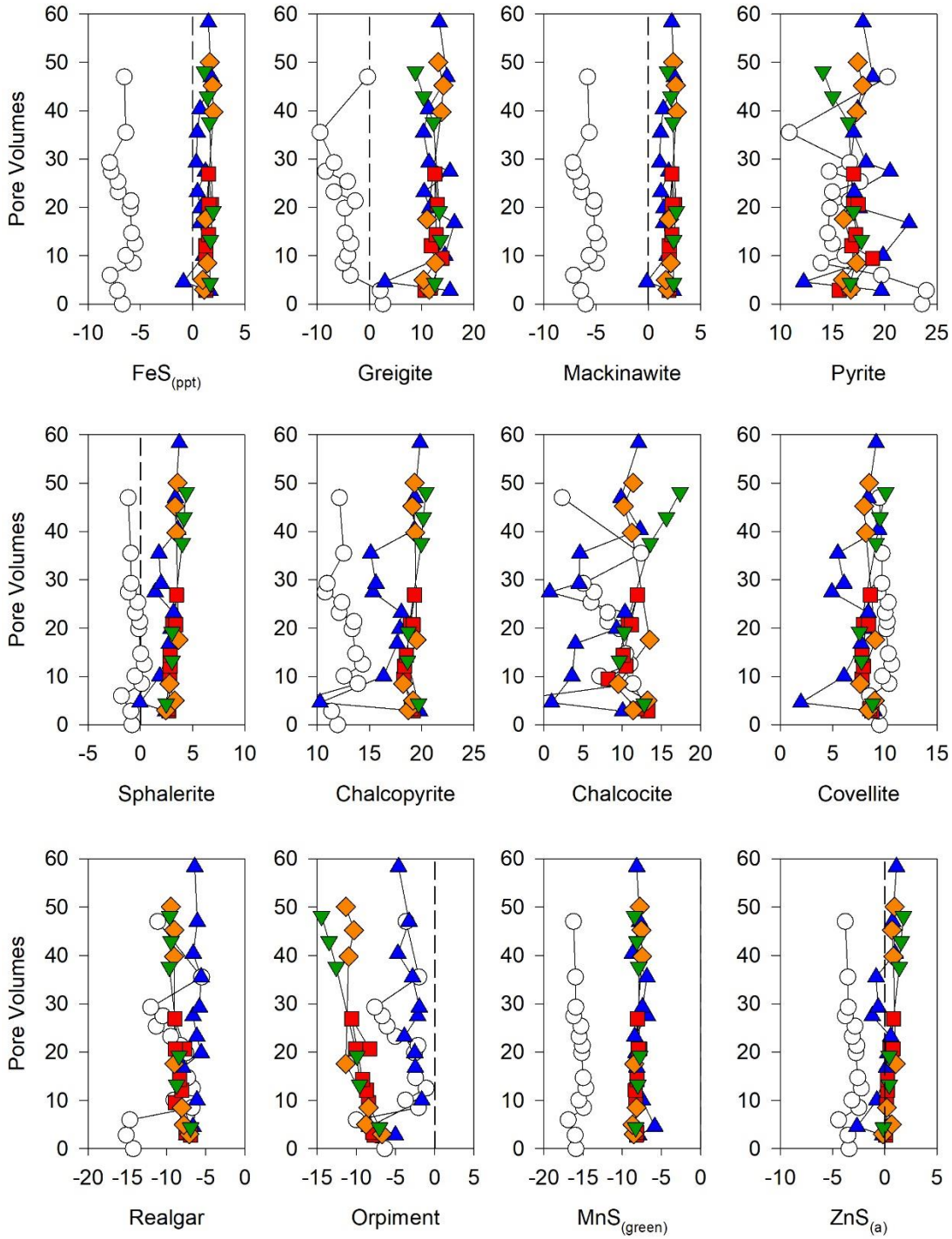

Figure A.9 Saturation indices calculated using PHREEQCI with the WATEQ4F database for sulfide phases. The colours represent the different columns; the white circle is the influent, the blue triangle is T0, the red square is T1, the orange diamond is T2, and the green triangle is T3.

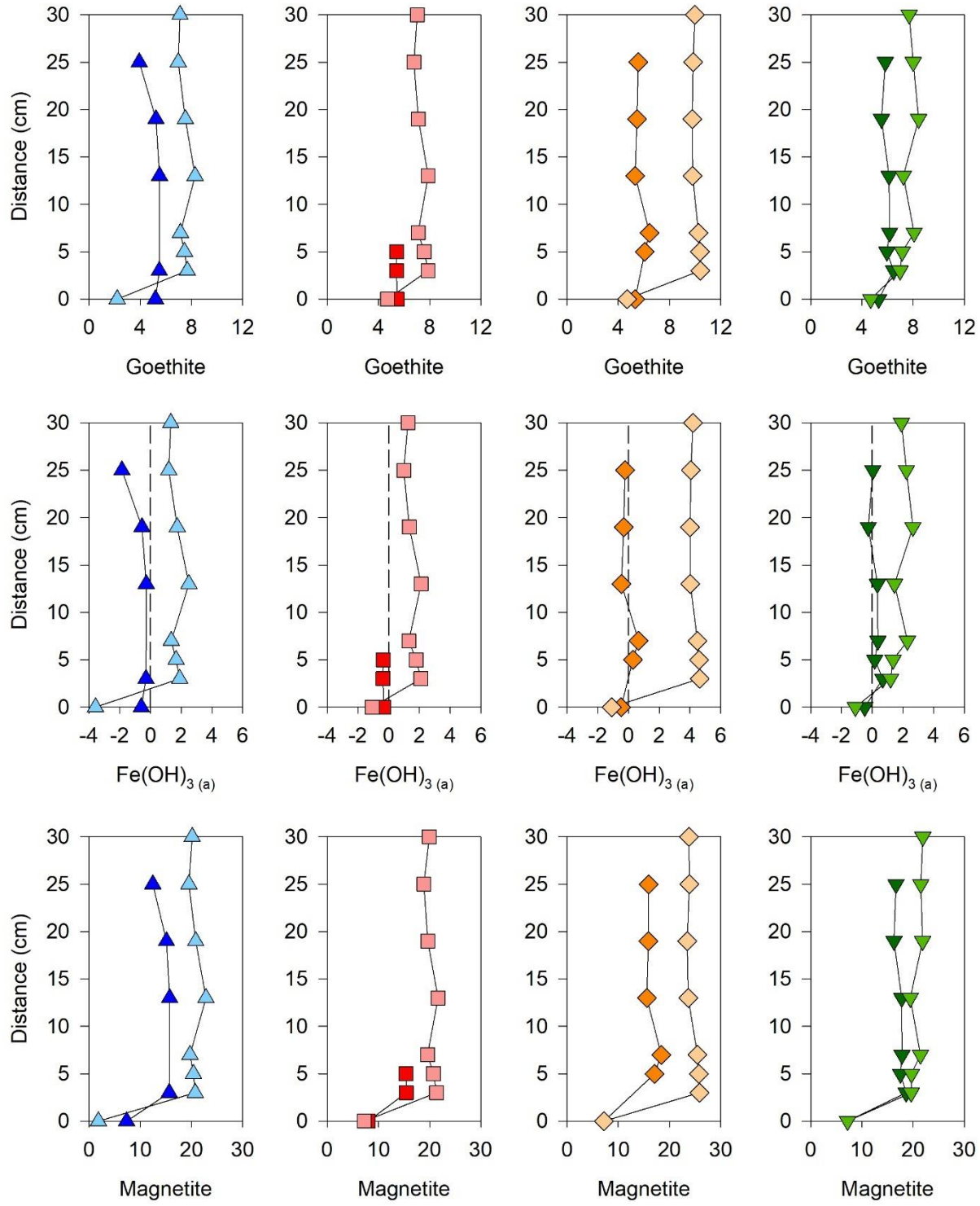

Figure A.10 Saturation indices profiles calculated using PHREEQCI with the WATEQ4F database for goethite, $Fe(OH)_3$, and magnetite. The colours represent the different columns; the white circle is the influent, the blue triangle is T0, the red square is T1, the orange square is T2, and the green triangle is T3. The darker shade of the same colour represents an earlier profile and lighter shades represent a later profile, collected towards the end of the experiment. Distance 0 cm represents the influent SI and 30 cm represents the effluent SI.

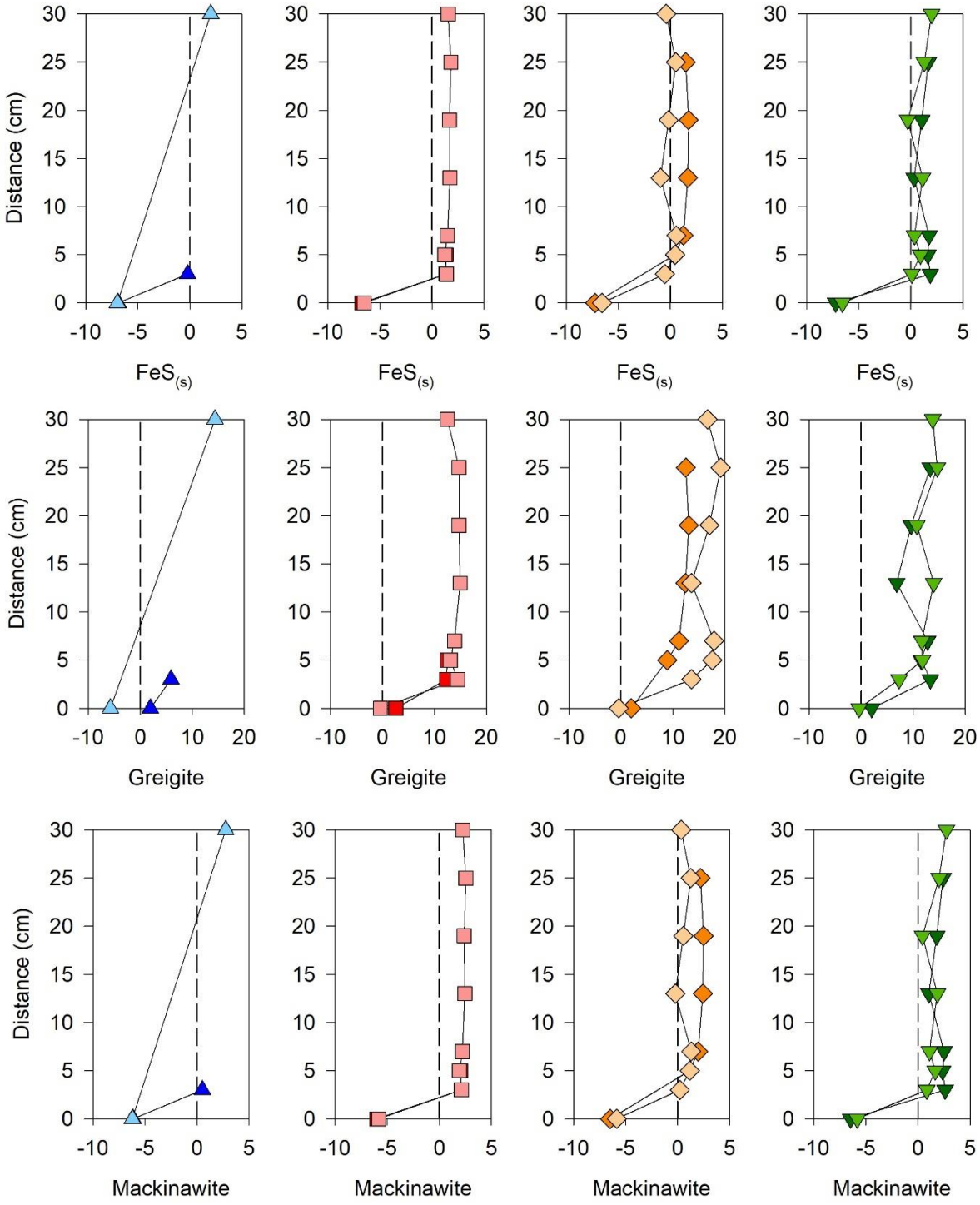

Figure A.11 Saturation indices calculated using PHREEQCI with the WATEQ4F database for $FeS_{(s)}$, greigite, and mackinawite. The colours represent the different columns; the white circle is the influent, the blue triangle is T0, the red square is T1, the orange square is T2, and the green triangle is T3. The darker shade of the same colour represents an earlier profile and lighter shades represent a later profile, collected towards the end of the experiment. Distance 0 cm represents the influent SI and 30 cm represents the effluent SI.

Table A.1 Characteristics of the reactive material.

Property	Silica Sand	Pea Gravel	Limestone	Woodchips	Leaf Compost	Zerovalent Iron
Moisture Content (%)	n/a	n/a	n/a	35.7	9.95	n/a
Bulk Density (g mL^{-1})	1.88	1.90	1.70	0.53	0.77	3.19

Table A.2 Average chemical composition of influent solution (n = 23).

Parameter	Influent Solution
pH	3.50
Eh (mV)	420
Alk (mg L^{-1} as $CaCO_3$)	< 1
As (mg L^{-1})	6.2[a]
Mn (mg L^{-1})	0.66
Cl (mg L^{-1})	0.40
NO_3-N (mg L^{-1})	0.05
SO_4^{2-} (mg L^{-1})	214
Ca (mg L^{-1})	25.4
K (mg L^{-1})	1.5
Mg (mg L^{-1})	12.0
Na (mg L^{-1})	10.2
Si (mg L^{-1})	22.8
Fe (mg L^{-1})	52.3[b]
Al (mg L^{-1})	6.9
Cu (mg L^{-1})	0.14
Ni (mg L^{-1})	0.23
Zn (mg L^{-1})	0.27

[a] *Mean concentration of As during stage II and IV*
[b] *Mean concentration of Fe following spike of $FeSO_4$*

Table A.3 A list of genera detected in the laboratory column samples that are known to catalyze sulfate reduction.

SRB	Mean % of total reads
Desulfovibrio	1.17
*Desulfovibrionaceae**	0.57
Desulfomicrobium	0.52
*Desulfobulbaceae**	0.42
Desulfobulbus	0.41
*Desulfuromonadales**	0.25
*Desulfovibrionales**	0.24
*Desulfobacteraceae**	0.22
Desulfurispora	0.18
Desulfatiglans	0.18
Desulfobacca	0.17
Desulfitibacter	0.16
Desulfomonile	0.11
Desulfitobacterium	0.08
Dethiobacter	0.08
Desulfoprunum	0.08
Desulfuromonas	0.07
Desulfosporosinus	0.07
Desulfurivibrio	0.06
Desulfatitalea	0.05
Desulfotomaculum	0.04
Dethiosulfatibacter	0.04
*Desulfuromonadaceae**	0.03
Desulfocurvus	0.03
*Desulfobacterales**	0.02
Desulfobulbaceae_ge	0.02
*Desulfarculaceae**	0.02
Desulfatirhabdium	0.01
Desulfosarcina	0.01
Desulfovirga	0.01
*Desulfomicrobiaceae**	0.01
Desulfocarbo	<0.01
Desulfuromonadales_ge	<0.01

** Higher taxa that could not be identified on the genus level*

Appendix B: *Additional Data Presented for Chapter 3*

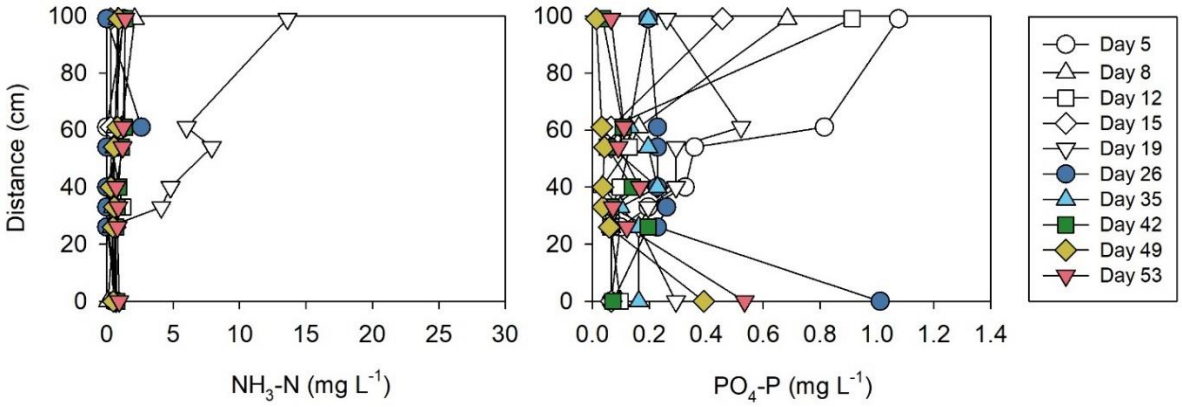

Figure B.1 Nutrient (NH_3-N and PO_4-P) concentrations in aqueous samples collected along the reaction cell length. Distance 0 cm represents influent concentrations and 100 cm represents effluent concentrations.

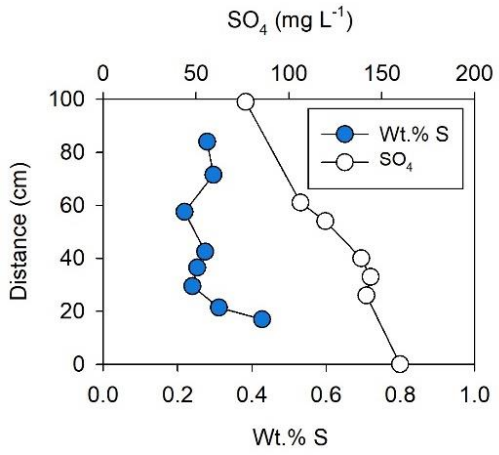

Figure B.2 Wt. % S in the solid reaction cell material and aqueous SO_4^{2-} concentrations from Day 49 in the reaction cell pore water.

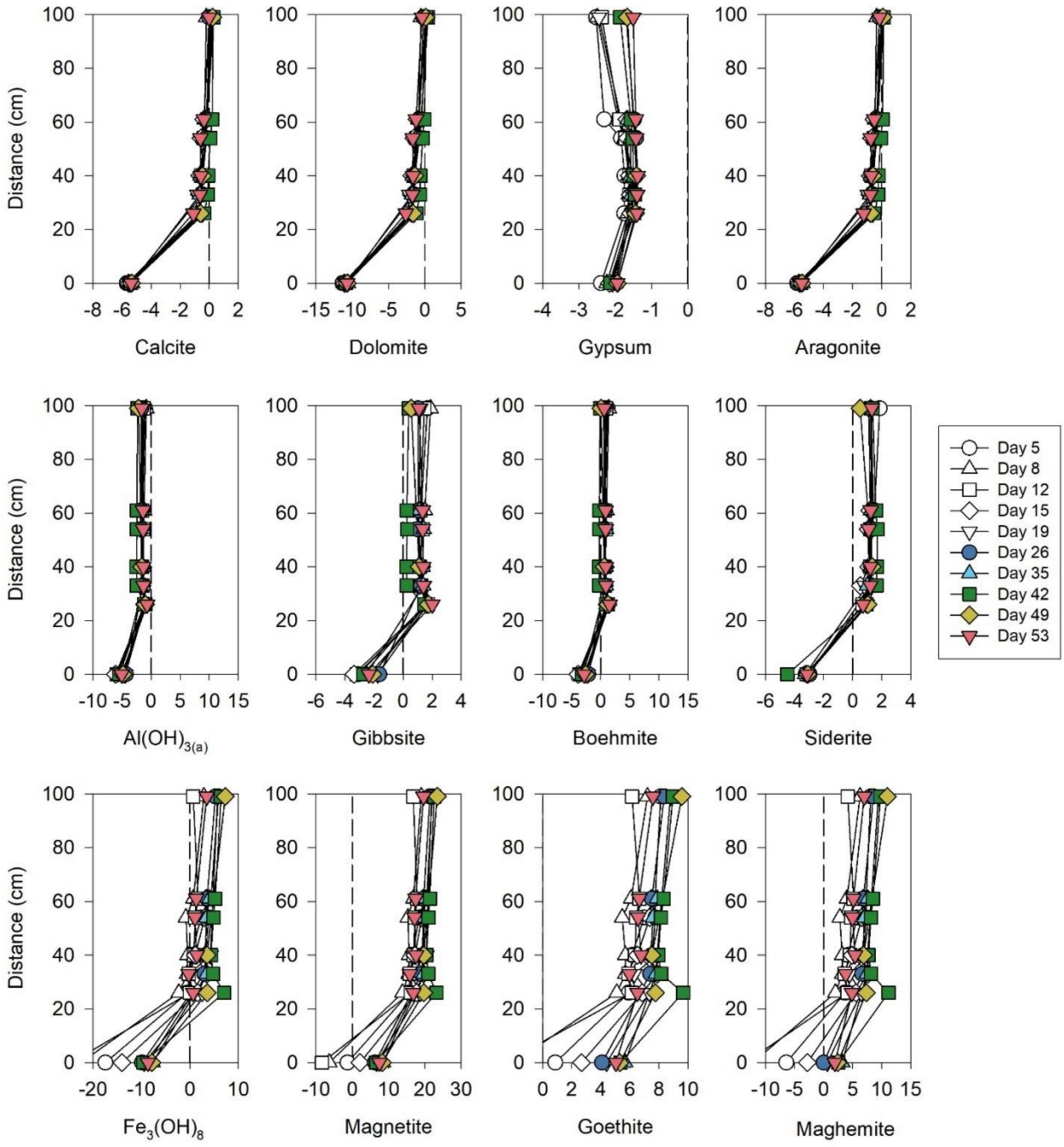

Figure B.3 Saturation indices calculated using PHREEQCI with the WATEQ4F database for potential reaction products. Distance 0 cm represents influent SI and 100 cm represents effluent SI.

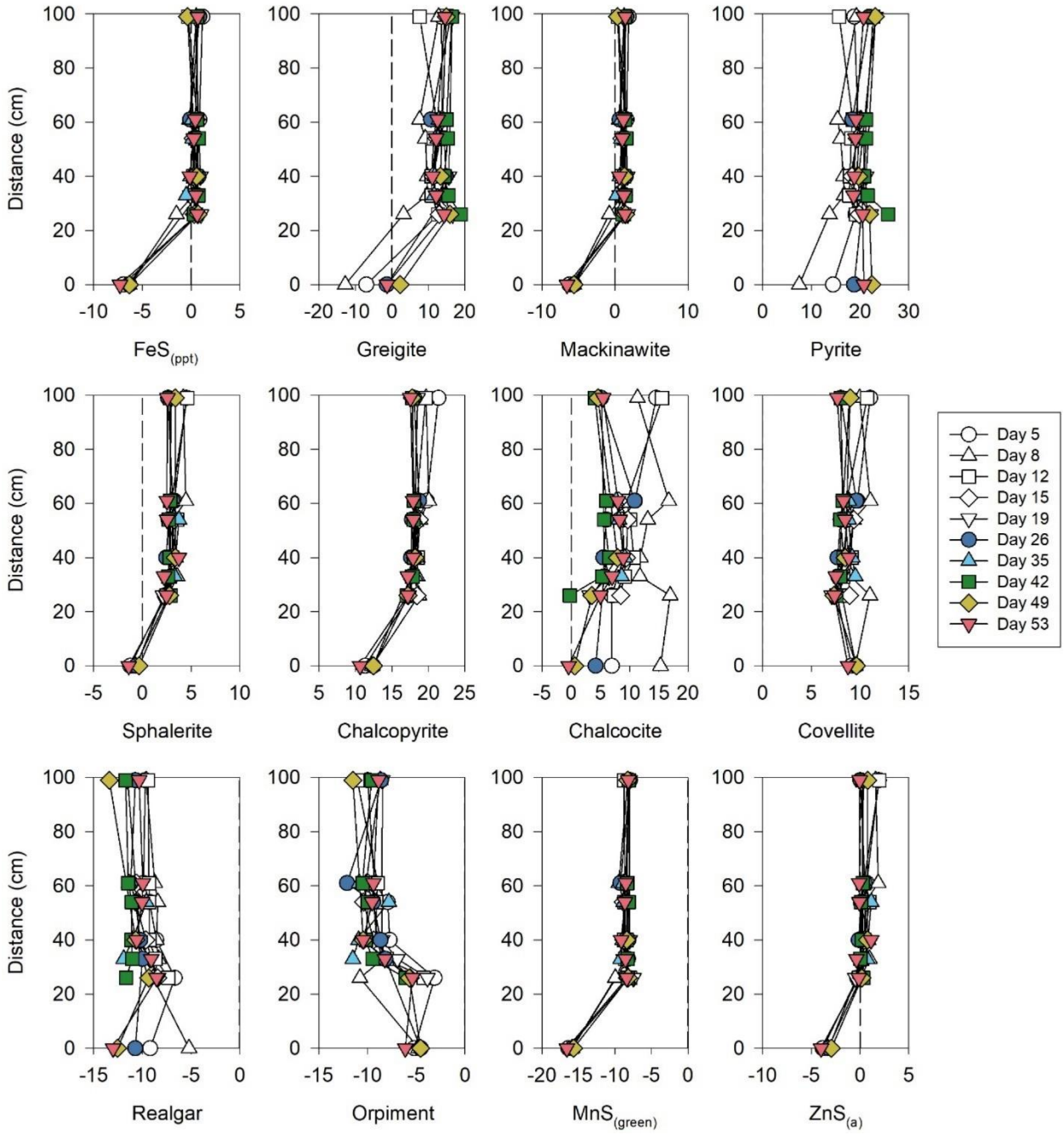

Figure B.4 Saturation indices calculated using PHREEQCI with the WATEQ4F database for sulfide phases. Distance 0 cm represents influent SI and 100 cm represents effluent SI.

Table B.1 Mean chemical composition of influent solution (n = 10).

Parameter	Summer Cell
pH	3.48
Eh (mV)	500
Alk (mg L^{-1} as $CaCO_3$)	< 1
As (mg L^{-1})	1.1
Mn (mg L^{-1})	0.41
Cl (mg L^{-1})	0.20
NO_3-N (mg L^{-1})	0.02
SO_4^{2-} (mg L^{-1})	137
Ca (mg L^{-1})	15.0
K (mg L^{-1})	1.6
Mg (mg L^{-1})	7.3
Na (mg L^{-1})	6.7
Si (mg L^{-1})	22.8
Fe (mg L^{-1})	17.7
Al (mg L^{-1})	3.4
Cu (mg L^{-1})	0.07
Ni (mg L^{-1})	0.13
Zn (mg L^{-1})	0.26

Table B.2 A list of genera detected in the reaction cell samples that are known to catalyze sulfate reduction.

SRB	Mean % of total reads
Desulfomicrobium	0.46
Desulfovibrio	0.36
Desulfitibacter	0.26
Desulfosporosinus	0.23
Desulfurispora	0.13
*Desulfuromonadales**	0.09
Desulfuromonas	0.07
Dethiobacter	0.07
Desulfitobacterium	0.05
Desulfotomaculum	0.04
Desulfobulbus	0.04
*Desulfuromonadaceae**	0.04
Dethiosulfatibacter	0.03
*Desulfobacteraceae**	0.03
*Desulfobulbaceae**	0.03
Desulfurivibrio	0.01
Desulfuromusa	0.01
*Desulfovibrionaceae**	0.01
*Desulfovibrionales**	0.01
Desulfobacca	0.01
Desulfuribacillus	0.01
Desulfatiferula	<0.01
Desulfatirhabdium	<0.01
Desulfobulbaceae_ge	<0.01
Desulfomonile	<0.01
Desulfosarcina	<0.01
Desulfuromonadales_ge	<0.01

** Higher taxa that could not be identified on the genus level*

Appendix C: *Additional Data Presented for Chapter 4*

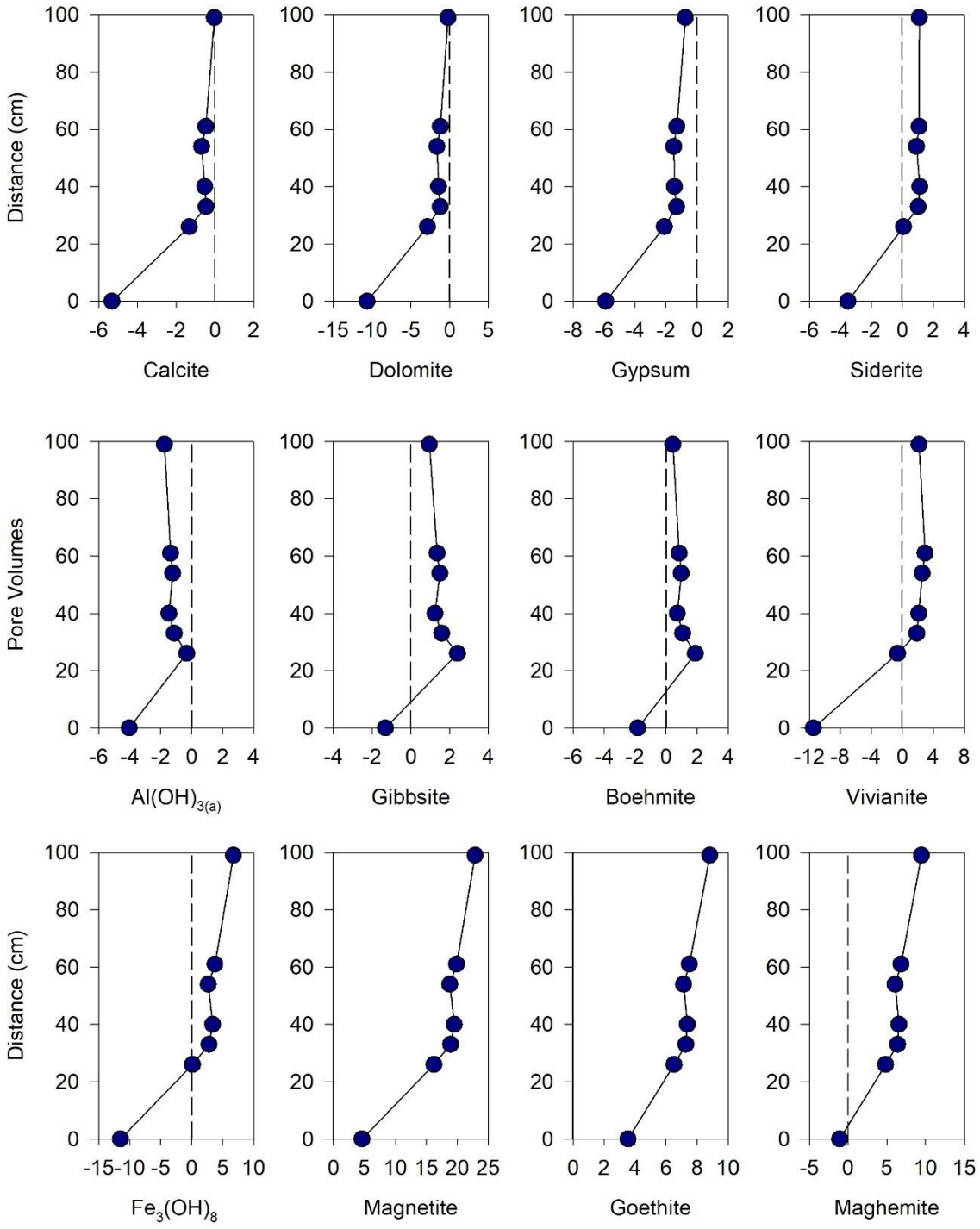

Figure C.1 Saturation indices calculated using PHREEQCI with the WATEQ4F database for potential reaction products. The profile shown was collected on Day 9 of the autumn cell trial. Distance 0 cm represents influent SI and 100 cm represents effluent SI.

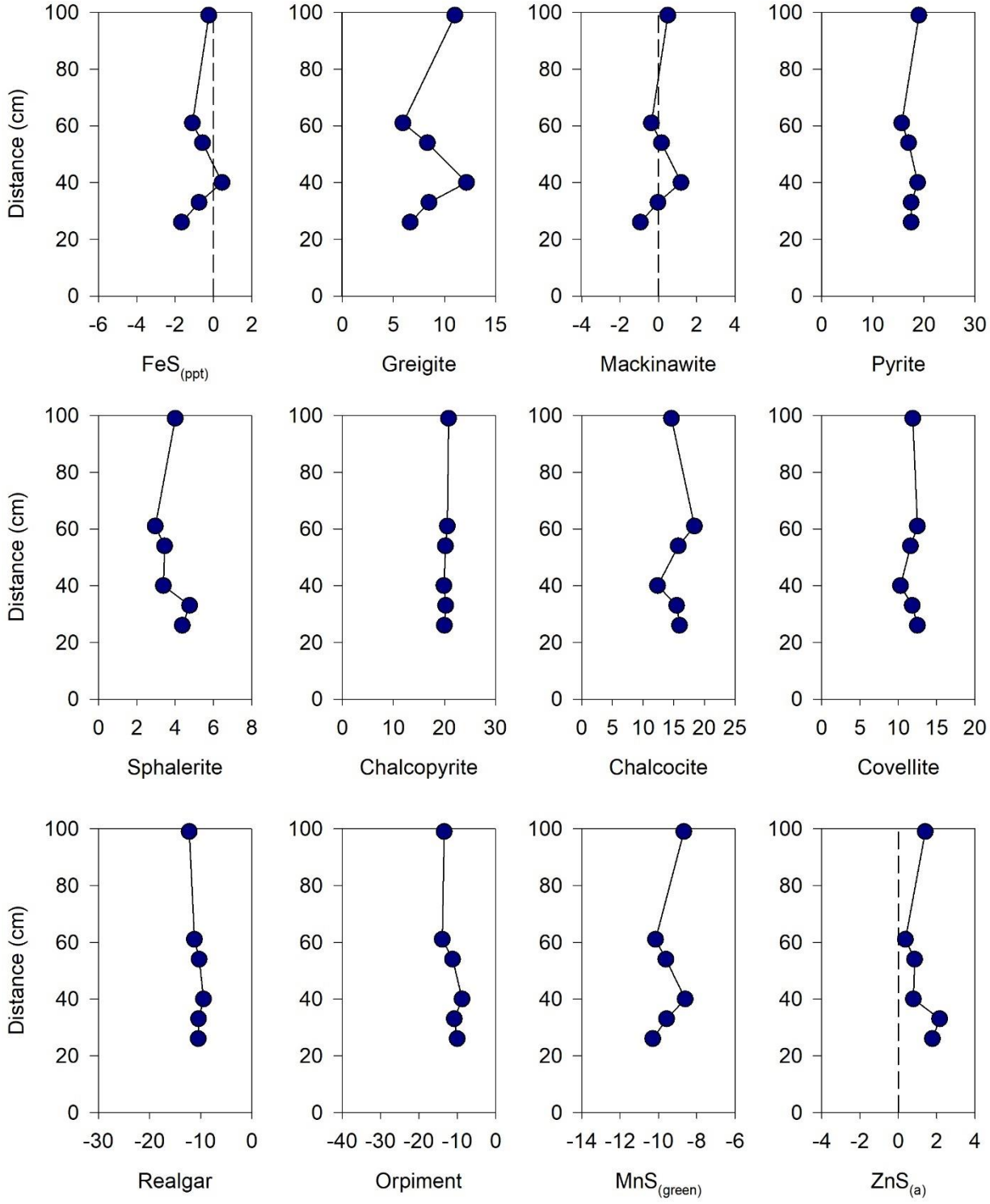

Figure C.2 Saturation indices calculated using PHREEQCI with the WATEQ4F database for sulfide phases. The profile shown was collected on day 9 of the autumn cell trial. Distance 0 cm represents influent SI and 100 cm represents effluent SI.

Table C.1 A list of genera detected in the autumn reaction cell samples that are known to catalyze sulfate reduction.

SRB	Mean % of total reads
*Desulfuromonadales**	0.26
Desulfitibacter	0.22
Desulfobulbus	0.14
*Desulfobacteraceae**	0.12
Desulfomicrobium	0.10
Desulfuromonas	0.08
Dethiobacter	0.07
Desulfovibrio	0.06
Desulfurivibrio	0.06
*Desulfuromonadaceae**	0.05
Desulfitobacterium	0.04
Desulfotomaculum	0.04
*Desulfobulbaceae**	0.03
*Desulfovibrionales**	0.02
Desulfurispora	0.02
Desulfosporosinus	0.02
Desulfuromonadales_ge	0.01
Dethiosulfatibacter	0.01
Desulfatiglans	0.01
Desulfocurvus	0.01
Desulfobacca	0.01
Sulfurospirillum	0.01

** Higher taxa that could not be identified on the genus level*